University of Computer Studies (Mandalay)

Department of Advanced Science and Technology

Ministry of Science and Technology

The Republic of the Union of Myanmar

JOURNAL OF INFORMATION TECHNOLOGY, RESEARCH AND INNOVATION

December, 2024

JiTRi 2024

JOURNAL OF INFORMATION TECHNOLOGY, RESEARCH AND INNOVATION

December, 2024

Organized by

University of Computer Studies

(Mandalay)

Volume-4, Issue-2

JOURNAL OF INFORMATION TECHNOLOGY, RESEARCH AND INNOVATION

JITRI, 2024

Vol-4, Issue-2

UNIVERSITY OF COMPUTER STUDIES (MANDALAY)

Acknowledgements for Reviewers and Organizing members of JITRI

The Journal of Information Technology, Research and Innovation (JITRI) 2024 technical program committee would like to express the deepest appreciation to the external reviewers and organizing members for collaborating to publish this journal successfully. JITRI (2024) is published as the seventh time in order to undertake research in their respective fields of studies. Finally, we would like to thank all the authors who had submitted their research papers by making their great efforts in the Journal of Information Technology, Research and Innovation (JITRI), 2024, Vol-4, Issue-2.

Table of Contents

Journal of Information Technology, Research and Innovation 2024, Vol-4, Issue-2

ANALYZING MOTION DETECTION PATTERNS USING PIR SENSOR AND ARDUINO WITH PLX DAQ SYSTEM

Phyu Thel Ei[1], and Hmwe Hmwe Kyu[2]

[1,2] Department of Physics, East Yangon University
phyuthel.ei92@gmail.com,hkyu332@gmail.com

ABSTRACT

This research investigates motion detection patterns using a PIR sensor integrated with an Arduino microcontroller, with real-time data logging facilitated by the PLX DAQ system and Microsoft Excel. The primary objective is to develop and analyse a cost-effective and efficient motion detection system suitable for applications such as security monitoring and automation. The system utilizes the PIR sensor to detect infrared radiation emitted by moving objects, with event data logged into Excel for analysis. Graphs are generated to visualize motion trends over time. The study evaluates the performance of the system under various conditions, including detection accuracy, range, and response time. Results demonstrate the reliability of the system for practical applications, while also highlighting potential limitations such as environmental sensitivity. This project contributes to the growing assumption of low-cost microcontroller-based solutions in automation and monitoring systems.

KEYWORDS

Arduino, Microsoft Excel, PIR, PLX DAQ

1. INTRODUCTION

Motion detection systems play a crucial role in modern automation and security applications, ranging from home security systems to industrial monitoring. Traditional motion detection systems often involve complex and costly setups, which may not be accessible to all users. This project focuses on developing a cost-effective and efficient motion detection system using an Arduino microcontroller and a Passive Infrared (PIR) sensor.[1]

The PIR sensor detects infrared radiation emitted by moving objects, making it an ideal choice for detecting human or animal motion. Data from the sensor is logged in real-time using the PLX DAQ system, which interfaces with Microsoft Excel. This approach enables convenient data visualization and analysis, providing insights into motion patterns [3,6].

The aim of this research is to evaluate the performance of the proposed motion detection system in various conditions, including its accuracy, response time, and detection range. Additionally, the project explores the possibility of using such systems in practical applications, such as energy-efficient automation and security monitoring.[5] By using the Arduino platform and open-source tools, this project explores to promote affordable and customizable solutions for motion detection challenges. The architecture of the whole system is as shown in Figure 1.

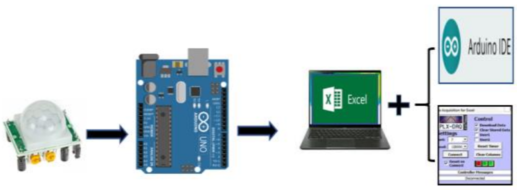

Figure 1. The architecture of the whole system

2. METHODOLOGY

The methodology of this project involves the design, implementation, and testing of a motion detection system using an Arduino microcontroller and a Passive Infrared

(PIR) sensor. The system logs motion detection data in real time to Microsoft Excel via the PLX DAQ platform. This structured methodology ensures the systematic design, implementation, and evaluation of the motion detection system, contributing to the development of a practical and affordable solution for automation and security purposes.

2.1. Arduino Microcontroller

The Arduino microcontroller is an open-source, user-friendly platform designed for creating electronic projects. It serves as the brain of the system, capable of reading inputs from sensors, processing data, and controlling outputs like LEDs, motors, or other devices.[2] With its functional and conveniently of programming, it is widely used in educational, experimental, and prototyping applications. Figure 2. shows the photograph of Arduino Uno microcontroller.

Figure 2. The photograph of the Arduino Uno Microcontroller

2.2. Passive Infrared (PIR) sensor

A Passive Infrared (PIR) sensor is an electronic device used to detect motion by measuring infrared radiation emitted by objects in its field of view. PIR sensors are commonly used in security systems, automatic lighting, and occupancy detection. They operate by detecting changes in infrared radiation caused by the movement of warm objects, such as humans or animals, within their detection range. The sensor is energy-efficient, cost-effective, and easy to integrate with microcontrollers like Arduino, making it ideal for various motion-sensing applications.[4] Figure 3. shows the front side view and back side view of PIR sensor.

Figure 3. The front side view and back side view of PIR sensor

2.3. PLX DAQ Software

PLX DAQ (Parallax Data Acquisition) is a free software tool that enables real-time data logging from microcontroller-based systems, like Arduino, directly into Microsoft Excel. It allows users to visualize and analyze sensor data efficiently by providing features such as time-stamping, live graphs, and custom data fields. PLX DAQ simplifies the process of interfacing hardware with Excel, making it a powerful solution for experiments, monitoring, and data-driven projects in fields like physics, engineering, and IoT. The installation photo of PLX DAQ software is illustrated in Figure 4. The control box view of PLX DAQ window is illustrated in Figure 5.

Figure 4. The installation photo of PLX DAQ software

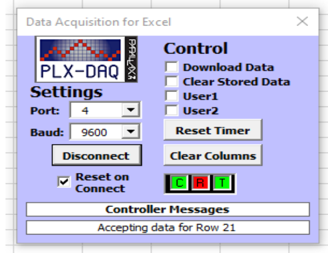

Figure 5. The control box view of PLX DAQ window

2.4. Circuit Construction

The circuit for the motion detection system using Arduino and a PIR sensor is simple and straightforward. Firstly, VCC pin of PIR sensor connects with 5V pin of Arduino microcontroller. Then, GND pin of PIR sensor connects with GND pin of Arduino microcontroller. The output pin of PIR sensor connects with Digital Pin 2 of Arduino microcontroller. The schematic circuit diagram is as illustrated in Figure 6. After making connection between PIR and Arduino, link with Arduino Uno to the computer using a USB cable. This will provide power to the Arduino and establish communication for data logging. The Arduino code is written in the Arduino IDE and uploaded to the microcontroller. The code continuously monitors the PIR sensor and logs the motion detection status ("Motion Detected" or "No Motion") with timestamps in Excel using the PLX DAQ interface. The PIR sensor detects motion by sensing changes in infrared radiation. The PIR sensor is connected to the Arduino's digital input pin to transmit motion signals. The Arduino is powered via USB and communicates with the PC for data logging. The system is configured to trigger motion detection events when the PIR sensor outputs a HIGH signal. Motion detection events are recorded in Excel, including timestamps for each event. The logged data is visualized using graphs to analyse motion patterns over time. To monitor serial output in Arduino IDE, open serial monitor window and set the baud rate to 9600, then observe status "Motion Detected" or "No Motion". The photograph of viewing on serial monitor box in Arduino IDE is illustrated in Figure 7. Then close the serial monitor before connecting to PLX DAQ. After then match the COM port number between Arduino IDE and PLX DAQ. This software links with Excel to enable real-time data logging. The recorded data are displayed on Excel spreadsheet. The data on Excel spreadsheet can express the current value and it can be logged like computer manner. The live graph can be drawn as usual Excel spreadsheets for user need. The Figure 8 shows the list of data on Excel spreadsheet. The list of data with live graph is showed in Figure 9. The successful implementation of the system is illustrated in Figure 10.

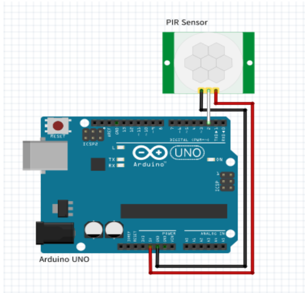

Figure 6. The schematic circuit diagram

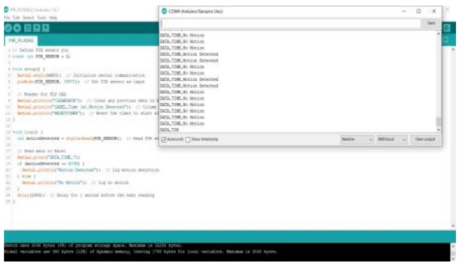

Figure 7. The photograph of viewing the data on serial monitor

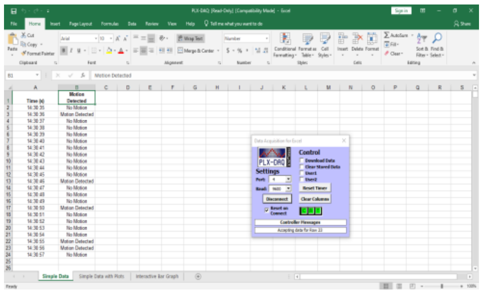

Figure 8. The list of data on Excel spreadsheet

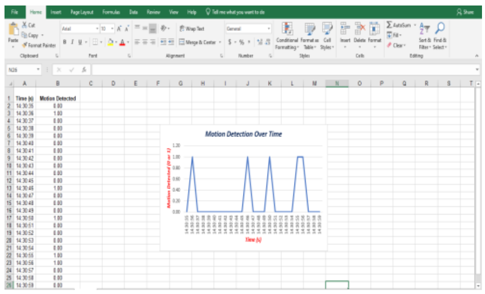

Figure 9. The list of data with graph

Figure 10. The successful implementation of the system

2.5. Results and Discussion

The motion detection system was implemented and tested successfully, with the PIR sensor reliably detecting motion and logging events into Microsoft Excel via the PLX DAQ system. The PIR sensor effectively detected motion within its specified range (up to 7 meters) and field of view (approximately 120°). The system responded promptly to movements, demonstrating high sensitivity under optimal conditions. The PLX DAQ system successfully recorded motion events in Excel with timestamps. The logged data provided clear insights into motion patterns over time, which were visualized through graphs. These visualizations are crucial for analyzing motion trends in applications such as security monitoring or automation. The system logged events almost instantaneously, with negligible delays, ensuring real-time monitoring capability.

This project highlights the effectiveness of using Arduino and a PIR sensor for motion detection. The integration with PLX DAQ and Excel provides an accessible platform for data logging and analysis. The system demonstrated a cost-effective and innovative solution for motion detection. Its assembly and low power consumption make it suitable for applications such as home security systems, automatic lighting, and occupancy monitoring. Future enhancements could include wireless connectivity, additional sensors for integration with IoT platforms to expand its functionality and scope. Overall, the system meets its intended objectives, offering a practical and affordable solution for motion detection and data analysis.

3. Conclusions

This project successfully demonstrated a low-cost, efficient motion detection system using an Arduino microcontroller and a PIR sensor, with data logged in real-time using the PLX DAQ system integrated with Microsoft Excel. The system was able to detect motion accurately and log corresponding events, providing a clear visualization of motion patterns over time. The simplicity of the design, combined with the functionality of Arduino and Excel, makes this system suitable for applications in security, automation, and monitoring. The results confirm the possibility of using an Arduino-based platform for motion detection, highlighting its potential for customization and ability. However, further enhancements, such as integrating additional sensors or wireless communication modules, could improve functions of the system and extend its range of applications. This study contributes to the development of accessible and affordable technologies for real-world motion detection and monitoring systems.

Acknowledgements

I would like to thank my deep appreciation to Rector, Pro-rectors, Professor and Head, Reviewers, Editorial Board and organizing committee at University of Computer Studies (Mandalay) for allowing this paper. I would like to express my gratitude to everyone who supported me throughout this research work.

References

[1] A. Mahmood, I. Ahmad, and M. Saeed, "Cost-Effective Motion Detection Using PIR Sensors," *International Journal of Electronics and Communication Engineering*, vol. 12, no. 3, pp. 45–50, 2020.
[2] Arduino Uno Datasheet. [Online]. Available: https://www.arduino.cc.
[3] J. Smith and A. Brown, "Real-Time Data Logging and Analysis Using Arduino and

Excel," *Journal of Embedded Systems*, vol. 15, no. 2, pp. 121–127, 2019.
[4] M. Rouse, "What is a PIR Sensor?" *TechTarget* [Online]. https://www.techtarget.com.
[5] P. Wilson, "Infrared Technology in Modern Sensor Systems," *Sensors and Actuators Journal*, vol. 25, no. 4, pp. 67–75, 2017.
[6] R. Johnson, *Microcontroller Applications for Monitoring and Control Systems*. New York: McGraw Hill Education, 2018.

Authors Biography

First Author

Daw Phyu Thel Ei was born in Thongwa Township, Yangon Division. She obtained her first degree (B.Sc.) in 2011 from Yangon University of Distance Education followed by master degree (M.Sc.) in 2016 and master of research degree (M.Res.) in 2017 from East Yangon University. She received the Young Researcher Best Paper Award for Sciences at EYU 25th Anniversary Silver Jubilee Research Symposium. She is currently serving as a demonstrator in Physics Department at East Yangon University. She was conducted the departmental research and published her works in University Research Journals. Her areas of interest include Electronics and Engineering Physics.

Second Author

Dr. Hmwe Hmwe Kyu is working as Professor and Head of Physics Department, East Yangon University. She got the PhD degree from Yangon Technological University. She is always happy to help her students and contributes to their understanding of papers. She regularly conducts reviews of research papers with other students and teachers. She is currently working enthusiastically in field of Electronics.

EXPLORING IDEOLOGICAL DISCOURSE IN STATE-RUN NEWSPAPERS THROUGH LATENT DIRICHLET ALLOCATION (LDA) TOPIC MODELLING

Moe Phyu Phyu Khaing[1], Khaing Zar Win[2], and Nan Saw Kalayar[3]

[1,3]Faculty of Information Science, University of Computer Studies (Taunggyi),
[2]Department of Information Science, University of Technology, (Yatanarpon Cyber City)
moephyuphyukhaing23@gmail.com, khaingzarwinms@gmail.com,
nansawkalayar@ucstgi.edu.mm

ABSTRACT

State-run media significantly influence public opinion and governmental ideologies, reflecting the political landscape and societal norms. This paper examines the ideological discourse in state-run newspapers using Latent Dirichlet Allocation (LDA) topic modelling. By analyzing editorial article from "The Global New Light of Myanmar," this analysis uncovers key themes that reveal governmental narratives and societal values. Nuclear issue is chosen for analysis due to its critical implications for national security, international relations, and public safety. The discourse on nuclear topics in state media can shape public perceptions, intertwining with national identity and geopolitical strategy. The experimental results show that the results in (table-2) are strong and highly interpretable topics with high perplexity and coherence scores. Results in (table-2) identifies three main topics related to nuclear issues: (1) Global Nuclear Weapons Landscape, (2) Nuclear Incidents and Their Consequences, and (3) WWII Atomic Bomb. These findings offer insights into how state-run newspapers influence public discourse on nuclear matters, that enhances understanding of the media's role in shaping or challenging governmental authority.

KEYWORDS

LDA Topic Modelling, State-Run media, Public Opinion, Governmental Narratives

1. INTRODUCTION

State-run newspapers serve as a critical medium for disseminating governmental ideologies and shaping public discourse. These publications often reflect the political landscape and can significantly influence societal norms and values. By analyzing the language and themes present in state-run media, researchers can gain insights into how these outlets construct narratives that align with governmental objectives. This analysis employs Latent Dirichlet Allocation (LDA) topic modelling to explore the ideological discourse in state-run newspapers, providing a quantitative approach to understanding the underlying themes that emerge from these publications.

Critical Discourse Analysis (CDA) has been widely utilized to examine how language functions within media contexts, revealing the connections between language, power, and ideology [3]. For instance, Fairclough's Three-Dimensional Model has been instrumental in analyzing news reports by focusing on textual features, discursive practices, and sociocultural contexts [4]. Recent studies have demonstrated the effectiveness of LDA in uncovering latent themes within media texts.

The choice of “The Global New Light of Myanmar” as the sole data source was based on its status as the primary state-run newspaper in Myanmar, reflecting the official ideological stance of the government. As a key medium for disseminating ideological discourse, this newspaper provides valuable insights into government perspectives. However, this choice limits the generalizability of the findings to other media sources or different geopolitical contexts. Future studies could expand the analysis by including multiple newspapers to enhance the generalizability of the results.

This paper aims to build on existing research by applying LDA topic modelling to a corpus of articles from state-run newspapers. By identifying key topics and their prevalence over time, this analysis seeks to understand how these publications shape public perception and reflect governmental priorities. Additionally, this analysis will analyze how the identified topics shift in response to political events and policy changes, providing a nuanced understanding of the role that state-run media plays in constructing ideological discourse. By utilizing LDA topic modelling, this analysis provides valuable insights into how state-run newspapers construct and disseminate ideological discourses that influence public opinion and shape public discourse.

2. Literature Review

Discourse analysis has long been a vital tool in understanding how language constructs social realities, particularly within media contexts. Researchers have employed various frameworks to investigate the interplay between language, ideology, and power dynamics. Gee (2014) emphasizes that discourse is not merely a reflection of reality but a means through which social practices are enacted and reproduced. This perspective aligns with the views of Fairclough (1989), who argues that language is intrinsically linked to power relations, shaping how individuals and groups perceive and interact with the world around them. The application of these theories to media studies has led to a deeper understanding of how news narratives can influence public opinion and reinforce societal norms [3][4].

Recent advancements in computational linguistics have introduced innovative methodologies for analyzing large corpuses of text. Latent Dirichlet Allocation (LDA) has gained traction as an effective tool for topic modelling, enabling researchers to uncover latent themes within textual data. Blei et al. (2003) introduced LDA as a generative probabilistic model that can identify topics based on word co-occurrence patterns, making it particularly useful for analyzing media content. Studies such as those conducted by Marjanen et al. (2021) have demonstrated LDA's efficacy in exploring thematic structures in journalism, revealing how different topics emerge and evolve over time. This methodological advancement allows for a more nuanced examination of ideological discourse within state-run newspapers [5][6].

In the context of state-run media, previous research has highlighted the strategic use of language to promote governmental narratives. Such findings underscore the importance of understanding the ideological implications of media narratives, particularly in environments where state control over information is prevalent. By employing LDA topic modelling, this study aims to extend this body of research by systematically analyzing the thematic content of state-run newspapers, thereby contributing to a more comprehensive understanding of how these publications shape public discourse and reflect governmental ideologies [5][6].

The paper "Predicting Trends and Research Patterns of Smart Cities: A Semi-Automatic Review Using Latent Dirichlet Allocation (LDA)" by Sharma et al. presents a comprehensive analysis of research trends in smart cities, focusing on the integration of Internet of Things (IoT) technologies. Utilizing a corpus of 8,320 articles from the Scopus database published between 2010 and 2022, the authors employed LDA to identify emerging themes and patterns in the literature. Their findings highlight key areas of growth, such as smart transportation and energy management, while also mapping the geographical distribution of research contributions from various countries and institutions. The study emphasizes the importance of scientific collaboration in advancing smart city initiatives and formulates three research questions to guide future investigations. Overall, this work serves as a valuable roadmap for understanding the evolving landscape of smart city research, indicating that while significant progress has been made, many areas still require further exploration [1].

The research paper "Enhanced Sentiment Analysis and Topic Modeling During the Pandemic Using Automated Latent Dirichlet Allocation" by Amreen Batool and Yung-Cheol Byun explores the profound societal impacts of the COVID-19 pandemic, particularly focusing on public sentiment and topic trends through advanced data analysis techniques. Utilizing a sophisticated automated Latent Dirichlet Allocation (LDA) model, the study analyzes a large corpus of pandemic-related data to visualize sentiments and identify key topics, with Topic 8 emerging as the most prominent. The authors employ text-mining tools such as WordCloud and Word2Vec, alongside t-SNE for semantic clustering, to uncover critical terms associated with the pandemic, including "Origin," "Symptom," and "Transmission." This innovative approach not only enhances understanding of public sentiment dynamics during the pandemic but also aims to provide actionable insights for healthcare practitioners and policymakers. By offering a rapid and automated framework for analyzing large datasets, this study contributes significantly to the discourse on effective responses to public health crises [2].

3. METHODOLOGY

The main contribution of this paper is the identification of how state-run media, particularly through the analysis of editorial article from "The Global New Light of Myanmar," employs ideological discourse and topic modelling to shape public perceptions, revealing key governmental narratives and societal values that are interconnected with national identity and broader geopolitical dynamics.

This section outlines the detailed methodology employed in this paper to analyze ideological discourse in state-run newspapers using Latent Dirichlet Allocation (LDA) topic modelling. The methodology is structured into several key phases: topic modelling, data collection, pre-processing and LDA implementation.

3.1. Topic Modelling

Topic modelling is a technique used in machine learning and natural language processing that identifies the themes within a document. It assesses the likelihood of specific words or phrases being associated with particular topics and groups documents according to their similarities. This process involves examining the frequency of words and phrases throughout the text. Additionally, topic modelling has various applications, including text summarization, recommendation systems, spam detection, and more [2].

3.2. Data Collection

The first step involves gathering a comprehensive dataset of articles from state-run newspapers. This process includes:

- **Selection of Newspapers**: The selection of "The Global New Light of Myanmar" as a state-run newspaper is based on a comprehensive evaluation of various state-run publications. Criteria for selection include the newspaper's circulation, historical significance, and political affiliation, ensuring that the chosen outlet is both relevant and accessible for analysis.
- **Time Frame**: An article from “The Global New Light of Myanmar”, published on August 11, 2024, was collected to effectively capture shifts in discourse surrounding significant political events or policy changes.
- **Data Storage**: The collected article is stored in a structured format (e.g., CSV) for easy access during the analysis phase.

3.3. Pre-processing

After data collection, several pre-processing steps are applied to prepare the dataset for LDA analysis:

- **Tokenization:** The text is segmented into individual words or tokens. This step facilitates the analysis of term frequency within the article.

- **Lowercasing:** The text is converted to lowercase to ensure uniformity.
- **Stop-word Removal:** Commonly used words that carry little semantic value (e.g., "and," "the," "is") are eliminated from the dataset.

3.4. LDA Implementation

3.4.1 Theory Background of Latent Dirichlet Allocation (LDA)

Latent Dirichlet Allocation (LDA) is a generative probabilistic model widely used in natural language processing and machine

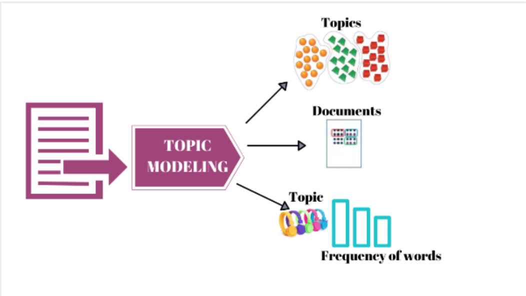

Figure 1. Latent Dirichlet Allocation (LDA)

learning for topic modelling that was introduced by Blei, Ng, and Jordan in 2003. LDA provides a framework for automatically discovering topics within large collections of text documents [5]. The model operates under the assumption that documents are mixtures of topics, where each topic is characterized by a distribution over words. This allows LDA to identify latent structures in textual data, making it an effective tool for analyzing large corpuses where manual categorization would be impractical.

The foundational concept of LDA is rooted in Bayesian statistics, where the model assumes that each document is generated from a mixture of topics represented by Dirichlet distributions. In this context, the Dirichlet distribution serves as a prior for the topic distributions, allowing for flexibility in modelling the uncertainty inherent in topic assignment [5].

The generative process involves two main steps: first, selecting a distribution over topics for each document; and second, generating words from these selected topics. This hierarchical structure enables LDA to capture the underlying relationships between documents and their associated topics effectively.

LDA's ability to uncover latent topics has been applied across various fields, including social sciences, computational biology, and digital humanities [5]. For instance, researchers have utilized LDA to analyze themes in social media discussions. The model's flexibility and scalability make it suitable for diverse applications, allowing scholars to gain insights into complex datasets by revealing hidden thematic structures that inform understanding and decision-making processes.

With the pre-processed data ready, LDA topic modelling is implemented with:

- **Model Configuration**: The LDA model is configured using Python's Gensim library. Key parameters include:
  - **Number of Topics**: An initial guess for the number of topics to be extracted is made based on prior research and exploratory analysis.
  - **Iterations**: The number of iterations for model convergence is set to ensure that the algorithm adequately learns the topic distributions.
- **Model Training**: The LDA model is trained on the Document-Term Matrix. During this phase, the algorithm identifies patterns in word co-occurrences across documents to determine underlying topics.
- **Hyperparameter Tuning**: Various hyperparameters (e.g., alpha and beta) are adjusted based on coherence scores to optimize topic representation.

3.4.2 Perplexity and Coherence

Two key metrics used to evaluate the performance of LDA models are perplexity and coherence.

Perplexity: Perplexity measures how well a probability model predicts a sample. In the context of LDA, it assesses the model's ability to predict the words in a document based on its learned topics. A lower perplexity score indicates better predictive performance, meaning that the model is more effective at capturing the underlying structure of the data [9].

Coherence: Coherence measures the interpretability of topics generated by LDA. It evaluates how semantically related the top words in a topic are to each other. Higher coherence scores indicate that the topics are more meaningful and interpretable to humans. There are various methods to compute coherence, including UMass and C_V coherence scores. These scores assess different aspects of topic quality based on word associations and co-occurrences within documents [10].

4. Evaluation Of Results

After training the LDA model, this analysis evaluates the results to extract meaningful insights:

- **Topic Interpretation**: Each identified topic is analyzed by examining its most significant words. The words are assigned with descriptive labels that reflect the themes represented by each topic.
- **Visualization**: Word cloud is employed to visualize word frequencies, providing a clear and engaging representation of the most frequently occurring terms in the dataset. This method facilitates effective communication of findings by highlighting key themes and concepts in a visually impactful way.

5. Proposed System Design And Implementation

Proposed system design is depicted in figure 2. The first step is to input the editorial article. Next, the text is pre-processed to clean and prepare it for analysis, which may involve tasks such as tokenization, lowercasing and removing stop words. After

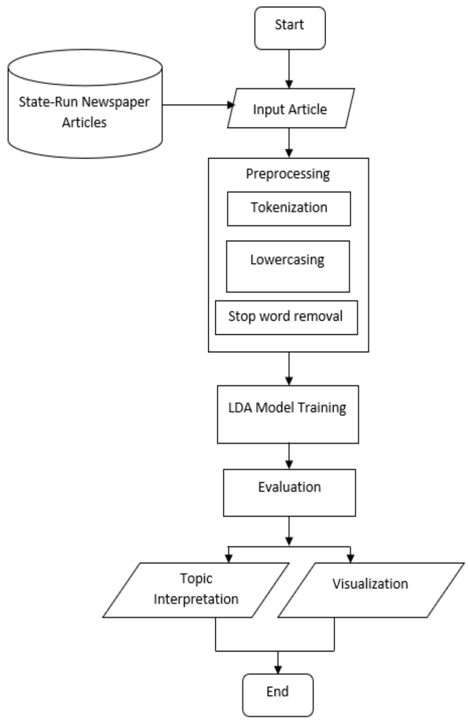

Figure 2. System Flow Diagram

pre-processing, the LDA model is trained on the cleaned text data. During training, the model learns these distributions by iteratively assigning words to topics and adjusting the topic assignments based on the overall structure of the document collection. Once the model is trained, the next step is evaluation, where the quality of the topics generated by the model is assessed. This can be done using metrics such as coherence score and perplexity to ensure the topics are meaningful and interpretable. Following evaluation, the topics are interpreted by examining the most representative words for each topic. Finally, the results are visualized to provide a clearer understanding of the topics and their distribution across the documents using word clouds.

6. Results And Contribution To Knowledge

The analysis of ideological discourse surrounding nuclear issues has yielded with different number of topics that significantly enhance the understanding of global nuclear dynamics and their implications in table 1, 2 and 3.

Table 2 shows the experimental results of key terms, perplexity and coherence scores for the number of topics (k=3).

- **Topic 0**: Global Nuclear Weapons Landscape

  Key Terms: "nuclear", "weapons", "world", "countries", "powerful", "global"

  Theme: This topic focus on the global implications of nuclear weapons, emphasizing their power and the involvement of various countries.

Figure 3. Word Cloud of Topic 0

- **Topic 1**: Nuclear Incidents and Their Consequences

  Key Terms: "nuclear", "incidents", "consequences", "people", "world", "provisions"

  Theme: This topic addresses the consequences of nuclear incidents and their impact on people and society at large.

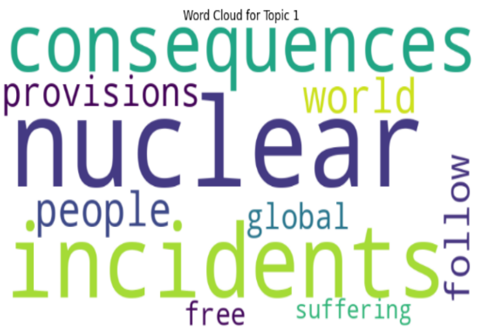

Figure 4. Word Cloud of Topic 1

- **Topic 2**: WWII Atomic Bomb

  Key Terms: "atomic", "bomb", "due", "hiroshima", "events", "boy"

  Theme: This topic centers around historical events related to atomic bombs, particularly referencing Hiroshima and possibly the bomb's nickname ("Little Boy").

Figure 5. Word Cloud of Topic 2

6.1 Results and Analysis

Perplexity Analysis: In table 2, the perplexity scores for the three topics are negative, indicating that the LDA model effectively predicts the words in the documents associated with these topics. Specifically, Topic 2 exhibits the lowest perplexity score of -13.4, suggesting it has a strong predictive capability compared to Topics 0 and 1, which have scores of -6.6 and -7.5, respectively.

Coherence Evaluation: The coherence scores reflect the interpretability of the topics. Topic 2 again stands out with a coherence score of 0.64, indicating a high degree of semantic relatedness among its key terms, making it more meaningful and interpretable to human evaluators. In contrast, Topics 0 and 1 have lower coherence scores of 0.35 and 0.39, respectively, suggesting they are less interpretable.

Topic 2 (k=3) yielded the best coherence score (0.64) because its key terms (atomic, bomb, Hiroshima, events, boy) are semantically closely related and clearly reflect a specific historical context, the atomic bombings of Hiroshima and Nagasaki. The strong thematic focus on a well-defined historical event contributes to the high coherence score.

Topics 0 and 1 (k=3) have lower coherence scores (0.35 and 0.39, respectively) because their key terms are more general and encompass a wider range of subtopics. For example, Topic 0 includes terms like nuclear, weapons, world, countries, powerful, global, which could relate to multiple themes such as nuclear proliferation, geopolitical power dynamics, and global security.

Similarly, Topic 1 includes terms like nuclear, incidents, consequences, people, world, provisions, which could refer to historical incidents, policy measures, or humanitarian impacts. The broader scope of these topics reduces their semantic cohesion, making them less interpretable compared to Topic 2. This suggests that the model may struggle to capture distinct themes when the discourse is more generalized or multifaceted.

Selecting the optimal number of Topics: The optimal number of topics (k) was determined using a combination of perplexity scores and topic coherence metrics. For this study, k=2, k=3, and k=4 was tested. Perplexity measures how well the model predicts the data, with lower values indicating better performance. Coherence scores, on the other hand, evaluate the interpretability of topics based on the semantic similarity of top terms.

After evaluating these metrics, k=3 was selected as the optimal number of topics because it provided a balance between interpretability (coherence) and model performance (perplexity). Specifically, Topic 2 (k=3) achieved the highest coherence score (0.64), indicating strong thematic cohesion.

Overall Assessment: The combination of low perplexity and high coherence scores for Topic 2 supports the conclusion that it is a strong and highly interpretable topic. This aligns with the understanding that effective topic models should not only predict well but also produce topics that are coherent and meaningful to users.

6.2 Overall Implications

Topic modelling has revealed three distinct themes related to nuclear issues, each with varying degrees of coherence. In table 2, the historical context provided by Topic 2 stands out as particularly coherent, while Topics 0 and 1 address broader implications and consequences of nuclear weapons but could benefit from clearer connections among their terms.

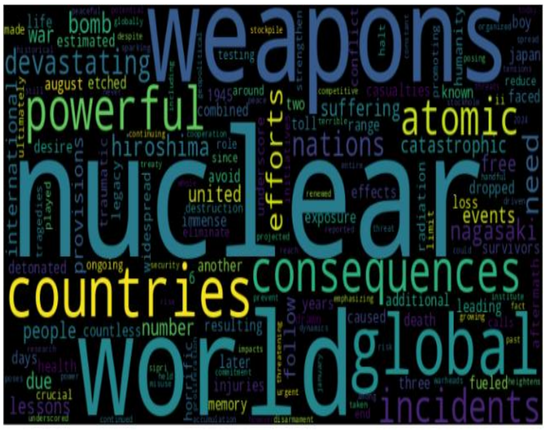

Figure 6. Word Cloud of Frequent Terms in Article

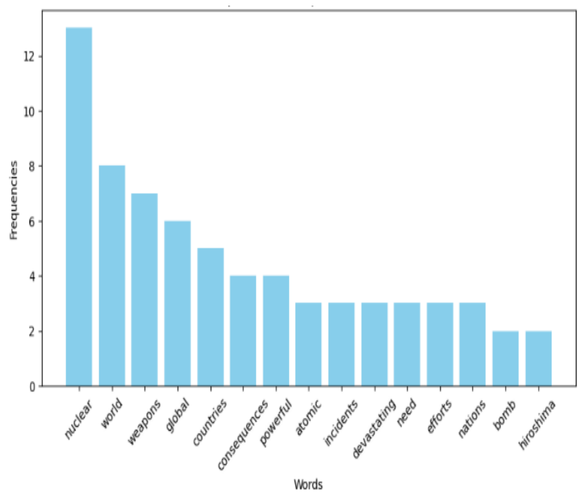

Figure 7. Top 15 Most Frequent Words in Article

Raise nuclear non-proliferation activities worldwide

On 6 august 1945, the atomic bomb known as "Little Boy" was dropped on Hiroshima, Japan, leading to an immense loss of life and widespread injuries. Just three days later, another atomic bomb was detonated over Nagasaki, resulting in additional catastrophic casualties. The combined death toll from these two incidents is estimated to range between 129,000 and 226,000 people, with countless more suffering from long-term health effects. The survivors faced years of suffering due to radiation exposure and the traumatic aftermath.

These events are etched in global memory for all of humanity. They underscore the devastating consequences of war and have fueled a global desire for a world free from nuclear weapons. It was a horrific legacy that caused atomic conflict and the need to avoid such destruction.

Since the end of World War II, countries around the world have drawn lessons from the tragedies of Hiroshima and Nagasaki. Efforts have been made to limit, reduce, and ultimately eliminate nuclear weapons. There have been ongoing calls to halt nuclear testing and to strengthen global non-proliferation efforts. The United Nations has played a crucial role in promoting these initiatives, emphasizing the need for international cooperation to prevent the spread of nuclear weapons.

However, despite these efforts, the number of nuclear weapons globally has continued to rise, driven by the competitive dynamics among powerful nations. The Stockholm international peace research institute (sipri) reported that the number of nuclear warheads held by powerful countries is projected to reach 12,121 by January 2024. This growing stockpile of nuclear weapons poses a constant threat to global security.

The potential consequences of nuclear proliferation are underscored by historical incidents. The continuing accumulation of nuclear weapons heightens the risk of catastrophic events that could have devastating consequences for the entire world. As such, the need for renewed global commitment to nuclear non-proliferation and disarmament has never been more urgent.

In fact, terrible lessons should be taken from the impacts of the misuse of nuclear power because past incidents are still posing threats to the world today. Nuclear weapons from a handful of powerful countries are threatening the world due to sparking geopolitical tensions. So, the United Nations organized all global countries, including powerful countries, to follow the provisions of the nuclear non-proliferation treaty. Only when they all follow these provisions will the whole world be peaceful and the people of the world be free from devastating consequences.

Figure 8. Sample Editorial [7]

Table 1. Number of Topics (k=2)

Topic	**Key Terms**	**Perplexity**	**Coherence**
Topic 0	nuclear, global, countries, powerful, need, weapons	-6.2	0.5
Topic 1	world, nuclear, weapons, consequences, incidents, devasting	-6.2	0.35

Table 2. Number of Topics (k=3)

Topic	Key Terms	Perplexity	Coherence
Topic 0	nuclear, weapons, world, countries, powerful, global	-6.6	0.35
Topic 1	nuclear, incidents, consequences, people, world, provisions	-7.5	0.39
Topic 2	atomic, bomb, due, hiroshima, events, boy	-13.4	0.64

Table 3. Number of Topics (k=4)

Topic	Key Terms	Perplexity	Coherence
Topic 0	weapons, nuclear, efforts, nations, powerful, number	-9.3	0.9
Topic 1	countries, powerful, suffering, nuclear, provisions, follow	-9.7	0.438
Topic 2	nuclear, global, weapons, bomb, atomic, hiroshima	-9.3	0.43
Topic 3	world, nuclear, consequences, devastating, need, global	-9.3	0.36

7. Conclusions

This paper contributes the effectiveness of Latent Dirichlet Allocation (LDA) topic modelling in examining ideological messages in state-run newspapers. By revealing hidden themes, this analysis provides valuable insights into how these publications shape public opinion and reflect government priorities. The findings emphasize the significant role of state-run media in crafting narratives that align with political agendas, influencing societal norms and values. Additionally, the analysis sheds light on how these media outlets frame discussions around nuclear issues, uncovering narratives related to security, power dynamics, and the consequences of nuclear technologies. This understanding enhances awareness of how media impacts public opinion, policy decisions, and international relations concerning nuclear weapons. Ultimately, this analysis underscores the importance of critically examining media discourse to grasp its implications for democracy and public awareness in contemporary society.

8. Limitations And Future Works

The inherent complexity of tuning LDA parameters (such as the number of topics) adds additional layer of difficulty. A balance between model accuracy and computational feasibility must be achieved by conducting multiple runs with varying parameters to obtain optimal results.

Future research could explore hybrid models that combine LDA with other techniques, such as Non-negative Matrix Factorization (NMF) or neural network-based methods. These alternatives may enhance topic coherence and better capture nuanced relationships within the text.

Expanding the analysis to include a wider range of state-run newspapers or comparing different media outlets could yield insights into regional variations in governmental discourse and media influence on public opinion.

ACKNOWLEDGEMENTS

The author expresses sincere gratitude to Dr. Nang Saw Kalayar, Head of the Department at the Faculty of Information Science, University of Computer Studies (Taunggyi), for her invaluable guidance and support throughout the implementation of this paper. Dr. Kalayar's insightful suggestions and comprehensive feedback have significantly enhanced the content and quality of this work.

REFERENCES

[1] C. SHARMA and I. BATRA, "Predicting Trends and Research Patterns of Smart Cities: A Semi-Automatic Review Using Latent Dirichlet Allocation (LDA)," *IEEE Access*, vol. 10, 2022, doi: 10.1109/ACCESS.2022.3214310.

[2] A. BATOOL and A. Y.-C. BYUN, "Enhanced Sentiment Analysis and Topic Modeling During the Pandemic Using Automated Latent Dirichlet Allocation," *IEEE Access*, vol. 12, 2024, doi: 10.1109/ACCESS.2024.3411717.

[3] J. P. Gee, *How to do Discourse Analysis: A Toolkit*. 2011.

[4] N. Fairclough, *Language and Power*. 1989.

[5] D. M. Blei, A. Y. Ng, and M. I. Jordan, "Latent Dirichlet Allocation," *Journal of Machine Learning Research*, vol. 3, pp. 993–1022, 2003.

[6] J. Marjanen, E. Zosa, S. Hengchen, L. Pivovarova, and M. Tolonen, "Topic Modelling Discourse Dynamics in Historical Newspapers," in *CEUR Workshop Proceedings*, vol. 2865, 2021.

[7] "Raise nuclear nonproliferation activities worldwide," *The Global New Light of Myanmar*, Aug. 11, 2024.

[8] "Topic Modeling Coherence Score," Baeldung, 2024. [Online]. Available: https://www.baeldung.com/cs/topic-modeling-coherence-score.

[9] "Interpreting perplexity, U-Mass coherence, and C_V score trends for a Latent Dirichlet Allocation (LDA) model." Stack Overflow. https://stackoverflow.com/questions/77984467/interpreting-perplexity-u-mass-coherence-and-cv-score-trends-for-a-latent-diric

[10] "Latent Dirichlet Allocation (LDA) Tutorial: Topic Modeling," Neptune.ai. [Online]. Available: https://neptune.ai/blog/latent-dirichlet-allocation-lda-tutorial-topic-modeling.

Authors

Biography

Moe Phyu Phyu Khaing received M.C.Sc. in Computer Science from the University of Computer Studies, Mandalay (UCSM) in 2022. She currently works as a tutor at the University of Computer Studies (Taunggyi). She interests in Data Mining, Machine Learning, Image Processing and Deep Learning.

Khaing Zar Win, she got the B.C.Sc., B.C.Sc.(Hons;), M.C.Sc and Ph.D (IT). degrees in 2003, 2004, 2009 and 2024 from the University of Computer Studies, Monywa, University of Computer Studies, Mandalay for Master degree and University of Computer Studies, Yangon for Ph.D. (IT) degree respectively. She serves as a Lecturer in the Department of Information Science, from the University of Technology (Yatanarpon Cyber City). She interests in Multimedia, Multimodal Communication, QoS Control and QoE assessment in networked haptic communication, Artificial Intelligence and Data Science.

Nan Saw Kalayar received the Ph. D (IT) from University of Computer Studies (Yangon), Myanmar. Now she is working as the Professor, Faculty of Information Science, University of Computer Studies (Taunggyi). Her research interest fields are Data Science, Machine Learning, Deep Learning, Image Processing.

EFFECT OF SOLVENTS AND CONCENTRATIONS ON SOLUBILITY OF NATURAL DYES EXTRACT FROM SEIN-PAN FLOWER FOR DYE SENSITIZED SOLAR CELLS

Zin Mar Myint[1], Mu Mu Win[2], and Thaung Hlaing Win[3]

[1,2,3] Department of Physics, Pakokku University
zinmarmyint.zm.rl@gmail.com,
mumuwin@gmail.com,thaung.naing001@gmail.com

ABSTRACT

The field of solar electricity or photovoltaics (PV) is rich in that there are many materials and concepts for converting sunlight into electricity. The technologies accepted as conventional are those well along in the process of commercialization. In this study, effect of solvents and concentrations on natural dye sensitizer were successfully extracted from sein-pan flower by solvent method. Two distinct types of solvents (distilled water and ethanol) were used for extraction of natural dye from fresh or dry sein-pan flower. Extracted natural dyes were characterized by UV–Vis spectrophotometer and atomic force microscopy (AFM). There is an absorbance peak at 436 nm and the other optical absorbance peak at 677 nm. The highest optical absorbance peak was observed in ethanol solvent. Upon increasing dye concentrations (volume ratios 1:1, 1:2 and 1:3), the highest optical absorption peak intensity was observed. It may be due to its better solubility of natural dye solution.

KEYWORDS

natural dye, absorbance, solvent, distilled water, ethanol.

1. INTRODUCTION

Solar energy has enormous potential to satisfy the demand for clean and green energy. There has been an exponential growth in photovoltaic technologies over the past three decades. Dye sensitized solar cells (DSSC) are one of the most promising alternatives of solar energy conversion. First DSSC was developed in 1991 marked by the breakthrough work by Gratzel, which opened up new possibilities in the field of photovoltaic. DSSCs are relatively low cost with simple fabrication procedures comparing with the silicon-based solar cells. They are lightweight and can be fabricated with flexibility in terms of transparency, appearance, shape, size and color. They can work in diffuse light conditions such as in sunrise, cloudy climate and nightfall. They are integrable into different products for energy conversion, harvesting and storage. In general, a DSSC consist of five basic components i.e. counter electrode, electrolyte, photo anode, semiconductor oxide layer and photo sensitizer. Intensive research has been directed towards the Journal Pre-proof improvement of these components for optimized performance in terms of efficiency and stability.

For electrolytes, the iodide/triiodide (I- /I3-) couple is the preferred redox couple because of its good solubility, long term stability and high conductivity. Recently this field has received considerable attention and new redox shuttles, ionic, polymer, gel polymer, cobalt copper complexes based redox mediators and organic– inorganic gel electrolytes have been used for the realization of stable and high performance DSSCs. Quasi-solid-state printable electrolytes based DSSCs also exhibited superior stability with a potential for application in diffused light.

Dyes plays very important role in absorbing sunlight and transforming solar energy into electrical energy. Conventional dyes are metal complexes such as Ruthenium (Ru) with auxiliary ligands generally pyridines, bipyridines, Phosphine etc. Despite of high photoelectric conversion efficiencies Ruthenium dyes are not suitable for mass production due to high cost and harmful environmental effect. The other substitutes of metallic dyes are metal-free organic dyes and natural dyes. Metal free organic dyes are cost effective with diversity in molecular structures and high molar extinction coefficient. Recently ullazine, triazatruxene (TAT) based organic dyes and dyes in combination with Chenodeoxycholic acid (CDA) exhibited superior performance than metallic dyes. A combination of metallic and organic dyes by co-sensitizing Ruthenium complex with novelorganic dyes have also shown improved efficiencies than organic dyes based DSSCs. In a recent research work non-toxic flower dyes (fresh sein pan flower and dry sein pan flower) are also reported to have potential for DSSCs applications. The main objective of the present work is to investigate the effect of natural dyes (papaya leaves, red spinach leaves), effect of solvents, and effect of temperature and dye concentrations.

2. EXPERIMENT

2.1. Extraction of Natural Dyes

Solvent extraction process is simple, investment of equipment is low, the technology is easy to learn, grasp and has the most practical applications. In this research, fresh and dry sein-pan (*DelonixRegia*) flowers were collected and washed with water to remove impurities. The natural dyes solutions were extracted with distilled water and ethanol were employing the following procedure. After crushing into small pieces in a pestle, these were kept in a glass bottles filled with ethanol and distilled water. The solid residues in solution were then filtrated out, and the filtrates were concentrated for the use as sensitizers. In this present work, the effect of solvent (ethanol, distilled water) and dyes concentrations (1:1, 1:2 and 1:3) on optical absorption of natural dyes from fresh sein-pan flowers was studded. In addition, the natural dyes from dry sein-pan flower were extracted with different solvents (distilled water, ethanol) and dye concentration (molar ratios 1:1, 1:2 and 1:3). They were dried at room temperature to prevent some reactions of the organic constituents present in samples with sun light. The air dried plant samples were cut into species and ground in grinding mill to get a coarse powder. The powder samples were store in air tight containers for the experimental works. In the preparation of solvents extract (distilled water and ethanol), 100 g of dried powdered samples was soaked in distilled water/ ethanol in the conical flask. The flask was stirring on a water bath for 5 hours and then filtrated. The process was carried out for three times. The combined filtrates solution was used for optical characterization. Fig. 3 (a-b) and 4 show the flow chart and preparation of natural dye-sensitizers from fresh and dry sein-pan flowers.

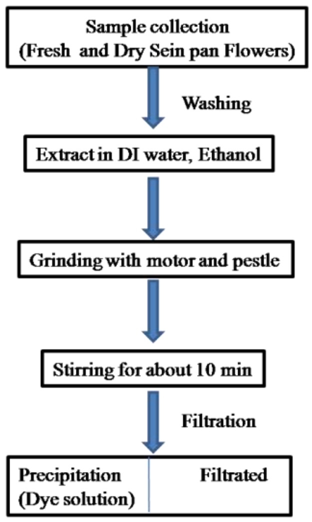

Figure 1.(a) Flow chart for natural dyes extracts from fresh and dry Sein-pan flower

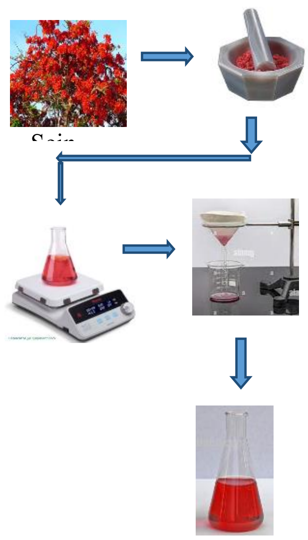

Figure1. (b) Steps of sample preparation for natural dyes extract from Sein-pan flower

2.2 UV-Vis Spectrophotometry

UV-Vis Spectrophotometry is a technique to measure either absorbance or transmittance of the sample in ultraviolet and visible region. The optical properties of natural dyes were measured by UV-Vis spectrophotometer: GENESYS 10S UV-Vis (Materials Research Lab, Department of Physics, and University of Mandalay), as shown in Figure 2. The absorption spectra of natural dyes were recorded in the wavelengths ranging from 300-900 nm. A glass substrate was used as baseline scanning before the measurement.

2.3 Atomic Force Microscopy (AFM)

AFM is a high-resolution non-optical imaging technique. Since then it has developed into a powerful measurement tool for surface analysis. AFM allows accurate and non-destructive measurements of the topographical, electrical, magnetic, chemical, optical, mechanical, etc. properties of a sample surface with very high resolution in air, liquids or ultrahigh vacuum. Figure 3 involves scanning an AFM probe with a sharp AFM tip over a sample surface in a raster pattern. The AFM tip is usually made of silicon or silicon nitride and is integrated near the free end of a flexible AFM cantilever. A piezoelectric ceramic scanner controls the lateral and the vertical position of the AFM probe relative to the surface. The coordinates that the AFM tip tracks during the scan are combined to generate a three-dimensional topographic image of the surface pens able in most advanced science and technology labs around the world.

Figure 2. UV-Vis Spectrophotometer (GENESYS 10S)

Figure 3. Atomic Force Microscope

3. Results and Discussion

This chapter deals with absorption and characterization of natural dyes with different solvent and dye concentration of the present work.

3.1. Effect of Solvents on Optical Properties of Natural Dyes from Fresh and Dry Sein Pan Flowers

Firstly, effect of solvent on optical absorption of natural dye extracts from fresh sein-pan flower was studied. Figure 4 shows the effect of solvent optical absorption spectra of dry sein-pan flower with volume ratio (1:1) in distilled water and ethanol. The optical absorption peak maximum (λ_{max}) is observed at (517–676) nm in ethanol and (519- 674) nm in distilled water. With ethanol solvent, the optical absorption peak maximum (λ_{max}) is remaining unchanged and the optical absorption peak intensity significantly increased. The optical absorption peak intensity of natural dye from fresh sein-pan flower extracts in ethanol was higher than in distilled water. It is expected that the concentration of dye contents would be higher in ethanol, probably because of higher solubility in ethanol.

Figure 5 shows the effect of solvent on optical absorption spectra of fresh sein-pan flower with volume ratio (2:2) in distilled water and ethanol. The optical absorption peak maximum (λ_{max}) is observed at (517 – 673) nm in ethanol and (518- 674) nm in distilled water. With ethanol solvent, the optical absorption peak maximum (λ_{max}) is slightly changed and the optical absorption peak intensity significantly increased. The optical absorption peak intensity of natural dye from fresh sein-pan flower extracts in ethanol was higher than in distilled water. It is expected that the concentration of dye contents would be higher in ethanol, probably because of higher solubility in ethanol.

Figure 6 shows the effect of solvent on optical absorption spectra of fresh sein pan flower with volume ratio (3:3) in distilled water and ethanol. The optical absorption peak maximum (λ_{max}) is observed at (518 – 673) nm in ethanol and (517- 673) nm in distilled water. With ethanol solvent, the optical absorption peak maximum (λ_{max}) is slightly changed and the optical absorption peak intensity significantly increased. The optical absorption peak intensity of natural dye from fresh sein pan flower extracts in ethanol was higher than in distilled water.

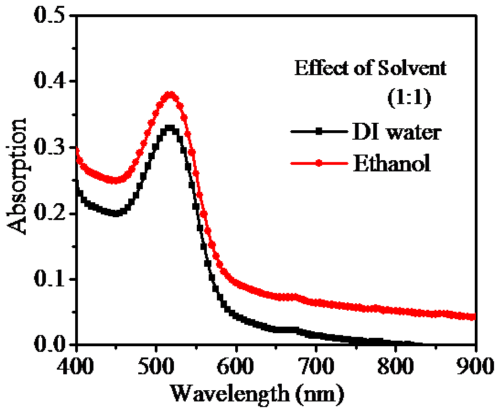

Figure 4. Effect of solvent on optical absorption of natural dye extracts from fresh sein-pan flowers (volume ratio 1:1)

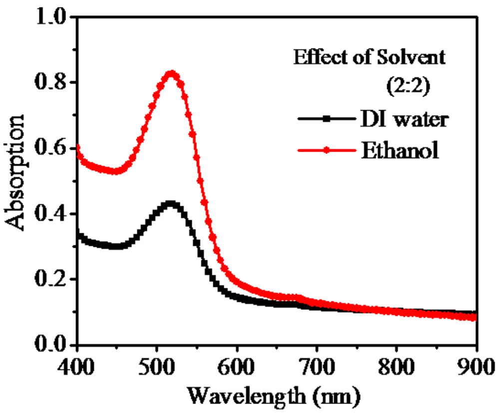

Figure 5. Effect of solvent on optical absorption of natural dye extracts from fresh sein-pan flower (volume ratio 2:2)

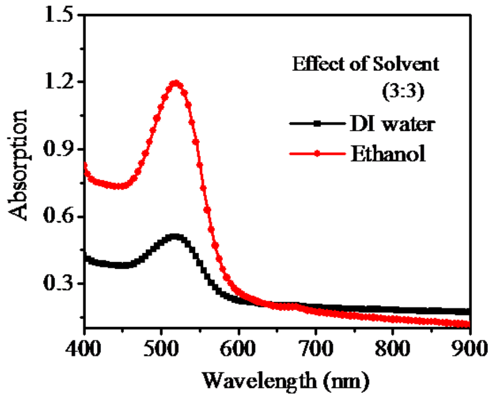

Figure 6. Effect of solvent on optical absorption of natural dye extracts from fresh sein-pan flower (volume ratio 3:3)

Secondly, effect of solvent on optical absorption of natural dye extracts from dry sein-pan flower was also studied. Figure 7 shows the effect of solvent optical absorption spectra of dry sein-pan flower with volume ratio (1:1) in distilled water and ethanol. The optical maximum (λ_{max}) absorption peak is observed at (517–676) nm in ethanol and (519 - 674) nm in distilled water. With ethanol solvent, the optical absorption peak maximum (λ_{max}) is remaining unchanged and the optical absorption peak intensity significantly increased. The optical absorption peak intensity of natural dye from dry sein-pan flower extracts in ethanol was higher than in distilled water. It is expected that the concentration of dye contents would be higher in ethanol, probably because of higher solubility in ethanol.

Figure 8 shows the effect of solvent on optical absorption spectra of dry sein-pan flower with volume ratio (2:2) in distilled water and ethanol. The optical maximum (λ_{max}) absorption peak is observed at (517 – 673) nm in ethanol and (518- 674) nm in distilled water. With ethanol solvent, the optical absorption peak maximum (λ_{max}) is slightly changed and the optical absorption peak intensity significantly increased. The optical absorption peak intensity of natural dye from dry sein-pan flower extracts in ethanol was higher than in distilled water. It is expected that the concentration of dye contents would be higher in ethanol, probably because of higher solubility in ethanol.

Figure 9 shows the effect of solvent on optical absorption spectra of dry sein-pan flower with volume ratio (3:3) in distilled water and ethanol. The optical absorption peak maximum (λ_{max}) is observed at (518 – 673) nm in ethanol and (517- 673) nm in distilled water. With ethanol solvent, the optical maximum (λ_{max}) absorption peak is slightly changed and the optical absorption peak intensity significantly increased. The optical absorption peak intensity of natural dye from dry sein-pan flower extracts in ethanol was higher than in distilled water.

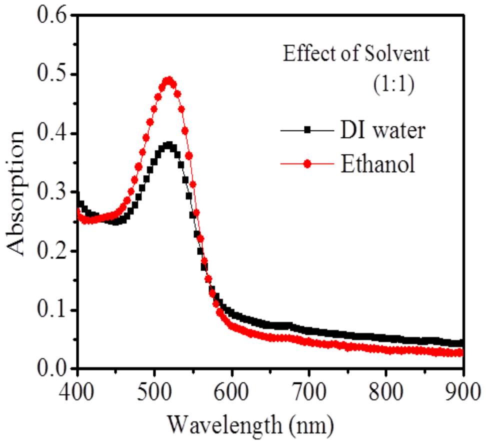

Figure 7. Effect of solvent on optical absorption of natural dye extracts from dry sein-pan flowers (volume ratio 1:1)

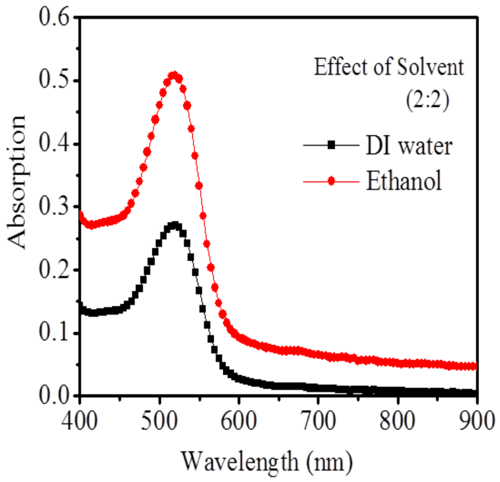

Figure 8. Effect of solvent on optical absorption of natural dye extracts from dry sein-pan flower (volume ratio 2:2)

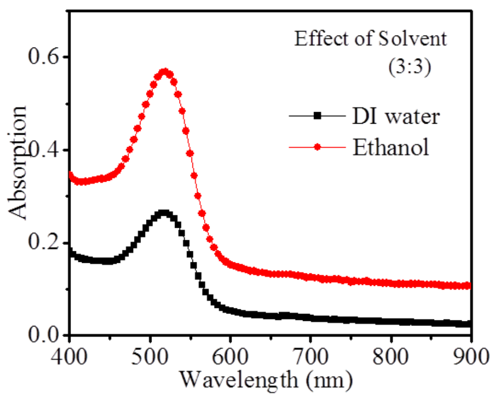

Figure 9. Effect of solvent on optical absorption of natural dye extracts from dry sein-pan flower (volume ratio 3:3)

3.2. Effect of Concentrations on Optical Properties of Natural Dyes Extract from Fresh and Dry Sein Pan Flowers

Figure 10 shows the optical absorption spectra of natural dye (fresh sein-pan flower) in distilled water with different concentrations (1:1, 2:1, 3:1). There is an absorbance peak at ~ 520 nm and ~ 675 nm wavelengths. While the other optical absorbance peak is at 672 nm wavelengths, so the dye solution of sein -pan flower will also work by absorbing the red color spectrum. The stronger optical absorption peak intensity was obtained at 520 nm wavelengths. Upon increasing dye concentration, (1:1 up to 3:1), the highest optical absorption peak intensity was observed at molar ratios (3:1).

Figure 11 shows the optical absorption spectra of dry sein-pan flower extracts with different dye concentration at room temperature (RT) in ethanol. The two optical absorption peak maximum (λ_{max}) is observed at ~ 520 nm and ~ 675nm. Upon increasing dye concentration (1:1, 2:1, 3:1), the color remained unchanged and the optical absorption peak intensity significantly increased. The peak maximum (λ_{max}) kept unchanged with different concentration despite changes in absorption intensity. The highest absorption peak intensity was observed at volume ratios (3:1). It may be due to the fact that the highest dye concentration at molar ratio (3:1).

Figure 12 shows the optical absorption spectra of dry sein-pan flower extracts with different dye concentration at room temperature (RT) in distilled water. Upon increasing dye concentration (1:1, 2:1, 3:1), the color remained unchanged and the optical absorption peak intensity significantly decreased. The maximum peak (λ_{max}) kept unchanged with increasing dye concentrations despite changes in absorption intensity. The highest absorption peak intensity was observed at volume ratios (1:1).

Figure 13 shows the optical absorption spectra of dry sein-pan flower extracts with different dye concentration at room temperature (RT) in ethanol. Upon increasing dye concentration (1:1, 2:1, 3:1), the color remained unchanged and the optical absorption peak intensity significantly decreased. The maximum peak (λ_{max}) kept unchanged with increasing dye concentrations despite changes in absorption intensity. The highest absorption peak intensity was observed at volume ratios (3:1).

Table 1 shows the effect of concentrations (1:1,2:1, 3:1) with ethanol and distilled water solvents on optical absorbance values for natural dyes extracted from fresh and dry sein-pan flower. In ethanol and distilled water extracted solutions, the maximum and minimum absorbance values are found at the shorter and longer wavelengths in the visible region, respectively. This indicates the presence of more anthocyanin compounds that absorbs a higher number of photon energy light.

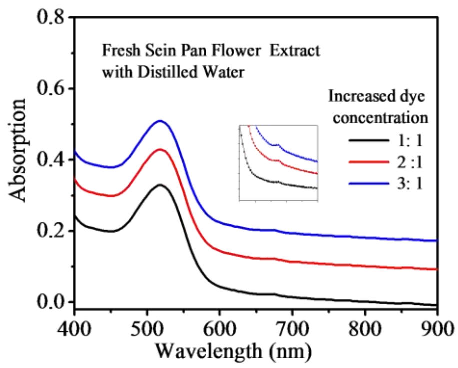

Figure 10. Effect of dye concentrations on optical absorption of natural dye extracts

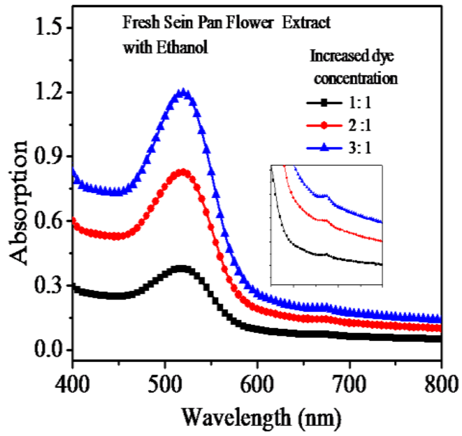

Figure 11. Effect of dye concentrations on optical absorption of natural dye extracts

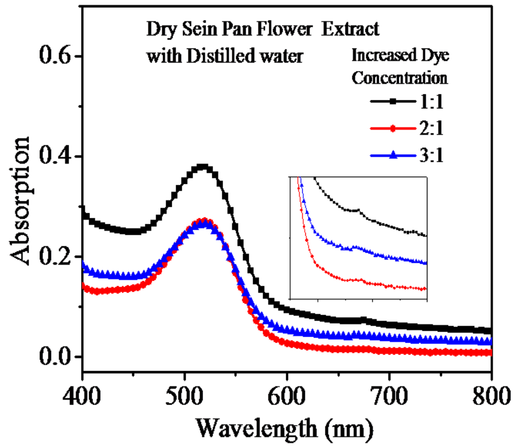

Figure 12. Effect of dye concentrations on optical absorption of natural dye extracts

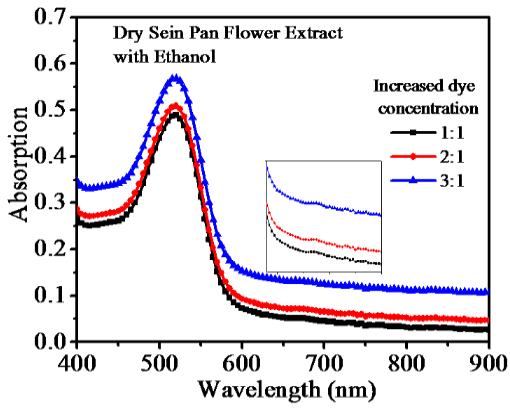

Figure 13. Effect of dye concentrations on optical absorption of natural dye extracts

Table 1. Absorbance values of Natural dyes solutions

Concentration	Absorbance	Wavelength
Fresh Sein Pan Extracted by Distilled Water		
1:1	0.3290 0.0231	520 675
2:1	0.4237 0.1231	525 675
3:1	0.5090 0.2031	520 675
Fresh Sein Pan Extracted by Ethanol		
1:1	0.3790 0.0731	520 675
2:1	0.8266 0.1440	520 670
3:1	1.1951 0.1958	520 675
Dry Sein Pan Extracted by Distilled Water		
1:1	0.4885 0.0518	520 665
2:1	0.5085 0.0718	520 665
3:1	0.5685 0.1318	520 665
Dry Sein Pan Extracted by Ethanol		
1:1	0.3787 0.0731	515 675
2:1	.2706 0.0156	520 680
3:1	0.2646 0.0426	520 665

3.3. Morphological Properties of Dry Sein Pan Dyes on TiO_2 Substrate

The topographies of various surfaces have been studied in many fields due to the significant influence that surfaces have on the practical performance of a given sample. In viewing the opportunity to enhance photovoltaic application, six samples having different solvent (distilled water and ethanol) were extracted by solution process. AFM study indicated the entire films exhibited single phase structure for all films. Atomic of roughness increased from 0.40 nm to 2.00 nm as the solvent changes, the films surface is porous. It is observed with different of dry and fresh sein-pan dyes in the Figure 14 (a-f) and 15 (a-f).

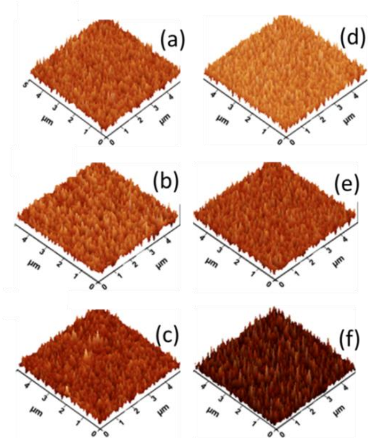

Figure 14. AFM images of dry sein-pan dyes (a-c) with ethanol and (d-f) distilled water solvents

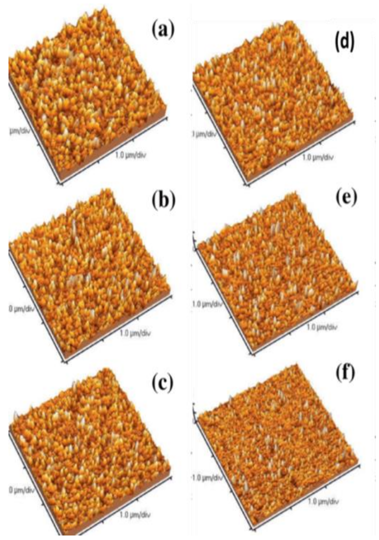

Figure 15. AFM images of fresh sein-pan dyes (a-c) with ethanol and (d-f) distilled water solvents

3.4. Estimation of Optical Band Gap Values

The optical band gap energy of fresh and dry Sein-pan flowers extracts (with distilled water and solvents) were calculated from their respective absorption spectra by using the following equation:

$$(\alpha h\nu)^m = A\,(h\nu - E_g)$$

Since natural dyes is direct band gap semiconductor, we plot $(\alpha h\upsilon)^2$ versus $h\upsilon$ taking m value of 2.

Figure16(a-b) show the plots of $(\alpha h\upsilon)^2$versus $(h\upsilon)$ for the natural dyes Sein-pan flowers with different solvents (distilled water and ethanol). The optical band gap energies were deduced from the extrapolation of the linear part of the plot $(\alpha h\upsilon)^2$ versus $(h\upsilon)$ abscissa. At dyes concentration (1:1), the optical band gap values decreased with ethanol solvent than the distilled water. The optical band gap values are observed at from 2.64 eV to 2.8 eV) in distilled water and (2.48 eV to 2.60 eV) with ethanol solvents.

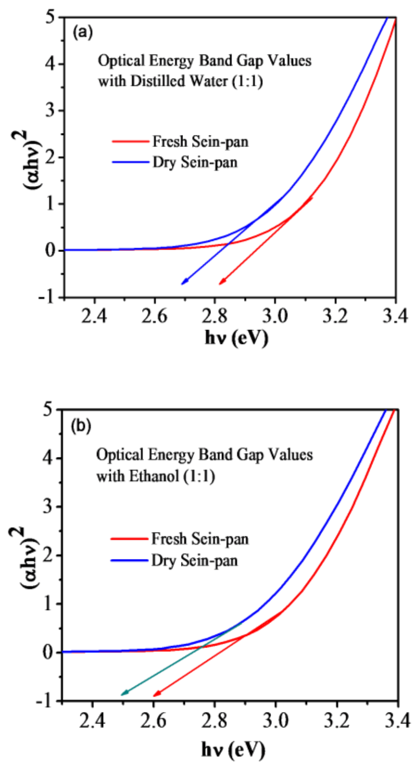

Figure 16. (a-b) Optical band gap values fresh and dry sein-pan dyes at concentration (1:1)

4. Conclusion

Natural dyes can be used in dye-sensitized solar cells (DSSCs) to convert sunlight into electricity. This is a promising, eco-friendly, and cost-effective method of energy production. Natural coloring materials can also be extracted using organic solvents such as ethanol and distilled water. In the first part, the effect of solvent on the optical properties of natural dyes (fresh and dry sein-pan ni flower) was studied. The optical absorption peak maximum (λ_{max}) is observed at (520-674) nm in distilled water and ethanol solvent. The absorption is relatively higher with ethanol solvent for fresh and dry sein pan flower extract. It may be due to its better solubility of natural dye in ethanol solvent. Upon increasing fresh sein-pan flower extract concentration (1:1,2:1 and 3:1), the maximum optical absorption peak intensity is observed at concentration (3:1).It may be due to its better solubility of natural dye in higher dyes concentration. An addition, the highest optical absorption peak intensity is observed at concentration (1:1) dry sein pan flower extract with distilled water solvent and (3:1) for ethanol solvent. According to the AFM results, the dyes treated TiO_2 films are observed at porous structures. The energy band gap values of fresh and dry Sein-pan dyes are ~ 2.64 eV in distilled water and ~ 2.48 eV in ethanol solvent.

Acknowledgments

We would like to thank Dr Tin Tun Aung, Acting Rector, Pakokku University. We are also thankful to Dr Win Win Ei (Pro-rector) and Dr Khin Khin Htoot, (Pro-rector), Pakokku University. We would like to express my gratitude to Dr Win Mar (Professor and Head), and Dr Win Myint Kyu (Professor), Department of Physics, Pakokku University, for their kind permission to give us the opportunity to do research. We would like to express my appreciation to the department of physics, Pakokku University for their use of research facilities.

References

[1] M. Gratzel*et al.,* J. Photochem. Soc. **6**, (2003) 889.

[2] O'Regan and M. Gratzel, Nature 353, (1991) 737.

[3] C. Deibel and V. Dyakonov, Rep. Prog. Phys. 73, (2010) 39.

[4] F. Gaoet al., J. Am. Chem. Soc. 130, (2008) 10720.

[5] H. J. Snaith and L. Schmidt-Mende, Adv. Mater 19, (2007) 3187.

Authors

Biography

First A. Daw Zin Mar Myint

Demonstrator
Department of Physics
Pakokku University

Second B. Dr Mu Mu Win

Associate Professor
Department of Physics
Pakokku University

Third C. Dr Thaung Hlaing Win

Lecturer
Department of Physics
Pakokku University

OPTICAL ABSORPTION AND BAND GAP ENERGY CONTROL OF COPPER NANOPARTICLES ON TITANIUM OXIDE FILMS

Thaung Hlaing Win[1]

[1]Department of Physics, Pakokku University
thaung.naing001@gmail.com

ABSTRACT

The n-type semiconducting titanium oxide thin films are well-known as electron transporting interlayer in photovoltaic cells. The favorable characteristics of interlayers in photovoltaics are high optical transmittance (T%), wide band gap energy (Eg) and high electrical conductivity (σ). Modifying titanium oxide films with metal nanoparticles would increase electrical conductivity but reduce optical band gap energy. In this present work, the sol-gel methods was used. We developed the sol-gel derived titanium suboxide (TiOx) films modified with (Cu) nanoparticles (NPs). This study explores a tradeoff between narrowing optical band gap and enhancing electrical conductivity of nanostructured TiOx films by controlling the Cu-NPs loading concentrations (mol%) in titania. The Cu-NPs loading concentration of 4 mol% should meet a trade-off which yields the higher T%, and wider band gap compared to those of pure TiOx films.

KEYWORDS

Titanium suboxide, copper nanoparticles, electrical conductivity, band gap energy.

1. INTRODUCTION

Nanotechnology is the most promising technology that can be applied in almost all spheres of life, ranging from electronics to pharmaceutical. Its application entirely depends on the types of nanostructures (metallic, nonmetallic and semiconducting) and shape of nanostructures (nanoparticles, nanorods, nanotubes and so on). Metallic nanoparticles are of great interest due to their excellent physical and chemical properties, such as high surface-to-volume ratio and high heat transfer (thermal conductivity). In particular, copper nanoparticles (CuNPs) have become an intensive area of scientific research as they exhibit many excellent physical and chemical properties such as high electrical conductivity and chemical activity.

Copper nanoparticles are considered possible replacements for gold and silver particles in some potential applications, such as in catalysts, conductive pastes, cooling fluid, and solar cells. Copper nanoparticles synthesis specifically has attracted more interest compared to other nanoparticles synthesis because of their useful properties achievable at much less cost than silver and gold. In particular, silver with its high conductivity is of great interest and has led too much development with commercially available products. However, these noble metals are too expensive to be used in large quantities. In this context, copper is a good candidate material. However, copper nanoparticles synthesized in ambient atmospheric temperature and pressure inevitably have surface oxide layers because the copper oxide phases are thermodynamically more stable than pure copper.

Following the stability issue of CuNPs, another important aspect is its applications. One of the applications we are interested in is photovolatics. Exploiting metal nanoparticles enable (i) to increase absorption due to surface plasmons and light trapping effects, (ii) to promote electron transfer from metal to semiconductor and to minimize the surface charge recombination in semiconductor since they serve as electron trapping media. A better understanding of these effects was crucial in exploiting the beneficial aspects of metal nanoparticles in photovolatics. In the nanoparticles integrated solar cells, NPs can be integrated at several places in solar cells structures. In the case of metal NPs embedded in interlayer of solar cells, the advantages of increased absorption in light absorber layer and promoted charge transport in electrode interface would be expected. It is also noted that the favorable characteristics of interlayer are high optical transmission, wide band-gap, and good electrical conductivity. By varying nanoparticles loading concentration, size and shape of nanoparticles in interlayer, aforementioned interlayer properties of optical transmission, band-gap, and electrical conductivity can be modulated, thereby influencing the device performance of solar cells.

2. Experiment

This experimental section describes the synthesis of copper nanoparticle (CuNPs) colloids and titanium suboxide sol-gel. In addition, the fabrication and characterization of CuNPs/TiO_x composite films is also presented.

2.1. Synthesis of Copper Nanoparticles Colloids and Titanium Suboxide Sol-gel

Copper nanoparticles colloids were synthesized by chemical reduction method. Copper (II) sulfate pentahydrate salt, $CuSO_4.5H_2O$ (purity 98%) was dissolved in distilled water. Polyethylene glycol 6000 (PEG 6000) was used as the capping agent. Sodium borohydride ($NaBH_4$) was used as the main reducing agent, while ascorbic acid ($C_6H_8O_6$) was used as the antioxidant of colloidal copper. Sodium hydroxide NaOH was also used to adjust the solution pH and accelerate the reduction reaction in distilled water. The solution pH was adjusted to 12.

The four-step scheme for the flow charts and synthesis of colloidal copper nanoparticles is shown in Figure 1 and 2. It starts with dissolving copper (II) sulfate pentahydrate salt, $CuSO_4.5H_2O$ (0.01M) in distilled water to obtain a blue solution. Next, polyethylene glycol 6000, PEG 6000 (0.02M) was dissolved in distilled water and added to the aqueous solution containing the copper salt while vigorously stirring. In this step, the solution changed from blue to white. In the third step, ascorbic acid (0.02M) and sodium hydroxide (0.1M) were dissolved and added to the synthesis solution. color changed in the aqueous phase from white to yellow. Finally a solution of sodium borohydride $NaBH_4$ (0.1M) in distilled water was prepared and added to the solution under continuous rapid stirring. The color immediately changed in the aqueous phase from yellow to black/red. The appearance of this dark color indicated that the reduction reaction had started. The source of electrons for the reaction was BH_4^-. The mixture was further stirred rapidly for around 10 min in ambient atmosphere, to allow the reaction to complete.

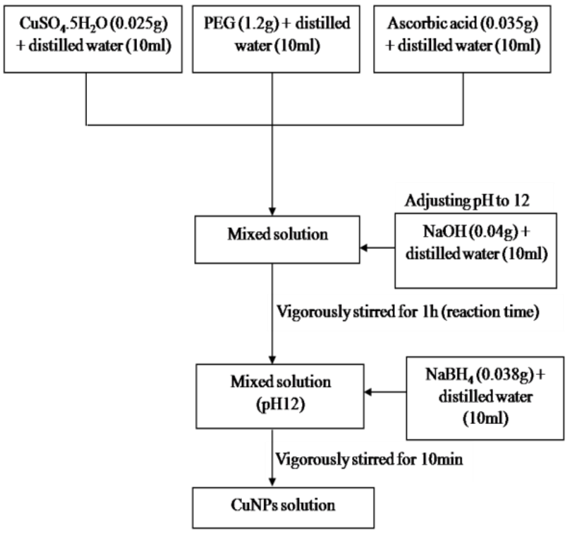

Figure 1. Preparation steps for copper nanoparticles

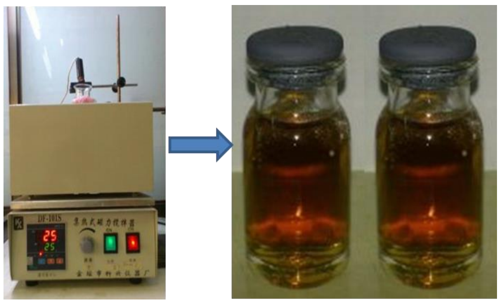

Figure 2. Experimental setup for preparation of colloidal CuNPs solution

2.2. UV-vis Spectrophotometry

The optical absorption and transmission spectra of pure TiO_x films and CuNPs/TiO_x composite films were recorded in the spectral range of 300 nm to 900 nm using UV-Vis spectrophotometer (Thermo Scientific GENESIS 10S). The baseline scan was taken using distilled water (for CuNPs colloids) and bare glass substrate (for thin films) prior to the measurement.

3. RESULTS AND DISCUSSION

This section presents three parts: (i) the surface plasmon resonance properties of colloidal copper nanoparticles (CuNPs) by varying the solution pH, reaction time and molar ratios of reducing agent: Cu precursor and stabilizer: Cu precursor, (ii) time evolution of surface plasmon resonance of colloidal CuNPs and (iii) the optical and electrical properties of CuNPs/TiO_x composite films.

3.1. Surface Plasmon Resonance Properties of Colloidal CuNPs

This section presents the effects of (i) pH, (ii) reaction time, (iii) reducing agent to precursor molar ratio, and (iv) stabilizer to precursor molar ratio on surface plasmon resonance properties of colloidal copper nanoparticles.

3.1.1 Effect of pH

The prior reports showed that the pH in aqueous media has an influence on the progress of the copper reduction reaction. With the dropwise addition of 0.1M NaOH solution, the pH of copper nanoparticles solutions was adjusted from pH 6 to pH 14. Figure 3 shows the UV-vis absorption spectra of five colloidal solutions synthesized under the same conditions except the solution pH ranging from pH 6 to pH 14. It is seen in Figure 4 that the plasmon absorption was revealed for copper nanoparticle colloids of pH 10, 12, and 14. There is no absorption peak at pH 6 and 8 which probably indicates very small particles at these low pH values. Plasmon resonance is clearly visible for pH from 10 to 12 (slightly higher intensity at pH 12). At pH 14, the peak is still detectable but much weaker. The absorption bands for colloidal copper nanoparticles are in the range of 570-750 nm peaking at 630 nm, 650 nm, and 680 nm for pH 10, pH 12, and pH 14 respectively. The exact position of the plasmon absorption band would depend on the several factors including particles size, shape, and solvent type and capping agent. In this case, it may be due to some variation in the arrangement of the capping molecules around the copper particles as a consequence of the variation of pH.

3.1.2 Effect of Reaction Time

Reaction time is very important parameter in nanoparticle synthesis. To study the effect of reaction time during synthesis on the formation of product with the only variable being the duration of stirring with ascorbic acid before pouring the sodium borohydride. Figure 4 shows the UV-vis absorption spectra of four colloidal solutions synthesized under the same conditions except differing in reaction time. The reaction times with ascorbic acid up to 60 min give higher surface plasmon absorption intensity suggesting the formation of well-defined nanoparticles with a decrease in the mean particle size with time. plasmon resonance band maximum (λ_{max}) as function of reaction time during synthesis are listed in Table 1.

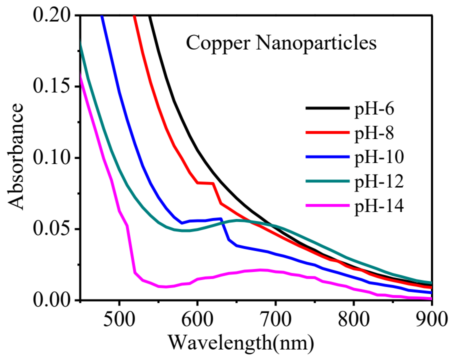

Figure 3. The UV-vis absorption of copper nanoparticles with different values of pH

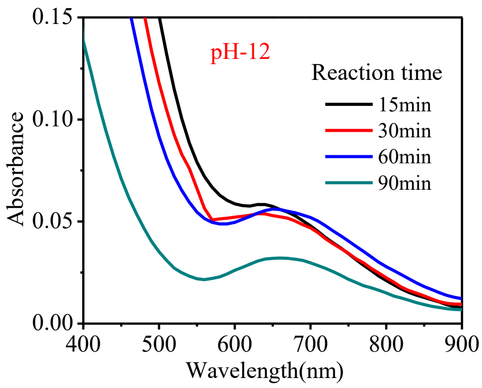

Figure 4. The UV-vis absorption of copper nanoparticles prepared under various reaction times

Table 1. Plasmon resonance band maximum (λ_{max}) against the reaction time

Samples	Reaction time of solution(min)	λ_{max} (nm)
1	15	640
2	30	630
3	60	650
4	90	660

3.1.3 Effect of Reducing Agent [$NaBH_4$] to Precursor [Cu^{2+}] Molar Ratio

In addition to the effects of pH and reaction time, we also investigated the effect of varying reducing agent to copper molar ratio. We choose sodium borohydride ($NaBH_4$) as a reducing agent because of its strong reducing properties. Figure 5 shows the absorption spectra of colloidal copper nanoparticles prepared using different molar ratios of $NaBH_4$ to Cu^{2+}. It is observed that the peak intensity decreases upon increasing $NaBH_4$ concentration. Plasmon resonance band maximum (λ_{max}) against the molar ratio ($NaBH_4$ to Cu^{2+}) are listed in Table 2.

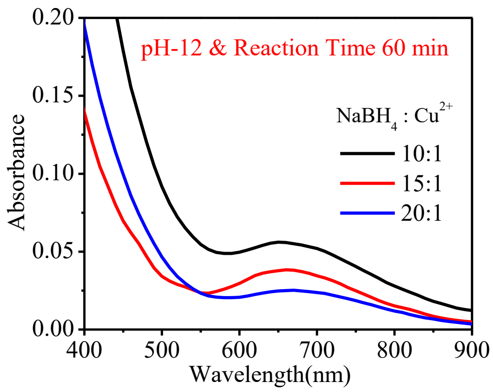

Figure 5. The UV-vis absorption spectra of copper using different molar ratios of $NaBH_4$ to Cu^{2+}

Table 2. Surface plasmon resonance band maximum (λ_{max}) against the molar ratio ($NaBH_4$ to Cu^{2+})

Samples	$NaBH_4/Cu^{2+}$ Molar Ratio	λ_{max}(nm)
1	10:1	650
2	15:1	660
3	20:1	670

3.1.4 Effect of Stabilizer [PEG] to Precursor [Cu^{2+}] Molar Ratio

Polyethylene glycol (PEG) is frequently used as the surfactant to prepare nanoparticles and as the stabilizer of metal colloids, because of its availability, low cost and non toxicity. It has already been shown that the size and shape of nanomaterials strongly depends on the solution concentration of PEG. One way to prevent nanoparticles from aggregation is the use of substances that lead to steric repulsion between individuals. PEG is an example of this type of growth and aggregation inhibitors. We studied the effect of varying molar ratios (PEG to Cu^{2+}) on surface plasmon resonance properties of CuNP colloids. The molar ratios of PEG to Cu^{2+} against the obtained λ_{max} values are tabulated in Table 3. Figure 6 shows the UV-vis absorption spectra of colloidal copper nanoparticles prepared using different molar ratios of PEG to Cu^{2+} (2:1, 4:1, and 6:1). The absorption peak maximum (λ_{max}) of colloidal CuNPs (4:1) is 690 nm which is red-shifted as compared to those of the solutions (2:1 and 6:1). It is speculated that the relatively larger NPs would be produced with 4:1 molar ratio. The larger NPs usually give lower absorption intensity due to lower surface-to-volume ratio. As expected, the absorption intensity of CuNPs colloids with (4:1) is lower than those with (2:1) and (6:1) (Fig. 6).

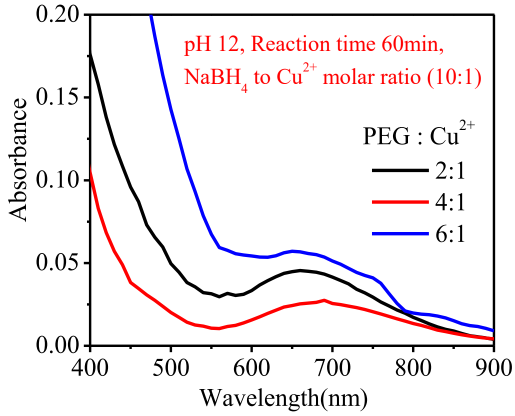

Figure 6. The UV-vis absorption spectra of colloidal copper nanoparticles using different molar ratios of PEG to Cu^{2+}

Table 3. Surface plasmon resonance band maximum (λ_{max}) against the molar ratio (PEG to Cu^{2+})

Samples	PEG/Cu^{2+} Molar Ratio	λ_{max}(nm)
1	2:1	660
2	4:1	690
3	6:1	650

3.1.5 Time Evolution of Surface Plasmon Resonance Bands of Colloidal CuNPs

In order to examine the stability of the CuNPs colloids, time evolution of surface plasmon resonance properties of CuNPs colloids was studied. We used the CuNPs colloid prepared using the optimum conditions extracted from my previous study (section 4.1) [pH (12), reaction time (1h), $NaBH_4$:Cu^{2+} (10:1) and PEG 6000: Cu^{2+} (6:1)]. Figure 8 and Figure 9 (a-d) show the SPR absorption spectra of CuNPs colloids recorded during 1 hr time period with step 1 min. Time record has started immediately upon adding $NaBH_4$ into the mixture solution. It can be seen in Figure 7 that no surface plasmon resonance (SPR) peak appears within the first record time 7 min beyond which it tends to appear suggesting that the colloidal CuNPs were formed. The SPR peak of as-obtained colloidal CuNPs is at $\lambda \sim 565$ nm.

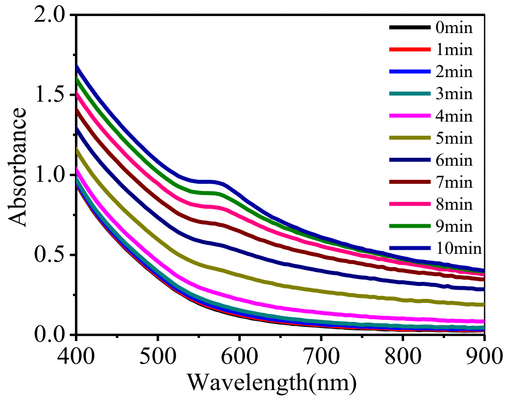

Figure 7.Time evolution of surface plasmon resonance of copper nanoparticles (record time period 0 min-10 min).

3.1.6 Optical Transmission of CuNPs/TiO$_x$ Composite Films: Varying CuNPs Loading Concentrations

We investigated the effects of CuNPs concentration on the optical properties of CuNPs/TiO_x composite films by acquiring the optical absorption and transmittance spectra in the spectral range of 300nm-900nm. Figure 8 (a-c) shows the optical transmittance spectra for the composite films with different CuNPs concentrations that were annealed at three different temperatures (100°C, 200°C, and 300°C). In the 100°C annealed films (Figure 8 (a)), the composite films with CuNPs (2, 4 and 6 mol%) exhibit higher transmission (T%) than the pure TiO_x film. The composite film with highest CuNPs loading (8mol%) decrease T% as compared to that of pure TiO_x film which is attributed to higher scattering cross-section of overloaded CuNPs in TiO_x matrices.

At elevated temperatures of 200°C and 300°C, T% of all the composite film (2 to 8 mol%) is higher than that of pure TiO_x film (Figure 8 (b, c)). It may be ascribed to the increased particle size and number of voids in the films upon annealing the film. Using the absorption spectra of pure TiO_x film and CuNPs/TiO_x composite films (not shown here), their optical band gap energies were achieved by the relation $(\alpha h\upsilon)^{1/n} = A(h\upsilon - E_g)$, where α is absorption coefficient, $h\upsilon$ is incident light energy and E_g is the band gap of the material. The exponent 'n' depends on the type of transition. For direct allowed transition, n = 2, n = 1/2 for indirect allowed transition, and for direct forbidden transition, n = 3/2. We plot the $(\alpha h\upsilon)^{1/2}$ against photon energy ($h\upsilon$) for pure

TiO_x film and CuNPs/TiO_x composite films (Figure 9 (a-c)). When the straight portion of the $(\alpha h\upsilon)^{1/2}$ against $(h\upsilon)$ plot is extrapolated to the point $\alpha = 0$, we extract the band gap energy of the materials being studied.

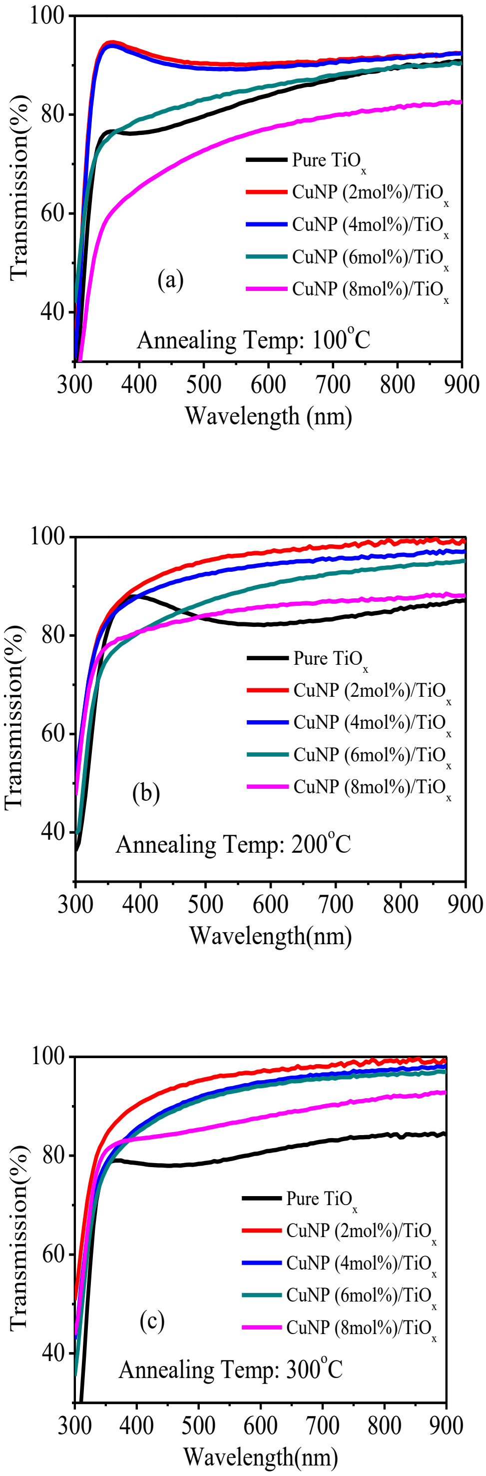

Figure 8. Optical transmission spectra of pure TiO_x film and CuNPs/TiO_x composite films annealed at different temperatures (a) 100°C, (b) 200°C, (c) 300°C

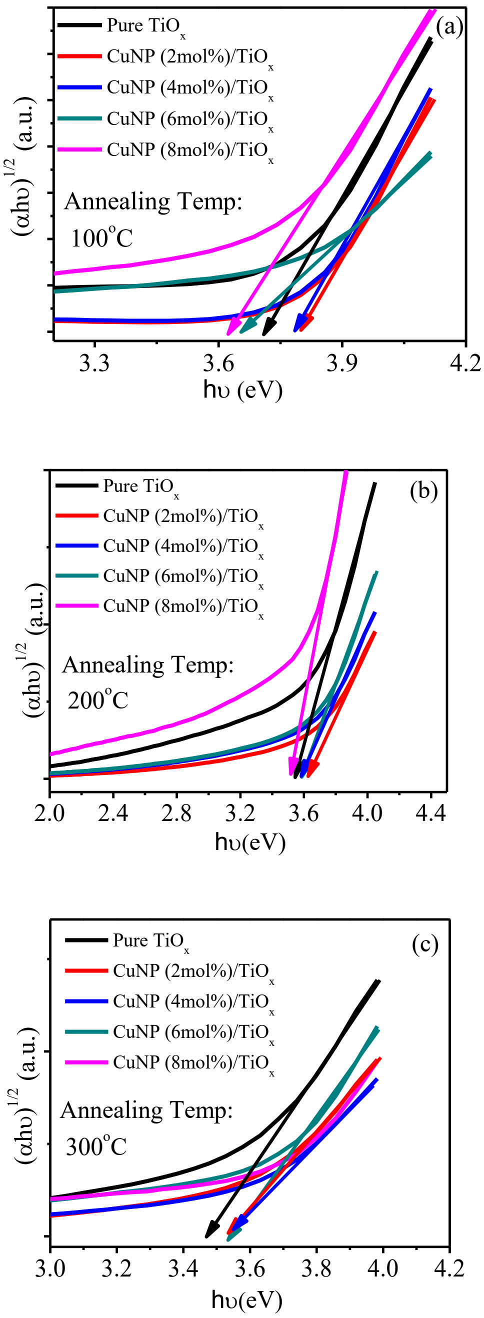

Figure 9. Plots of $(\alpha h\nu)^{1/2}$ vs. $h\nu$ for pure TiO_x film and CuNPs/TiO_x composite films annealed at different temperatures (a) 100°C, (b) 200°C, (c) 300°C.

To observe clearly the effect of CuNPs concentration (mol%) on the optical transmission (T%) and band gap (E_g) of CuNPs/TiO_x films, we plot the T% vs. CuNPs concentration and E_g vs. CuNPs concentration for the films and they are depicted in Figure 10 (a-b). Among all the different loading (mol%) of CuNPs in TiO_x films, CuNPs loading of 2 mol% provides the maximum T% (97%) and maximum optical band gap energy (3.8 eV). Higher transmission and wider band gap are favorable characteristics of interlayer (window layer) in photovoltaic cells.

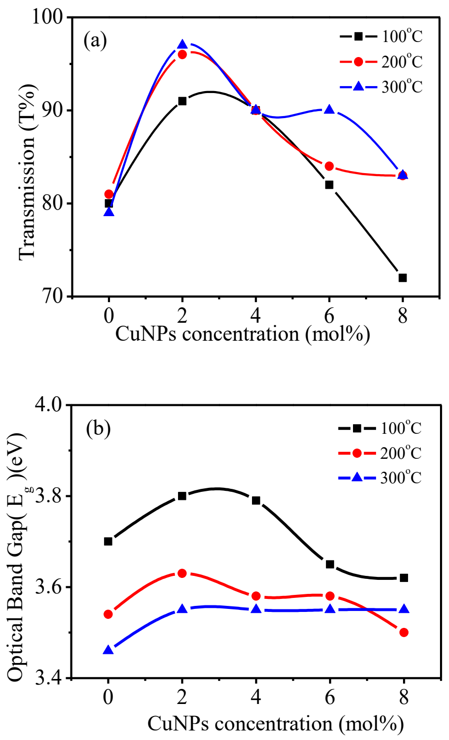

Figure 10. Plots of (a) T% against CuNPs loading (mol%) and (b) E_g against CuNPs loading (mol%) for the films annealed at different temperatures

4. Conclusion

Effectively of copper nanoparticles is found in varied applications such as antifungal, antiviral, antibiotics, anticancer, photocatalytic, in biomedical, agriculture fields etc. Titanium dioxide (TiO_2) nanoparticles have a high refractive index, making them ideal for various applications, including medicines, coatings, inks, plastics, food, cosmetics, and textiles. The colloidal CuNPs were synthesized by chemical reduction method. The sol-gel derived metal NPs/TiOx films were fabricated by spin-coating method. Varying NPs loadings in titania, we have extracted a trade-off which offers a more favorable properties of nanocomposite films for interlayer application in photovoltaics. CuNPs loading of 4 mol% should meet a trade-off which wider band gap energy as compared to those of pure TiOx film. The interlayer with high electrical conductivity would promote the charge transport at the electrode interface and the wide band-gap interlayer would transmit the wider range of incoming photon energies into the light absorber layer, thereby increasing the photovoltaic device efficiency.

Acknowledgements

Special thanks to members of Materials Research Lab, Department of Physics, University of Mandalay, for their help in experimental work.

References

[1] A. Umer *et al.,* Phys. Rev. **7,** (2012) 1230005.
[2] D.L. Feldheim *et al.,*"Synthesis, Characterization and Applications", Marcel Dekker, New York (2002).

[3] H. Zhu *et al.*, Nanotec. **16,** (2005) 3070.

[4] S.H. Wu *et al.,* J. Colloid Interface Sci. **273,** (2004) 165.

[5] G. Li and Y. Luo, Inorg. Chem. **1,** (2008) 360.

[6] H.R. Stuart and D.G. Hall, Appl. Phys. Lett. **73,** (1998) 3815.

[7] Y. Tian and T. Tatsuma, Chem. Commun. **16,** (2004) 1810.

[8] Y. Tian and T. Tatsuma, Chem. Commun. **16,** (2004) 1810.

[9] Y. Tian and T. Tatsuma, J. Chem. **127,** (2005) 7632.

[10] S. Mubeen *et al.,* Nano Lett. **11,** (2011) 5548.

Authors

Biography

First . Dr Thaung Hlaing Win

Lecturer

Department of Physics

Pakokku University

EFFECT OF AGEING AND PH-VALUES ON OPTICAL AND ELECTROCHEMICAL PROPERTIES OF COLLOIDAL COPPER NANOPARTICLES

Myat Phu Wai[1], Phyu Thazin Aung[2], and Thaung Hlaing Win[3]

[1,2] Department of Physics, Pakokku University
myatphuwai18@gmail.com,thazinaungphyu791@gmail.com,thaung.naing001@gmail.com

ABSTRACT

Nanoparticles have been extremely small dimensions and a high surface to volume ratio such as catalytic reactivity and electrical conductivity. Green synthesis of copper nanoparticles by using plant extracts as producing agents is of particular interest. This research aimed to explore, the natural dyes was extracted from red onion peel with different concentrations (10 ml, 20 ml and 30 ml) by solvent extraction method. This present work reports a green method where copper nanoparticles were synthesized using copper sulphate ($CuSo_4$) and the aqueous extract Red Onion Peels as the reductant and the capping agent. In addition, the synthesized copper nanoparticle (CuNPs) was carried out at different conditions, including pH and concentration ratios were characterized with UV-Vis Spectrophotometry. In ageing study on pH values, the highest optical absorption peak observed at 0 day (as-prepared) and pH values ~ 5.2. The optimum scan range was observed at 50 mV allowing a suitable formation of colloidal copper nanoparticles.

KEYWORDS

Reducing agent, green synthesis, pH-values, natural dyes, copper nanoparticles.

1. INTRODUCTION

Metallic nanoparticles have received significant attention by researchers due to their unique properties, such as depression of melting temperature, electrical conductivity, magnetism and light absorption in comparison with bulk metal. Among various metal nanoparticles, copper nanoparticles (CuNPs) are attracting increased attention because of their optical and electrical conducting properties at a significantly lower cost than gold and silver. CuNPs are particularly attractive for applications in catalysts, conductive ink and cooling fluid. CuNPs have been synthesized by different methods. Chemical reduction is one of the most convenient methods for the synthesis of metallic nanoparticles because the synthesis process is simple and the size of nanostructured copper can easily be controlled. Compared with conventional methods, it is much faster, cleaner and more economical.

Colloidal particles are increasingly receiving attention as important staring points for the generation of micro and nanostructures. These particles are under active research because they possess interesting physical properties differing considerably from that of the bulk phase. It comes from small sizes and high surface/ volume ratio. Manufacturing entire objects from pure metal or coating them with copper is prohibitively expensive for consumer items but research has found that impregnating other materials with copper nanoparticles is a practical way to exploit them germ fighting properties of copper.

However, copper nanoparticles (CuNPs) tend to be fairly unstable in solution and therefore special precautions have to be taken to avoid their aggregation or precipitation and oxidation during the preparation of such colloidal CuNPs in solution. To protect CuNPs against oxidation during preparation and storage, the reaction is in many cases performed in non-aqueous media, at low precursor concentration and in an inert atmosphere, ascorbic acid is often used to play the role of reducing agent and antioxidant of colloidal CuNPs.

Surfactants or stabilizing agent such as Red Onion Peels natural dyes was applied to the synthetic system as dispersant or modifier. These materials were used not only to control the particle size, particle size distribution and shape but also to prevent aggregation and further oxidation.

Sodium borohydride, sodium hypophosphite and ascorbic acid were utilized as reductant for the chemical reduction synthesis of nanostructure copper. CuNPs colloids were synthesized by green synthesis method with distilled water. The protective role of Red Onion Peels was also investigated with different capping agent concentrations.

2. EXPERIMENTAL WORK

In this section deals with the extraction of natural dyes, the green synthesis and characterization of colloidal copper nanoparticles (CuNPs) with different Red Onion Peels.

2.1. Extraction of Natural Dyes from Red Onion Peels

The plant materials (Red Onion Peels) specimens were collected from local market, Pakokku Township, Magway Region. The botany name (Scientific name) of Red Onion Peels is known as *Allium cepa L.* The collected specimens were cleaned and rinsed thoroughly 2-3 times with water to remove visible dust particles and air dried at room temperature.

The fine dried Red Onion Peels were cutting into small pieces. 5 g of finely cut Onion Peels were kept in a breaker containing 200 ml of distilled water, immersed for 30 min and filtrated using filter paper. The color of the solution appeared orange-red color, indicating the formation of Red Onion Peels dye. The effect of ageing on pH of Red Onion Peels solution was measured by pH meter.

Figure 1 show the flow chart and sample preparation of the natural dye extracted from Red Onion peels.

2.2. Synthesis of Copper Nanoparticle Colloids

Copper oxide (CuO) powder was used as a metal salts precursor for the formation of copper nanoparticles (CuNPs). For the preparation of metal nanoparticles, various concentrations of Red Onion peels dyes (10 ml, 20 ml and 30 ml) were mixed copper oxide powder (0.2 g). These mixed solutions were stirring for about 15 min at room temperature.

The physical color of solution changed from blue color to red-purple color, indication the formation of copper nanoparticles. This sample was further measured for its optical and electrochemical properties by using UV-Vis Spectrophotometry and Cyclic Voltammetry (CV). Figure 2 (a-b) shows the flow chart and sample preparation of copper nanoparticles with different capping agent concentrations.

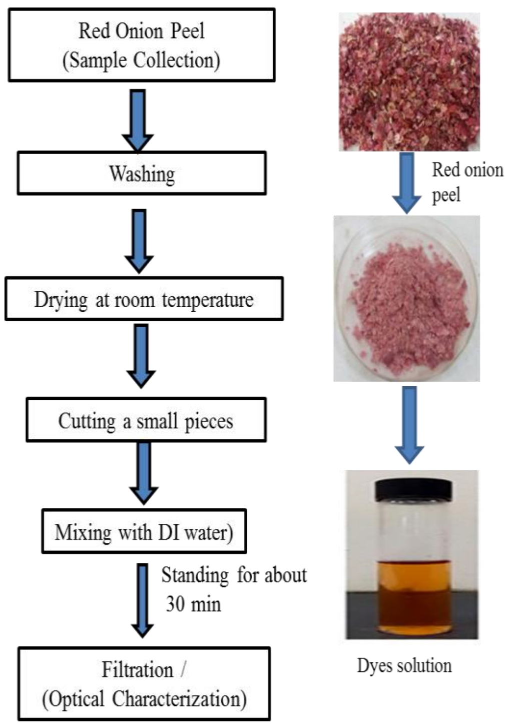

Figure 1. Flow charts and sample preparation steps of the dye solution extracted from Red Onion Peels

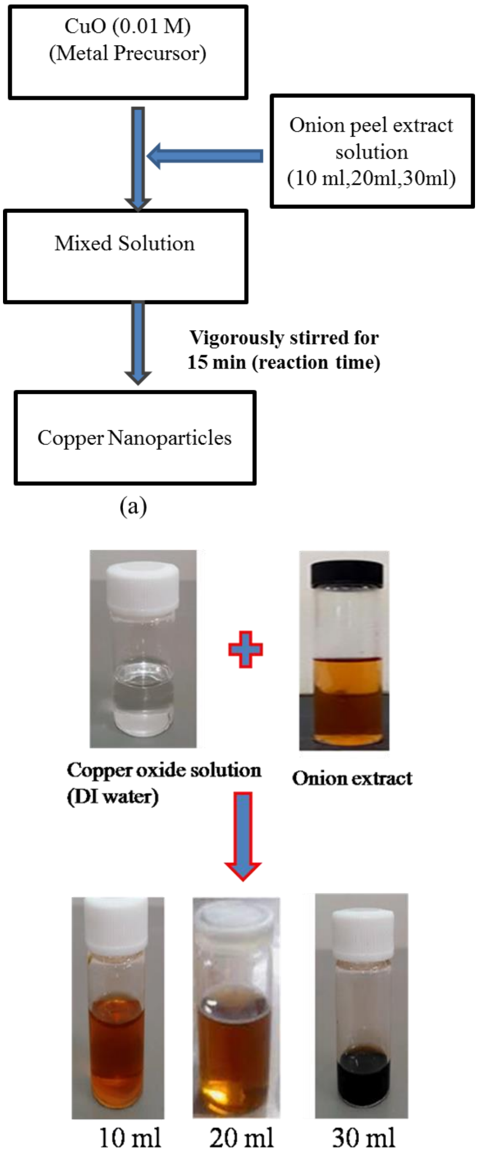

Figure 2 (a-b) Flow chart and sample preparation of copper nanoparticles with different capping agent concentrations

3. Characterization

The characterization methods consist of UV-Vis spectrophotometry and Cyclic Voltammetry (CV).

3.1. UV-Vis Spectrophotometry

UV-Vis Spectrophotometry is analytical method to measure the absorption, transmission and emission of ultraviolet and visible light wavelengths by sample. The optical properties and stability of colloidal copper nanoparticles was measured UV-Vis spectrophotometry: (GENESIS 10SUV) - (Materials Research Lab, Department of Physics, and University of Mandalay) as shown in Figure 3. The optical absorption of CuNPs was recorded in the wavelengths ranging from 300-900 nm. Distilled water was used as baseline scanning before the measurement.

3.2. Cyclic Voltammetry

Potentiostat (Digi-DY2000) with three electrode systems consisting of a glassy carbon working electrode, platinum wire counter electrode and Ag/AgCl reference electrode at a scan rate of 50 mV/s. A few drops of dye or meal nanoparticles solutions were placed on the glassy carbon working electrode and allowed to dry at room temperature before immersing the electrode in a supporting electrolyte. The supporting electrolyte was 0.1 M KNO_3 in distilled water. For solution measurement, the copper nanoparticles solution was used as the working electrode, platinum wire and Ag/AgCl were used as counter electrode and reference electrode respectively. The scan rate in range (10-50) mV/s and supporting electrode KNO_3 were also used for thin film measurement as shown in Figure 4.

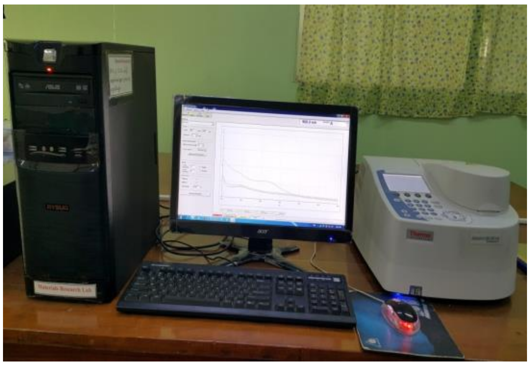

Figure 3. UV-Vis Spectrophotometry (GENESIS 10S)

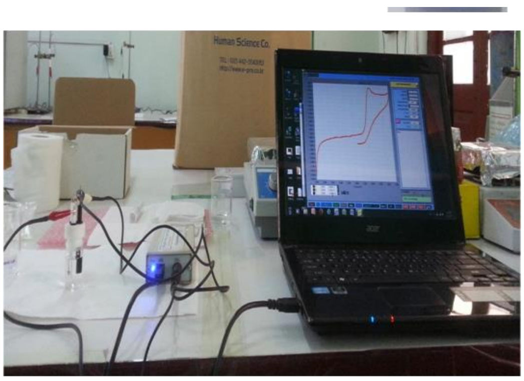

Figure 4. Cyclic Voltammetry (CV)

4. RESULTS AND DISCUSSION

The optical absorption properties and electrochemical properties of copper nanoparticles (CuNPs) were explored varying with the volume ratio of reducing agents (natural dyes) concentrations.

4.1 Extinction of CuNPs Colloid: (Varying capping agent concentrations)

The first part of present work, the effect of capping agent (red onion peels dye) concentrations on optical extinction properties of CuNP colloids with distilled water was studied. Figure 5 (a-b) shows optical extinction spectra of colloidal CuNPs with capping agent concentrations (10 ml) and plots of the extinction peak maximum (λ_{max}) versus wavelength. Upon ageing 0 day up to 27 day, the extinction peak intensity was decreased and extinction peak position was red shifted from 556 nm to 584 nm. The value of pH slightly increased from 5.10 to 5.47. Upon ageing 21 day up to 27 day, the values of pH remained unchanged at pH value 5.50. The maximum extinction peak intensity was observed at pH values 5.10 (as-obtained). According to the above results, the highest dispersion solution of CuNPs was observed at acidic condition and zero day ageing.

The second part of present work, the effect of capping agent (red onion peels dye) concentrations on optical extinction properties of CuNP colloids with distilled water was studied. Figure 6 (a-b) shows optical extinction spectra of colloidal CuNPs with capping agent concentrations (20 ml) and plots of the extinction peak maximum (λ_{max}) versus wavelength. Upon ageing 0 day up to 27 day, the extinction peak intensity was decreased and extinction peak position was red shifted from 561 nm to 577 nm. The value of pH slightly increased from 5.18 to 5.70. Upon ageing 21 day up to 27 day, the values of pH remained unchanged at pH value 5.80. The maximum extinction peak intensity was observed at pH values 5.18 (as-obtained). According to the above results, the highest dispersion solution of CuNPs was observed at acidic condition and zero day ageing.

The third part of present work, the effect of capping agent (red onion peels dye) concentrations on optical extinction properties of CuNP colloids with distilled water was studied. Figure 7 (a-b) shows optical extinction spectra of colloidal CuNPs with capping agent concentrations (30 ml) and plots of the extinction peak maximum (λ_{max}) versus wavelength. Upon ageing 0 day up to 27 day, the extinction peak intensity was decreased and extinction peak position was red shifted from 571 nm to 596 nm. The value of pH slightly increased from 5.80 to 6.17. Upon ageing 21 day up to 27 day, the values of pH remained unchanged at pH value 6.20. The maximum extinction peak intensity was observed at pH values 5.80 (as-obtained). According to the above results, the better solubility solution of CuNPs was observed at acidic condition and zero day ageing.

Figure 8 shows the effect of ageing day vs. pH values with different capping agent concentration (10 ml, 20 ml, 30 ml). Upon increasing capping agent concentrations, the pH values increased from 5.10 up to 6.20. For all capping agent concentrations (10 ml, 20 ml, 30 ml), the pH values was observed at under acidic conditions. The stable pH values observed at over 21 day.

4.2. Optimum Condition of Extinction Band of CuNPs Colloids: (Varying Capping Agent Concentrations)

Figure 9 shows the copper nanoparticles with different capping agent concentrations (10 ml, 20 ml and 30 ml). Upon increasing capping agent concentrations, the extinction band of CuNPs was red-shifted and peak intensity decreased. The spectroscopic results, CuNPs size may be large at higher capping agent concentrations. Table (1) shows the capping agent concentrations on extinction peak position of copper nanoparticles.

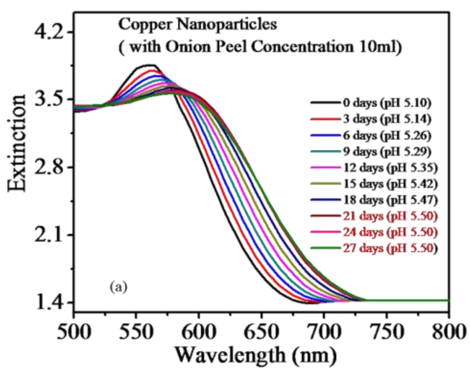

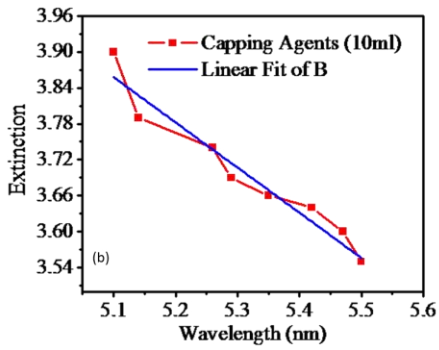

Figure 5. (a-b) Optical extinction spectra of CuNPs with capping agent concentrations (10ml) and plots of the extinction peak maximum (λ_{max}) versus wavelength

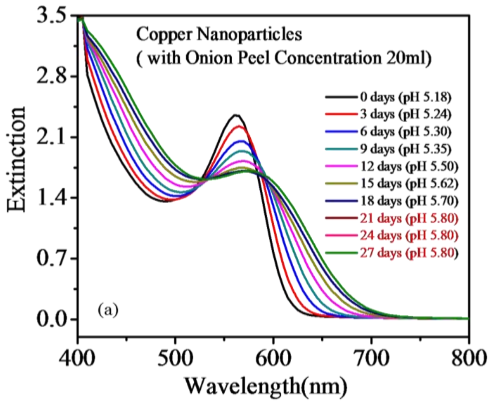

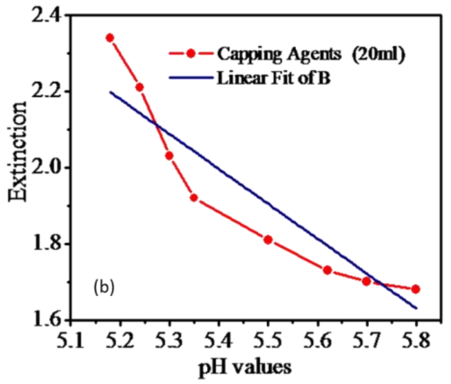

Figure 6. (a-b) Optical extinction spectra of CuNPs with capping agent concentrations (20 ml) and plots of the extinction peak maximum (λ_{max}) versus wavelength

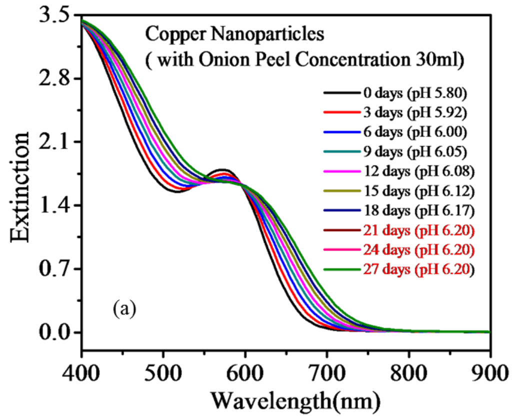

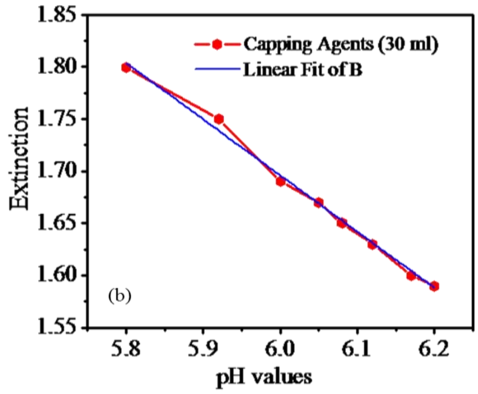

Figure 7.(a-b) Optical extinction spectra of CuNPs with capping agent concentrations (30 ml) and plots of the extinction peak maximum (λ_{max}) versus wavelength

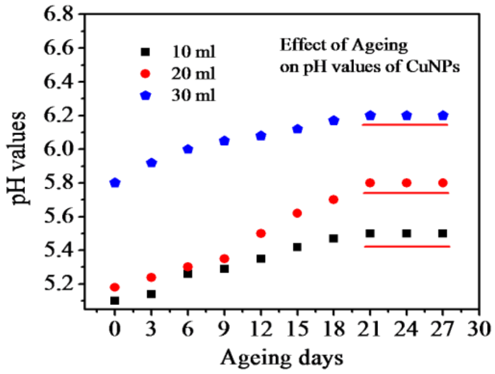

Figure 8. Effect of ageing day vs. pH values with different capping agent concentrations (10 ml, 20 ml, 30 ml)

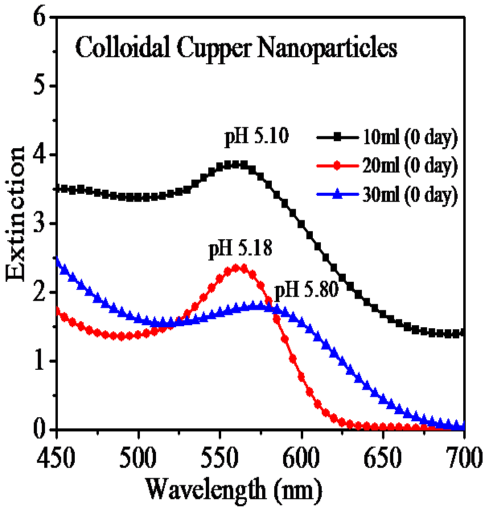

Figure 9. Copper nanoparticles with different capping agent concentrations (0 day)

Table 1. The capping agent concentrations on optical extinction peak of CuNPs

Samples	Capping agent concentrations	λ_{max} (nm)
1	10 ml	556
2	20 ml	561
3	30 ml	571

4.3. Cyclic Voltammograms Measurement of Colloidal Copper Nanoparticles

Figure 10 (a) shows the Cyclic Voltammograms measurement of colloidal CuNPs (capping agent concentrations 10 ml) with scan rates from 5 mV up to 100 mV. The dependencies of anodic peak current values against the cycle number were plotted for different scan rates in the electrolyte. In all CV curves, the anodic peak current significantly increased and red-shifted from 0.02 up to 0.15 with cycle number. Upon increasing scan rates, the cathodic peak current significantly decreased and blue-shifted from 0.32 up to 0.42. It suggested that the increase of copper content in the solution as NPs. Upon increasing the scan rates (5 - 100) mV facilitates the particle formation rate and increased the copper film deposition rate.

Figure 10 (b) shows the Cyclic Voltammograms measurement of colloidal CuNPs (capping agent concentrations 20 ml) with scan rates from 5 mV up to 100 mV. The dependencies of anodic peak current values against the cycle number were plotted for different scan rates in the electrolyte. In all CV curves, the anodic peak current significantly increased and red-shifted from 0.30 up to 0.38 with cycle number. Upon increasing scan rates, the cathodic peak current was significantly decreased and blue-shifted from 0.2 up to 0.28. Upon increasing the scan rates (5-100) mV facilitates the particle formation rate and increased the copper film deposition rate.

Figure 10 (c) shows the Cyclic Voltammograms measurement of colloidal CuNPs (capping agent concentrations 30 ml) with scan rates from 5 mV up to 100 mV Upon increasing the scan rates (5 - 100) mV, the anodic peak current significantly increased and red-shifted from 0.22 up to 0.4 with cycle number. The cathodic peak current was significantly decreased and blue-shifted from 0.03 up to 0.22. This diminution of anodic peak current as increasing CuNPs electro-synthesis rate and one may thus suggest that a suitable formation of CuNPs should be around scan rate 10 mV.

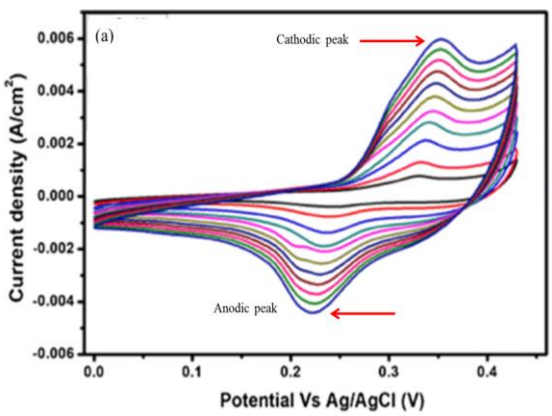

Figure 10 (a) Cyclic Voltammograms measurement of CuNP (capping agent concentrations 10 ml) with scan rates from 5 mV up to 100 mV

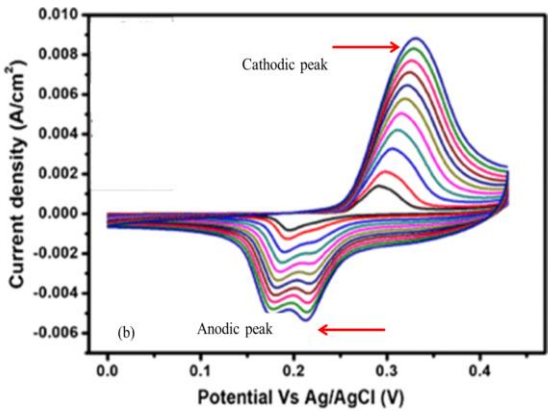

Figure 10 (b) Cyclic Voltammograms measurement of CuNPs (capping agent concentrations 20 ml) with scan rates from 5 mV up to 100 mV

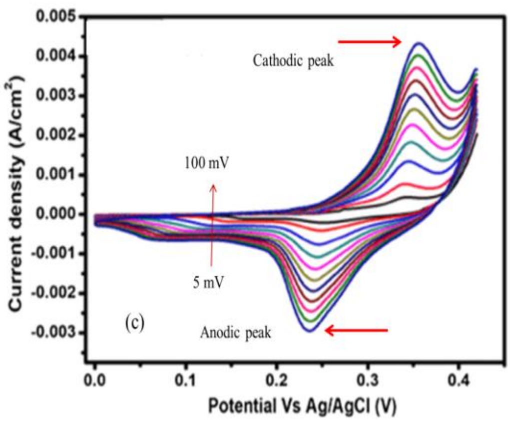

`Figure 10 (c) Cyclic Voltammograms measurement of colloidal CuNPs (capping agent concentrations 30 ml) with scan rates from 5 mV up to 100 mV

5. Conclusion

The first part of the present work, the colloidal copper nanoparticles was synthesized by green synthesis method. The effect of capping agents concentration (10ml, 20ml, 30ml)on optical absorption of CuNPs by UV-Vis Spectrophotometry. Upon ageing 0 day up to 27 day, the optical extinction peak intensity decreased and peak position shifted to the longer wavelength regions. The value of pH increased 5.10 up to 5.50 with capping agent concentrations 10 ml, 5.18 up to 5.80 with 20 ml and 5.80 up to 6.20 with 30 ml. Upon ageing 21 day up to 27 day, the absorption peak intensity and pH values remains unchanged.

In a dye-sensitized solar cell (DSSC), cyclic voltammetry results are primarily used to analyze the redox properties of the sensitizing dye, providing crucial information about its ability to inject electrons into the TiO2 semiconductor, which is critical for efficient charge separation and photovoltaic performanceIn another study, the effect of scan rate (10 mV up to 50 mV) on the electrochemical properties of CuNPs with different capping agent concentrations (10ml, 20 ml and 30 ml) were also studied by Cyclic Voltammograms (CV). In all CV curves, the anodic peak current significantly increased with cycle number, thus proving the increase of copper content in the solution as nanoparticles. Upon increasing the scan rate (10-50) mV facilitates the particle formation rate and increases the copper film deposition rate. The results presented by CV display that the anodic peak current varies linearly with the scan rate and a shift in the potential to more positive values with increasing scan rate was observed for each attached nanoparticles. This indicates that these nanoparticles were conductive while transferring electrons with the electrode surface. It suggested that the optimum scan range (50 mV) allowing a suitable formation of copper nanoparticles.

Acknowledgements

Special thanks go to members of Materials Research Lab, Department of Physics, University of Mandalay, for their help in experimental work.

References

[1] J. Liu *et al*., Colloids Surf. A, **302** (2007) 276.

[2] D.R. Duran N *et al*., Silver Nanopar, **13** (2012) 12.

[3] M. K. Fahadi*et al*., J. Eng. Env. Sic, **34** (2011) 281.

[4] F.M. Al-Khateeb*et al*., Adv. ApplPhys and Mater Sci, **134** (2018) 217.

[5] G.M. Azizan*et al*., Int. J. Auto and MechanEngi, **10** (2014) 1920.

[6] T. Markvart*et al*., J. Appl. Phys. **29**, (2003) 300.

[7] D. MuthuvinothiniA *et al*., J. Nanotechnol, **2** (2015) 3.

[8] T.X. Chen Li *et al*., J. Open Surf Sci,**3** (2011) 76.

Authors

Biography

First A. Daw Myat Phu Wai

Demonstrator

Department of Physics

Pakokku University

Second B. Daw Phyu Thazin Aung

Demonstrator

Department of Physics

Pakokku University

Third C. Dr Thaung Hlaing Win

Lecturer

Department of Physics

Pakokku University

AUTOMATIC NUMBER PLATE RECOGNITION SYSTEM FOR MYANMAR VEHICLES USING RASBERRY PI: A CASE STUDY AT THE UNIVERSITY OF COMPUTER STUDIES, MAGWAY

Khin Thet Thet Naing[1], and Ko Ko Zaw[2]
[1,2]Department of Electronic Engineering, Technological University (Taunggyi)
khinthetthetnaing3@gmail.com,kokozawec2021@gmail.com

ABSTRACT

Automatic Number Plate Recognition (ANPR) systems are integral to Intelligent Transport Systems (ITS) for ensuring security and effective law enforcement. This research aims to design and implement of Number Plate Recognition focusing on use within the University of Computer Studies, Magway. So, Input data is used from the University of Computer Studies, Magway. Utilizing a Raspberry Pi and webcam setup, the system captures video, preprocesses frames, and applies Canny Edge detection, feature extraction, and recognition techniques using Easy OCR. Experimental results indicate a high accuracy rate in plate recognition, demonstrating the system's potential for enhancing campus security and broader urban applications. When Real time data and online data are compared, real time data is more accuracy.

KEYWORDS

ANPR, Edge detection, Bilateral filter, Easy OCR Python (3.12.0) version and PyCharm Community Edition 2024.2.1(IDE)

1. INTRODUCTION

Automatic Number Plate Recognition (ANPR) systems have emerged as pivotal tools in enhancing security, streamlining traffic management, and ensuring compliance with local regulations. By automatically capturing and analyzing vehicle license plates, ANPR technology aids law enforcement agencies in monitoring vehicular movements, identifying stolen vehicles, and managing toll collection systems more efficiently. The implementation of ANPR systems can lead to significant improvements in urban safety and operational efficiency, allowing for rapid responses to traffic violations and enhancing overall public safety.

In Myanmar, the Road Transport Administration Department oversees the registration of vehicles, having introduced a significant update to the license plate format in July 2021. The new design features a structured format that includes a three-letter regional code, which is followed by the township number, the license plate number, and the vehicle model. This unique configuration presents both opportunities and challenges for ANPR systems. For instance, the varied size of license plates, along with diverse illumination conditions and potential rotations during image capture, necessitates tailored solutions that can effectively recognize and process these specific formats.

The proposed ANPR system utilizes a Raspberry Pi and webcam setup, specifically designed to cater to the vehicle registration format used in Myanmar. By focusing on the University of Computer Studies, Magway, this research aims to provide a practical application of ANPR technology within an academic institution, enhancing security on campus while also contributing valuable data and insights to the Road Transport Administration Department.

This collaboration is essential for developing an effective model that can be adapted for broader use in urban environments across Myanmar.

The rest of the paper is organized as follows: Section 2 shows proposed system's design. Experimentation and results are presented in Section 3. and presents conclusion and discussion.

2. Proposed System's Design

In this section, the essential components and workflow of proposed Automatic Number Plate Recognition (ANPR) system designed specifically for Myanmar's vehicle license plates. The system's hardware comprises a compact and efficient Raspberry Pi, which serves as the processing core, a webcam for capturing video frames, an SD card for data storage, and an LCD display for real-time output.

These components work together seamlessly to capture, process, and display license plate information, enhancing campus security through automated recognition. The image-processing pipeline, central to the system's functionality, is described in detail, starting with image acquisition and progressing through preprocessing steps like grayscale conversion, noise filtering, and feature enhancement.

The pipeline continues with detection and mask, where the CNN (Convolutional Neural Network) model localizes and isolates characters on the plate, preparing them for Optical Character Recognition (OCR). Finally, recognized characters are displayed on the LCD for verification. This structured, resource-efficient approach makes the system both practical and scalable for real-time license plate recognition applications. The following is a visual representation of the system's setup and processing pipeline:

- AVI videos extract the frame and perform grayscale, Bilateral filter for image preprocessing.
- And the datasets create by using Canny Edge detection, Mask & Extract and Locate & Crop.
- Deep Learning like Convolutional Neural Network is applied for number plate recognition using Easy OCR.

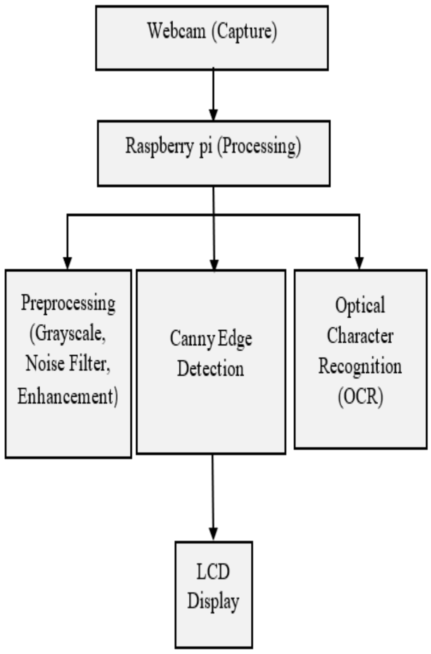

Figure 1. Overall System Design

Image-Processing Pipeline

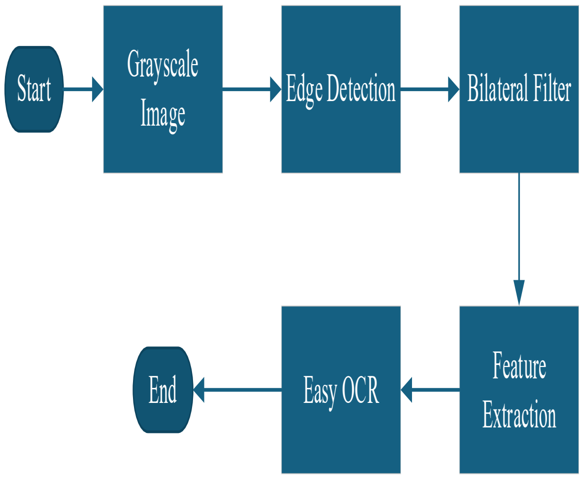

Figure 2. Image-Processing Pipeline

Software requirements are as follow:

Figure 3. Python (3.12.0) Version, PyCharm Community Edition 2024.2.1(IDE) and OpenCV

Figure 3 is applied softwares that are . Python (3.12.0) Version, PyCharm Community Edition 2024.2.1(IDE) and OpenCV.

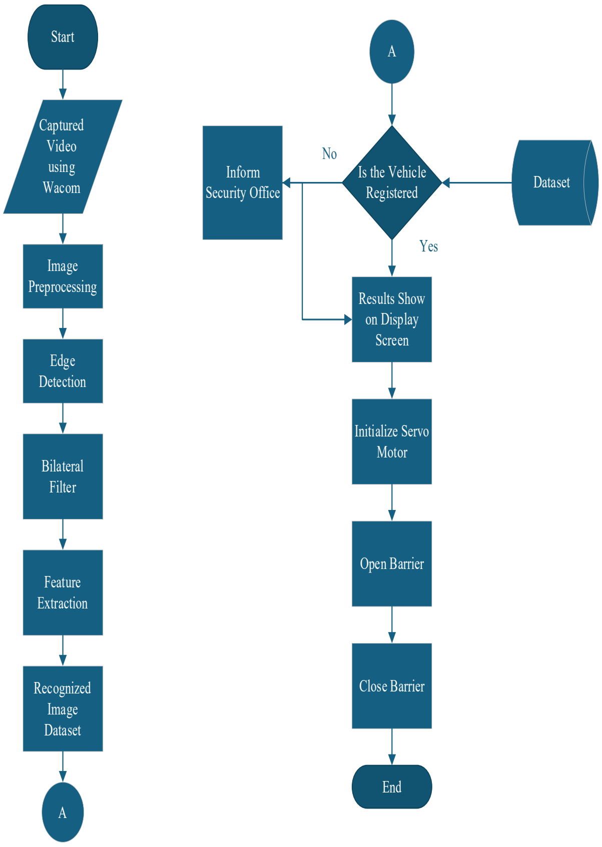

Figure 4. Flowchart of the whole operation System

2.1. Experimentation and Results

The ANPR system was evaluated under various conditions to assess its robustness and reliability. Tests were conducted across three primary variables:

Lighting Condition

- **Illumination Testing**: The system was evaluated under varying lighting environments, including bright sunlight, low light, and artificial lighting, to assess its adaptability to different levels of illumination.

Angles

- **Viewpoint Variation**: License plates were photographed from multiple angles—such as head-on, tilted, and from the side—to replicate real-world conditions where vehicle plates may not always be perfectly aligned or positioned.

Plate Condition

- **Diverse Plate Scenarios**: A range of license plates with differing levels of clarity was utilized, including clean, dusty, and worn plates. This was done to challenge the system's ability to perform under a variety of common, real-life circumstance.

Performance Evaluation

- **Assessment Metrics**: Key performance indicators, including accuracy, detection speed, and the reliability of optical character recognition (OCR), were meticulously recorded for each testing scenario. Additionally, limitations such as false positives and errors in character recognition on blurred images were documented to better understand the system's constraints.

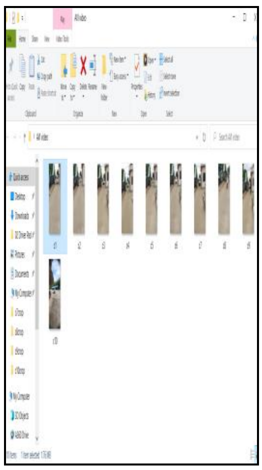

Figure 5. Mp4 Videos Figure 6. AVI Video

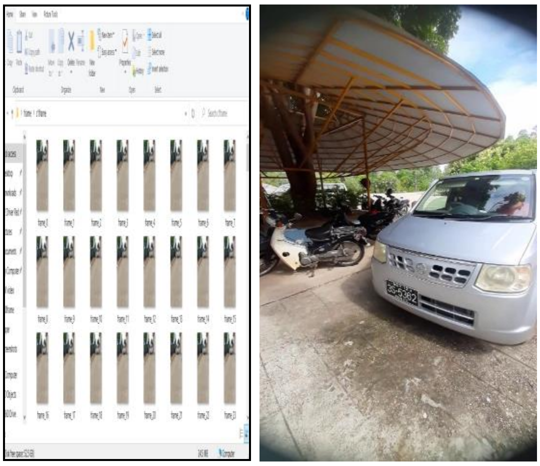

Figure 7. Framing in Python

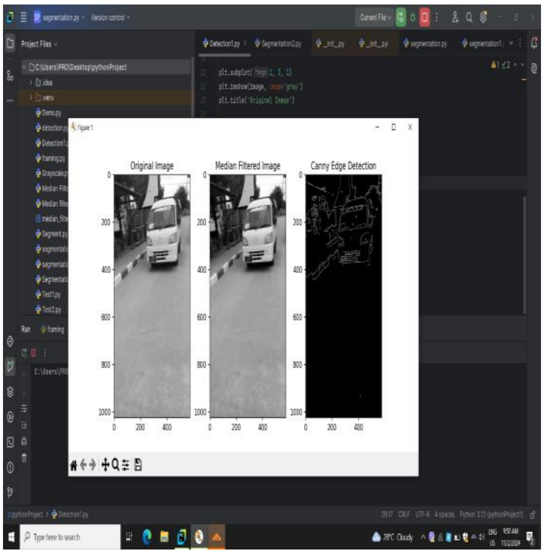

Figure 8. Canny Edge Detection

Figure 9. Results of OCR for Nissan

Figure 10. Results of OCR Toyota Nissan

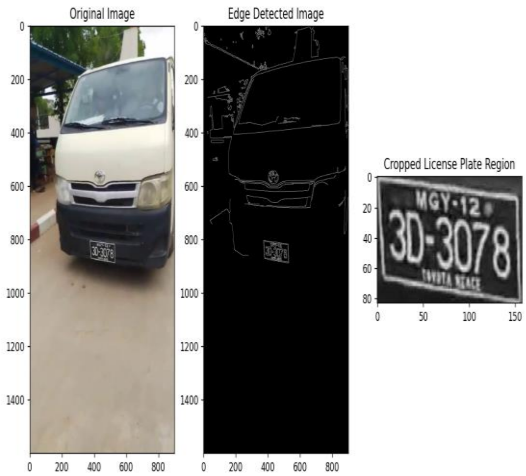

Figure 11. Results of OCR Toyota NIACE

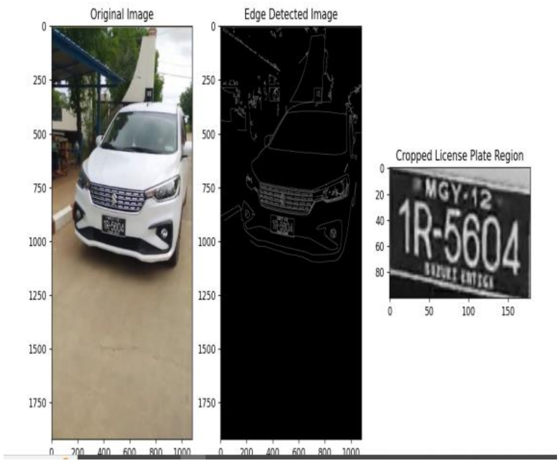

Figure 12. Results of OCR for Hyundai

Figure 13. Results of OCR for Bongo

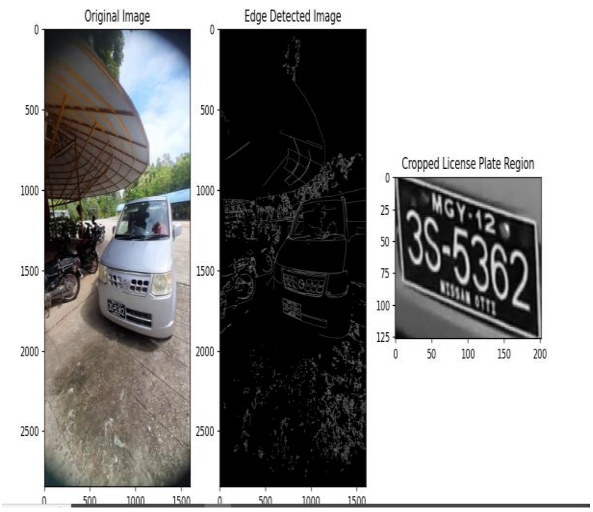

Figure 14. Results of OCR for Nissan OTTI

- The results were obtained using Python (3.12.0) version and PyCharm Community Edition 2024.2.1(IDE).
- The system was tested 1050 car images captured by camera.
- Number Plate images were captured using the built-in camera of a smartphone as an alternative for LPR: Galaxy A30s Samsung smartphone with 6” full – high definition active – matrix organic light-emitting diode display, a full metal body, and six distinct colours.
- The camera has 13 mega pixel resolution.
- Python program founds a little error in Package Installation.
- The research founds that the image size is a significant feature.
- The number plate is resulted mostly between 5’ and 10’ distance.
- The results are runed between 10 seconds and 12 seconds.
- The most results are **Toyota NIACE** and **Nissan OTTI**

2.3. Accuracy Metrics and Comparative Analysis

The system's performance was evaluated using six distinct vehicle types, with 1050 frames processed for each vehicle. The evaluation focused on three key metrics: Accuracy, Average Processing Time Per Frame, and Frame Rate (FPS).

2.4. Experimental Setup

The test involved capturing frontal and rear views of vehicles to assess the system's robustness under varying conditions [10]. Figures 5 through 14 show examples of the run outputs, including successful recognition and cases where the system struggled due to occlusions or poor lighting.

2.5. Performance Metrics

Accuracy: The percentage of correctly identified characters in the license plates, calculated using:

$$\text{Accuracy} = \frac{\text{Number of Correctly Recognized Plates}}{\text{Total Number of Plates Tested}} \times 100\%$$

Average Processing Time Per Frame: The time taken to process each frame, computed as:

$$\bar{T} = \frac{1}{N} \sum_{i=1}^{N} \text{Ti}$$

Where, Ti is the processing time for the ith frame

N is the total number of frames processed.

Frame Rate (FPS): The number of frames processed per second, derived as:

$$FPS = \frac{1}{T}$$

2.6. Analysis Table

The following table summarizes the results, using data from the processed frames of Figure 10 to Figure 15 which illustrate the resuls of Edge Detecion and Easy OCR for each vehicle type:

Table 1 Analysis Table of Real Time Data of University of Computer Studies, Magway

Vehicle Type (Figure)	Accuracy (%)	Average Processing Time Per Frame (s)	Frame Rate (FPS)
Nissan	50	10	0.1
Toyota Nissan	70	10	0.1
Toyota NIACE	45	10	0.1
Hyundai	97.5	10	0.1
Bongo	45	10	0.1
Nissan OTTI	100	10	0.1

Table 2 Analysis Table of Online Data

Frame	Accuracy of Number Plate Recognition	Average Processing Time Per Frame	Frame Rate (FPS)
Front View of Cars Picture(near)	45%	10 second	0.1
Back View of Cars Picture(near)	33 %	12 seconds	0.08

3. Conclusions and Discussion

The proposed ANPR system demonstrates effective real-time license plate recognition tailored to Myanmar's vehicle plates. By leveraging the Raspberry Pi, webcam, and Canny Edge for detection with OCR for recognition, the system proves valuable for campus security applications, offering quick, accurate license plate identification.

When Table1 and Table 2 are analyzed, Table 1 is more satisfied because of resize the picture. The system's success on the University of Computer Studies, Magway campus suggests scalability for broader urban applications in Myanmar, potentially aiding law enforcement and traffic management. However, to improve accuracy and robustness under challenging conditions, future work should consider:

Diverse AI Integration: Enhance system performance by incorporating a wider array of artificial intelligence models, particularly transformer-based architectures. These models are known for their ability to deliver superior accuracy when analyzing intricate datasets and navigating complex scenarios.

Vehicle Model Recognition: Enhanced

Vehicle Identification: Extend the system's capabilities to include the recognition of various vehicle makes and models. This improvement will provide a more holistic understanding of traffic patterns, thereby optimizing traffic monitoring efforts and enriching data collection for better decision-making.

Acknowledgements

Firstly, I would like to express my deepest gratitude to Dr. Khin Htike Htike Lwin, the rector of Technological University (Taunggyi), for her invaluable guidance, patience, and support throughout the course of this research. And I would like to express my deepest gratitude to my Chairperson, Dr. Aye Aye New, Professor and Head of the Electronic Engineering Department, for her exceptional guidance, unwavering support, and mentorship throughout the course of this research. Then I am deeply grateful to my supervisor, U Ko Ko Zaw, Associate Professor, for his exceptional guidance, support, encouragement throughout the course of this research. I would like to extend my heartfelt thanks to all the team members, whose dedication and hard work have greatly contributed to the success of this research. Your collaboration, ideas, and efforts have made this experience both rewarding and productive. Thank you all for your commitment, teamwork, and professionalism. I deeply appreciate each one of you.

REFERENCES

[1] Nur Liyana Yaacob & Ammar Ahmed Alkahtani, 2021 "License plate recognition for campus auto-gate system", ABC *Transactions on ECE*, Vol. 10, No. 5, pp120-122 Indonesian Journal of Electrical Engineering and Computer Science Vol. 21, No. 1, pp. 128~136 ISSN: 2502-4752, DOI: 10.11591/ijeecs. v21.i1. pp128-136.

[2] Shenghui Wang & Jin Xu ,2021 "Application of License Plate Number Recognition Based on Deep Learning Method in Intelligent Building Security System", International Conference on Networking Systems of AI (INSAI) 978-1-6654-0859-2/21/$31.00 ©2021 IEEE | DOI: 10.1109/INSAI54028.2021.00053.

[3] Tharaa Aqaileh & Faisal Alkhateeb, 2023 "Automatic Jordanian License Plate Detection and Recognition System Using Deep Learning Techniques",https://doi.org/10.3390/jimaging9100201

[4] Sachin Shrivastava & Sanjeev Kumar Singh, 2020 "2nd International Conference on Advances in Computing, Communication Control and Networking (ICACCCN)", 978-1-7281-8337-4/20/$31.00 ©2020 IEEE |DOI: 10.1109/ICACCCN51052.2020.9362737.

[5] Naaman Omar Yaseen & Salim Ganim Saeed Al-Ali, 2019 "Development of New Anpr Dataset for Automatic Number Plate Detection and Recognition in North of Iraq'', 978-1-7281-3992-0/19/$31.00 ©2019 IEEE.

[6] Farhan M. Nashwan & Khaled A. M. Al Soufy, 2023 "Design of Automatic Number Plate Recognition System for Yemeni Vehicles with Support Vector Machine", I.J. Intelligent Systems and Applications, MECS Press (http://www.mecs-press.org/) DOI: 10.5815/ijisa.2023.04.04

[7] Miss. Shraddha S. Ghadage & Mr. Sagar R. Khedkar, 2020 "," Automatic Number Plate Recognition System Using Deep Learning Techniques", International Research Journal of Engineering and Technology (IRJET) e-ISSN: 2395-0056 Volume: 07 Issue: 07, www.irjet.net p-ISSN: 2395-0072

[8] Sachin Shrivastava & Kiranpreet Kaur, 2024 "An Intelligent Architecture for Automatic Number Plate Detection Using OCR and YoloV8 Model", Tuijin Jishu/Journal of Propulsion Technology ISSN: 1001-4055 Vol. 45 No. 1

EFFECT OF AGEING ON BAND GAP ENERGY CONTROL OF NATURAL DYES EXTRACTS FOR DYES SENSITIZED SOLAR CELLS

San Yu Maw[1], Thaung Hlaing Win[2], and Kudae Than[3]

[1,2,3,] Department of Physics, Pakokku University
sanyumawpku2580@gmail.com, thaung.naing001@gmail.com, kudaethan055@gmail.com

ABSTRACT

Dye-sensitized solar cells (DSSCs) have emerged as a promising technology for solar energy conversion due to their affordability and adaptability. Natural dyes derived from various botanical and fruit sources are gaining attention as an eco-friendly alternative to synthetic counterparts in DSSCs. This comprehensive review offers insights into the extraction techniques, characterization methods and effectiveness of natural dyes as sensitizers in DSSCs. In the present study, the optical absorption, band gap values and conductivity of natural dye extracted from lemon fruits peel was studied. The aims of this present work is to investigate the effect of ageing day (0 day up to 4 day) on optical and electrochemical properties of natural dyes from lemon fruits peel. The optical absorption properties of extracted natural dye were investigated by using UV-Vis Spectrophotometry. There is an absorbance peak was observed at ~ 285 and ~ 320 nm. In addition, the optical band gap values of natural dyes were estimated by using Tauc's equation. The optical band gap values of natural dyes were observed around ~ 2.59 and 2.82 eV in all stages (harvested immature, ripening process and fully mature). In addition, the electricity of natural dyes was studied by portable conductivity meter. Upon ageing 0 day up to 4 day, the conductivity values of natural dyes were decreased at different stages. The highest conductivity values were observed upon ageing zero days.

Keywords:

natural dye, absorbance, solvent, band gap, conductivity.

1. INTRODUCTION

The escalating demand for sustainable energy solutions has propelled the exploration of innovative technologies, with DSSCs emerging as a promising avenue in the field of renewable energy research. Within the intricate framework of DSSCs, the selection of sensitizers assumes a pivotal role in shaping device efficiency and mitigating environmental impact.

In this context, natural dyes have garnered significant attention as potential sensitizers due to their renewable and eco-conscious origins. The pioneering work of O'Regan and Gratzel from UC Berkeley in 1991 marked the inception of DSSCs, instigating extensive research endeavors aimed at enhancing their efficiency. The appeal of DSSCs lies in their cost-effective fabrication and minimal ecological and health ramifications, captivating the academic community.

In comparison to both traditional and contemporary photovoltaics, DSSCs offer expedited, simpler and more affordable production, achieving efficiencies surpassing 14%. Particularly intriguing are DSSCs incorporating natural dyes sourced from leaves, flowers and fruit peels. However, the efficacy of such DSSCs is contingent upon variables such as the charge collection efficiency, photo-scattering capabilities and recombination rates. Despite their potential, the efficiency of natural dye-based DSSCs trails behind established photovoltaic technologies such as silicon solar cells.

Before the advent of synthetic dyes in 1856, humanity depended on the first generation of natural dyes derived from various sources, classified broadly as plant, mineral, animal and microbial dyes. Plant-derived pigments are most prevalent, encompassing leaves, roots, berries, wood, flowers, bark, seeds and fruits. Beyond textiles, these natural dyes found utility in food, medicine, crafts, toys and leather products. Being renewable and biodegradable, natural dyes hold an edge over their synthetic counterparts and have consequently found their way into solar cell applications.

The industrialization of DSSC production in the early 19th century propelled various nations toward the development of commercial solar cells, potentially rendering traditional energy sources obsolete. However, mounting environmental concerns associated with synthetic dye production reignited enthusiasm for natural dyes in the 20th century. The appeal of natural dyes lies in their exclusion of rare, toxic or inorganic metals or metal ions, rendering them a viable alternative energy source. Researchers have been zealously exploring plant and fruit sources to ascertain their potential as sensitizers for solar cells.

In dye sensitized solar cells, several natural dye pigments such as chlorophyll are successfully used as sensitizers. A lot of research is going to improve the efficiency of the natural dye sensitizer by using the combination of dyes, increasing on the concentration of the dye and extraction in various solvents. Natural dye is obtained by extracting from parts of plants such as leaves, flowers and fruits. These organic natural dyes are easily available, inexpensive, non-toxic, environmentally friendly and fully bio-degradable for DSSCs application.

Different types of plant extracts have been used as photo sensitizers in dye sensitized solar cell systems. Organic dye stuffs are highly competitive to serve as dye materials for solar cells because of the low cost of production and the manufacturing process does not require large equipment, but also the process is also easier.

The main objective of the present work is to investigate the effect of ageing day on optical absorbance, band gap and conductivity of natural dyes extracted from lemon fruits peel at different stages (harvested immature, ripening process and fully mature).

2. EXPERIMENT

2.1. Natural Dyes Extracts From Lemons Fruits

The natural dyes solutions were extracted from lemon fruits peel at different stages (harvested immature, ripening process and fully mature) in ethanol solvent employing the following procedure. The lemon fruits were collected and thoroughly washed with water to remove the adhering particles and dust from the surface. The natural dye solution was extracted from lemon fruits, (1 g) of lemon peel (at different stages) are added 100 ml of ethanol solvent. These mixing solutions were stirring and heating (50^{o}C) for about 7 min and solid residues were filtrated out to obtain clear dye solution. Figure 1and 2 show the flow chart and preparation of natural dye-sensitizers for lemon fruits peel at different stages.

3. CHARACTERIZATION

The characterization method consists of UV-Vis spectrophotometry, Portable Conductivity Meter.

3.1. UV-Vis Spectrophotometry

UV-Vis spectrophotometry was a technique to measure absorbance of the sample in the visible region. The optical absorption spectra of natural dyes were measured at room temperature using the GENESYS 10S UV-Vis spectrophotometry (Materials Research Lab, Department of Physics, University of Mandalay), Figure 3 The scanning ranges of natural dyes were recorded from 300 nm to 900 nm.

3.2. Conductivity Measurements

Conductivity is a measure of how well a solution conducts electricity. To carry a current a solution must contain charged particles, or ions. The conductivity meter is a precision instrument used to measure the conductivity of various liquid media. It is widely used in scientific research, teaching, industry, agriculture, environmental protection and other fields. By measuring the electrical conductivity of a liquid, the composition and concentration of the solute contained in the liquid being detected can be determined. Figure 4 shows the portable Digital Conductivity Meter.

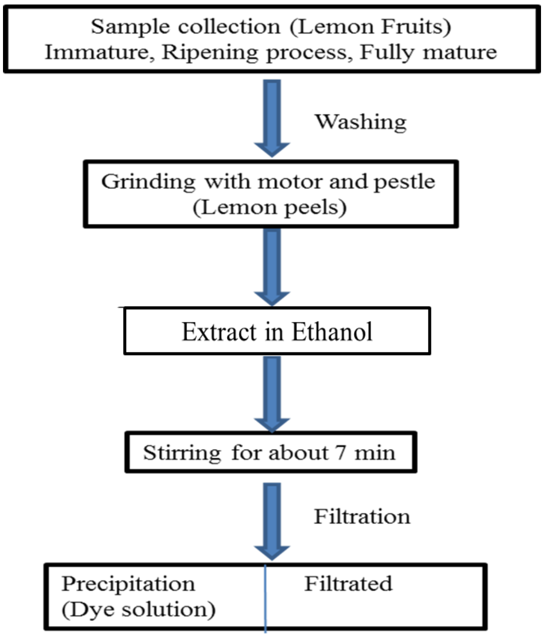

Figure 1. Flow chart for lemon fruits extract at different stages

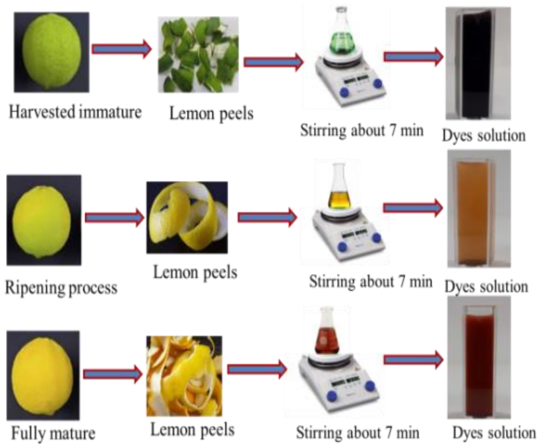

Figure 2. Steps of sample preparation for lemon fruits peel extract

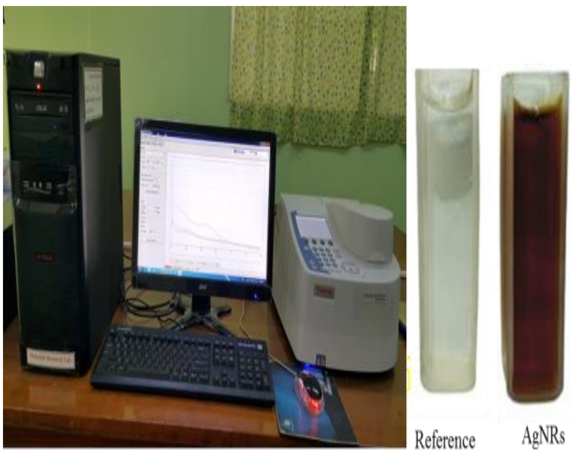

Figure 3. UV-Vis Spectrophotometry (GENESYS 10S)

Figure 4. Portable Digital Conductivity Meter

4. Results and Discussion

In this section deals with effect of ageing on absorption and characterization of natural dyes lemon fruits peel at different stages.

4.1. Effect of Ageing on Optical and Conductivity of Lemon Fruits Peel Dyes

Firstly, effect of ageing on optical absorption of dye extracted from lemon fruits peel (harvested immature) was studied. Figure 5 (a-b) shows the effect of ageing on maximum absorption peak of lemon fruits extract in ethanol solvent and plots of the dyes concentration versus the absorption peak intensity. The maximum absorption peak was observed at 285 nm with ethanol solvents. Upon ageing 0 day up to 4 day, the optical absorption peak position was shifted to the shorter wavelength regions. The optical absorption peak intensity significantly decreased. According to the above results, the optimum concentrations were observed as-prepared natural dyes solution.

Secondly, effect of ageing on optical absorption of dye extracted from lemon fruits peel (ripening process) was studied. Figure 6 (a-b) shows the effect of ageing on maximum absorption peak of lemon fruits extract in ethanol solvent and plot of the dyes concentration versus the absorption peak intensity. The maximum absorption peak was observed at 305 nm with ethanol solvents. Upon ageing 0 day up to 4 day, the optical absorption peak position was shifted to the shorter wavelength regions (305-285) nm. The optical absorption peak intensity significantly decreased. It is suggested that the lower solubility of natural dyes was observed at beyond 4 day.

Figure 7 (a-b) shows the effect of ageing on maximum absorption peak of lemon fruits extract at fully mature stage in ethanol solvent and plot of the dyes concentration versus the absorption peak intensity. The maximum absorption peak was observed at 320 nm with ethanol solvents. Upon ageing 0 day up to 4 day, the optical absorption peak position was shifted to the shorter wavelength regions (320-310) nm. The optical absorption peak intensity significantly decreased. It is suggested that the lower solubility of natural dyes was observed at beyond 4 day.

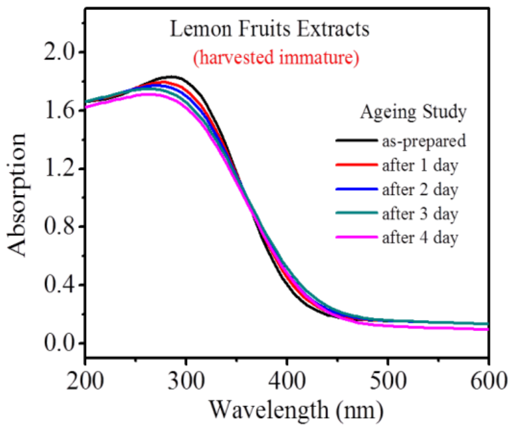

Figure 5 (a). Effect of ageing on optical absorption of lemon fruits extract

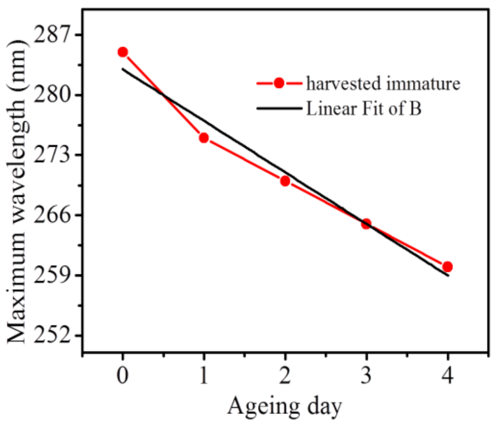

Figure 5 (b). Plots of the dyes concentration versus the absorption peak intensity in ethanol

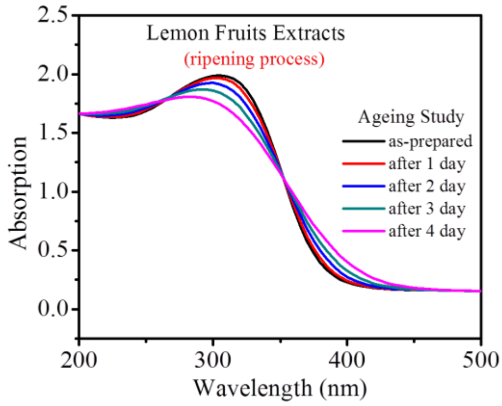

Figure 6 (a). Effect of ageing on optical absorption of lemon fruits extract

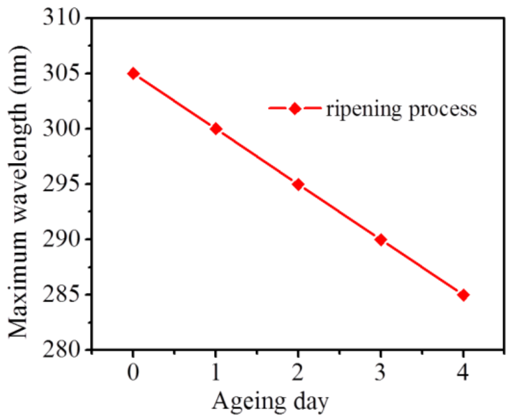

Figure 6 (b). Plots of the dyes concentration versus the absorption peak intensity in ethanol

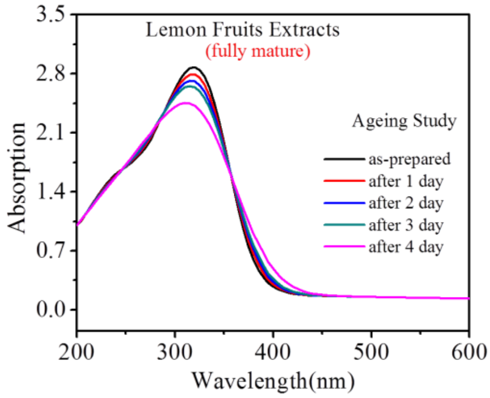

Figure7 (a). Effect of ageing on optical absorption of lemon fruits extract

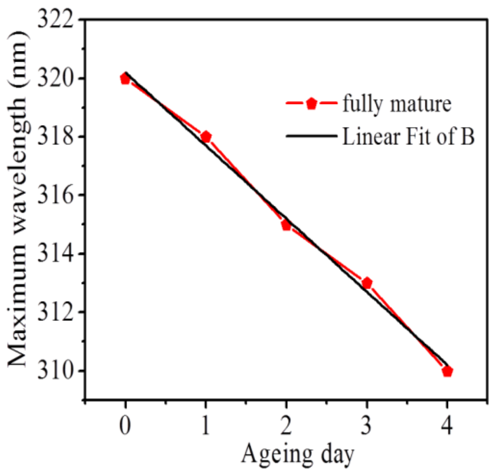

Figure 7 (b). Plots of the dyes concentration versus the absorption peak intensity in ethanol

4.2. Estimation of Optical Band Gap Energy

The optical band gap is crucial factor that determines what portion of the solar spectrum a photovoltaic cell absorbs. The optical band gap energy of fresh Lemons fruits extracts with ethanol solvents were calculated from their respective absorption spectra by using the following equation:

$$(\alpha h\nu)^m = A\,(h\nu - E_g)$$

Where α is absorption coefficient, $h\upsilon$ is the incident photon energy, A is the proportionality constant, $E_g$is the band gap energy and m is a constant that determines the type of optical transition. The values of m is taken as 2 for direct and ½ for indirect allowed transitions. Since natural dyes is direct band gap semiconductor, we plot $(\alpha h\upsilon)^2$ versus $h\upsilon$ taking m value of 2.

Figure 8 (a-c) show the plots of $(\alpha h\upsilon)^2$ versus $(h\upsilon)$ for the natural dyes extracted from lemon fruits peel at harvested immature stage. The optical band gap values were deduced from the extrapolation of the linear part of the plot $(\alpha h\upsilon)^2$ versus $(h\upsilon)$ abscissa.

Upon increasing ageing 0 day up to 4 day, the narrowest optical band gap values were observed at ageing 4 day and the widened band gap values were observed at ageing zero day. The optical band gap values are decreased from around 2.82 eV to 2.59 eV at different stages with ethanol solvents.

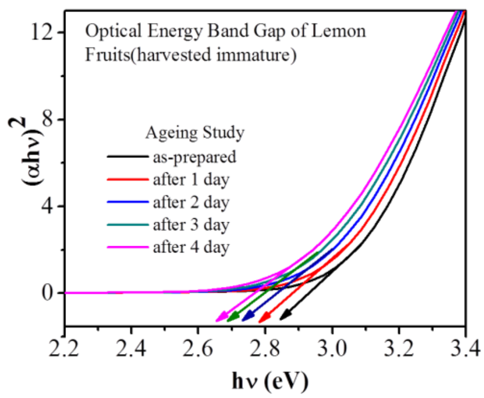

Figure 8 (a). Plots of $(\alpha h\nu)^2$ versus $h\nu$ for lemon fruits extract at harvested immature

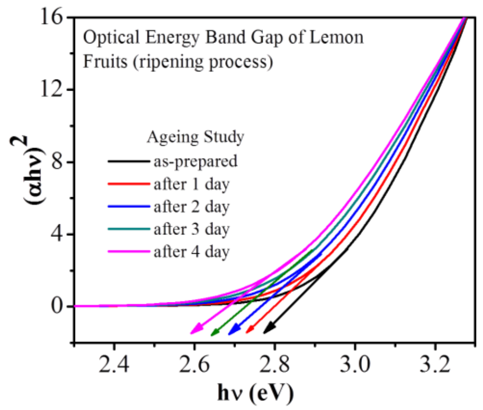

Figure 8(b). Plots of $(\alpha h\nu)^2$ versus $h\nu$ for for lemon fruits extract at ripening process

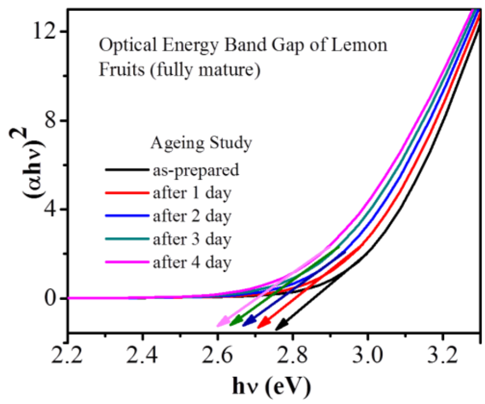

Figure 8 (c). Plots of $(\alpha h\nu)^2$ versus $h\nu$ for lemon fruits extracts at fully mature.

4.3. Optimum Absorption and Band Gap Values of Lemon Fruits Extract

Figure 9 shows the optical absorption spectra of lemon fruits extracts with different stages. According to the above results, the highest optical absorption peak intensity was observed at fully mature stage. It may be due to its better solubility of natural dye at fully mature stage. Figure 10 shows the Plots of $(\alpha h\nu)^2$ versus $h\nu$ for lemon fruits extracts with different stages. The narrowest band gap values were observed at fully mature stage.

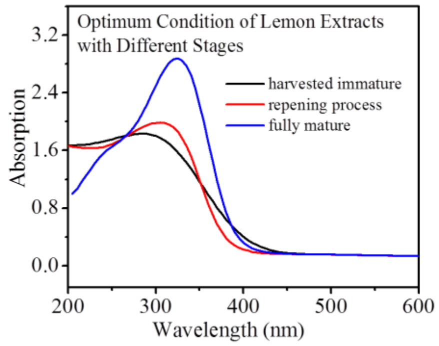

Figure 9. Optical absorption spectra of lemon fruits extracts with different stages

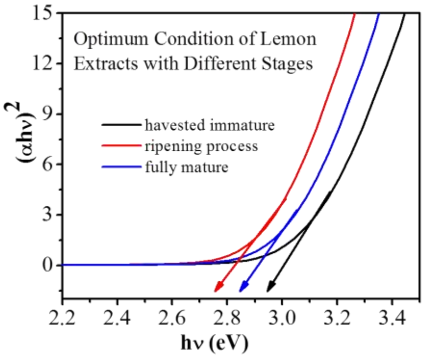

Figure 10. Plots of $(\alpha h\nu)^2$ versus $h\nu$ for lemon fruits extracts with different stages.

4.4. Electrical Conductivity of Lemon Fruits Extract

Finally, the electrical conductivity of lemon fruits peel extracts was also investigated. Figure 11 show the effect of ageing day on electrical conductivity of lemon fruits peel extracts. For all stages (harvested immature, ripening process and fully mature) of lemon fruits peel extract, the conductivity values of dyes solution are decreased. According to the above results, the higher conductivity of natural dyes is observed upon ageing zero day. Figure 12 shows the electrical Conductivity of lemon fruits peel extracts with different stages (optimum condition). In this comparative study, the largest conductivity values are observed at ripening stage.

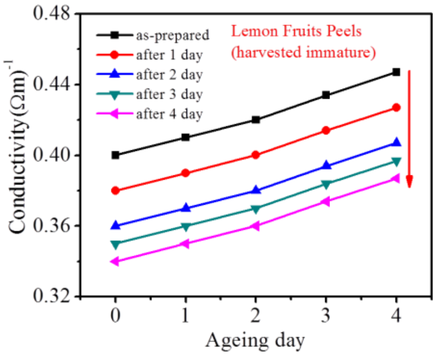

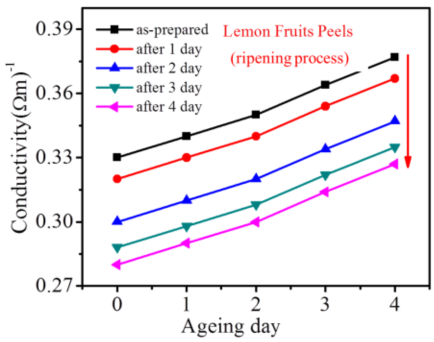

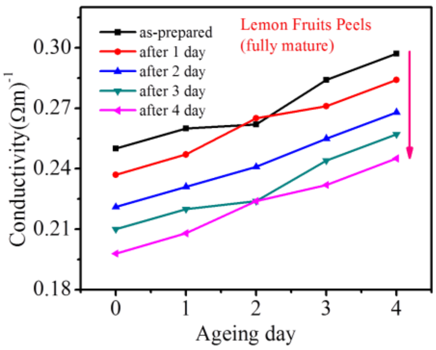

Figure 11. Effect of ageing day on electrical conductivity of lemon fruits peel extracts

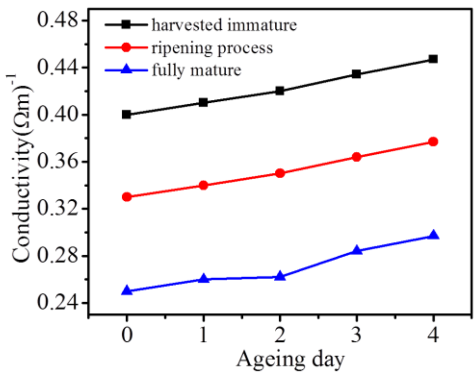

Figure 12. Electrical Conductivity of lemon fruits peel extracts with different stages (optimum condition)

5. Conclusion

Plants, animals, and minerals have been used as primary sources for colourants, dyes or pigments since ancient times. In the first part of the present work, the effect of ageing on the optical and band gap value of lemon peel dyes was studied. The natural dyes with higher conductivity can improve the efficiency of dye-sensitized solar cells (DSSCs). The optical absorption peak maximum (λ_{max}) was observed at 285 nm for harvested immature, 305 nm for ripening process, 320 nm for fully mature in ethanol solvent. Upon ageing 0 day up to 4 day, the optical absorption peak intensity was decreased and slightly shifted to the shorter wavelength region for all different stages (harvested immature, repining process and fully mature). The highest optical maximum absorption peak was observed at as-prepared (ageing zero day).

In the second part of the present work, the optical band gap values of the natural dyes lemon fruits peel was also studied at different ageing day (0 day up to 4 day). The optical band gap values were observed at around ~ 2.82 eV (maximum value) and ~ 2.59 eV (minimum value) for all stages of harvested immature, repining process and fully mature. The narrower optical band gap values were observed at ageing 4 day for all stages.

In the second step of present study, the electrical conductivity of lemon fruits peel extracts was also investigated. Upon increasing ageing day, the conductivity values of dyes solution are decreased at different stages (harvested immature, ripening process and fully mature). According to the above results, the higher conductivity of natural dyes is observed upon ageing zero day.

Acknowledgements

We would like to thank Dr Tin Tun Aung, Acting Rector, Pakokku University. We are also thankful to Dr Khin Khin Htoot, (Pro-rector), Pakokku University. We would like to express my gratitude to Dr Win Mar (Professor and Head) and Dr Win Myint Kyu (Professor), Department of Physics, Pakokku University, for their kind permission to give us the opportunity to do research. We would like to express my appreciation to the department of physics, Pakokku University for their use of research facilities.

References

[1] G X.W. Guoyun*et al.*, 2014. Journal of Nanoscience.

[2] T. Markvart*et al.*, 2003. Journal of environmental science.

[3] H. Hahn *et al.*, 1998. Optical properties of natural dyes.

[4] D.R. Duran N *et al.*, 2012. Introduction to general information of natural dyes.

[5] F.M. Al-Khateeb*et al.*, 2018. Apply Physics and Material Science.

Biography

First A. Author :
Daw San Yu Maw
Demonstrator
Department of Physics
Pakokku University

Second B. Author :
Dr Thaung Hlaing Win
Lecturer
Department of Physics
Pakokku University

Third C. Author:
Daw Kudae Than
Demonstrator
Department of Physics
Pakokku University

STUDY OF PH ON ABSORPTION AND ADSORPTION PROPERTIES OF NATURAL DYES EXTRACTS FROM MANGOSTEEN *(GARCINIAN MANGOSTANA* L.*)* FRUITS

May Phyo Lin[1], Thaung Hlaing Win[2], and Lwin Lwin Htwe[3]

[1,2,3] Department of Physics, Pakokku University
mayphyolin28@gmail.com, thaung.naing001@gmail.com

ABSTRACT

The extracted mangosteen dyes can be a good source of natural sensitizer for dye sensitized solar cells and can produce different shades of colors using different kinds of fabrics and is useful as a substitute for synthetic dyes. The objectives of this research were studied the flesh, skin and petal of mangosteen fruits (Garcinian mangostanaL.) extract in ethanol solvent. The color of extracted mangosteen dyes is reddish brown color. The optical absorption and adsorption of natural dyes were studied by UV-Vis spectrophotometry and contact angle by CMOS camera. The contact angle is the angle at the interface where water, air and solid meet and its value is a measure of how likely the surface is to be wetted by the water. The most common method for surface wetting characterization is sessile-drop goniometry, due to its simplicity. The adsorption properties and surface energy of natural dyes was also calculated by Thomas Young's equation.

KEYWORDS

Mangosteen dyes, contact angle, surface energy, absorbance, ethanol.

1. INTRODUCTION

Surfaces of materials strongly affect functional properties such as mechanical, biological, optical, acoustic and electronic properties of materials, particularly at the micro/nano scale. Surface effects stem from the interplay of surface morphology and surface chemical properties. This dissertation focuses on 1) modeling the effect of surface roughness parameters on solid-solid contact and solid-liquid interaction as well as developing a surface engineering method that can generate random surfaces with desired amplitude and spatial roughness parameters for tribological and biomimetic applications. Autocorrelation length (ACL) is a surface roughness parameter that provides spatial information of surface topography that is not included in amplitude parameters such as root mean-square roughness.

A relationship between ACL and the friction behavior of a rough surface was developed. The probability density function of peaks and the mean peak height of a profile were given as functions of its ACL. These results were used to estimate the number of contact points when a rough surface comes into contact with a flat surface, and it was shown that the larger the ACL of the rough surface, the less the number of contact points.

Based on Hertzian contact mechanics, it was shown that the real area of contact increases with increasing of number of contact points. Results from microscale friction experiments (where friction force is proportional to real area of contact) on polished and etched silicon surfaces are presented to verify the analysis.

A versatile surface processing method based on electrostatic deposition of particles and subsequent dry etching was shown to be able to independently tailor the amplitude and spatial roughness parameters of the resulting surfaces. Both adhesion and friction force of the processed surfaces were reduced comparing to that of the flat surfaces. The process is also used to generate superhydrophobic engineering surfaces by mimicking the structure of lotus leaves. A geometric model was developed to related air-trapping ability of hydrophobic surfaces with hillock features to process variables (hillock diameter, etching depth and coverage) and contact angle. The model is shown to be able to predict minimum coverage of hillocks required for air-trapping on hydrophobic rough surfaces. The model predictions agree with experimental observations reasonably well. This model can particularly be extended to utilizing statistical roughness parameters to predict air-trapping for rough hydrophobic surfaces.

Solid-solid contact is very common in mechanical and electrical systems, for example, rolling bearing, and electrical switch. For rough surfaces, the real area of contact is much smaller than the nominal area of contact. The reduction of contact area affects friction, adhesion, wear and other tribological phenomena as well as electrical conductivity. The real area of contact is not only a function of surface roughness, but also a function of applied normal load. For elastic contact, real area of contact increases with an increase of normal load.

2. EXPERIMENT

2.1. Extraction of Natural Dyes from Mangosteen Fruits

The plant materials of mangosteen fruits (flesh, skin and petal) specimens were collected from local market, Pakokku Township, Magway Region. The botany name (Scientific name) of mangosteen fruits is known as *Garcinian mangostana L.* The collected specimens were cleaned and rinsed thoroughly 2-3 times with water to remove visible dust particles and air dried at room temperature.

The mangosteen fruits (flesh, skin and petal) were cutting into small pieces. 5g of finely cut mangosteen fruits were kept in a breaker containing 200 ml of ethanol solvent stirring for 5 min and filtrated using filter paper.

The color of the solution appeared orange-red color, indicating the formation of mangosteen dyes. The effect of ageing on pH of natural dyes solution was measured by pH meter. Figure 1 (a-b) shows the flow chart and sample preparation of the natural dye extracted from mangosteen fruits (flesh, skin and petal).

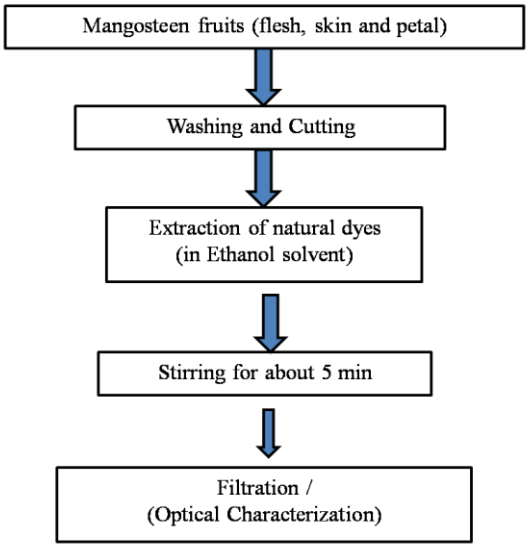

Figure 1. (a) Flow chart of the skin orange dyes extract

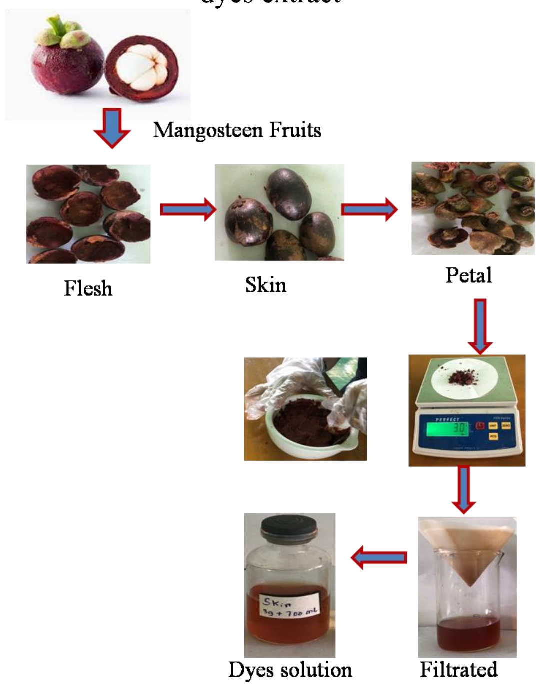

Figure 1. (b) Sample preparations of natural dyes extracted from mangosteen fruits

3. CHARACTERIZATION

The characterization method consists of UV-Vis spectrophotometry, CMOS camera.

3.1. UV-Vis Spectrophotometry

UV-Vis spectrophotometry was a technique to measure absorbance of the sample in the visible region. The optical absorption spectra of natural dyes were measured at room temperature using the GENESYS 10S UV-Vis spectrophotometry (Materials Research Lab, Department of Physics, University of

Mandalay), Figure 2. The scanning ranges of dyes were recorded from 300 nm to 900 nm. A glass substrate was used as baseline scanning before the measure measurement of natural dyes. Baseline measurement is made with distilled water as reference solution.

3.2. Contact Angle Measurement

Wettability (adsorption) of the substrate (TiO_2) to the liquid droplet (dye solutions) was studied by contact angle measurement as shown in Figure 3. In this measurement, CMOS camera was used. The image analysis was performed by using the Axisymmetric Drop Shape Analysis (FTA 32) software.

Figure 2. UV-Vis Spectrophotometry (GENESYS 10S)

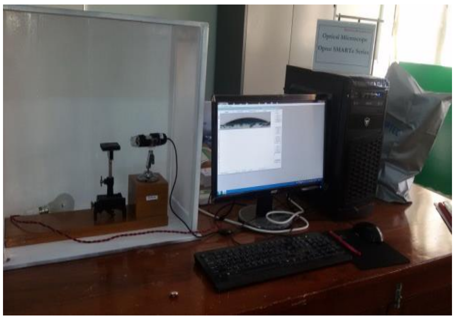

Figure 3. Atomic Force Microscopy (CMOS)

4. RESULTS AND DISCUSSION

This section following the effect of ageing on pH of mangosteen dyes (flesh, skin and petal) on optical absorption and adsorption in ethanol solvent were studied.

4.1. Effect of Concentration on Optical Absorption of Natural Dyes

In the first part of present work, the optical absorption spectra of natural dye extracted from flesh mangosteen in ethanol solvent (ageing 0 day up to 18 day) as shown in Figure 4.

The result of the absorption using the UV-Vis spectrophotometer showed that the resulting spectrum of peaks in the area of the visible range of light. Upon ageing 0 day up to 9 day, the maximum absorption peak position (λ_{max}) at 554 nm and peak intensity increased (1.93 to 2.65). Beyond the 9 day ageing, the absorption peak intensity decreased. The highest peak intensity was observed at 9 day and pH values 3.7.

In addition, the optical absorption spectra of natural dye extracted from skin mangosteen in ethanol solvent (ageing 0 day up to 18 day) as shown in Figure 5. The optical absorption of skin mangosteen dyes was studied. Upon ageing 0 day up to 7 day, the maximum position (λ_{max}) at 535 nm and peak intensity increased (1.0 to 1.42). Beyond the 7 day ageing, the absorption peak intensity decreased. The highest absorption peak intensity was observed at 7 day and pH values 3.7.

The optical absorption spectra of natural dye extracted from petal mangosteen in ethanol solvent (ageing 0 day up to 18 day) as shown in Figure 6. The optical absorption of petal mangosteen dyes was studied. Upon ageing 0 day up to 7 day, the maximum position (λ_{max}) at 518 nm and peak intensity increased (0.76 to 0.92). Beyond the 7 day ageing, the absorption peak intensity decreased. The highest absorption peak intensity was observed at 7 day and pH values 5.8.

Figure 7 shows the optical absorption spectra of natural dye extracted from flesh, skin and petal of mangosteen in ethanol solvent. The maximum absorption peak was observed at 554 nm for flesh mangosteen, 535 nm for skin mangosteen and 518 nm for petal of mangosteen fruits.

The highest optical absorption peak was observed flesh mangosteen fruits. Figure 8 shows the comparative study of the effect of ageing day on optical absorption spectra of natural dye extracted from flesh, skin and petal of mangosteen in ethanol solvent. Table 1 shows the effect of ageing day on absorption and maximum peak position of natural dye extracted from flesh, skin and petal of mangosteen in ethanol solvent.

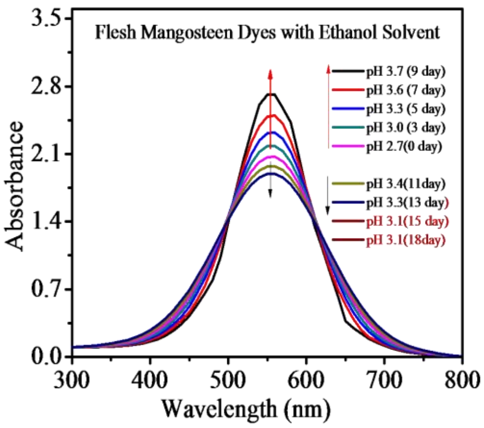

Figure 4. Optical absorption spectra of natural dye extracted from Flesh Mangosteen in ethanol solvent (Ageing 0 day up to 18 day)

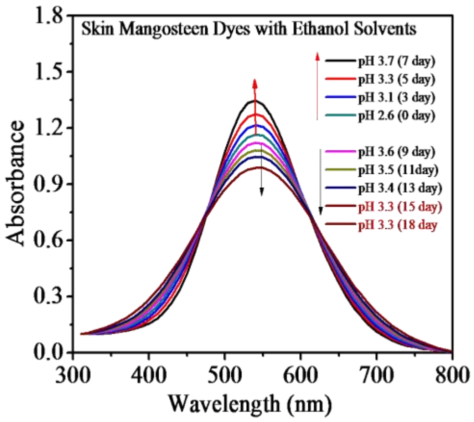

Figure 5. Optical absorption spectra of natural dye extracted from Skin Mangosteen in Ethanol solvent (Ageing 0 day up to 18 day)

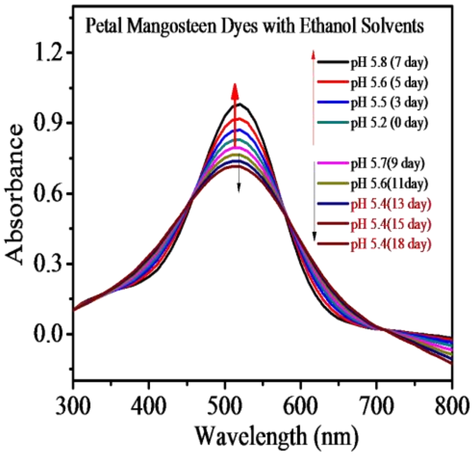

Figure 6. Optical absorption spectra of natural dye extracted from Petal Mangosteen in Ethanol solvent (Ageing 0 day up to 18 day)

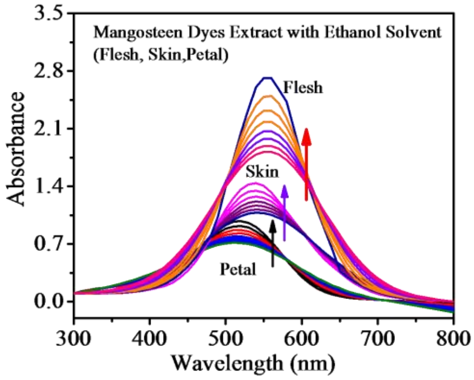

Figure 7. Optical absorption spectra of natural dye extracted from Flesh, Skin and Petal of mangosteen in ethanol solvent

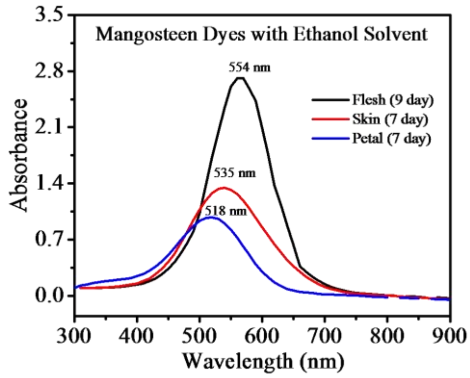

Figure 8. Effect of ageing day on optical absorption spectra of natural dye extracted from Flesh, Skin and Petal of Mangosteen in ethanol solvent

Table 1. Effect of ageing day on absorption and maximum peak position of natural dye extracted from Flesh, Skin and Petal of Mangosteen in ethanol solvent

Samples	Mangosteen dyes (ethanol solvent)	λ_{max} (nm)	Absorbance (a.u.)
1	flesh	554	2.65
2	skin	535	1.42
3	petal	518	0.92

4.2. Effect of Dye Concentration on the Wettability of Tio_2 Surface

Wettability involves the interaction between liquid and solid in contact. The wetting behaviour of thin film is characterized by the value of contact angle. The contact angle is an important parameter in surface science and its measurement provides a simple and reliable technique for the interpretation of surface energies. Depending on the contact angle, the surface of TiO_2 is classified as;

$\theta > 150^0$ superhydrophobic
$65^0 < \theta < 150^0$ hydrophobic
$0^0 < \theta < 65^0$ hydorphilic
$\theta \approx 0^0$ superhydrophilic

Where θ refers to the contact angle. In order to investigate the interfacial properties of the TiO_2 following the flesh, skin and petal of mangosteen, the wettability of the dyes treated TiO_2 layers was characterized by contact angle measurements. The surface energy of TiO_2 was also considered from the contact angle measurement.

Figure 9 Contact angle measurement of flesh, skin and petal of mangosteen dye extracts with ethanol solvent. The contact angles is $\theta = 32^o$ for bare TiO_2. The mangosteen fruits, the contact angles decreased $\theta = 13^o$ for flesh, $\theta = 15^o$ for skin and $\theta = 18^o$ for petal. The contact angle of liquid drop (flesh, skin and petal of mangosteen dyes) on TiO_2 surface is considerably influenced by the types of dye, i.e. as the flesh dye is used, the contact angle decreases and the surface becomes more hydrophilic and good adsorption.

Surface energies of the TiO_2 and dyes treated TiO_2 layers calculated using experimental liquid surface tension and contact angle data and the procedure below.

$$\gamma_l \cos\theta = \gamma_s - \gamma_{sl}$$

Here, γ_s , γ_l , γ_{sl} are the interfacial surface energies of the solid, liquid and solid- liquid interfaces, respectively. The surface energies of γ_s and γ_{sl} and contact angle of flesh, skin and petal of mangosteen dye on TiO_2 modified films are summarized in Table (1) with ethanol solvent.

As seen in Table 2, the higher surface energies for flesh of mangosteen dyes were observed while decreasing the solid-liquid interfacial tension. It may be attributed to the fact that the force of attraction between the liquid molecules and the atoms in the solid becomes more than the force of attraction between the liquid molecules.

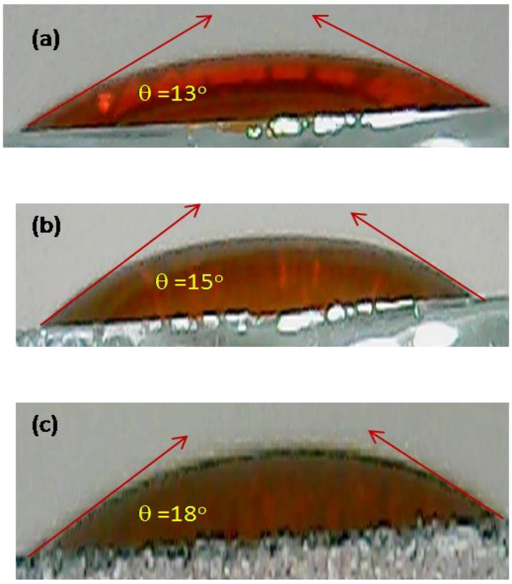

Figure 9. Contact angle measurement of mangosteen dye extracts with ethanol (flesh, skin and petal).

Table (2) Surface energies of γ_s, γ_{sl} and contact angle of skin orange dye solutions on TiO_2 substrate with ethanol solvent

Samples		Contact angles $(\theta)^o$	Surface energies γ_s (N/m)	Surface energies γ_{sl} (N/m)
Mangosteen Dyes (Ethanol)	Bare TiO_2	32	19.3	-3.23
	Dye treated TiO_2			
	Flesh	13	21.53	-0.56
	Skin	15	21.35	-0.75
	Petal	18	21.17	- 0.94

5. Conclusion

Primarily, this study successfully extracted a natural dye from mangosteen fruits (flesh, skin and petal) that was found partly effective for dye sensitized solar cells. In this present work, the mangosteen (flesh, skin and petal) fruits were extracted by using solvent extraction method. The extracted dye was characterized using UV-Vis Spectrophotometry and contact angles by CMOS camera. In the above UV-Vis measurement, the maximum absorption peak position (λ_{max}) was observed at 554 nm for flesh, 535 nm for skin and 518 nm for petal of mangosteen fruits extract. Upon ageing 0 day up to 7 day and 9 day, the absorption peak intensity increased. The highest absorption peak intensity was observed at flesh mangosteen extract.

The contact angle is a measure of the ability of a liquid to wet the surface of a solid. The contact angle measurement of mangosteen dye solutions on Dyes treated TiO_2 with ethanol solvent is also studied. The contact angle, $\theta = 13^o$ for flesh dyes, $\theta = 15^o$ for skin dyes and $\theta = 18^o$ for petal of mangosteen dyes. The lower contact angle values of mangosteen dye on TiO_2 modified substrate was observed with flesh mangosteen extract. According to the above results, the contact angle decreases and the surface becomes more hydrophilic and good wettability with flesh dyes extract.

ACKNOWLEDGEMENTS

We would like to thank Dr Tin Tun Aung, Acting Rector, Pakokku University. We are also thankful to Dr Khin Khin Htoot, (Pro-rector), Pakokku University. We would like to express my gratitude to Dr Win Mar (Professor and Head) and Dr Win Myint Kyu (Professor), Department of Physics, Pakokku University, for their kind permission to give us the opportunity to do research. We would like to express my appreciation to the department of physics, University of Mandalay for their use of research facilities.

REFERENCES

[1] D.R. Duran N *et al*., 2012. Application of natural dyes.

[2] F.M. Al-Khateeb*et al*., 2018. Apply Physics and Material Science for natural sources.

[3] A.C. Chan *et al*., 2005. Journal of Physical Chemistry.

[4] M.L. Almeida *et al., 1983.* Journal of wetting properties and surface energy.

[5] M.C. Martin *et al*., 1998. Journal of Physical and chemical structure.

Authors

Biography

First A. Author:

Daw May Phyo Lin

Second B. Author:

Dr Thaung Hlaing Win

Second B. Author:

Daw Lwin Lwin Htwe

CLASSIFICATION OF SLEEP DISORDERS USING MACHINE LEARNING: ANALYZING THE IMPACT OF LIFESTYLE FACTORS ON SLEEP HEALTH

Moe Phyu Phyu Khaing[1], Khaing Zar Win[2], and Nan Saw Kalayar[3]

[1,3]Faculty of Information Science, University of Computer Studies (Taunggyi),
[2]Department of Information Science, University of Technology, (Yatanarpon Cyber City)

moephyuphyukhaing23@gmail.com, khaingzarwinms@gmail.com, nansawkalayar@ucstgi.edu.mm

ABSTRACT

Sleep disorders significantly impact both physical and mental health, with modern lifestyles often worsening these conditions. Poor-quality or insufficient sleep has been associated with serious health issues, such as obesity, cardiovascular diseases, and mental disorders. Despite the critical importance of addressing sleep health, there is a need for effective methods to classify and understand sleep disorders, particularly in relation to lifestyle factors like occupation, physical activity, stress levels, and daily steps. This paper aims to bridge this gap by leveraging machine learning techniques to classify sleep disorders using the Sleep Health and Lifestyle dataset from Kaggle. The analysis evaluates five machine learning algorithms—Random Forest, K-Nearest Neighbors (KNN), Support Vector Machine (SVM), XGBoost, and Logistic Regression—based on performance metrics like accuracy, precision, recall, and F1 score. The findings highlight XGBoost's superior performance with a classification accuracy of 95%, offering valuable insights into how lifestyle modifications can mitigate sleep disorders.

KEYWORDS

Sleep Disorders, Sleep Health, Modern Lifestyles, Random Forest, K-Nearest Neighbors (KNN), Support Vector Machine (SVM), XGBoost, Logistic Regression

1. INTRODUCTION

Sleep is a fundamental physiological process essential for maintaining overall health and well-being, playing a critical role in cognitive performance, emotional regulation, and physical restoration. However, insufficient or poor-quality sleep has been linked to various health problems, including chronic diseases like obesity, diabetes, and cardiovascular conditions. Beyond physical health, inadequate sleep can also negatively impact mental health, contributing to issues such as anxiety and depression, which can further disrupt sleep patterns. These challenges highlight the importance of understanding and addressing the factors that influence sleep disorders.

Modern lifestyles have introduced numerous factors that negatively impact sleep patterns. Irregular work schedules, high stress levels, sedentary behavior, poor dietary habits, and excessive screen time are just some of the lifestyle elements that can lead to sleep disorders such as insomnia or obstructive sleep apnea. Environmental factors like noise, light exposure, and temperature can exacerbate these issues. Research has shown that healthy sleep depends not only on duration but also on quality and consistency. Identifying how specific lifestyle choices influence sleep disorders is critical for developing targeted interventions aimed at improving sleep health.

This analysis focuses on the classification of sleep disorders using machine learning, specifically analyzing the impact of lifestyle factors on sleep health. The use of machine learning enables more accurate classification and prediction of sleep disorders based on lifestyle data, providing actionable insights for individuals and healthcare professionals to mitigate the effects of poor lifestyle choices on sleep health. Ultimately, this study contributes to raising awareness about the importance of quality sleep while offering data-driven solutions to improve overall well-being.

The sections of this paper are organized as follows: Section 2 describes review of relevant research on sleep disorders and machine learning. Section 3 presents description of the machine learning models used (Random Forest, KNN, SVM, XGBoost and Logistic Regression). Dataset information is described in section 4. Feature importance, identifying and ranking influential factors affecting sleep health is described in section 5. Section 6 presents System Design and Implementation. Section 7 details the Evaluation, the definitions and formulas for accuracy, precision, recall, and F1 score. Finally, it concludes with a results and discussion section summarizing findings and implications for future research.

2. Related Works

This literature review focuses on existing research related to sleep disorders classification and the application of machine learning techniques in this domain. Existing studies have explored the use of machine learning algorithms to improve the accuracy and efficiency of sleep disorder diagnosis, particularly focusing on the limitations of manual classification methods. These studies have investigated various approaches, including the use of traditional machine learning algorithms, deep learning models, and feature engineering techniques to effectively classify sleep disorders from diverse datasets.

Paper [1] discusses the importance of accurate sleep disorder classification for improving human health. Manual classification by sleep experts is time-consuming and error-prone, so the authors explore the use of machine learning algorithms (MLAs) for sleep disorder classification. The paper compares traditional MLAs and deep learning algorithms for this task. They propose a method for sleep disorder classification using a publicly available sleep health and lifestyle dataset. Genetic algorithms are used to optimize the parameters of the different machine learning algorithms. The authors evaluate their proposed method against existing state-of-the-art algorithms. The dataset used includes 400 rows and 13 columns with various features related to sleep and daily activities.

Paper [2], "Classification of Sleep Disorders," provides a comprehensive overview of the evolution and current state of sleep disorder classification systems, particularly focusing on the International Classification of Sleep Disorders (ICSD) version 2. Historically, early classification systems were symptom-based, categorizing disorders into insomnia, excessive sleepiness, and abnormal events during sleep, which limited their ability to address underlying pathophysiology due to the unknown etiology of many conditions. The first significant effort in this area was the Diagnostic Classification of Sleep and Arousal Disorders published in 1979, followed by the ICSD in 1990, which aimed to enhance diagnostic accuracy and facilitate global research communication. The ICSD-2, introduced in 2005, organizes sleep disorders into 81 diagnostic categories across eight major classifications, integrating symptomatic presentations with pathophysiological considerations. This dual approach is crucial for accurately diagnosing and treating various disorders, as it aids clinicians in differentiating between conditions like primary and adjustment insomnia or understanding the mechanisms behind obstructive sleep apnea and narcolepsy.

Thorpy emphasizes that ongoing revisions to the ICSD reflect the need for an adaptive classification system that can incorporate new research findings and clinical insights, particularly regarding the overlap between psychiatric conditions and sleep disorders. Overall, his work highlights the importance of structured classification systems in enhancing our understanding of sleep disorders and ensuring that clinicians have access to relevant diagnostic criteria and treatment guidelines that reflect current knowledge.

The study by Y. Wang et al. [3] presents a robust algorithm for distinguishing between sleep apnea and hypopnea events using electrocardiogram (ECG) signals, achieving impressive performance metrics including an accuracy of 97.96%, sensitivity of 98.10%, and specificity of 97.83%. By leveraging Heart Rate Variability (HRV) and nonlinear dynamics, the authors effectively classified various types of sleep Apnea-Hypopnea Syndrome (SAHS) events, including obstructive apnea (OA), central apnea (CA), and mixed apnea (MA), with classification accuracies exceeding 90%. The research utilized polysomnography (PSG) data from 25 patients with varying Apnea-Hypopnea Index (AHI) values, ensuring a comprehensive dataset that included both apneic and normal sleep states. The study emphasizes the importance of HRV features derived from ECG signals, which reflect autonomic nervous system activity and its relationship with respiratory events during sleep.

The ethical considerations regarding patient data were also addressed, ensuring confidentiality through the use of anonymized records. Overall, this work contributes significantly to the field of sleep medicine by providing a high-accuracy, algorithmic approach for the detection and classification of sleep-related breathing disorders based on easily obtainable ECG signals.

3. METHODOLOGY

The main contribution of this paper is to advance the classification of sleep disorders through machine learning by uniquely analyzing lifestyle factors (e.g., occupation, physical activity, stress levels, and daily steps). By employing multiple machine learning algorithms and achieving high classification accuracy, this paper provides insights into how lifestyle adjustments can influence sleep health, offering a complementary perspective to existing diagnostic methods. These findings have the potential to guide individuals and healthcare providers in addressing sleep-related issues more effectively.

Machine Leaning

Machine learning (ML) is a subfield of artificial intelligence (AI) that enables computers to learn from data and improve their performance over time without being explicitly programmed. This capability allows machines to identify patterns, make decisions, and perform tasks autonomously by leveraging algorithms that analyze large datasets. According to SAP (Systems, Applications, & Products in Data Processing), machine learning is focused on teaching computers to learn from data and to improve with experience, rather than relying on pre-defined instructions [1] [5].

The process of machine learning typically involves several key steps: data collection, data pre-processing, model training, and evaluation. Initially, a dataset is gathered, which may include various features relevant to the problem at hand. The data is then cleaned and transformed to ensure quality and consistency. Following this, machine learning algorithms are applied to the training data to create a model that can generalize from the examples provided. Once trained, the model can be tested with new data to assess its accuracy and effectiveness in making predictions or classifications [2][4].

3.1. Random Forest

Random Forest is an ensemble learning method primarily used for classification and regression tasks. It operates by constructing multiple decision trees during training and outputs the mode of their predictions for classification or the mean prediction for regression. The strength of Random Forest lies in its ability to reduce overfitting by averaging the results of numerous trees, which are trained on different subsets of the data through a process known as bootstrap sampling.

This method not only enhances accuracy but also provides insights into feature importance, allowing practitioners to identify which variables contribute most significantly to predictions.[1], [4], [5]. The model's robustness against noise and its capability to handle large datasets make it a popular choice in various fields, including finance and healthcare.

3.2. K-Nearest Neighbors (KNN)

K-Nearest Neighbors (KNN) is a simple yet effective instance-based learning algorithm used for classification and regression tasks. It operates on the principle that similar instances are likely to belong to the same class. When making a prediction for a new instance, KNN identifies the 'k' closest training examples in the feature space and assigns the most common class among them (for classification) or averages their values (for regression). The distance metric used (commonly Euclidean distance) plays a crucial role in determining proximity. KNN is particularly advantageous due to its simplicity and ease of implementation; however, it can be computationally expensive as it requires calculating distances to all training samples during inference [4], [5]. Additionally, KNN's performance can degrade with high-dimensional data due to the curse of dimensionality.

3.3. Support Vector Machine (SVM)

Support Vector Machine (SVM) is a powerful supervised learning algorithm primarily used for classification tasks but can also be adapted for regression. SVM works by finding the optimal hyperplane that separates different classes in the feature space with the maximum margin. This hyperplane is defined by support vectors—data points that are closest to the hyperplane and influence its position. SVM is particularly effective in high-dimensional spaces and is robust against overfitting, especially when using kernel functions that allow it to create non-linear decision boundaries. Common kernels include linear, polynomial, and radial basis function (RBF) kernel [4], [5]. SVM's ability to handle both linear and non-linear data makes it versatile across various applications, from text classification to image recognition.

3.4. XGBoost

XGBoost (Extreme Gradient Boosting) is an advanced implementation of gradient boosting that has gained immense popularity due to its performance in machine learning competitions. It builds an ensemble of weak learners—typically decision trees—by sequentially adding trees that correct the errors made by previous ones. XGBoost incorporates regularization techniques that help reduce overfitting, making it highly effective for complex datasets. Its speed and efficiency are enhanced through parallel processing and optimized memory usage during training [4], [5]. XGBoost also provides built-in cross-validation capabilities, making it easier for practitioners to tune hyperparameters effectively. This model has been widely adopted in various domains, including finance for risk assessment and healthcare for predictive modelling.

3.5. Logistic Regression

Logistic Regression is a statistical method used for binary classification problems. Despite its name, it is a linear model that predicts the probability of an outcome based on one or more predictor variables. The logistic function (or sigmoid function) transforms linear combinations of input features into probabilities ranging between 0 and 1. Logistic Regression is particularly valued for its interpretability; coefficients derived from the model indicate how changes in predictor variables affect the odds of the outcome occurring [4]. While it assumes a linear relationship between independent variables and the log-odds of the dependent variable, it can be extended through techniques like polynomial features or interaction terms to capture non-linear relationships. Logistic Regression is commonly used in fields such as medicine for disease diagnosis and marketing for customer segmentation.

4. Dataset

No.	Attributes
1	Gender
2	Age
3	Occupation
4	Sleep Duration
5	Quality of Sleep
6	Physical Activity Level

7	Stress Level
8	BMI Category
9	Blood Pressure
10	Heart Rate
11	Daily Steps
12	Sleep Disorders

This system uses the "Sleep Health and Lifestyle Dataset" from Kaggle [6]. This dataset contains 374 samples with 12 features.

1. **Gender**: This attribute identifies the gender of the individual, typically categorized as Male or Female. It can be used to analyze differences in sleep health and lifestyle between genders.
2. **Age**: This numeric attribute represents the age of the individual in years. Age can significantly influence sleep quality and duration, making it a critical factor in sleep health studies.
3. **Occupation**: This categorical attribute describes the individual's job or profession. Different occupations may have varying impacts on sleep due to work hours, stress levels, and physical demands.
4. **Sleep Duration**: Measured in hours, this attribute indicates the total amount of sleep an individual gets per night. It is essential for assessing whether a person meets recommended sleep guidelines.
5. **Quality of Sleep**: This attribute is rated on a scale from 1 to 10, where 1 indicates poor quality and 10 indicates excellent quality. It reflects how restful and restorative the individual perceives their sleep to be.
6. **Physical Activity**: This attribute measures the level of physical activity in minutes per day. Regular physical activity is linked to better sleep quality and duration.
7. **Stress Level**: Rated on a scale from 1 to 10, this attribute assesses the individual's perceived stress level, which can adversely affect sleep quality and duration.
8. **BMI Category**: This categorical variable classifies individuals based on their Body Mass Index (BMI), which can influence both sleep health and overall well-being.
9. **Blood Pressure**: This attribute records systolic and diastolic blood pressure measurements, which are important indicators of cardiovascular health that can be related to sleep disorders.
10. **Heart Rate**: Measured in beats per minute, this attribute reflects the individual's resting heart rate, which can be influenced by stress levels and overall health.
11. **Daily Steps**: This numeric attribute tracks the number of steps an individual takes each day, serving as a measure of physical activity that can correlate with sleep patterns.
12. **Sleep Disorders**: This categorical attribute indicates whether an individual has been diagnosed with any sleep disorders, such as Insomnia or Sleep Apnea, which can significantly impact sleep quality and overall health.

5. DATA PRE-PROCESSING

Data pre-processing in machine learning is a crucial step that involves cleaning, transforming, and organizing raw data to make it suitable for training machine learning models. Raw data is often incomplete, inconsistent, and in a format that algorithms can't directly use. Pre-processing aims to improve data quality, reduce noise, and extract meaningful features, thereby enhancing model accuracy, efficiency, and generalization.

Due to the dataset containing a mix of categorical and numerical features, several preprocessing steps are necessary. Categorical features such as 'Gender,' 'Occupation,' 'BMI Category,' and 'Sleep Disorder' are transformed into numerical representations using label encoding. Numerical features—including 'Age,' 'Sleep Duration,' 'Quality of Sleep,' 'Physical Activity Level,' 'Stress Level,' 'Heart Rate,' and 'Daily Steps' were standardized to ensure consistent contribution to the models using StandardScaler. The label-encoded and standardized data frames for the first five rows are described in Figures 2 and 3, respectively.

6. Feature Importance

Figure 4 identifies and ranks the most influential factors affecting sleep health in the context of sleep disorder classification. The x-axis represents feature importance values derived from machine learning models, which quantify how strongly each factor contributes to predicting sleep disorders.

Blood Pressure column is divided into BloodPressure_Upper and BloodPressure_Lower columns, renames them, and converts their data types. This is a typical data pre-processing step for machine learning.

Top-Features: BloodPressure_Upper, BloodPressure_Lower, and Occupation are the most important features, showing that they have the greatest influence on sleep health.

Mid-Level Features: Factors like Age, BMI Category, and Sleep Duration hold moderate importance.

Lower Features: Features such as Stress Level, Quality of Sleep, and Gender are less influential for sleep health.

7. System Design and Implementation

This system is implemented using Python programming language. The first step of the system is to import the dataset. Subsequently, pre-processing steps are applied, including label encoding for categorical variables, splitting the data into training 80% and testing 20% for model evaluation, and standardizing features for improved model performance.

After pre-processing, various machine learning models Random Forest, KNN, SVM, XGBoost, and Logistic Regression are trained on the training data using appropriate hyperparameter tuning. The performance of each model is then evaluated on the test set using metrics like accuracy, precision, recall, and F1 score. Finally, the comparison results are displayed, highlighting the model with the best performance in classifying sleep disorders.

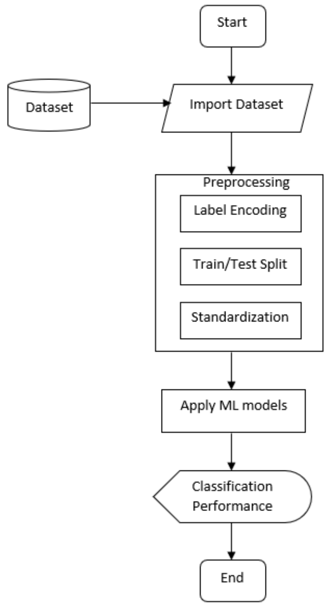

Figure 1. System Flow Diagram

8. Evaluation Metrics

To analyze performance, this system uses accuracy, precision, recall and F1 score [4].

Accuracy refers to the proportion of items that are correctly classified as either true positives or true negatives relative to the total number of items assessed.

Precision, also referred to as Positive Predictive value, measures the fraction of items identified as belonging to the positive class that are actually positive, compared to all items labeled as positive.

Recall, which is also known as sensitivity or True Positive Rate, is the ratio of correctly identified positive items to the total number of actual positives.

The F1 score is a metric that ranges from 0 to 1. A score of 0 signifies the lowest performance (indicating no correct positive predictions), while a score of 1 represents ideal precision and recall (where all positive predictions are accurate).

$$Accuracy = \frac{(TP+TN)}{(\mathrm{TP + TN + FP + FN})} \quad (1)$$

$$Precision = \frac{TP}{(TP+FP)} \quad (2)$$

$$Recall = \frac{TP}{(TP+FN)} \quad (3)$$

$$F1 = 2 * \frac{(\mathrm{Precision} * \mathrm{Recall})}{(\mathrm{Precision} + \mathrm{Recall})} \quad (4)$$

	Gender	Age	Occupation	Sleep Duration	Quality of Sleep	Physical Activity Level	Stress Level	BMI Category	Heart Rate	Daily Steps	Sleep Disorder	BloodPressure_Upper	BloodPressure_Lower
0	1	27	9	6.1	6	42	6	2	77	4200	2	126.0	83.0
1	1	28	1	6.2	6	60	8	0	75	10000	2	125.0	80.0
2	1	28	1	6.2	6	60	8	0	75	10000	2	125.0	80.0
3	1	28	6	5.9	4	30	8	1	85	3000	1	140.0	90.0
4	1	28	6	5.9	4	30	8	1	85	3000	1	140.0	90.0

Figure 2. Label-Encoded Data Frame

	num__Age	num__Sleep Duration	num__Quality of Sleep	num__Physical Activity Level	num__Stress Level	num__Heart Rate	num__Daily Steps	num__BloodPressure_Upper	num__BloodPressure_Lower	cat__Gender	cat__Occupation	cat__BMI Category	cat__Sleep Disorder
0	-1.753096	-1.298887	-1.098280	-0.825418	0.347021	1.654719	-1.619584	-0.330002	-0.268102	1.0	9.0	2.0	2.0
1	-1.637643	-1.173036	-1.098280	0.039844	1.475592	1.170474	1.970077	-0.459239	-0.755640	1.0	1.0	0.0	2.0
2	-1.637643	-1.173036	-1.098280	0.039844	1.475592	1.170474	1.970077	-0.459239	-0.755640	1.0	1.0	0.0	2.0
3	-1.637643	-1.550588	-2.771424	-1.402260	1.475592	3.591698	-2.362273	1.479309	0.869486	1.0	6.0	1.0	1.0
4	-1.637643	-1.550588	-2.771424	-1.402260	1.475592	3.591698	-2.362273	1.479309	0.869486	1.0	6.0	1.0	1.0

Figure 3. Standardized Data Frame

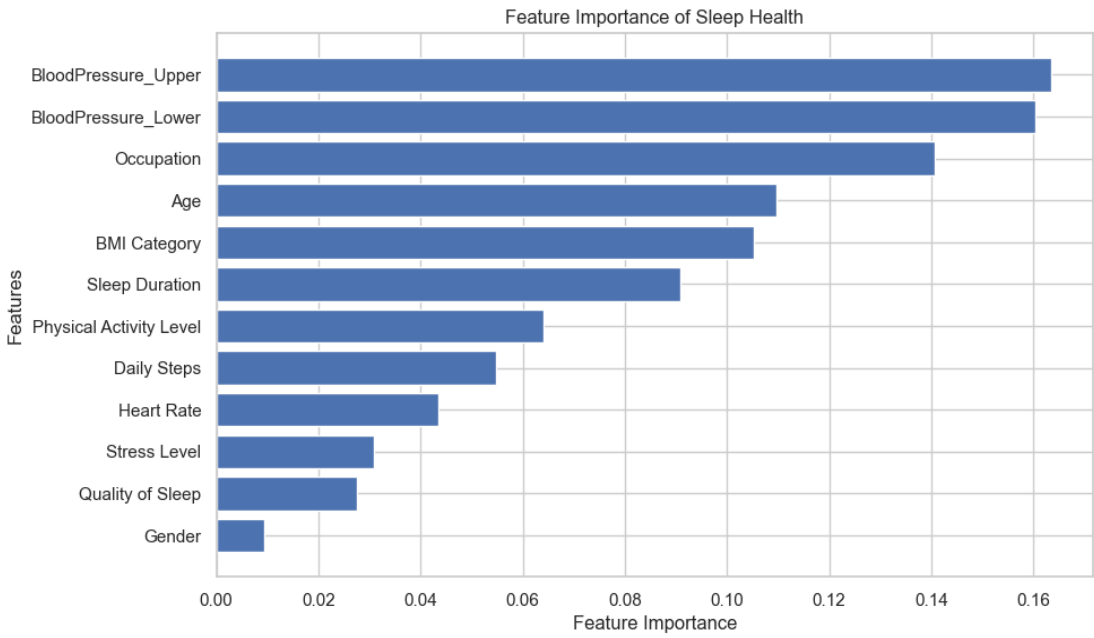

Figure 4. Feature Importance of Sleep Health

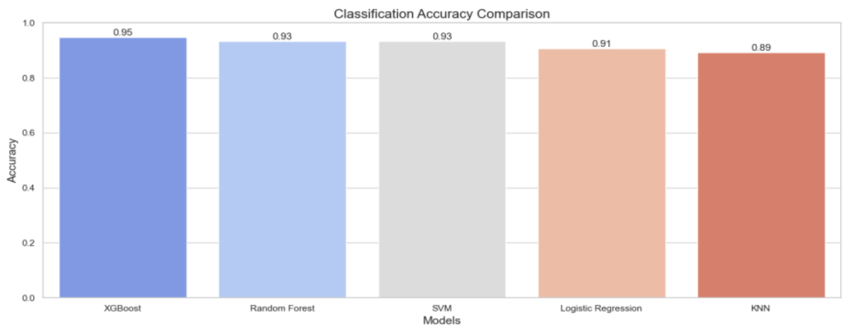

Figure 5. Classification Accuracy Comparison

Table 1. Classification Performance Comparison

ML Models	Accuracy	Precision	Recall	F1 Score
XGBoost	0.95	0.95	0.94	0.94
Random Forest	0.93	0.93	0.92	0.92
SVM	0.93	0.92	0.92	0.92
Logistic Regression	0.91	0.90	0.88	0.89
KNN	0.89	0.89	0.86	0.87

9. Experimental Results

Figure 5 and Table 1 show classification performance of five machine learning models based on their accuracy, precision, recall and F1 score. XGBoost is the best-performing model, achieving the highest accuracy of 95%. Random Forest and SVM follows closely with an accuracy of 93%, Logistic Regression and KNN have lower accuracies, with KNN being the lowest at 89%.

10. Conclusions And Future Work

This paper proposes the classification of sleep disorders by analyzing the significant influence of lifestyle factors on sleep health. Utilizing the Sleep Health and Lifestyle dataset from Kaggle, key variables such as blood pressure, BMI, occupation, and sleep duration were analyzed to understand their correlation with sleep disorders. Feature importance analysis revealed that blood pressure and occupation are critical determinants of sleep health, indicating that these factors should be prioritized by individuals and healthcare professionals when addressing sleep-related issues. Additionally, factors like age, BMI category, and sleep duration showed moderate importance, emphasizing the multifaceted nature of sleep disorders. The findings underscore the necessity of understanding and addressing lifestyle factors to mitigate sleep disturbances and promote better health outcomes. By leveraging machine learning, this paper provides actionable insights for developing targeted interventions that can help improve sleep quality by focusing on modifiable lifestyle elements. Future work could expand on these findings by exploring additional variables or utilizing larger datasets to enhance predictive accuracy and generalizability.

References

[1] T. S. ALSHAMMARI, “Applying Machine Learning Algorithms for the Classification of Sleep Disorders,” *IEEE Access*, vol. 12, 2024, doi: 10.1109/ACCESS.2024.3374408.

[2] M. J. Thorpy, “Classification of Sleep Disorders,” *Springer*, doi: 10.1007/s13311-012-0145-6.

[3] Y. Wang and S. Ji, “An Effective Method for Distinguishing Sleep Apnea and Hypopnea Based on ECG Signals,” *IEEE Access*, vol. 9, 2021, doi: 10.1109/ACCESS.2021.3077030.

[4] J. Han, M. Kamber, and J. Pei, *Data Mining*, Third Edition, 2011.

[5] T. Erl, W. Khattak, and P. Buhler, *Big Data Fundamentals*.

[6] “Sleep Health and Lifestyle Dataset.” [Online]. Available: https://www.kaggle.com/datasets/uom190346a/sleep-health-and-lifestyle-dataset

[7] E. Urtnasan, E. Y. Joo, and K. H. Lee, “AI-Enabled Algorithm for Automatic Classification of Sleep Disorders Based on Single-Lead Electrocardiogram,” vol. 11, no. 2054, Nov. 2021, doi: 10.3390/diagnostics11112054.

[8] E. Alickovic and A. Subasi, ‘‘Ensemble SVM method for automatic sleep stage classification,’’ *IEEE Trans. Instrum. Meas.*, vol. 67, no. 6, pp. 1258–1265, Jun. 2018.

[9] “What is machine learning?”[Online]. Available: https://www.sap.com/sea/products/artificial-intelligence/what-is-machine-learning.html.

[10] “What is Random Forest?,” [Online]. Available: https://careerfoundry.com/en/blog/data analytics/what-is-random-forest/.

CHARACTERIZATION OF CALCIUM-DOPED LANTHANUM MANGANITE MATERIALS BY USING XRD, FTIR, UV-VIS

Yin Nu[1], Zin Mo Naing[2], and Aye Aye Soe[3]

[1,3] Department of Natural Science, University of Computer Studies (Mandalay)
[2]Department of Engineering Physics, Technological University (Kyaing Tong)

yadanaryin477@gnail.com

ABSTRACT

Calcium-doped lanthanum manganite (LCMO) powder was synthesized via the solid-state reaction method. The structural and optical properties of the resulting powders were characterized by X-Ray Diffraction (XRD), Fourier Transforms Infrared spectroscopy (FTIR), and UV-Vis spectroscopy (UV–Vis). The XRD results showed the existence of a crystalline phase. From the FTIR analysis, the band that appeared at wave numbers 594.87 and 596.67 cm^{-1} were responsible for the formation of the $LaMnO_3$ compound, which was attributed to the stretching vibration of the Mn-O band of the MnO_6 octahedron. The UV-Vis result was observed that the calculated values of the band gap energy of these samples were about 3 and 3.25 eV respectively.

KEYWORDS

LCMO, XRD, FTIR, UV-Vis, LaMnO3

1. INTRODUCTION

The perovskite type mixed oxides with the general formula ABO_3 containing rare earth elements (in A position) and 3d transition metals (in B position) are considered strategic materials due to their interesting electrical, magnetic, optical, and catalytic properties[1]. Among them, manganese perovskites have been largely studied for sixty years and their rich variety of properties has shown to be useful for several applications (electronics, depollution, fuel cells, biomedical field, etc.). Manganites are mixed oxides of manganese that crystalize in the perovskite structure, and whose broad stoichiometric formula is $ABO_{(3\pm\delta)}$, where A is a lanthanide element and B is manganese[2]. Among the ABO_3 perovskite structure, they could present an ideal cubic structure of the Pm3m space group as well as structures belonging to the orthorhombic Pbnm space group or rhombohedral R_{3CH} space group. In recent years, lanthanum manganites ($La_{1-x}Ca_xMnO_3$) with unique electrical, magnetic, and catalytic properties have attracted increasing interest for their applications in solid oxide fuel cells, giant magnetoresistance, and catalytic combustion. They can be synthesized by different methods. Typically, sol-gel techniques are employed although they could require the use of expensive alkoxides as raw materials and need long time reactions. In turn, sol-gel combustion is a combination of the chemical sol-gel process and the combustion process; it constitutes a fast, simple fast, simple, economical synthesis process to prepare nanometric powders. On the other hand, the auto-combustion technique uses simple precursors and also constitutes a fast, simple, and economical way to prepare this type of material [3]. The main objective of this work is to find novel anode materials with high electrical conductivity, good matching of thermal expansion coefficient with electrolyte, and materials that can prevent the formation of secondary phases at the anode/electrolyte interfaces[3]. Calcination, the powders were again ball-milled in ethanol to break down agglomerates to obtain sub microns powders. The structural characterization of sample were identified by X-ray powder diffraction (XRD). The bond structure of $La_{1-x}Ca_xMnO_3$ where x = 0.3 and 0.5 was studied by Fourier transform infrared spectroscopy (FTIR). The block diagram of sample preparation is shown in Figure 1. Considering the potential opto-catalytic applications for LCMO in the photodegradation process, the optical absorption spectrum was obtained. Figure 5 indicates the UV-Vis optical absorption spectra of the synthesized specimen[4].

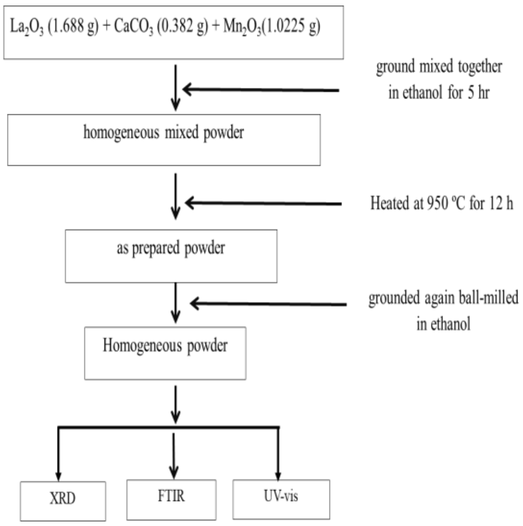

Figure 1. Sample Preparation of LCMO Powder

2. EXPERIMENTS

2.1. Measurement of X-Ray Diffractometer (XRD)

The phase structure was characterized by X-ray powder diffraction (XRD). The structure refinement reveals that $La_{1-x}Ca_xMnO_3$ with x = 0.1, 0.3 and 0.5 has orthorhombic symmetry with space group Pnma[2]. The phase identification of samples and their refined lattice parameters were carried out by XRD (X-ray diffractometer) in air with Cu K_β radiation (λ = 1.3922 Å) of the Rigaku smart lab model in association with Rietveld analysis. The scanning region and range were equal to 10° < 2θ < 80° with a step of 0.05° and a counting time of 10 s/step. The phase identification was done using the ICDD PDF-4 database. The obtained diffraction reflections and calculated values of d_{hkl} fit in the values of the perovskite-type standard. The average crystallite size was calculated by the Debye Scherrer formula

$$D = k\lambda/\beta \cos\theta ,$$

Where k = Scherrer constant = 0.94

λ = X-ray wavelength (nm)

β = (FWHM) of the diffraction peak,

D = Size of the particle

2.2. UV-Vis Spectrometer

UV-Vis spectrophotometry is a technique to measure either absorbance or transmittance of the sample. The optical absorption transmission spectra of samples were recorded in the wavelength ranging from 200-700 nm.

2.3. FTIR Spectrometer

FTIR spectroscopy is an analytical technique to determine its molecular vibration. It uses infrared light to scan test samples and observe chemical properties. The molecular vibrations of synthesized $La_{1-x}Ca_xMnO_3$ measured by Perkin Elmer Spectrum Two.

3. RESULTS AND DISCUSSION

3.1. FTIR Analysis

The room temperature FTIR spectra of synthesized $La_{1-x}Ca_xMnO_3$ where x = 0.3 and 0.5 materials in the wavelength range of 400-1000 cm^{-1} were shown in Figure 2 and Figure 3. It was observed that the peaks at ~ 600 cm^{-1} represent La-O and Mn-O stretching vibrations corresponding to octahedral LaO_6 and MnO_6 groups the lower peaks at ~ 400 cm^{-1} represent La-O-La-O and Mn-O-Mn deformation vibrations. A sharp peak at 419 cm^{-1}, a weakly developed doublet in the range of 440-460 cm^{-1}, a peak at 526 cm^{-1}, and a very broad peak at 660 cm^{-1} with a shoulder at 568 cm^{-1}. The peaks above 500 cm^{-1} were due to stretching modes of the Mn-O-Mn bond and the peak at 419

cm^{-1} and the 440-460 cm^{-1} doublets are due to the bending and tilting of the Mn-O-Mn bond, respectively. The clearest peak observed at 541.70 cm^{-1} for both spectra belongs to La-O in La_2O_3. The band that appeared at wavenumber 594.87 and 596.67 cm^{-1} was responsible for the formation of the $LaMnO_3$ compound, which was attributed to the stretching vibration of the Mn-O band of the MnO_6 octahedron. The significant absorption bands were located between 874.67 and 403.14 cm^{-1} wave numbers. These bands were assigned to stretching vibrations due to interactions between the cations and oxygen in the synthesized compounds. This indicates the formation of perovskite-type structures.

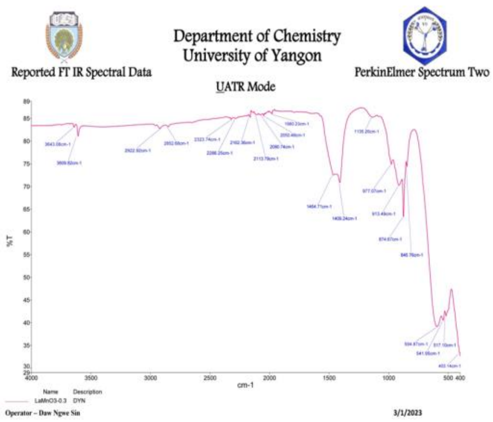

Figure 2. FTIR spectrum of the synthesized sample ($LaMnO_3$ 0.3)

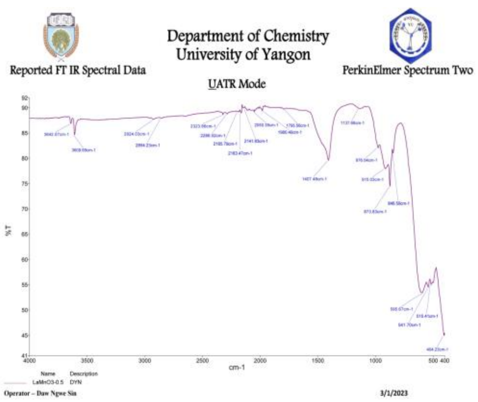

Figure 3. FTIR spectrum of synthesized sample ($LaMnO_3$ 0.5)

3.2 XRD Analysis

An X-ray diffractometer is a device for analyzing and measuring the crystal structure of samples. The XRD pattern of Lanthanum Manganite Powder is shown in Figure 4. The crystalline size of Lanthanum Manganite powder (x = 0.1, 0.3 and 0.5) are shown in Table 1.

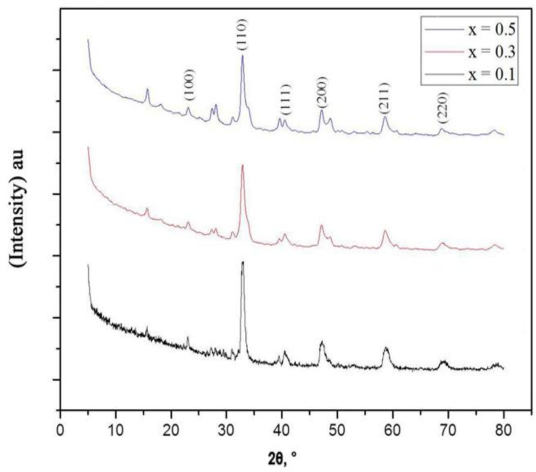

Figure 4. The XRD pattern of Lanthanum Manganite powder

Table 1. Calculated by Crystallite size of Lanthanum Manganite Power (x=0.1,0.3 and 0.5)

Samples	2θ (degree)	FWHM β(degree)	Crystallite Size(D) nm
$La_{0.9}Ca_{0.1}MnO_3$	32.8	0.6741	12.16
$La_{0.7}Ca_{0.3}MnO_3$	33.16	0.5432	14.3
$La_{0.5}Ca_{0.5}MnO_3$	22.82	0.4552	16.8
Average crystallite size			14.42

3.3. Optical Bandgap Investigation

The UV-vis spectra of $La_{1-x}Ca_xMnO_3$ powder were shown in Figure 5. The $LaMnO_3$ sample exhibited absorption bands below 400 nm which could be assigned to the charge transfer from the valence band (VB) of O atoms to the conduction band (CB) of the La atoms. In Figure 6, three obvious peaks are observable due to the optical response in the sample.

The first peak is observed around 235 nm (5.2 eV), a strong absorption peak is observed at wavelengths about 325–380 nm (3.8–3.3 eV) and the third peak occurs as shown in the inset of Figure 6 around 950 nm(1.3 eV) for the sample. The band gap energy of the LCMO powder was evaluated from the UV–Vis spectra by Tauc's plot of $(\alpha h\nu)^2$ vs. $(h\nu)$ and extrapolation of the linear portions of the curve to the energy axis according to the equation $(\alpha h\nu)^2 = A(h\nu - E_g)$, where α is the absorption coefficient, E_g the band gap energy, hν the photon energy and A the constant dependent on the effective masses of the electron, the hole, and the material refractive index.

The estimated bandgap energy values were calculated from the Tauc plots as shown in Figure. The bandgap for all the samples are obtained by drawing a tangent to the slope. The data revealed that the band gap energy for the $La_{0.5}Ca_{0.5}MnO_3$ sample (3.25 eV) is higher than that of the $La_{0.7}Ca_{0.3}MnO_3$ sample (3 eV)[2]. The UV-Vis spectrum and optical band gap of $LaMnO_3$ materials (2.82 eV) synthesized by Ahmed Hussain Jawhari et al were shown in Figure 7[5].

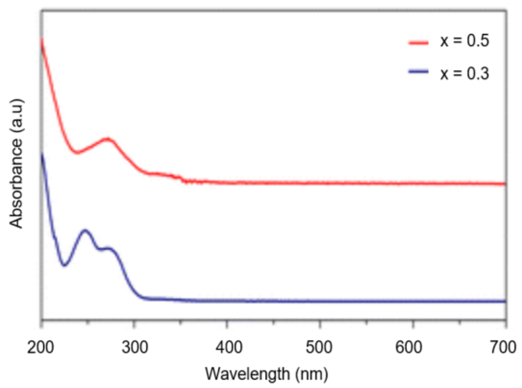

Figure 5. Room temperature UV-Vis spectra of the powder

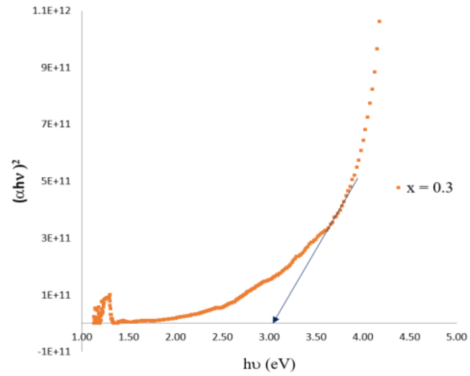

Figure 6. The plot of $(\alpha h\upsilon)^2$ vs. photon

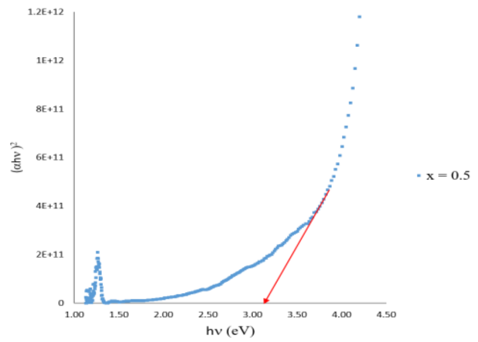

Figure 7. The plot of $(\alpha h\upsilon)^2$ vs. photon energy (hυ) of the $La_{0.5}Ca_{0.5}MnO_3$ powder

4. Conclusions

In this study, $La_{1-x}Ca_xMnO_3$ powder (x = 0.3 and 0.5) was synthesized by a solid-state reaction method. XRD results showed that obtained sample had a perovskite structure. Using Tauc's equation, it was obtained that the product has a direct band gap value of 3 and 3.25 eV. Lanthanum oxide improves the alkali resistance of glass: it is used in making special optical glasses, such as infrared-absorbing glass, as well as camera and telescope lenses, because of the high refractive index and the low dispersion of rare-earth glass. Manganese oxide minerals have been used for thousands of years—by the ancients for pigments and to clarify glass, and today as ores of Mn metal, catalysts, and battery material. More than 30 Mn oxide minerals occur in a wide variety of geological settings. Calcium carbonate is a dietary supplement used when the amount of calcium taken in the diet is not enough. Calcium is needed by the body for healthy bones, muscles, nervous system, and heart. Calcium carbonate also is used as an antacid to relieve heartburn, acid indigestion, and upset stomach Jun 20, 2024.

Future Plan

$La_{1-x}A_xMnO_{3-\delta}$ (A = Ca and Sr) perovskite will be synthesized using different methods, such as solid-state reaction and sol-gel methods for solid oxide fuel cells (SOFCs) for use as a cathode material. The pristine material will be characterized by X-ray diffraction, thermogravimetric analysis (TGA-DTA), scanning electron microscopy (SEM-EDS), electrical conductivity and electrochemical impedance analysis.

ACKNOWLEDGEMENTS

The authors would like to thank Dr San San Tint, Pro-Rector, University of Computer Studies (Mandalay)for her encouragement and thanks research journal organizing committee JITRI-2024. I thank indeed my Head of Physics Department, Professor Dr Nwe Nwe Htoon University of Computer Studies (Mandalay). I would like to express my sincere thank to Professor Dr Ye Chan, Head of the Universities' Research Centre for XRD measurements. I am greatly indebted to my supervisor Dr Min Maung Maung, Professor Department of Physics, at the University of Yangon for his valuable guidance, helpful device, and supervision.

REFERENCES

[1] S. Paul, Manokamna, A. Kumar, and A. Kumar, "Synthesis and Characterization of La 0.70 Ca 0.30 MnO 3 System for Solid Oxide Fuel Cell Applications", IOP Conf. Ser. Mater. Sci. Eng., vol. 1225, no. 1, p. 012054, 2022, doi: 10.1088/1757-899x/1225/1/012054.

[2] A. Mahata, P. Datta, and R. N. Basu, "Synthesis and characterization of Ca doped LaMnO3 as potential anode material for solid oxide electrolysis cells," Ceram. Int., vol. 43, no. 1, pp. 433–438, 2017, doi: 10.1016/j.ceramint.2016.09.177.

[3] Z. M. Myat, P. Y. Thein, T. T. Win, Y. M. Maung, K. Ko, and K. Soe, "Characterization and Dielectric Properties of LaMnO 3 Thin Films by Spin Coating Method," pp. 370–374.

[4] M. C. Dimri, H. Khanduri, and R. Stern, "Effects of aliovalent dopants in LaMnO3: Magnetic, structural and transport properties," J. Magn. Magn. Mater., vol. 536, no. December 2020, p. 168111, 2021, doi: 10.1016/j.jmmm.2021.168111.

[5] A. Khalid, S. A. Siddiqi, and A. Aslam, "Synthesis and characterization of alkaline-earth metal (Ca, Sr, and Ba) doped nanodimensional LaMnO3 rare-earth manganites," Chinese Phys. Lett., vol. 30, no.7,2013,doi:10.1088/0256307X/30/7/077501.

Biography

Authors

First A. Daw Yin Nu graduated M.Sc(Physics) degree in 2005 at the University of Magway. She first served as a Tutor in 2005 at (TU) Magway. Then, she was promoted to Assistant Lecturer in 2013 at the (TU) Magway. She was transferred and promoted as a Lecturer to the UCS(Maubin) in 2017. After about 3 years she was transferred to UCS (Magway). And then transferred and promoted as an Associate Professor to the UCS(Mandalay) in 2021. She is currently serving as an Associate Professor in the Department of Natural Science at the University of Computer Studies (Mandalay). She attended PhD Preliminary Course (2021-2022) in Physics to be a doctoral candidate at the University of Yangon. She conducted research projects in the fields of Electronics, Material Science, Theoretical Physics, and Nuclear Physics during her PhD Preliminary Course of study. She is interested in the fields of all the subjects. Now, She is conducting research on Material Science as a 3-PhD-Phys researcher at the University of Yangon. She has received the publication paper from (TUMGJRI) 2023, Vol-1, Issue-3. Currently, She is interested in doing research in the field of Material Science. So, she would like to keep on doing research in this field.

. **Second B.** Daw Zin Mo Naing graduated the M.Sc (2016) and MRes (2016) degrees from Shwebo University and Mandalay University. She first served as a Tutor in 2017 at University of Computer Studies (Banmaw). And then she was promoted to Assistant Lecturer in 2021 at University of Computer Studies (Mandalay) . She is now serving as a Lecturer at the Department of Engineering Physics in Technological University (KyaingTong).

Third C. Daw Aye Aye Soe graduated M.Sc (Physics) degree in 2005 from Mandalay University. She is now serving as an Associate Professor at the Department of Natural Science in University of Computer Studies (Mandalay).

APPLICATIONS OF ABOODH TRANSFORM AND ITS PROPERTIES

Nwe Ni Aung[1]

[1] Department of Engineering Mathematics, Technological University (Taunggyi)
dawnweniaung110@gmail.com

ABSTRACT

The Aboodh transform is a mathematical tool used in solving the differential equations by converting them from one form into another form. It makes it easier to solve the problem in engineering application and make differential equations simple to solve. It is applied in different areas of science, engineering and technology. Ordinary linear differential equation with constant coefficient and variable coefficient can be easily solved by the Aboodh transform method without finding the generally solution and the arbitrary constant. The differential equations arising in science and engineering problems are usually solved by the methods Laplace transform, convolution method, calculus method, Elzaki transform, Residue theorem and so on. In this paper, basic concepts of Aboodh transform are firstly described. Next, Aboodh transform and inverse Aboodh transform of some elementary functions are presented. And then, the existence and uniqueness of Aboodh transform are expressed. And then the application of Aboodh transform to simultaneous differential equations.

KEYWORDS

Aboodh transform, system of differential equations, applications.

1. INTRODUCTION

The Aboodh transform is a type of integral transform. Khalid Suliman Aboodh formulated it in 2013. The Aboodh transform has been used in fields such as a double, triple, and quadruple Aboodh transforms, fuzzy logic and fractional theory. The Aboodh transform is a relatively new integral transform used in mathematical analysis, particular engineering and applied mathematics. It is similar in concept to other integral transforms like the Laplace transform, and Fourier transform but it has unique properties that can be advantageous in certain applications. It is applicable to a variety of functions and can handle both continuous and discrete data.

2. BASIC DEFINITIONS

In this section, basic definitions, Aboodh transform of some elementary functions and derivatives of the functions are expressed.

2.1. Exponential Order

A function $f(t)$ is said to be of exponential order if there exists constant M and b such that $|e^{-bt} f(t)| \le M$ for $t \ge t_0$, where t_0 is a fixed value of t. If a constant b exists such that $\lim_{t\to\infty} e^{-bt} f(t)$ exists (finite value), then $f(t)$ is of exponential order.

2.2. Piecewise Continuous

The function $f(t)$ is **piecewise continuous** on a finite interval $a \le t \le b$, where f is defined, if this interval can be divided into finitely many subintervals in each of which f is continuous and has finite limits as t approaches either endpoint of such a subinterval from the interior.

2.3. Aboodh Transform

The **Aboodh transform** of the function $f(t)$ of exponential order is defined over the set of functions

$$A = \left\{ f(t) : \exists M, k_1, k_2 > 0, \; |f(t)| < M e^{-vt} \right\}$$

by the following integral

$$A[f(t)] = K(v) = \frac{1}{v}\int_0^\infty e^{-vt} f(t)\,dt;\ t \geq 0, k_1 \leq v \leq k_2$$

(1)

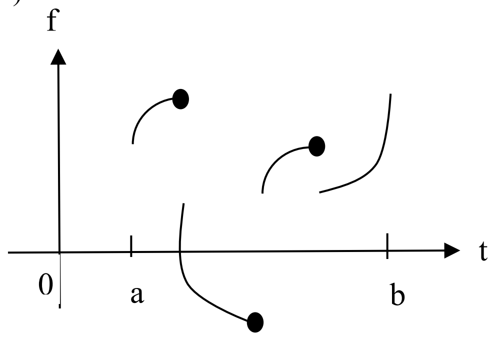

Figure 1. piecewise continuous function $f(t)$

2.4. Aboodh transforms of some elementary functions

For any function $f(t)$, we assume that the integral equation (1) exists. The sufficient conditions for the existence of Aboodh transform are that $f(t)$ for $t \geq 0$ be piecewise continuous and of exponential order, otherwise Aboodh transform may or may not exist.

Aboodh transforms of some functions are

(i) $A(1) = \frac{1}{v^2}$,

(ii) $A(t) = \frac{1!}{v^3}$,

(iii) $A(t^2) = \frac{2!}{v^4}$,

(iv) $A(t^n) = \frac{n!}{v^{n+2}}\ (n = 0, 1, 2, \ldots)$,

(v) $A(e^{at}) = \frac{1}{v^2 - av}$,

(vi) $A(\sin at) = \frac{a}{v(v^2 + a^2)}$,

(vii) $A(\cos at) = \frac{1}{(v^2 + a^2)}$,

(viii) $A(\sinh at) = \frac{a}{v(v^2 - a^2)}$,

(ix) $A(\cosh at) = \frac{1}{(v^2 - a^2)}$.

(i) Indeed, if $f(t) = 1$, then by definition

$$A(1) = \frac{1}{v}\int_0^\infty e^{-vt}\,dt$$

$$= \frac{1}{v}\left[\frac{e^{-vt}}{-v}\right]_0^\infty$$

$$= -\frac{1}{v^2}\left[\frac{1}{e^{vt}}\right]_0^\infty.$$

Hence, $A(1) = \frac{1}{v^2}$.

(ii) Indeed, if $f(t) = t$, then by definition

$$A(t) = \frac{1}{v}\int_0^\infty t e^{-vt}\,dt$$

$$= \frac{1}{v}\left[\frac{-te^{-vt}}{-v} - \frac{e^{-vt}}{v^2}\right]_0^\infty.$$

Hence, $A(t) = \frac{1}{v^3}$.

(iii) Indeed, if $f(t) = t^2$, then by definition

$$A(t^2) = \frac{1}{v}\int_0^\infty t^2 e^{-vt}\,dt$$

$$= \frac{1}{v}\left[\frac{-t^2 e^{-vt}}{v} - \frac{2te^{-vt}}{v^2} - \frac{2e^{-vt}}{v^3}\right]_0^\infty$$

$$= \frac{1}{v}\left[\frac{2}{v^3}\right] = \frac{2}{v^4}.$$

Hence, $A(t^2) = \frac{2!}{v^4}$.

(iv) Indeed, if $f(t) = t^n$, then by definition

$$n = 0,\ A(t^0) = A(1) = \frac{1}{v^2} = \frac{0!}{v^{0+2}}$$

,

$$n = 1,\ A(t^1) = A(t) = \frac{1}{v^3} = \frac{1!}{v^{1+2}}$$

,

$$n = 2,\ A(t^2) = A(t^2) = \frac{2}{v^4} = \frac{2!}{v^{2+2}}$$

Hence,

$$A(t^n) = \frac{n!}{v^{n+2}} \quad (n=0,1,2,\ldots).$$

2.5. Inverse Aboodh transforms of some elementary functions

If $K(v)$ is the Aboodh transform of $f(t)$, then $f(t)$ is called the inverse Aboodh transform of $K(v)$ and in mathematical terms, it can be expressed as $f(t)=K^{-1}(K(v))$, where K^{-1} is an operator and it is called as inverse Aboodh transform operator. For example,

(i) $K^{-1}\left[\frac{1}{v^2}\right] = 1$,

(ii) $K^{-1}\left[\frac{1}{v^3}\right] = t$,

(iii) $K^{-1}\left[\frac{1}{v^4}\right] = \frac{t^2}{2!}$,

(iv) $K^{-1}\left[\frac{1}{v^{n+2}}\right] = \frac{t^n}{n!}$, $(n = 0,1,2,\ldots)$

(v) $K^{-1}\left[\frac{1}{v^2 - a v}\right] = e^{at}$,

(vi) $K^{-1}\left[\frac{a}{v(v^2 + a^2)}\right] = \frac{1}{a}\sin at$,

(vii) $K^{-1}\left[\frac{1}{v^2 + a^2}\right] = \cos at$,

(viii) $K^{-1}\left[\frac{a}{v(v^2 - a^2)}\right] = \frac{1}{a}\sinh at$,

(ix) $K^{-1}\left[\frac{1}{v(v^2 - a^2)}\right] = \cosh at$.

2.6. Aboodh transforms of the derivatives of the function $f(t)$

If Aboodh transform of the function $f(t)$ is given by $A[f(t)] = K(v)$, then

(i) $A[f'(t)] = vK(v) - \frac{f(0)}{v}$,

(ii) $A[f''(t)] = v^2 K(v) - \frac{f'(0)}{v} - f(0)$,

(iii) $A\left[f^n(t)\right] = v^n K(v) - \frac{f(0)}{v^{2-n}} - \frac{f'(0)}{v^{3-n}} - \cdots - \frac{f^{n-1}(0)}{v}$,

(iv) $A[t f(t)] = -\frac{d}{dv}K(v) - \frac{1}{v}K(v)$,

(v) $A[t f'(t)] = -\frac{d}{dv}\left[vK(v) - \frac{f(0)}{v}\right] - \frac{1}{v}\left[vK(v) - \frac{f(0)}{v}\right]$,

(vi) $A\left[t^2 f'(t)\right] = v\frac{d^2}{dv^2}K(v) + 2\frac{d}{dv}K(v) - 2\frac{f(0)}{v^3}$,

(vii) $A[t f''(t)] = -\frac{d}{dv}\left[v^2 K(v) - \frac{f'(0)}{v} - f(0)\right]$

$$-\frac{1}{v}\left[v^2 K(v) - \frac{f'(0)}{v} - f(0)\right],$$

(viii) $$A\left[t^2 f''(t)\right] = v^2 \frac{d^2}{dv^2} K(v) + 4v \frac{d}{dv} K(v)$$

$$+ 2K(v) - 2\frac{f'(0)}{v^3}.$$

(i) Indeed,

$$A[f'(t)] = \frac{1}{v}\int_0^\infty e^{-vt} f'(t)\, dt,$$

by using integration by parts,

$$\int_0^\infty e^{-vt} f'(t)\, dt = \left[e^{-vt} f(t)\right]_0^\infty + v\int_0^\infty e^{-vt} f(t)\, dt$$

$$= -f(0) + v\int_0^\infty e^{-vt} f(t)\, dt$$

$$= -f(0) + v^2 A[f(t)]$$

$$A[f'(t)] = vK(v) - \frac{f(0)}{v}.$$

(ii) Indeed,

$$A[f''(t)] = \frac{1}{v}\int_0^\infty e^{-vt} f''(t)\, dt,$$

by using integration by parts,

$$\int_0^\infty e^{-vt} f''(t)\, dt = \left[e^{-vt} f'(t)\right]_0^\infty + v\int_0^\infty e^{-vt} f'(t)\, dt$$

$$= -f'(0) + v\left[vA(f'(t))\right]$$

$$= -f'(0) + v^2\left[A(f'(t))\right]$$

$$= -f'(0) + v^2\left[vK(v) - \frac{f(0)}{v}\right]$$

$$= -f'(0) + vf(0) + v^3 K(v)$$

$$= \frac{1}{v}\left[-f'(0) + vf(0) + v^3 K(v)\right].$$

Hence,

$$A[f''(t)] = v^2 K(v) - \frac{f'(0)}{v} - f(0)$$

.

(iii) Indeed,

$$A[f(t)] = K(v) = \int_0^\infty \frac{1}{v} e^{-vt} f(t)\, dt$$

Then,

$$\frac{d}{dv}K(v) = K'(v) = \frac{d}{dv}\int_0^\infty \frac{1}{v} e^{-vt} f(t)\, dt$$

$$= \int_0^\infty \frac{d}{dv}\left(\frac{1}{v} e^{-vt}\right) f(t)\, dt$$

$$\frac{d}{dv}K(v) = -\int_0^\infty \frac{1}{v} e^{-vt}\, t f(t)\, dt$$

$$-\int_0^\infty \frac{1}{v^2} e^{-vt} f(t)\, dt$$

$$= -A[tf(t)] - \frac{1}{v} A[f(t)].$$

Hence,

$$A[tf(t)] = -\frac{d}{dv}K(v) - \frac{1}{v}K(v)$$

.

3. Existence And Uniqueness Of Aboodh Transform

In this section, existence and uniqueness of Aboodh transform are expressed.

3.1. Theorem (Existence of the Aboodh transform)

If $f(t)$ is piecewise continuous in every finite interval $0 \le t \le k$ and of exponential order r, for $t > k$, then its Aboodh transform $A(f(t))$ exists for all $v > r$.

Proof:

We have for every positive number k

$$\frac{1}{v}\int_0^\infty f(t) e^{-vt}\, dt = \frac{1}{v}\int_0^k f(t)\, e^{-vt}\, dt + \frac{1}{v}\int_k^\infty f(t)\, e^{-vt}\, dt$$

Since $f(t)$ is piecewise continuous in interval $0 \le t \le k$, there is the first integral on the right. Also, there is a second integral on the right. So $f(t)$ is of exponential r for order $t > k$. To see this we have only to observe that in such case:

$$\left|\frac{1}{v}\int_k^{\infty} f(t)\, e^{-vt}\, dt\right| \leq \frac{1}{v}\int_k^{\infty}\left|f(t)e^{-vt}\right| dt$$

$$\leq \frac{1}{v}\int_0^{\infty}|f(t)|\, e^{-vt}\, dt$$

$$\leq \frac{1}{v}\int_k^{\infty} e^{-vt} M\, e^{-rt}\, dt$$

$$= \frac{M}{v}\int_0^{\infty} e^{-vt} e^{rt}\, dt$$

$$= \frac{M}{v}\int_0^{\infty} e^{-(v-r)t}\, dt$$

$$\leq \frac{M}{v}\left[\frac{e^{-(v-r)t}}{-(v-r)}\right]_0^{\infty}$$

$$= \frac{M}{v}\left[\frac{1}{(v-r)}\right]$$

$$\left|\frac{1}{v}\int_k^{\infty} f(t)\, e^{-vt}\, dt\right| = \frac{M}{v(v-r)}.$$

$A(f(t))$ exists for all $v > r$.

3.2. Theorem (Uniqueness of the Aboodh transform)

Let $f_1(t)$ and $f_2(t)$ be continuous functions defined for $t \geq 0$ and have Aboodh transforms, $K_1(v)$ and $K_2(v)$ respectively. If $K_1(v) = K_2(v)$, then $f_1(t) = f_2(t)$, where $v > 0$.

Proof:

Let $K_1(v)$ and $K_2(v)$ be the Aboodh transforms of $f_1(t)$ and $f_2(t)$, respectively.

$$A[f_1(t)] = K_1(v) = \frac{1}{v}\int_0^{\infty} e^{-vt} f_1(t)\, dt,$$

$$A[f_2(t)] = K_2(v) = \frac{1}{v}\int_0^{\infty} e^{-vt} f_2(t)\, dt.$$

Suppose $K_1(v) = K_2(v)$ for all $v > 0$.

If $K_1(v) = K_2(v)$, then

$$\frac{1}{v}\int_0^{\infty} e^{-vt} f_1(t)\, dt$$

$$= \frac{1}{v}\int_0^{\infty} e^{-vt} f_2(t)\, dt,$$

$$\frac{1}{v}\int_0^{\infty} e^{-vt}\left[f_1(t) - f_2(t)\right] dt = 0.$$

Let $h(t) = f_1(t) - f_2(t)$,

$$\frac{1}{v}\int_0^{\infty} e^{-vt} h(t)\, dt = 0 \quad \text{for all}$$

$v > 0$.

Hence, $\qquad h(t) = 0$

and so $\qquad f_1(t) = f_2(t)$.

4. Applications Of Aboodh Transform

In this section, we solve the system of differential equations by using Aboodh transform method.

4.1. Example

Consider the tank T_1 in Fig initially contains 100 gal of pure water. Tank T_2 initially contains 100 gal of water in which 150lb of salt are dissolved. The inflow into T_1 is 2 gal/min from T_2 and 6 gal/min containing 6lb of salt from the outside.

The flow into T_2 is 8 gal/min from T_1. The outflow from T_2 is 2+6 = 8 gal/minas shown in the Fig. The mixtures are kept uniform by stirring. Find and plot the salt contents y_1 and y_2 in T_1 and T_2 respectively.

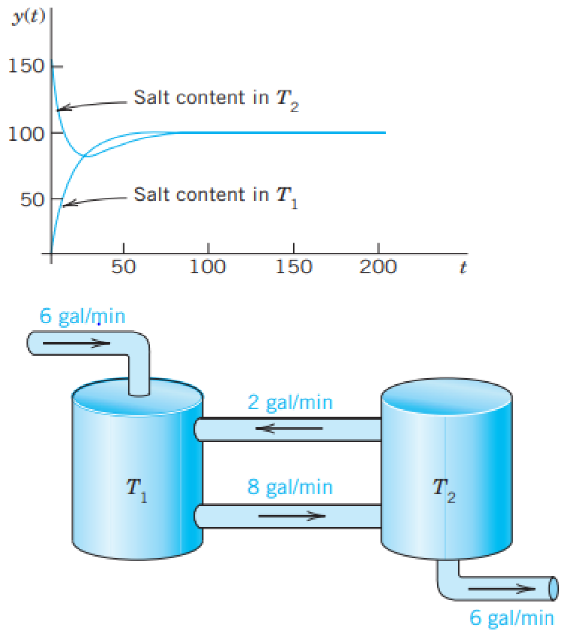

Figure 2. Mixing Problem

The model is obtained in the form of two equations.

Time rate of change = Inflow/min – Outflow/min for the two tanks.

$$y_1' = -\frac{8}{100}y_1 + \frac{2}{100}y_2 + 6$$

$$y_2' = \frac{8}{100}y_1 - \frac{8}{100}y_2,$$

The initial conditions are $y_1(0) = 0, y_2(0) = 150$.

$$y_1' = -0.08\,y_1 + 0.02\,y_2 + 6$$
(2)

$$y_2' = 0.08y_1 - 0.08y_2 \qquad (3)$$

Taking Aboodh transform to (2) gives

$$A(y_1') = -0.08\,A(y_1) + 0.02\,A(y_2) + A(6)$$

$$(v + 0.08)\,A(y_1) - 0.02\,A(y_2) = \frac{6}{v^2}$$
(4)

Taking Aboodh transform to (3) gives

$$A(y_2') = 0.08A(y_1) - 0.08A(y_2)$$

$$-0.08\,A(y_1) + (v + 0.08)\,A(y_2) = \frac{150}{v}$$
(5)

From (4) and (5),

$$A(y_1) = \frac{1}{v}\left[\frac{9v + 0.48}{v(v+0.12)(v+0.04)}\right]$$

By using partial fraction,

$$A(y_1) = \frac{1}{v}\left[\frac{100}{v} - \frac{62.5}{v+0.12} - \frac{37.5}{v+0.04}\right]$$

$$= \frac{100}{v^2} - \frac{62.5}{v^2 + 0.12v} - \frac{37.5}{v^2 + 0.04v}$$

Taking the inverse Aboodh transform,

$$y_1(t) = 100 - 62.5\,e^{-0.12\,v} - 37.5\,e^{-0.04\,v}$$

$$A(y_2) = \frac{1}{v}\left[\frac{150v^2 + 12\,v + 0.48}{v(v+0.12)(v+0.04)}\right]$$

By using partial fraction,

$$A(y_2) = \frac{1}{v}\left[\frac{100}{v} + \frac{125}{v+0.12} - \frac{75}{v+0.04}\right]$$

$$= \frac{100}{v^2} + \frac{125}{v^2 + 0.12v} - \frac{75}{v^2 + 0.04v}$$

Taking the inverse Aboodh transform,

$$y_2 = 100 + 125\,e^{-0.12\,v} - 75\,e^{-0.04\,v}$$

5. CONCLUSIONS

The main purpose of this paper is to give a brief idea about applications of Aboodh transform in various areas and how to solve the simultaneous linear differential equations with initial conditions. Aboodh transform is a very useful mathematical tool to make simpler complex problems. The Aboodh transform method can be extended to solve many ordinary differential equations with constant coefficients and variable coefficients which arise in physical and engineering applications.

ACKNOWLEDGEMENTS

I sincerely thanks Dr Khin Htike Htike Lwin, Rector, Dr. Khin May Win, Pro-

Rector of Technological University (Taunggyi) for permitting the opportunity to present this paper. I would like to express thanks to Professor Dr. Swe Swe Kyaw, Head of Department of Engineering Mathematics, Technological University (Taunggyi), for her kind permission to perform this paper. I am grateful to my supervisor Dr. Khin Than Sint, Professor, Department of Mathematics, University of Mandalay, for her advice and suggestion to implement this kind of research paper. Finally, I thank my parents for their support throughout my life and encouragement.

REFERENCES

[1] Aboodh, K. S., "*The New Integral Transform: Aboodh Transform*", Global Journal of Pure and Applied Mathematics, Vol. 9, No. 1, pp. 35-43, 2013.

[2] Debnath, L. and Bhatta, D., "Integral Transform and Their Applications", Third Edition, CRP Press, New York, 2015.

[3] Kreyszig, E., "Advanced Engineering Mathematics", Tenth Edition, John Wiley and Sons, New York, 2011.

[4] Mahgoub, M. M. A. and Alshikh. A. A., "*On The Relationship between Aboodh Transform and New Integral Transform ZZ Transform*", Mathematical Theory and Modeling, Vol. 6, No. 9, pp. 71-76, 2016.

[5] Mahgoub, M. M. A., Aboodh, K. S. and Alshikh, A. A., "*On The Solution of Ordinary Differential Equation with Variable Coefficients using Aboodh Transform*", Advances in Theoretical and Applied Mathematics, Vol. 11, No. 4, pp. 383-389, 2016.

[6] Verma, D., Alam, A. and Singh, A. P., "*Applications of Aboodh Transform*", International Research Journal of Innovations in Engineering and Technology, Vol. 4, Issue 6, pp. 47-51, 2020.

[7] Wazwaz, A. M., "Linear and Nonlinear Integral Equations", Higher Education Press, Beijing, 2011.

Authors' Biography

Author: Daw Nwe Ni Aung, Associate Professor, Department of Engineering Mathematics, Technological University (Taunggyi). She achieved B.Sc. (Maths.) in 1998 and M.Sc. (Maths.) in 2002. The author has been worked at Myanmar Aerospace and Engineering University, West Yangon Technological University, University of Technology- Yatanarpon Cyber City and Technological University (Taunggyi). Her research filed of interests includes engineering mathematics and mathematical statistics. (email: dawnweniaung110@gmail.com)

ANALYSIS OF FACE RECOGNITION SYSTEMS BASED ON GOOGLENET AND VGG-16 DEEP LEARNING MODELS

Ei Shwe Sin[1], and Khin Zaw Oo[2]
[1,2]Department of Electronic Engineering, Technological University (Taunggyi)
shwesinec@gmail.com,zawoo.slg@gmail.com

ABSTRACT

Deep learning has revolutionized face recognition, with architectures like GoogLeNet and VGG-16 achieving state-of-the-art results. This study compares the performance of GoogLeNet and VGG-16 for face recognition using MATLAB, focusing on a training configuration of 25 classes and 555images. GoogLeNet, with its inception modules, is designed for computational efficiency and scalability, while VGG-16 relies on its deeper and more uniform convolutional layers to extract fine-grained features. Both models were fine-tuned and evaluated on a standard face recognition dataset using MATLAB's Deep Learning Toolbox. However, GoogLeNet outperforms VGG-16 in terms of computational speed and resource efficiency, making it suitable for real-time applications. The CNN models of GoogLeNet and VGG-16 were trained using parameter metrics for batch size, number of epochs, validation frequency, and learning rate, set to 5, 6, 35, and 0.003, respectively. The validation accuracy of GoogLeNet model achieved 97.24% and VGG-16 model achieved 83.44 % after training the models. The test accuracy of GoogLeNet model is 90 % and VGG-16 model is 80 % .

KEYWORDS

Image Classification, Face Recognition, Deep Learning, GoogLeNet, VGG-16, MATLAB Deep Learning Toolbox, Convolution Neural Network (CNN)

1. INTRODUCTION

As explained by MathWorks, face recognition involves identifying individuals in images or videos by analyzing and comparing patterns. These algorithms work by extracting a person's facial features, comparing them with those stored in a database, and finding the closest match. This technology has become a critical component of biometric systems, security and surveillance applications, and image and video indexing solutions.

Face detection is widely applied in computer vision due to its exceptional stability and adaptability, making it more versatile compared to fingerprint identification and similar technologies [1]. While humans naturally recognize faces daily, replicating this process with computer systems and enhancing accuracy remains a challenging endeavour. Research into facial recognition began in the 1950s [2]. However, recognizing faces remains a complex task in visual pattern recognition. Humans instinctively identify visual patterns, interpreting them as logical information through cognitive processes, whereas computers perceive visual data, such as images or videos, as a matrix of individual pixels [3].

Face identification is a significant challenge in image analysis and computer vision. This study, focused on Face Recognition, addresses these challenges by utilizing deep learning techniques to identify or verify individuals. Facial recognition automates the process of detecting a face within an image. The research involved analyzing 25 class and datasets containing up to 555 students faces, encompassing a diverse range of facial expressions, angles, and backgrounds.

A machine must determine the meaning of specific data points within a dataset, which presents a complex diagnostic challenge when identifying visual models. In facial recognition, it is crucial to establish which data corresponds to specific facial components. The key question is how to verify or confirm a person's identity using a given facial image in comparison to images from a student photo dataset [3].

Deep learning-based techniques are capable of identifying intricate facial features [4]. The deep learning-based approach, particularly Convolutional Neural Networks (CNNs), effectively addresses key challenges in intelligence, government, and commercial research by leveraging complex architectures to process high-quality visual data [5].

2. RELATED WORK

For facial recognition categorization, several studies have employed various Machine Learning, Deep Learning, and Hybrid algorithms. Some key examples are highlighted as follows:

This paper developed a facial recognition algorithm based on a convolutional neural network (CNN). Data sets were collected locally, and online data gathering required manual filtering of inappropriate images. The study focused on three Chinese individuals, collecting 200 images for each. The improved model achieved a recognition accuracy ranging from 68.85% to 79.41% after dataset validation [1].

This paper proposed a real-time attendance system utilizing a face recognition system based on the CNN-PCA method. The system identifies and records individuals by detecting and storing facial data in a database. Their approach achieved up to 98% accuracy in facial recognition [3].

This paper introduced a facial recognition system using neural network testing. The system employs the AdaBoost algorithm to accurately detect and measure faces in images, followed by the extraction of facial features using a deep convolutional neural network. Tested with the CMU PIE database and validated on laboratory staff, the system demonstrated reliable facial recognition functionality and improved visual accuracy [4].

This paper presents a face recognition system based on OpenFace and improved with an intelligent self-learning algorithm called S-DDL, which integrates an incremental SVM classifier to adapt in real time. Unlike traditional systems that use fixed models, this approach updates classification models dynamically by incorporating newly collected data, leading to enhanced accuracy and efficiency over time. Experimental results demonstrate that the system achieves strong real-time performance, balances accuracy with computational efficiency, and outperforms traditional SVM methods in adaptability. [6].

3. METHODOLOGY

A deep learning framework, referred to as Deep Convolutional Neural Networks (DCNN), is selected for the research. The model's weights are utilized, and its structure is fine-tuned to create a distinct architecture tailored for face recognition classification on a student face dataset containing 555 images across 25 classes:

3.1. Data Collection

For training, a student face dataset with a maximum of 555 faces and 25 class was used . The 25 features in this dataset include various facial expressions, viewpoints, and backgrounds. The sample properties included in this dataset are shown in Figure 1 and samples of the test image in Figure 2.

3.2. Training Datasets

In this system, the dataset has been divided for training and validation. Specifically, the proposed dataset is split in a 7:3 ratio, with 70% allocated for training and 30% for validation.

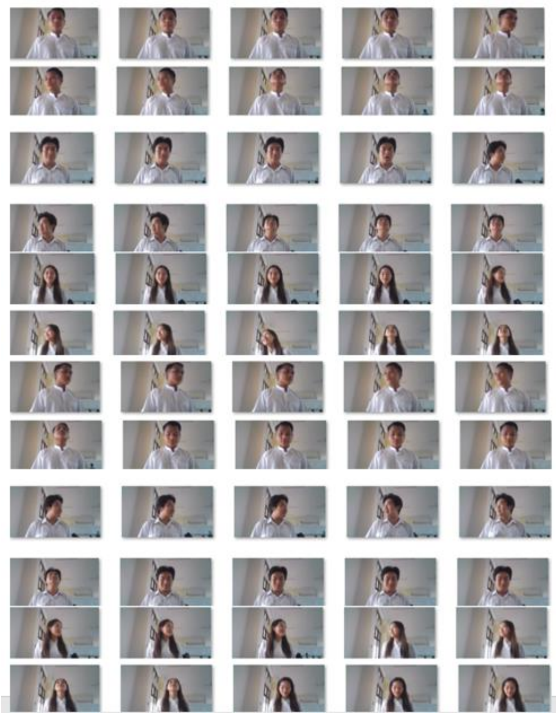

Figure 1. Samples of the Collecting Dataset

Figure 2. Samples of the Test Image

3.3. Transfer Learning:

Transfer learning is a key concept in deep learning, though its exact mechanics are not fully understood. This study explores the transferability of neural networks, demonstrating that transferring high-level features significantly enhances efficiency. Despite the uncertainties, transfer learning consistently outperforms building a network from the ground up. Fine-tuning pre-trained models, even minimally, delivers far better results than starting with random weights, highlighting the superior effectiveness of transfer learning over learning from scratch.

3.4. Applied Model

GoogLeNet is a pretrained model trained on a subset of the ImageNet database, which is utilized in the ImageNet Large-Scale Visual Recognition Challenge (ILSVRC), achieved a top-10 test accuracy of 80 % on the ImageNet dataset. This model, comprising 144 layers, has been trained on over a million images and is capable of classifying images into 1,000 distinct object categories.

VGG-16, a deep convolutional neural network widely used in image recognition, achieved a top-10 test accuracy of 90 % on the ImageNet dataset, by the Visual Geometry Group at University of Oxford, which contains 14 million images across 1,000 classes. The network comprises 41 layers. It processes images with dimensions of (224, 224, 3) and has a total of 138,357,544 parameters.

This section examines the performance metrics of the specified models, focusing on accuracy as the key quality measure for facial recognition. Two models, GoogLeNet and VGG-16 were applied to the student face dataset. On this dataset, GoogLeNet achieved a test accuracy of 90%, while VGG-16 reached 80%.

As training progressed, Figure 3 and Figure 4 show the performance of the GoogLeNet and VGG-16 networks in image label classification, including their accuracy on validation data and training time. GoogLeNet took 6 minutes 39 seconds, while VGG-16 took 37 minutes 28 seconds to complete training.

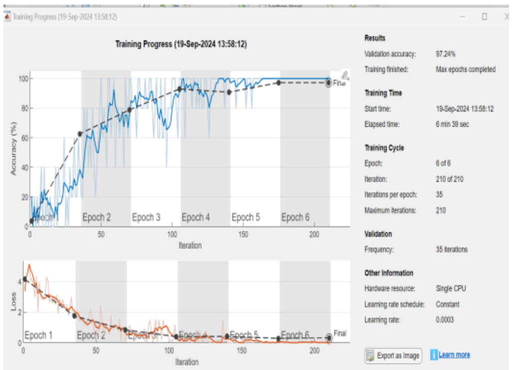

Figure 3. Training Progress for Human Faces Images Recognition using GoogLeNet

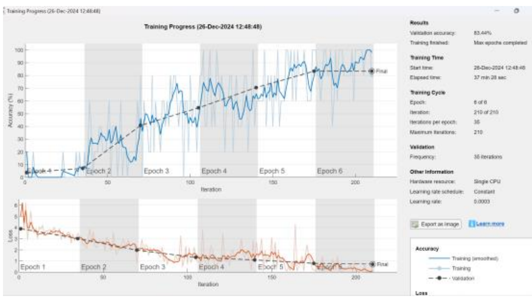

Figure 4. Training Progress for Human Faces Images Recognition using VGG-16

Table 1. Comparison of Validation Accuracy

Model	Validation Accuracy	Time
GoogLeNet	97.24%	6 min 39 sec
VGG-16	83.44%	37 min 28 sec

Table 1 compares the duration and validation accuracies obtained from Figure 3 and Figure 4, which show that GoogLeNet is better than VGG-16 and the validation accuracy.

Figure 5. Predicted Image and Actual Image using Training GoogLeNet Model

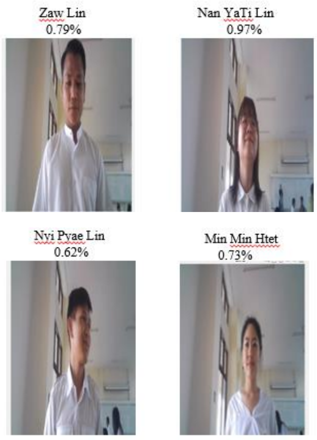

Figure 6. Predicted Image and Actual Image using Training VGG-16 Model

The predicted images and actual images, generated using the trained GoogLeNet and VGG-16 models, are shown in Figure 5 and Figure 6.

Table 2. Comparison of Test Accuracy

No.	**Class Name**	**GoogLeNet Accuracy**	**VGG-16 Accuracy**
1.	Nan Yati Lin	0.99	0.97
2.	Naw Ye Chel Htoo	0.98	0.86
3.	Har Kee Mhan	0.98	error
4.	Nyi Pyae Lin	0.98	0.62
5.	Seng Sant	0.97	0.84
6.	Hein Htet Kyaw	0.99	error
7.	Hnin Yu Hlaing	0.92	0.66
8.	Nan Thet Aung Su	error	0.72
9.	Nan Su Wai Kyaw	0.89	0.48
10.	Min Min Htet	0.97	0.73

$$\text{Accuracy} = \frac{\textit{Number of correct predictions}}{\textit{Total Number of predictions}} \times 100$$

Table 2 presents additional factors that could influence classification accuracy, either positively or negatively.

4. Conclusions

The study concluded that GoogLeNet outperforms VGG-16 in face recognition accuracy. It demonstrated the effectiveness of using modified pre-trained GoogLeNet and VGG-16 models for recognizing human face images. In most validation sessions, GoogLeNet achieved higher training and validation accuracy with lower error rates. The research highlighted that further improvements in deep CNN model classification accuracy are possible. The models, consisting of convolution layers, fully connected layers, and a softmax classification layer, were trained to optimize parameters using face image datasets. Overall, the results indicate that GoogLeNet is a strong candidate for face recognition and can be further enhanced.

Acknowledgements

I am grateful to all people who provide me an opportunity to do this research work. I am deeply indebted to my pupils, for their support throughout the period of work.

References

[1] Anjum D. Wang, H. Yu, D. Wang, and G. Li, "Face recognition system based on CNN," Proc. - 2020 Int. Conf. Comput. Inf. Big Data Appl. CIBDA 2020.

[2] M. Coskun, A. Ucar, O. Yildirim, and Y. Demir, "Face recognition based on convolutional neural network," Proc. Int. Conf. Mod. Electr. Energy Syst. MEES 2017, vol. 2018-Janua, no. January 2018.

[3] E. Winarno, I. H. Al Amin, H. Februariyanti, P. W. Adi, W. Hadikurniawati, and M. T. Anwar, "Attendance System Based on Face Recognition System Using CNN-PCA Method and Real-Time Camera," 2019 2nd Int. Semin. Res. Inf. Technol. Intell. Syst. ISRITI 2019.

[4] Y. Li, Z. Wang, Y. Li, X. Zhao, and H. Huang, "Design of face recognition system based on CNN," J. Phys. Conf. Ser., vol. 1601, no. 5, 2020.

[5] P. Dinkova, P. Georgieva, A. Manolova, and M. Milanova, "Face recognition based on subject

dependent Hidden Markov Models," 2016 IEEE Int. Black Sea Conf. Commun. Networking, BlackSeaCom 2016.

[6] Lufan Li, Zhang Jun, Jiawei Fei and Shuohao Li, "An Incremental Face Recognition System Based on Deep Learning" Fifteenth IAPR International Conference Nagoya University, Nagoya, Japan, May 8-12, 2017.

[7] S. Sharma, A. Kalyanam, and S. Shaik, "Technical Analysis of CNN-Based Face Recognition System—A Study", vol. 711. Springer Singapore, 2019.

[8] S. Sharma, M. Bhatt, and P. Sharma, "Face recognition system using machine learning algorithm," *Proc. 5th Int. Conf. Commun. Electron. Syst. ICCES 2020*.

[9] X. Qu, T. Wei, C. Peng, and P. Du, "A Fast Face Recognition System Based on Deep Learning," Proc. - 2018 11th Int. Symp. Comput. Intell. Des. Isc. 2018, vol. 1.

Journal of Information Technology, Research and Innovation 2024, Vol-4, Issue-2

EFFECT OF REACTION TEMPERATURE AND BILAYER PRODUCING AGENT CONCENTRATION ON OPTICAL AND ELECTROCHEMICAL PROPERTIES OF COLLOIDAL SILVER NANORODS

Kudae Than[1], San Yu Maw[2], and Thaung Hlaing Win[3]

[1,2,3] Department of Physics, Pakokku University
Kudaethan055@gmail.com, sanyumaw2580@gmail.com, thaung.naing001@gmail.com

ABSTRACT

Silver nanostructures are widely proposed in chemical sensing applications. Various types of sensors utilizing them have been developed. Recently, the non-spherical nanoparticles, such as silver nanorods (AgNRs), nanoprisms, nanoporous silver have attracted special attention, becoming a hotspot in the nanoscience. The anisotropic silver nanorods structure displays two surface plasmon bands, corresponding to surface electron oscillation on transverse and longitudinal sides. Advantages and shortcomings of the main techniques for the synthesis are discussed. Approaches to improve silver nanorods (AgNRs) characteristics are also considered. Along with various fields of science, silver nanorods are used in chemical analysis for sensitive determination of nanorods shape in diverse objects. Recent trends in the analytical use of AgNRs and their electrochemical properties are summarized. The synthesized nanorods were characterized by UV-Vis spectrophotometry and Cyclic voltammetry (CV). Basic principles of nanorods formation at different reaction temperature (50ºC, 60ºC, 70ºC) and bilayer producing agents as Cetyltrimethylammonium bromide (CTAB) concentration (1mM up to 5 mM) on optical and electrochemical properties of the AgNRs are pointed out and discussed. Main analytical features of the proposed approaches are represented.

KEYWORDS

absorbance, bilayer producing agent, silver nanorods, distilled water.

1. INTRODUCTION

Nanostructures are widely proposed in chemical sensing applications. Various types of sensors utilizing them have been developed. Recently, the non-spherical nanoparticles, such as silver nanorods (AgNRs), nanoprism, nanoporous gold, have attracted special attention, becoming a hotspot in the nanoscience. The wide use of these anisotropic nanoparticles in chemical analysis is caused by their greater reactivity in comparison to spherical particles. Anisotropic nanoparticles often are less stable turning into spherical particles during an interaction. Thus they show an increased sensitivity to the analytes [1].

Tréguer-Delapierre et al. summarized general information on non-spherical silver nanoparticles, including data on characteristic positions of surface plasmon resonance (SPR) bands for the most common types of nanoparticles. It should be noted that only AgNRs are characterized by two ranges in the spectrum. The transverse SPR band is located at about 520 nm while the position of the longitudinal one varies in a wide range depending on the AgNRs aspect ratio and their size. Such unique interaction of ellipsoids with exterior electromagnetic field and splitting of the SPR mode into two separate modes were predicted by Hans in 1912 and confirmed later by experimental data [2].

The non-spherical geometry of AgNRs opens new prospects for their use in chemical analysis. According to the annual number of Scopus publications with title, abstract or keywords containing information on the AgNRs use for determination/analysis, the application of AgNRs in analytical chemistry has been sufficiently rising over the last 20 years. This means that the topic represents a growing modern trend. Currently AgNRs are becoming a widely used tool in chemical analysis. They are used as enhancers of Raman scattering, colorimetric probes etc. Silver nanorods-based materials can be used in sensing, electrochemistry, catalysis, medicine, optoelectronics, imaging, and materials science [3].

A key feature of AgNRs, as typical non-spherical nanoparticles, is that their analytically important properties (intensities and spectral positions of SPR-bands, aggregative stability, electroconductivity, and redox potential) vary essentially with their physical dimensions. The ease of tuning these properties gradually by changing both particle size and shape makes AgNRs very promising versus traditional analytical reagents. Moreover, the presence of two SPR bands makes it possible to use both these oscillation frequencies for recording the analytical response, enhancing informatively of chemical analysis. For example, two similar approaches to the determination of catecholamines have been reported. One of them utilizes colloidal solutions of AgNRs and the other one – AgNRs-based nanocomposites. Both are based on measuring shifts of different SPR-maxima (the long- and the short-wavelength maximum respectively). In the case of the colloidal solutions, the choice of a proper SPR band helps to improve sensitivity, in case of the nanocomposites – to perform measuring with the use of an ordinary diffuse reflectance spectrophotometer or colorimeter [4].

The right choice of the synthesis technique makes it possible to produce nanocomposites with high content of AgNRs of a certain aggregation state. The assembly may consist of either isolated rods or side-by-side aggregates including percolated network of rods with both side-by-side and end-to-end arrangement. Sometimes alignment of AgNRs inside the nanocomposite can be changed simply by stretching such a material. The combination of nanorods and polymers is the basis for an increasing number of functional polymer nanocomposites. Chemical composition and shape of nanoparticles largely determine physical properties that the particles impart to the polymeric material. This review aims systematization and discussion on preparation and recent trends in the analytical use of both silver nanorods and their electrical chemical properties with different reaction temperature and bipolar producing agent concentrations [5].

2. Experiment

2.1 Synthesis of Silver Nanorods

The conventional chemical reduction method was used to produce the silver nanorods (AgNRs). In this experiment, sodium borodydride and Cetyltrimethylammonium bromide (CTAB) were used to prepare the silver nanorods. $AgNO_3$ of 0.17 g was dissolved in 100 mL of distilled water to make silver nitrate ($AgNO_3$) solution. The $AgNO_3$ solution was agitated at room temperature for 5 min before adding the reducing agents (sodium borohydride). The reaction mixture was then agitated for 4 h. When CTAB was added, the color of the solution immediately changed from colorless to yellowish brown. This color change confirmed AgNRs fabrication. In addition, the effect of reaction temperature (50^o C, 60^o C and 70^o C) and bilayer producing agent (CTAB) on optical and shape of silver nanoparticles were also studied. Figure 1 and 2 shows the Flow chart and preparation steps of the colloidal silver nanorods.

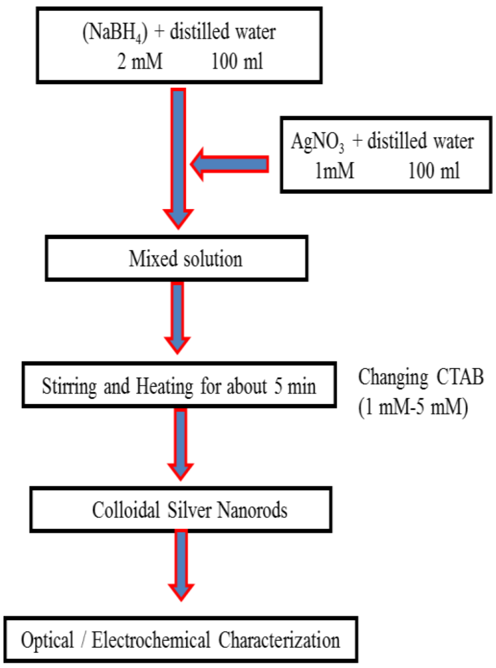

Figure 1. Flow chart of the colloidal silver nanorods

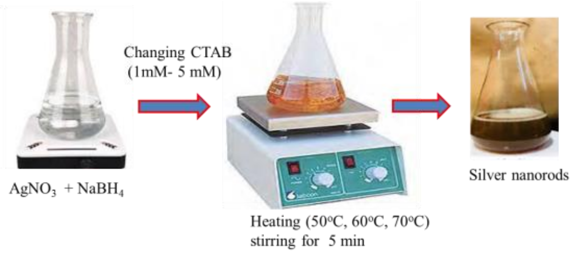

Figure 2. Preparation steps of the colloidal silver nanorods

2.2 Characterization of Silver Nanorods

The characterization methods consist of UV-Vis spectrophotometry, scanning electron microscopy (SEM) and Cyclic Voltammetry (CV).

2.2.1 UV-Vis Spectrophotometry

UV-Vis spectrophotometry was a technique to measure absorbance of the sample in the visible region. The optical absorption spectra of silver nanorods were measured at room temperature using the GENESYS 10S UV-Vis spectrophotometry (Materials Research Lab, Department of Physics, University of Mandalay), Figure 3. The scanning ranges of Ag NRs were recorded from 300 nm to 900 nm.

2.2.2 Scanning Electron Microscopy (SEM)

Silver nanoparticles solution was transferred onto the silicon substrate by a transfer drop casting methods. Ag NRs solution will run over the wafer relatively, producing thin film of Ag NRs. Scanning Electron Microscopy (Agilent 8500 SEM) in Figure 4 is an instrument, which is used to observe the surface morphology and size of Ag NRs at higher magnification, higher resolution and depth of focus compared to an optical microscope. The sizes of the silver nanorods were described by using Image J software from the SEM micrographs.

Figure 3. UV-Vis Spectrophotometry (GENESYS 10S)

Figure 4. Scanning Electron Microscopy (SEM)

3. RESULTS AND DISCUSSION

This section deals with absorption and characterization of natural dyes with different CTAB concentrations.

3.1 Effect of Reaction Temperature on Absorption of Silver Nanorods

Firstly, effect of CTAB concentration on optical absorption of silver nanorod at reaction temperature (50) °C was studied. Figure 5 (a) shows the silver nanorods with different CTAB concentration at reaction temperature (50° C). The optical absorption peak of silver nanorods with different CTAB concentration are evaluated by UV-Vis spectrophotometry. The first peak was observed at (394 nm for 1mM, 405 nm for 2 mM, 416 nm for 3 mM, 421 nm nm for 4mM and 432 nm for 5 mM. The second peaks are observed at 630 nm for 1mM, 648 nm nm for 2mM, 652 nm for 3mM and 640 nm for 4mM and 653 nm for 5mM. Upon increasing CTAB concentration, the optical absorption peak position of silver nanorods was shifted to the longer wavelength regions and the absorption peak intensity slightly decreased [6].

Secondly, effect of CTAB concentration on optical absorption of silver nanorod at reaction temperature (60) °C was studied. Figure 5 (b) shows the silver nanorods with different CTAB concentration at reaction temperature (60° C). The first peak of NRs was observed at (410 nm up 440 nm) with CTAB concentration concentrations (1mM up to 5 mM). The second peaks of NR are observed at (680 nm up to 710 nm) with CTAB concentration (1mM up to 5 mM). Upon increasing CTAB concentration, the optical absorption peak position of silver nanorods was shifted to the longer wavelength regions and the absorption peak intensity slightly decreased.

Thirdly, effect of CTAB concentration on optical absorption of silver nanorod at reaction temperature (70) ºC was studied. Figure 5 (c) shows the silver nanorods with different CTAB concentration at reaction temperature (70º C). The first peak of NRs was observed at (425 nm up 436 nm) with CTAB concentration concentrations (1mM up to 5 mM). The second peaks of NR are observed at (713 nm up to 738 nm) with CTAB concentration (1mM up to 5 mM). Upon increasing CTAB concentration, the optical absorption peak position of silver nanorods was shifted to the longer wavelength regions and the absorption peak intensity slightly decreased. It attributed to the smaller diameter of silver nanorods with CTAB concentration 5 mM.

Figure 6 shows the silver nanorods with optimum concentration of CTAB 1 mM at different reaction temperature. Upon increasing reaction temperature, the optical absorption peak position was shifted to the longer wavelength region. The highest optical absorption peak was observed at reaction temperature 60ºC.

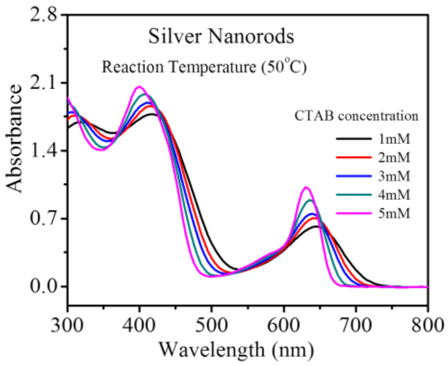

Figure 5 (a). Silver nanorods with different CTAB concentration s at reaction temperature (50º C)

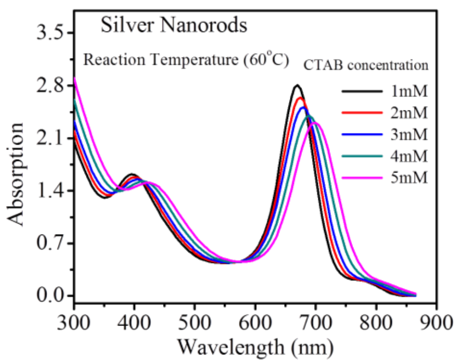

Figure 5 (b). Silver nanorods with different CTAB concentration s at reaction temperature (60º C)

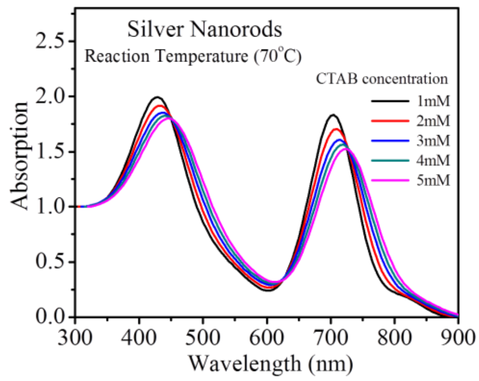

Figure 5 (c). Silver nanorods with different CTAB concentration s at reaction temperature (70º C)

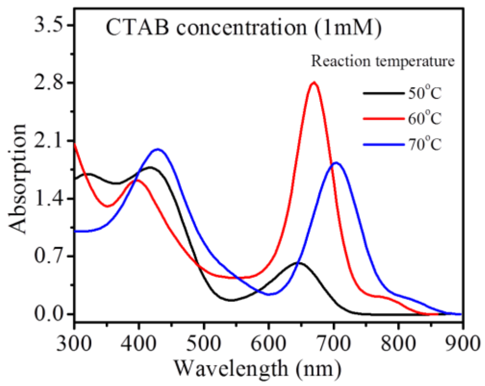

Figure 6. Silver nanorods with optimum concentration of CTAB 1 mM at different reaction temperature

3.2. Size Estimation of Colloidal Silver Nanorods

The colloidal silver nanorods solution was transferred onto the silicon substrates and their size was estimated by using field emission scanning electron microscope (FESEM). First part of this present work, thin films were washed in DI water to remove the excess surfactant and dispersed in PIA solution [7]. After that, this thin film was dipping into the Ag NRs solution and dried in air. The surface features of metal NRs were assembled on Si substrate by FESEM. The size and shape of nanostructures could be observed clearly under Scanning Electron Microscope. Figure 7 (a-c) shows FESEM images of Ag NRs colloids at different reaction temperature. The average diameter of silver nanorods size was observed at ~ 95 nm for the reaction temperature 50ºC, 75 nm for 60ºC and 65 nm for 70ºC. According to the above results that the diameter of silver nanorod size was increased with increasing reaction temperature which agreed well previous UV-Vis results.

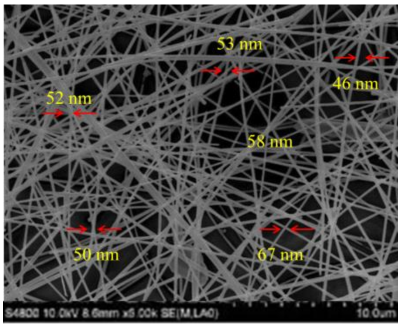

Figure 7 (a). The average size of silver NRs at 50ºC

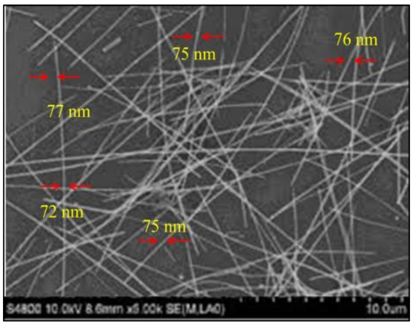

Figure 7(b). The average size of silver NRs at 60ºC

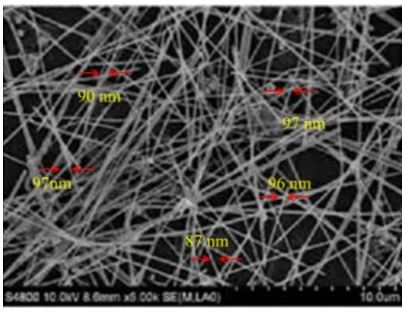

Figure7 (c). The average size of silver NRs at 70ºC,

3.3. Cyclic Voltammograms Measurement of Silver Nanorods

Figure 8 (a) shows the Cyclic Voltammograms measurement of colloidal AgNRs with optimum concentration of CTAB 1 mM at reaction temperature (50º C). In CV measurement with different scan rates from 0.1 mV up to 0.4 mV was also studied. An important use of CV in photovoltaics is the determination of anodic and cathodic peak potential of silver NRs. The results illustrated a linear regression current against the square root of the scan rate, which is a characteristic diffusion-controlled process. The anodic peak current values against the cycle number were plotted for different scan rates in the electrolyte solution. In all CV curves the anodic peak current significantly decreased and blue-shifted from 0.02 up to 0.15 to the shorter wavelength regions. Upon increasing scan rates, cathodic peak current significantly increased and red-shifted to the longer wavelength regions.

Figure 8 (b) shows the Cyclic Voltammograms measurement of colloidal AgNRs with optimum concentration of CTAB 1 mM at reaction temperature (60º C). At reaction temperature (60ºC), Increased of the scan rate, the anodic peak current was decreased and blue-shifted to the shorter wavelength regions. The cathodic peak current was increased and red-shifted to the longer wavelength regions.

Figure 8 (c) shows the Cyclic Voltammograms measurement of colloidal AgNRs with optimum concentration of CTAB 1 mM at reaction temperature (70º C). At reaction temperature (70ºC), Increased of the scan rate, the anodic peak current was decreased and blue-shifted to the shorter wavelength regions. The cathodic peak current was increased and red-shifted to the longer wavelength regions. According to the above results, increased of the scan rate (10-50) mV facilitates the particle formation rate and increased the copper film deposition rate.

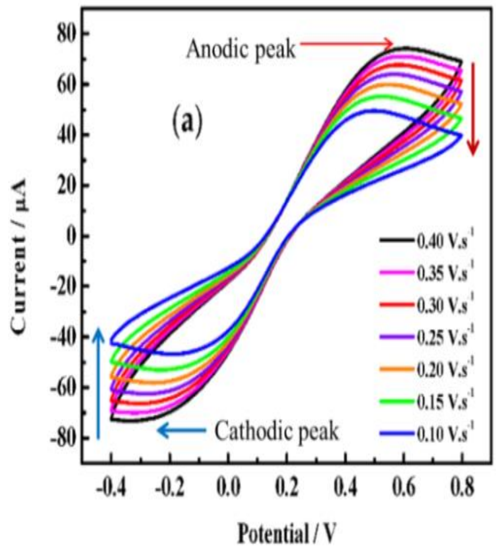

Figure 8 (a) Cyclic Voltammograms measurement of colloidal AgNRs (scan rates 10 mV- 50 mV)

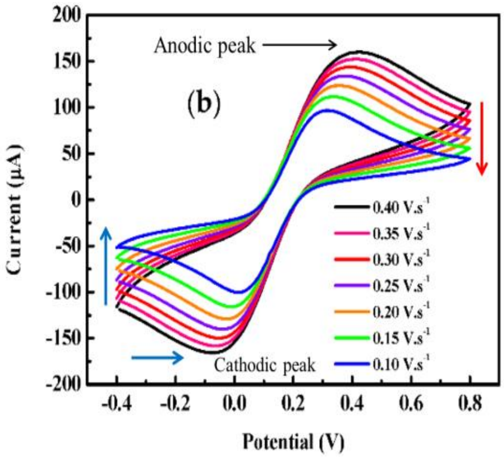

Figure 8 (b) Cyclic Voltammograms measurement of colloidal AgNRs (scan rates 10 mV- 50 mV)

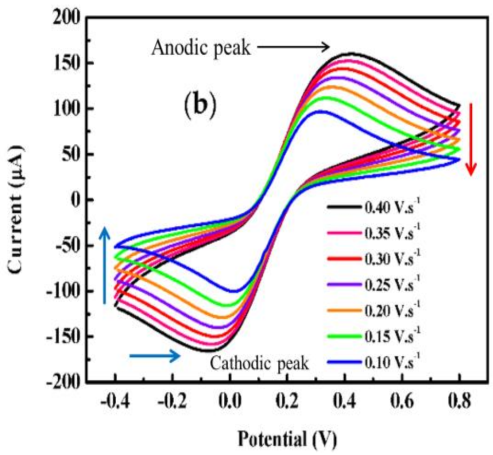

Figure 8(c). Cyclic Voltammograms measurement of colloidal AgNRs (scan rates 10 mV- 50 mV)

4. Conclusion

The colloidal silver nanorods were synthesized by chemical reduction methods. The effect of reaction temperature and bilayer producing agent (CTAB) concentration on optical absorption of silver nanorods were evaluated by UV-Vis Spectrophotometry. The UV-Vis results showed that the two absorption (TSPR and LSPR) peaks was observed. The absorption of TSPR peak at 405 nm, 410 nm, 425 and LSPR peak at 648 nm, 680 nm, 71 nm for reaction temperature (50°C, 60°C, 70°C). Upon increasing bilayer producing agent (CTAB), the optical absorption peak (TSPR, LSPR) was shifted to the longer wavelength regions and peak intensity decreased. The effects of scan rates (10 mV up to 50 mV) on the electrochemical properties of AgNR were also investigated by cyclic voltammograms (CV). In all CV curves, the anodic peak current significantly decreased with increasing scan rate, thus proving the decrease of silver content in the solution as nanorods. The results presented by CV display that the anodic peak current varies linearly with the scan rate and shifted to the potential to more positive values with increasing scan rate. This indicates that these nanorod were conductive while transferring electrons with the electrode surface.

Acknowledgments

Special thanks go to members of Materials Research Lab, Department of Physics, University of Mandalay, for their help in experimental work.

References

[1] G X.W. Guoyun*et al*., 2014. Journal of Nanoscience.

[2] T. Markvart*et al*., 2003. Journal of Apply Physics.

[3] H. Hahn *et al*., 1997.Nanostruct Mater.

[4] D.R. Duran N *et al*., 2012. Synthesis of Silver Nanoparticles.

[5] F.M. Al-Khateeb*et al*., 2018. Apply Physics and Material Science.

[6] A.C. Chan *et al*., 2005. Journal Of Physical Chemistry.

[7] M.L. Almeida *et al., 1983.* Journal of Crystal Growth.

Authors

Biography

First A- Daw Kudae Than
Demonstrator
Department of Physics
Pakokku University

Second B- Daw San Yu Maw
Demonstrator
Department of Physics
Pakokku University

Third C- Dr Thaung Hlaing Win
Lecturer
Department of Physics
Pakokku University

REAL-TIME SIGN LANGUAGE WORD RECOGNITION SYSTEM USING CONVOLUTIONAL NEURAL NETWORK (CNN)

Khaing Khaing Win [1], and Nu Nu Ye[2]
[1,2] Department of Electronic Engineering, Technological University (Taunggyi)[1]
junekhaingkhaing@gmail.com, nunuye.yykz@gmail.com

ABSTRACT

Sign language is a unique language specifically for the deaf, just as spoken languages are for hearing individuals. Myanmar sign language serves as a vital communication tool for the hearing-impaired community in Myanmar. However, there is a lack of technological solutions to bridge the communication gap between sign language users and the general public. This research is converting the 15 different hand gesture of Myanmar sign language to readable English text using computer vision , Convolutional Neural Network (CNN), TensorFlow and Python programming language. In this paper going to capture a real time translation of Myanmar sign language using single and double hand gestures and convert it into text. In this system, OpenCV is used to capture frame from the webcam, which are than processed, passed through the CNN, and the predicts word is displayed in real time. The CNN model was trained for 30 epochs on a dataset containing 15 gesture classes and one blank class. This paper discusses the system's architecture, dataset preparation, model training, and deployment for real-time use.

KEYWORDS

Sign language, TensorFlow, OpenCV, Convolution Neural Network (CNN), Image processing, Python

1. INTRODUCTION

The importance of sign language recognition systems has grown substantially in recent years, especially with the development of deep learning models capable of interpreting gestures. Sign language recognition is an essential area of research for enabling effective communication between the hearing-impaired and non-signing individuals. While research in sign language recognition for globally recognized sign languages has advanced significantly, Myanmar sign language recognition system remains relatively very little research work. This research aims to address communication gap by developing a real-time recognition system using openCV, CNN and python. In Myanmar, two primary Myanmar Sign Languages (MSL) Upper Myanmar and Lower Myanmar are used and this system is used Upper Myanmar Sign Language.

Sign gesture identification can be achieved using two primary approaches. The first approach involves a glove-based method, where the signer wears specialized data gloves to record hand movements. The second approach is vision-based, which is further divided into two categories: static and dynamic signs. Static signs involve a fixed hand shape held in a specific position without any movement. Examples of static signs include letters of the alphabet, numbers and certain basic nouns that remain stationary. In contrast, dynamic signs involve movement, where the hands may change shape, move through space, or rotate as part of the gesture in real time. These are often used for verbs, adjectives, adverbs, and more complex ideas. This system typically relies on computer vision and machine learning techniques, such as Convolutional Neural Networks (CNNs), to classify hand gestures into corresponding sign language words. A Convolutional Neural Network (CNN) is used to extract features from the pre-processed frames. Based on these features, the CNN classifies the gestures into predefined categories.

The remainder of this research is structured as follows: Section 2 provides an overview of the literature study conducted, while Section 3 discusses the sign language dataset. The architecture of the models used is described in Section 4, followed by details on model training in Section 5. Section 6 presents the experimental results, and finally, Section 7 concludes the paper.

2. Related Work

A review of the literature on the problem indicates that various approaches have been taken to address gesture recognition in video using different methods. In [1] Romala Sri Lakshmi Murali, L.D. Ramayya, and V. Anil Santosh explores a computer vision-based approach to bridging the communication gap between signers and non-signers. Utilizing Convolutional Neural Networks (CNNs) for feature extraction and classification, the study demonstrates the effectiveness of deep learning in recognizing and interpreting sign language gestures. The research emphasizes the practical significance of sign language recognition in assisting individuals with speech and hearing impairments. While the methodology appears robust, further details on the dataset, real-world testing, and potential scalability would enhance the paper's practical impact.

Prashant Verma and Khushboo Badli [2] addresses the challenge of real-time recognition of alphanumeric and common gestures in Indian Sign Language (ISL). Leveraging the SSD MobileNet V2 architecture, the study successfully implements a cost-effective, accessible solution for detecting 36 distinct gestures with an accuracy range of 70-80%. The system demonstrates significant potential in enhancing human-computer interaction (HCI) by enabling communication for deaf and hard-of-hearing individuals through real-time gesture detection. However, the model's performance in low-light and uncontrolled backgrounds highlights a need for further optimization and robustness improvements.

The paper by Mrs S Chandragandhi, Aakashrajr, Muhammed [3] proposes an innovative desktop application that translates Indian Sign Language (ISL) gestures into text and speech in real-time using a computer webcam. The integration of a Convolutional Neural Network (CNN) ensures efficient gesture recognition with high accuracy, while the system also facilitates bidirectional translation between speech and sign language. The project's focus on handling both single and double-hand gestures demonstrates a comprehensive approach to gesture recognition.

Similar work by Akhilesh Shukla, Dr. Devesh Katiyar, and Mr. Gaurav Goel [4] proposes a practical solution for real-time recognition of Indian Sign Language (ISL) gestures using a webcam-based system. Utilizing the SSD MobileNet V2 architecture and transfer learning, the model achieves reliable classification of 36 gestures, including alphabets and numerals, with 70-80% accuracy even in low-light and uncontrolled environments. The project emphasizes affordability and accessibility by avoiding expensive sensor-based technologies, making it highly user-friendly.

3. Sign Language Dataset

To train the CNN model, the dataset comprises 6425 images representing 15 distinct classes of basic hand gestures and one black class. These gestures were captured under varying conditions to simulate real-time classroom environments. Images were captured using an HD webcam at resolutions of 1920x1080. Each gesture corresponds to a predefined label such as "book", "drink", "eat", "hello", "help", "i love you", "no", "pencil", "question", "sit", "stand ","stop", "wait", "yes". The dataset is organized into folders, one for each gesture class as shown in Figure 1.

Figure 1. Image Dataset

Each sign was executed twice by the same individual under lighting conditions and different backgrounds. The videos were captured using a webcam and it was processed by converting each video into individual frames. These frames were then trimmed to a maximum of 300 frames per video. The proposed dataset is divided into training (5133 images) and testing (1292 images) subsets and processed for consistency, including resizing and normalization. The training and test images were resized to 48x48 pixels Both training and test images were prepared for multi-class classification using grayscale colour mode and categorical labels.

4. SYSTEM ARCHITECTURE

The flow diagram of the sign language recognition system as shown in Figure 2. This system employs a CNN-based approach for gesture recognition. The system comprises three main components:

Data Acquisition: The system used OpenCV to capture video from the webcam. A fixed Region of Interest (ROI) is defined to standardize the input size for gesture recognition.

Pre-processing: Extracts the region of interest (ROI) from frames and pre-processes the image. The captured ROI is converted to grayscale to reduce computational complexity. The images are resized to 48x48 pixels to match the model's input requirements.

Recognition: Utilizes a pre-trained CNN model to predict the gesture.

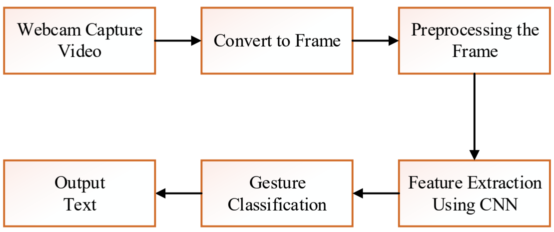

Figure 2. Flow Diagram of the System.

CNN is the type of neural network, commonly used for image recognition. Its architecture includes several convolutional layers, its learns to extract feature from the pre-processed image through multiple convolutional layers. Each convolutional layer detects different aspects of the image, while pooling layers help in reducing the size and improving computational efficiency. After passing through multiple layers, the image shrinks in size due to max pooling, making it easier for the network to process while retaining critical details. The final layer of the CNN uses the softmax activation function to classify the image into one of the predefined gesture categories.

The system uses a 2D CNN with TensorFlow, where each image is processed using a 3×3 filter. The convolution layer applies a 3×3 filter over the image, computing the dot product of pixel values and filter weights to extract essential features. This step extracts key features from the input image for further processing. By applying a 2×2 max pooling layer, the system reduces the dimensions of feature maps while keeping the most significant values. ReLU ensures that negative pixel values are converted to zero, allowing the network to focus on essential positive features for better learning. A dropout rate of 0.4 is used to prevent the model from memorizing patterns in the training data, improving overall performance on unseen data. After extracting features, the network flattens the 2D feature maps into a 1D vector, preparing them for classification. To improve learning efficiency, the model uses the Adam optimizer, which adjusts the learning rate dynamically, and categorical cross-entropy to measure classification performance.

5. MODEL TRAINING

The necessary libraries are imported, and the CNN architectures are selected for image detection tasks during the training process. The training of the Convolutional Neural Network (CNN) model is conducted using TensorFlow and Python. Training parameters are carefully optimized to ensure the model's effectiveness. The model is trained for 30 epochs with a batch size of 128 on Jupyter Notebook, and the training process is shown in Figure 3.

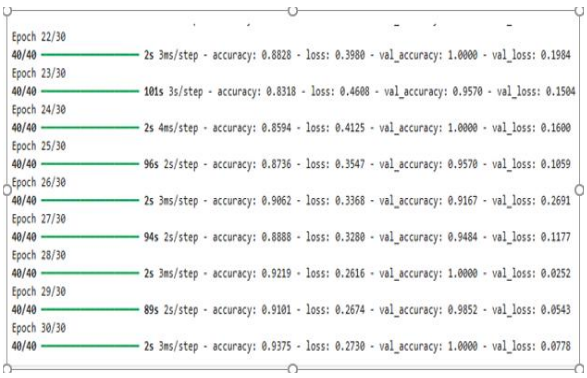

Figure 3. Model Training for 30 Epochs

During training, a gradual reduction in loss and an improvement in accuracy are observed, indicating that the model has successfully learned the features of the dataset. By the end of training, the CNN has been fine-tuned to classify the gestures with high accuracy under various conditions. The training accuracy increases steadily as the epochs progress, showing that the model is learning the training data well. The validation accuracy also increases but stabilizes near the later epochs, indicating the model generalizes well as shown in Figure 4. The training loss decreases consistently, reflecting the model's improved ability to minimize errors on the training data. The validation loss also decreases but stabilizes in the later epochs, showing reduced error on the validation dataset as shown in Figure 5.

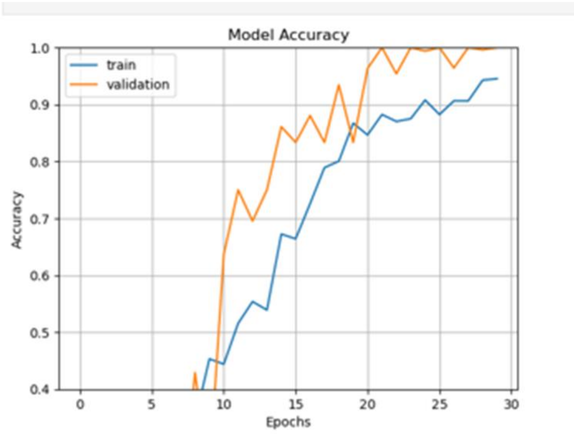

Figure 4. Training and Validation Accuracy for 30 Epochs

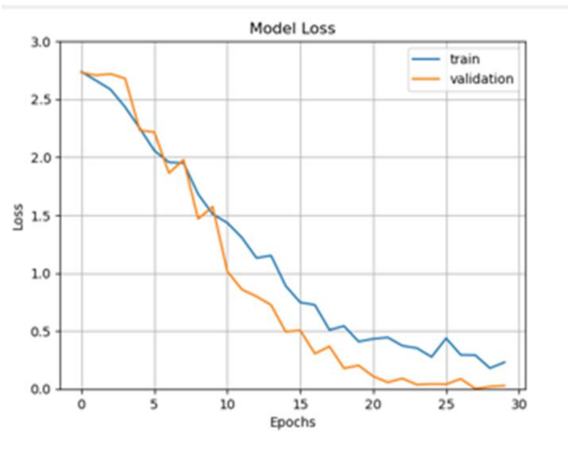

Figure 5. Training and Validation Loss of 30 Epochs

6. Real Time Test And Results

Real-time testing is conducted using the trained model. The system successfully recognizes gestures, however accuracy is affected by variations in lighting, background noise, and individual differences in performing gestures. The output text results (eg; "book," “drink, "yes," and "stand.") are displayed on the monitor with its accuracy percentage as shown in Figure 6, Figure 7, Figure 8 and Figure 9.

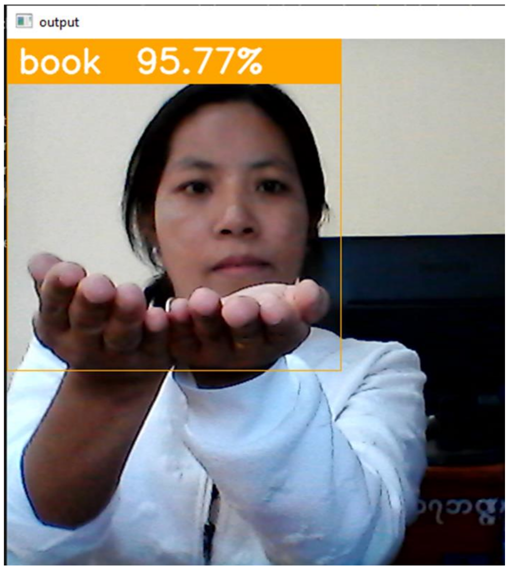

Figure 6. Detection Result of ‘book’ in Real-time

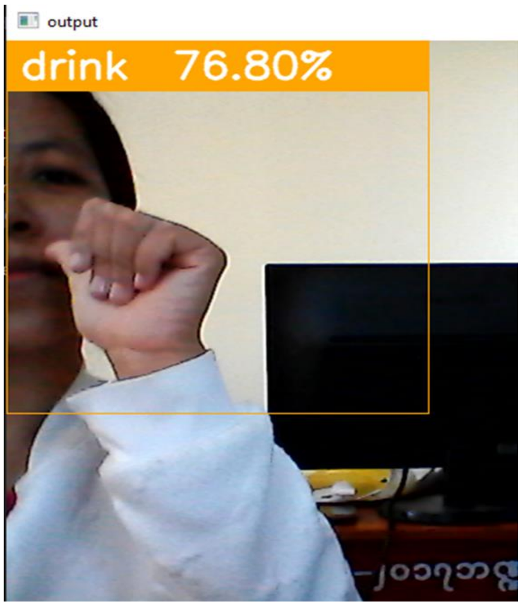

Figure 7. Detection Result of ‘drink’ in Real-time

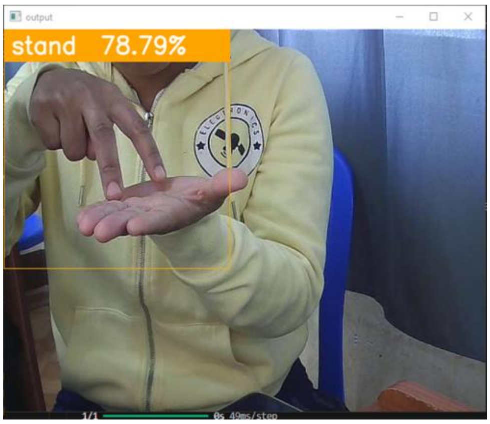

Figure 8. Detection Result of 'stand' in Real-time

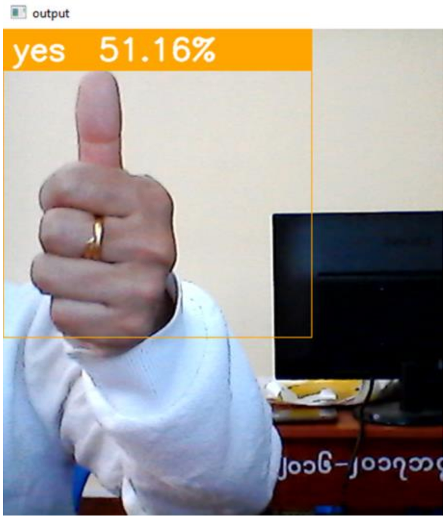

Figure 9. Detection result of 'yes' in real-time

Table 1. Training Results in Different Training Sessions

Training Times	**Training Accuracy (%)**	**Training Loss(%)**	**Validation Accuracy (%)**	**Validation Loss(%)**
First Training	0.8888	0.3280	0.9484	0.1177
Second Training	0.9219	0.2616	1.0000	0.0252
Third Training	0.9062	0.3368	0.9167	0.2691
Fourth Training	0.9101	0.2674	0.9852	0.0543
Fifth Training	0.9376	0.2730	1.0000	0.0778
Average	0.9129	0.4543	0.9700	0.1088

The training and validation accuracy/loss obtained after training the CNN model are shown in Table 1. The average values after the fifth training session were calculated using the following equation:

$$Average = \frac{\text{Total number of values}}{sum\ of\ all\ values}$$

$$Average = \frac{4.5646}{5} \times 100\%$$

$$= 91.29\ \%$$

Table 2. Real-time Results and Accuracy

Class	Real-Time Result within 20 seconds		Accuracy (%)
	True Result	False Result	
Book	27	3	90%
Drink	21	9	70%
Stand	23	7	76%
Yes	19	11	63%

The accuracy of sample classes for real- time testing are shown in Table 2. The accuracy percentage of the system for each sample image gesture, obtained after real-time testing, is calculated using the equation below;

$$\text{Accuracy} = \frac{\text{number of correct predictions}}{total\ number\ of\ predictions} \times 100\%$$

$$\text{Accuracy} = \frac{27}{30} \times 100\%$$

$$= 90\%$$

7. Conclusions

This paper presented a Myanmar sign language word recognition system using a CNN model. The system demonstrates the potential of deep learning for recognizing sign language gestures in real time. In this thesis, its training and validation accuracy/loss are evaluated in recognition sign language gestures for five times. The average training accuracy is 91.29 % and average validation accuracy is 97.00%. Despite its limitations, the proposed approach is a significant step toward bridging communication gaps for the hearing-impaired community in Myanmar.

8. Future Work

The complete system, including the webcam, Raspberry Pi 3, and monitor, will be tested. The dataset will be enhanced by including more classes and a variety of diverse conditions. The CNN architecture will be optimized to achieve improved accuracy and processing speed.

Acknowledgements

Firstly, I would like to special thanks to all people who provide me to do this research. I am deeply grateful to all my teachers for their support and invaluable guidance through the period of this research work.

References

[1] Romala Sri Lakshmi Murali "Sign Language Recognition System Using Convolutional Neural Network And Computer Vision", International Journal of Engineering Innovations in Advanced Technology ISSN: 2582-1431 (Online), Volume-4 Issue-4, December 2022.

[2] Prashant Verma and Khushboo Badli "Real-Time Sign Language Detection using TensorFlow, OpenCV and Python"International Journal for Research in Applied Science & Engineering Technology (IJRASET), Volume 10 Issue V May 2022.

[3] MrsS Chandragandhi, Aakashrajr, Muhammed Shamil Ml,Akhil s, Prabhashankarpt, "Real-Time Translation of Sign Language to Speech and Text". International Advanced Research Journal in Science, Engineering and Technology. Vol 8, Issue 4, April 2021.

[4] Akhilesh Shukla, Dr. Devesh Katiyar, and Mr. Gaurav Goel"Real-Time Sign Language Detector" International Research Journal of Engineering and Technology (IRJET), Volume 09, Issue 08, Aug 2022.

[5] Adithya V, Rajesh R., "A Deep Convolutional Neutral Network Approach for Static Hand Gesture"Third International Conference on Computing and Network Communications (CoCoNet'19) ,2020.

[6] Priyunka Mekala,Ying Gao,Jeffrey Fan, Asad Davari, "Real-Time Sign Language Recognition based on Neural Network Architecture", IEEE, 2011.

[7] Abhinav Yadav,Yash Saini,Yatharth Goswami,Abhash Chauhan and Mr.Md.Shahid, "Action Recognition System for Sign Language Using Tensorflow & OpenCV", Tuijin Jishu/Journal of Propulsion Technology.ISSN: 1001-4055. Vol.45 No.2(2024).

[8] Ni Htwe Aung, Su Su Maung,Ye Kyaw Thu "Sign Language Recognition for Myanmar Number Using Three Different SVM Classifiers", NCSE 2019,27th-28th June 2019, Yangon.

OPTICAL PROPERTIES OF NATURAL DYES EXTRACTED FROM RHINACANTHUS NASUTUS LEAVES FOR DYE-SENTIZIED SOLAR CELLS

Chit Myo Naing[1], and Zan Mo Mo Aung[2]

[1] Department of Engineering Physics, Myanmar Aerospace Engineering University
[2] Faculty of Computer Science, University of Computer Studies, Mandalay
chitmyonaing1992@gmail.com, zanmomoaung@ucsm.edu.mm

ABSTRACT

With fossil fuels becoming scarce due to rising energy demand and the environmental impact of the toxins they emit, scientists are under immense pressure to find alternative energy sources. To address these issues, innovative technologies have been developed to reduce the impact of excessive carbon emissions. Among these advancements is the creation of dye-sensitized solar cells (DSSCs), which utilize natural pigments from plants to convert solar energy into electricity. Natural dye extracted from Rhinacanthus nasutus leaves were fabricated and measured its light absorbing behavior using UV-Vis spectrophotometer. In addition to optical band gap energy value of dye solution was adjusted by adding ethanol and methanol with different temperature and difference values of pH. Then the absorption characteristic was investigated. It was found that the best absorption intensity of Rhinacanthus nasutus leaves at 60˚C in ethanol and at room temperature in methanol. The pH level of Rhinacanthus nasutus leaves dye was formed to be 6.8 in ethanol and 5.6 in methanol. The maximum absorbance between the wavelength 470 nm and 670 nm can be found.

KEYWORDS

Rhinacanthus nasutus leaves, ethanol and methanol, Natural dye, UV-Vis spectrophotometer, pH meter

1. INTRODUCTION

The modern age is the age of science and technology. The development of solar-powered lighting products has also become important in technological experiments. The world's energy consumption is continuously increasing this creates a heavy demand for renewable energy sources to be developed. The largest challenge for our global society is to find ways to replay the supplies by renewable resources and, at the same time, avoid negative effects from the current energy system on climate, environment, and health. The worldwide power consumption is expected to double in the next three decades because of the increase in world population and the rising demand of energy in the developing countries [1].

There are various types of solar cells that convert sun light into electrical energy. Dyes are classified into organic (natural dye) and inorganic dye. The commercially available solar cells are currently based on inorganic silicon semiconductors. Organic solar cells appear to be a highly promising and cost-effective alternative for the photovoltaic energy sector.

In this context, dry sensitized solar cells (DSSCs) have attracted considerable attention in recent year [2]. The DSSC is a device for the conversion of visible light into electricity, based on the sensitization of wide band gap semiconductors [3]. The performance of the cell mainly depends on a dye as sensitizer [4]. Natural products are also being tested for their ability to absorb light. Therefore, the absorption of light from natural resources was measured. In many technologies, DSSCs are being developed and tested by a wide range of natural resources. The natural dynes can be easily found in the flowers, leaves fruit and roots. DSSCs are one of the most promising devices for the solar energy conversion due to their low production cost and low environmental impact. Natural dyes can be extracted from various plants, fruits, flowers, and leaves [11].

2. Background Theory of DSSC

DSSC is a photo electrochemical solar cell using the electrolyte medium to transport electron charge. DSSC does not require materials with high purity and easy to obtain, so the production cost is relatively inexpensive. DSSCs consist of an electrode with a porous layer of a nanocrystalline wide band gap semiconductor. A counter electrode for instance platinized conductive glass. The working principle of the device is based on light absorption in the dye anchored to the TiO_2nanoparticles, followed by transfer of the resulting photoelectron from the excited level of the dye into the conduction band of TiO_2, and through the electrode into the external circuit. The electrolyte facilitates the transport of the electron and the regeneration of the sensitizer, through reduction of the triiodide ion at the counter electrode, followed by oxidation of the iodide ion at the dye [3]. The process of light absorption and separation of electric charge on the DSSC occur separately [5]. The property of DSSC is that the device can be designed by appropriate choice of the sensitizer to absorb and quantitatively convert incident photons to electric current. The absorption spectra of dye sensitizer and the anchorage of the dye to TiO_2 are the main factors that determine the performance of the cell. The dye is very simple functionally: it must only satisfy a few key requirements. The first of these is that it must absorb radiation across a broad visible spectrum. The second is that it must be small enough to enter the pores in the nanoporous semiconductor lattice. The third is that once inside the lattice, it must be able to chelate to the TiO_2 [6].

The dyes used in DSSC can be divided into two categories: metal-based complexes and metal-free organic dyes (including natural organic dye and synthetically organic dye) [7]. Several metal complexes and organic dyes have been synthesized and widely used as sensitizers because they have better efficiency and high durability. However, these advantages are offset by their high cost and their complicate synthetic routes [5].

The natural pigments can be extracted from plant parts like leaves, flowers or fruits. Dye from the organic material is very interesting to develop because of the abundant natural [8]. Important characteristics of a dye material that is capable of absorbing a broad spectrum of light and match the energy band of semiconductor materials are used. Natural dye compounds generally contain anthocyanin and chlorophyll which have been extensively investigated as sensitizers for DSSCs. Although the natural dyes have weak absorption and poor adsorption to TiO_2 scaffold, the absorption and adsorption properties of dyes can be improved by adjusting the pH, temperature and various solvents [9].

In this paper, the effect of optical properties with the different various temperatures, the effect of pH on light-absorbing behavior, and the optical band gap energies of natural dyes extracted from local Rhinacanthus nasutus leaves were investigated. It is very useful for dye sensitized solar cells.

2.1. Ultraviolet-visible (UV-Vis) Spectrophotometer

UV-Vis spectrophotometer is an analytical instrument used to quantitatively measure the transmission or reflection of visible light, UV light or infrared light. The spectrophotometer measures intensity as a function of light source wavelength. Spectrophotometers are widely used in various disciplines such as physics, molecular biology, chemistry and biochemistry.

The GENESYS 10S Vis spectrophotometer is used to measured light absorbance across the ultraviolet and visible ranges of the electromagnetic spectrum. A UV-Vis, a beam with a wavelength varying between 180 nm and 1100 nm passed through a solution in a cuvette. The sample in the cuvette absorbs this visible radiation. For each wavelength of light passing through the spectrophotometer, the intensity of the light passing through the sample cell is measured. The amount of light that is absorbed by the solution depends on the concentration, the path length of the light through the cuvette and the light absorbs at a certain wavelength. A UV-Vis, measures the intensity of light transmitted through a sample compared to references measured of the incident light source.

The important term for this spectrophotometer is absorbance, $A = -\log 10T = -\log 10(I/I_0)$, where T is transmittance, A is absorbance, I is the intensity emerging on the other side and $I_0$is the intensity of light entering the sample. The output of a spectrophotometer is a spectrum (usually). A spectrum is a graph displaying either value for transmitted, absorbed, or reflected light (Y axis) vs. various lights wavelength value (X axis) [10]. A schematic representation of the as-prepared UV-Vis spectrophotometer is displayed in Figure 1.

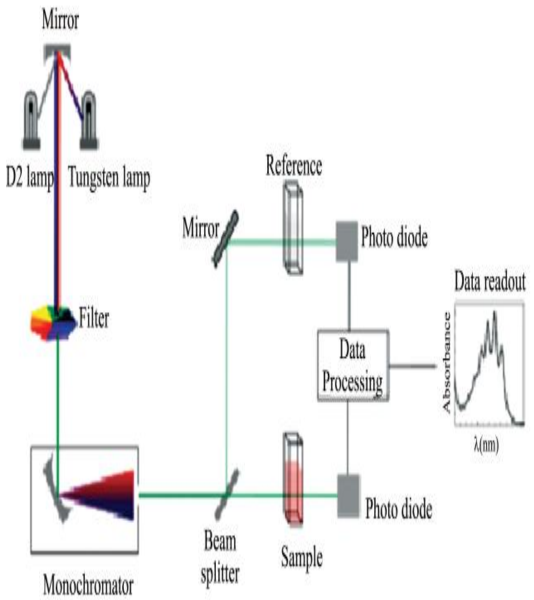

Figure 1. Schematic of UV- Visible Spectrophotometer

3. DATA ANALYSIS

In the present work, dye from Rhinacanthus nasutus leaves (chlorophyll pigment) was extracted and the optical properties of natural dye solutions were analyzed. Firstly, natural dye solutions was extracted by using different solvents. UV-vis spectrophotometry and band gap energy was used as characterization and measurement for the extracted dye solution.

3.1. Rhinacanthus nasutus Leaves

DSSCs were prepared using natural dye extracted from Rhinacanthus nasutus leaves which used as sensitizer. Rhinacanthus nasutusleaves-based dye has been selected due to its widely available in local area. The scientific name for Rhinacanthus nasutus (Rn), commonly referred to as snake jasmine because to the shape of its blossom in Figure 2 and 3.

Figure 2. Rhinacanthus nasutus leaves with Fruits

Figure 3. Rhinacanthus nasutus Tree

3.2. Preparation of Natural Dye-Sensitized Solutions

The collected Rhinacanthus nasutus leaves were thoroughly washed with water to remove the adhering particles and dust from the surface. The leaves were then dried in an oven at 60·Cand finely powdered. The extraction of Rhinacanthus nasutus leaves dye solution is shown in Figure. 4.

A mass of 2 g of the powdered Rhinacanthus nasutus leaves was weighed and mixed with 100 ml solvent (ethanol or methanol) and dissolved for 30 min at different temperatures (60°C and 45°C) respectively. To prevent the dye from light exposure for later use, the extracted were then place in FTO glass as Figure 5.

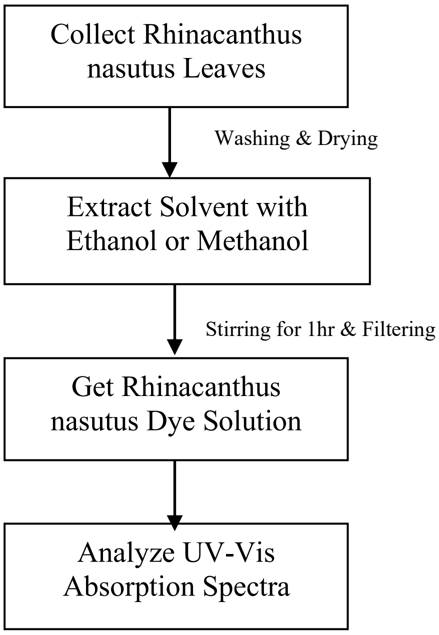

Figure 4. Flow Chart of Extraction and Characterization for Rhinacanthus nasutus Leaves Dye solution

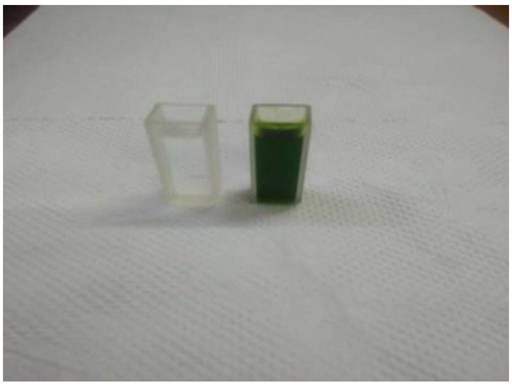

Figure 5. Rhinacanthus nasutus Leaves Dye Solution

3.3. Optical Properties of Dye Solution

The optical properties of natural dyes from Rhinacanthus nasutus leaves was determined using UV-Vis spectrophotometer method. UV-Vis spectroscopy alludes to ingestion spectroscopy or reflectance spectroscopy in the bright noticeable ghostly locale. This present man's that it utilizes light in the noticeable and adjoining (close UV and close infrared ranges). The retention or reflectance in the noticeable range straightforwardly influences the apparent shade of the synthetic compounds included. The absorption spectra of dry solutions were recorded using GENESYS 10S UV-Vis spectrophotometer. The photo electrochemical measurements of the cell were performer using a computer controlled. These experiments were conducted at the Material Science Laboratory, University of Mandalay.

To measure the optical properties of natural dyes, UV-Vis absorption spectrophotometer (GENESYS 10S) is used in this study, as shown in Figure 6.

Figure 6. UV-Vis Absorption Spectrophotometer (GENESYS 10S)

Figure 7. Measurement of pH on Rhinacanthus nasutus Leaves Dye Solution

The ability of leaf dyes for DSSCs to absorb light and transport electrons is greatly impacted by their pH level, which has a direct impact on the solar cell's overall efficiency, as described in Figure 7.

3.4. Change Measurement of UV-Vis Spectrophotometer

Optical characterization of Dye solutions had been characterized by UV-Vis spectrophotometer. Dyes extracts from Rhinacanthus nasutus leaves had been optically characterized by measuring their absorbance on an UV-1600 spectrophotometer. Light source is Tungsten & Deuterium providing the wavelength range of 190-1100 nm. Single beam optical system provides to measure the absorption properties of dye solution in photometric mode. Wavelength accuracy is ± 5 nm and resolution is ± 1 nm. To get accurate absorbance valves of the sample, base line scan was taken using the reference solution (ethanol in our case). UV-Vis absorption spectroscopy determines in the ultraviolet-visible spectral region. The absorption or reflectance in the visible range directly affects the perceived color of the chemicals involved.

A light emission structure a noticeable as well as UV light source (red color) was isolated into its part wavelength by a crystal or diffraction grinding. Each monochromatic bar as part into two equivalent intensity radiates by a half, reflected gadget. One bar, the example shaft, went through a little straightforward holder containing an answer of the compound being concentrated in a straight forward solvent. The filtered rage was from 300nm to 700nm. The pattern estimation was made with the reference test for arrangement, ethanol and for thin film.

4. RESULTS AND DISCUSSION

4.1. Effect of the Temperature on the Absorbance of Leaves

Figure 8 and Figure 9 show the absorption spectra of temperature-controlled dye solutions extracted from Rhinacanthus nasutus leaves. The maximum absorbance of Rhinacanthus nasutus leaves extracts at different temperature was examined by UV-Vis spectrophotometer in a wavelength range of 400-800 nm. It was found that Figure 8 exhibits the absorption spectra of Rhinacanthus nasutusleaves extracts at different temperatures (RT with 29˚C, 45˚C and 60˚C) in ethanol.

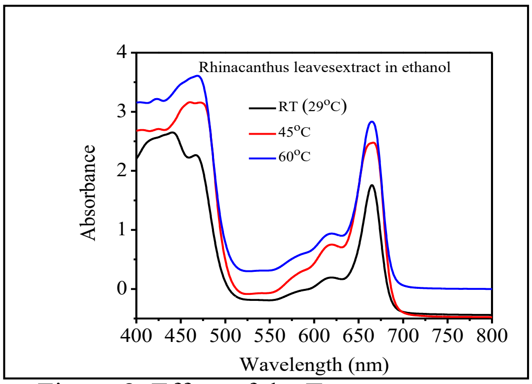

Figure 8. Effect of the Temperature on Absorbance in Ethanol

The absorption spectra of Rhinacanthus nasutus leaf extracts at RT, 45˚C, and 60˚C in ethanol were discovered to be displayed in Figure 8. It is clearly seen that the λ_{max} was almost the same but the absorption intensity of Rhinacanthus nasutusleaves extracts increases with increasing temperature (highest absorption intensity at 60˚C). It may be due to the better solubility [8]. Figure 9 shows the absorption spectra of Rhinacanthus nasutusleaves extracts at different temperatures (RT with 29˚C , 45˚C and 60˚C) in methanol. It was found that the absorption spectrum of Rhinacanthus nasutusleaves extracts was room temperature in methanol.

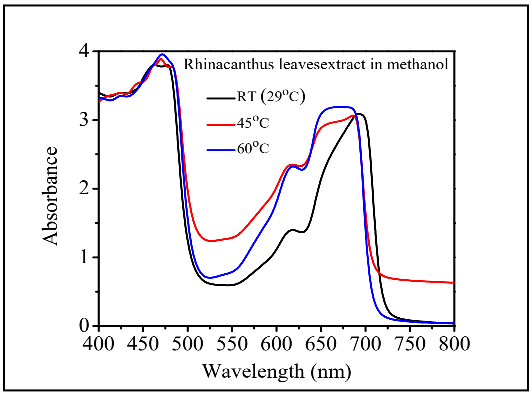

Figure 9. Effect of the temperature on absorbance in methanol

Table 1 shows that the band gap energy in ethanol (60°C) and methanol (45°C). In Table 1, the value of energy is 2.04 eV in ethanol (60°C) and 2.365 eV in methanol (45°C) by the wavelength was taken into account in Figure 8 and Figure 9. Therefore, the value of the band gap is smaller. Due to smaller value of the band gap, the maximum absorption behaviour was achieved.

Table 1. The band gap energy in ethanol (60°C) and methanol (45°C)

Chemical Name	Absorption Wavelength (A°)	Band Gap Energy (eV) $E_g= hc/\lambda$
Ethanol (60°C)	6050	2.04
Methanol (45°C)	5220	2.365

4.2. Effect of pH on the Absorption of Natural Dye Solutions

By including the sodium hydroxide (NaOH) and hydrochloric corrosive (HCl), the pH of common color arrangement was balanced expanding pH by NaOH while diminishing pH by HCl, the pH of natural dye solution was adjusted increasing pH by NaOH while decreasing pH by HCl.

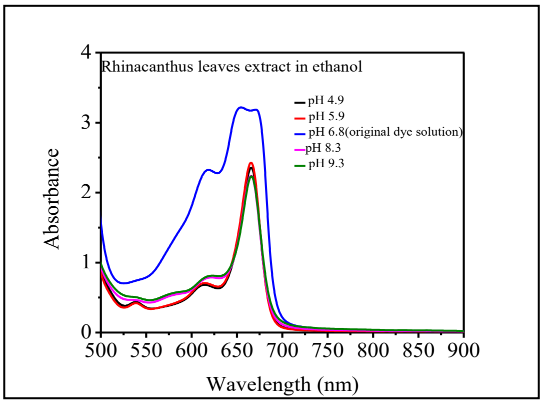

Figure 10. Effect of the pH on the Absorbance in Ethanol

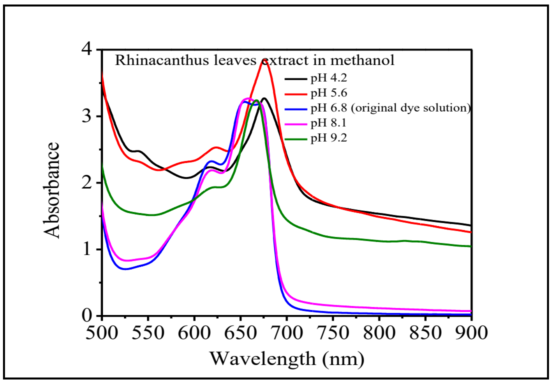

Figure11. Effect of the pH on the absorbance in Methanol

Figure 10 shows the absorption spectra of pH controlled dyes solutions extracted from Rhinacanthus nasutus leaves in ethanol. In ethanol, the original pH of Rhinacanthus nasutus leaves dye was formed to be 6.8. The absorption intensity was found to decrease with decreasing pH. Because the amine groups that exist in the compound of Rhinacanthus nasutus leaves can disturb the dye molecules to form hydrogen bonding [11].

Moreover, Figure 11 displays the absorption spectra of pH controlled dyes solutions extracted from Rhinacanthus nasutus leaves in methanol. In methanol, the original pH of dye solution was obtained to be 5.6. In more acidic condition, the peak intensity also decreased in methanol.

4.3 Characteristic Peak of Dye Solution

Basically, the absorption peaks are due to anthocyanin, chrolophyll obtained in Rhinacanthus nasutusleaves at room temperature, 45ºC and 60ºC. A natural dye solution was extracted from Rhinacanthus nasutusleaves at room temperature, 45ºC and 60ºC.The characteristic peak of dye solution at 60ºC ethanol and 29ºC in methanol, the absorption maximum wavelength are 470 nm and 660 nm the photo-response had been investigated. In ethanol, the absorption maximum is 650 nm with different values of pH the photo-response had been investigated. In methanol, it was seen that the absorption maximum is 670 nm with different values of pH the photo-response.

5. CONCLUSIONS

In this work, natural dyes extracted from the locally available plants such as Rhinacanthus nasutus leaves were used as sensitizers for DSSC. These natural dyes used as a light harvesting material were extracted using different solvents at different acid concentrations. The comparisons of different acid concentrations as an extracting solvent and its effect on the absorption spectra were investigated. In order to conduct, varying the solvents, temperature and pH would modulate the absorption properties of dyes. It was found that the best absorption intensity of Rhinacanthus nasutusleaves at 60˚C in ethanol and at room temperature (29ºC) in methanol. The higher absorption intensity is obtained at higher extracting temperature in ethanol. And then, the level of pH was 6.5 in ethanol and 5.6 in methanol. The absorption intensity decreases in more acidic solution (lower pH level). Therefore, ethanol is better than methanol for solubility of dye. It was concluded that, the optical properties using UV-Vis spectrophotometer showed that the extract Rhinacanthus nasutus leaves can be used as a dye-sensitizer in DSSC, because it has a wider absorption spectrum. The maximum absorbance is obtained at a wavelength 470 nm and 670 nm. Due to smaller value of the band gap, the maximum absorption behavior was achieved. The higher the absorbance dye solutions, the more efficiency of incoming intensity of sunlight. The higher the efficiency, the more energy our system can produce. Therefore, the maximum absorption behavior plays a crucial role.

ACKNOWLEDGEMENTS

The author would like to acknowledge the Myanmar Aerospace Engineering University's ERC committee for granting permission to submit this paper.

REFERENCES

[1] Lewis, Nathan S. "Toward cost-effective solar energy use." science 315.5813 (2007): 798-801.

[2] MGrätzel,"Photoelectrochemical cells," *Nature*, vol. 414, no. 6861, pp. 338–344, Nov. 2001, doi: https://doi.org/10.1038/35104607.

[3] M. Grätzel, "Conversion of sunlight to electric power by nanocrystalline dye-sensitized solar cells," *Journal of Photochemistry and Photobiology A: Chemistry*, vol. 164, no. 1–3, pp. 3–14, Jun. 2004, doi: https://doi.org/10.1016/j.jphotochem.2004.02.023.

[4] K. Tennakone, G.R.R.A. Kumara, A.R. Kumarasinghe, P.M. Sirimanne, and K.G.U. Wijayantha, "Efficient photosensitization of nanocrystalline TiO2 films by tannins and related phenolic substances," *Journal of Photochemistry and Photobiology A Chemistry*, vol. 94, no. 2–3, pp. 217–220, Mar. 1996, doi: https://doi.org/10.1016/1010-6030(95)04222-9..

[5] K. Tsunoda, E. Ohashi, and S. Adachi, "Spectroscopic characterization of naturally and chemically oxidized silicon surfaces," *Journal of Applied Physics*, vol. 94, no. 9, pp. 5613–5616, Oct. 2003, doi: https://doi.org/10.1063/1.1613792.

[6] A. Islam *et al.*, "Dye Sensitization of Nanocrystalline Titanium Dioxide with Square Planar Platinum(II) Diimine Dithiolate Complexes," vol. 40, no. 21, pp. 5371–5380, Sep. 2001, doi: https://doi.org/10.1021/ic010391y.

[7] L. ZHANG, P. LI, Z. GONG, and A. A. Oni, "Photochemical behavior of benzo[a]pyrene on soil surfaces under UV light irradiation," *Journal of Environmental Sciences*, vol. 18, no. 6, pp. 1226–1232, Nov. 2006, doi: https://doi.org/10.1016/s1001-0742(06)60067-3.

[8] Okoye, I. F., I. O. Alaekwe, and O. Abba. "Uv-vis spectrophotometer analysis of film grown using natural dye from lawsonia inermis (henna plant)." *Nigerian Journal of Physics* 30.2 (2021): 135-139.

[9] M. Hosseinnezhad, R. Jafari, and K. Gharanjig, "Characterization of a green and environmentally friendly sensitizer for a low cost dye-sensitized solar cell," *Opto-Electronics Review*, vol. 25, no. 2, pp. 93–98, Jun. 2017, doi: https://doi.org/10.1016/j.opelre.2017.04.007.

[10] Thein, N. K. K., Htet, A., & Aye, T. T. *Optical Properties of Natural Dye from Strawberry Fruits as Photosensitizer for Dye-Sensitized Solar Cells Application* (Doctoral dissertation, MERAL Portal).

Authors

Biography

Chit Myo Naing received the M.Sc. degree in Physics from Banmaw University in 2016. Moreover, he also obtained D.C.Sc. degree from Computer University, Banmaw. He is also a lecturer with the Department of Engineering Physics, Myanmar Aerospace Engineering University (MAEU). His research interests include in embedded systems, machine learning, artificial intelligence, and security.

Zan Mo Mo Aung received the Ph.D. degree in Information Technology from the University of Computer Studies, Mandalay (UCSM) in 2025. She is also a lecturer and is currently with the Faculty of Computer Science at UCSM. Her research interests include in natural language processing, machine learning, artificial intelligence, and computer networking.

A COMPARATIVE ANALYSIS OF DIFFERENT FEATURE EXTRACTION TECHNIQUES FOR URINARY CALCULI PARAMETERS USING 3D CT IMAGES

Lai Yee Myint[1]

[1] Department of Information Technology Engineering, Technological University (Toungoo)
leiyee2013@gmail.com

ABSTRACT

Urinary calculi disease is one of the leading causes of death throughout the world. CT (computed tomography) imaging is widely used for kidney disease diagnosis. The most common cause of diagnosis is the diagnostics using precise and fast algorithm. Feature extraction is one of the key technologies to improve the overall accuracy and the performance of the urinary calculi classification. Although feature extraction using vast number of features provides high diagnosis accuracy; it can be time consuming. Moreover, some irrelevant features are also decrease the classification accuracy. Therefore, one of the main factors is to find out the most relevant and effective features that yields maximum classification accuracy. This paper provides a comparison of six feature extraction techniques based on 3D matrix such as geometric feature, shape feature, first order statistical feature, 3D GLCM, 3D GLRLM and 3D GLSZM. Moreover, new region-based features are also introduced based on HU variation, namely average HU in core region and core-periphery HU variation. This study evaluates the performance of the proposed techniques under random forest (RF) classifier. The purpose of this study is to show the relevant feature extraction techniques for urinary calculi classification from CT imaging. Experimental analysis and validation are conducted on digitized transverse abdomen CT images from 75 patients with urinary calculi cases from No_2, Defense Services General Hospital, Yangon, Myanmar. From the experimental results, geometric feature extraction including two new features can provide greatest performances with 94.38% in accuracy, 97.2% in sensitivity and 85.84% in specificity among six proposed techniques.

KEYWORDS

3D Feature Extraction, Geometric Feature, Shape Feature, First Order Statistical Feature, 3D GLCM, 3D GLRLM and 3D GLSZM

1. INTRODUCTION

Increasing incidence and prevalence of urinary calculi is a growing concern throughout the world. According to the survey in 2009, there were approximately 1.3 million people of cases of urinary calculi disease in the United States [1]. Moreover, over the last 40 years from 1974 to 2010, the prevalence rate of urinary calculi disease in US was increased from 3.8 % to 8.8 % [2]. This problems lead to a high demand of detection, treatment, and prevention of urinary calculi disease. Nowadays, CT imaging becomes an initial evaluation to predict the condition of urinary calculi. Nevertheless, urinary calculi diagnosis on CT imaging demands the experts because of including multiple abdominal organs, bones and unexpected disturbances (calcification and stents). Moreover, calcification, stents, and bone fragments (segmentation error) have a huge variation in size, shape, position and gray level intensities [3][4]. To eliminate those disturbances, extracting the discriminative properties of features plays a crucial role for urinary calculi diagnosis. Feature extraction is an important process in medical image classification. By converting the input image into a set of image features, it can represent the content of images as perfectly as possible. And, analyzing the properties of these extracted features and organizing the numerical features into classes are crucial in feature extraction [5]. The performance of the classification depends mainly on the properties of the relevant features. To save the execution time with precise results, many feature extraction methods are being widely used. This study is conducted to review and examine six feature extraction methods and their properties for urinary calculi classification.

2. Review of Literature

In recent times, a number of feature extraction techniques have been proposed to build up the powerful and consistent urinary calculi diagnosis system on CT imaging. This study utilized MSER feature, texture (mean, standard deviation, local binary pattern-64 dimensions, histogram of oriented gradients-124 dimensions) and shape feature (volume, two aspect ratios, the distance between candidate and kidney boundary) under support vector machine classifier for renal calculi detection on CT image. The experiments validated that the proposed method could generate the good performance with 90% accuracy when considering only large and more clinically appropriate renal calculi [6]. Detection urinary calculi in renal CT image was performed by using 58 patch-based texture features and two context features under support vector machine classifier. This study supported urinary calculi detection with 99.63% specificity and 64.92% PPV (Positive predictive value). And, ROI segmentation using intensity and location threshold could segment the urinary calculi with 98.91% sensitivity, 98.96% specificity [7]. After segmentation of kidney region with hybrid Level Set method, a fully automated classification technique was introduced by using 64 features vector under RUSBoost classifier with decision trees learners. The proposed features could provide the various properties such as values and spatial neighborhood information, edge and region type information, orientation information. The empirical result indicated that the proposed scheme produced the good result with 92.1% accuracy [8]. This paper carried out urinary calculi prediction under neural networks classifier with GLCM (22 feature parameters). The image enhancement techniques (image padding and advanced filtering techniques) and manual segmentation were also used to provide the classification process. The classification accuracy revealed with the performance information such as Epoch1 (0.075151), gradient (decrease), mu value (decrease) and validation checks (steadily increase up to 6 at the 7th epoch) [9]. Each feature extraction technique has its strengths and limitation. The performance of image classification varies depend on the feature extraction techniques under different classifiers. From the best of our knowledge, there is a trade-off between the classification performance and the used number of features [6] [7] [8] [9]. Therefore, this study is concerned with the comparative study of six well-known feature extraction techniques in order to obtain the most relevant features for urinary calculi classification.

3. Techniques of Feature Extraction

This section describes six difference kinds of feature extraction techniques in 3D urinary calculi classification. A total of 47 features are grouped into six categories according to different information they provide [10][11] as shown in Figure 1:

3.1. Geometric Feature

Geometric feature is one of the important features that are extracted by using geometrical properties (such as sizes, concentration and positions) of the urinary calculi objects in the images. In this paper, three common features, two modified features and two proposed hybrid features are introduced as below.

3.1.1. Volume

Volume of the 3D object is estimated by multiplying the number of voxels with

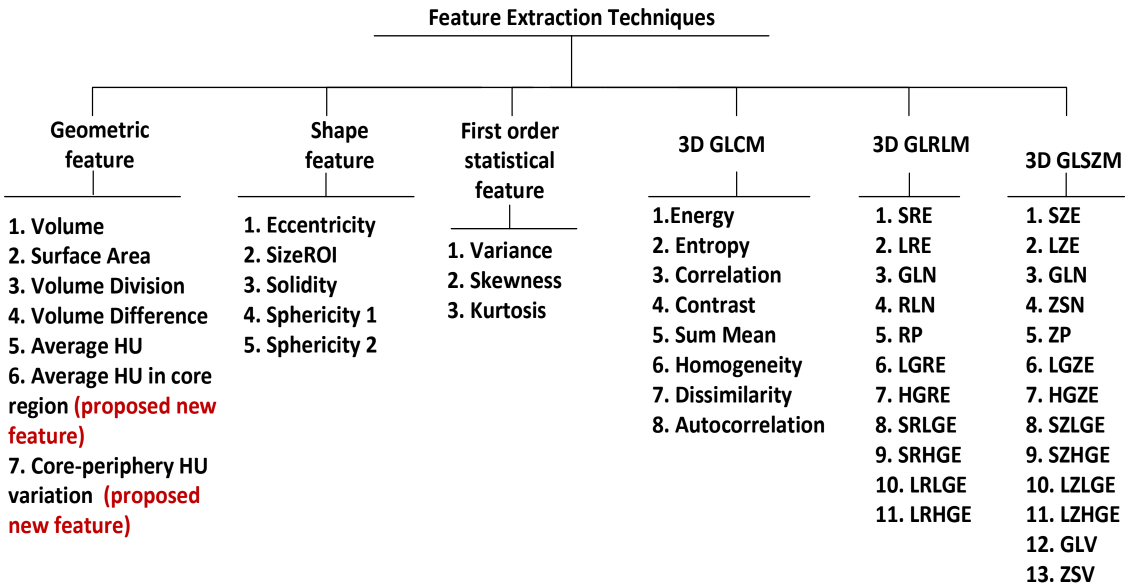

Figure 1. Six Different Categories of Feature Extraction Techniques

voxel resolution. In here, area of object is specified by counting the number of voxels in the specific object [12].

Volume(V) of Object = Area of Object × Resolution of Voxel (1)

3.1.2. Surface Area

Surface area of object is calculated by using 3D binary structure and image resolution that is a 1-by-3 vector consisting resolution in the X, Y and Z direction. This formula can be proved by theoretical formula of surface area of sphere ($4\pi r^2$) in [13].

$$SA = \sqrt{(x - res_x)^2 + (y - res_y)^2 + (z - res_z)^2} \quad (2)$$

Here, SA denotes surface area of stone, whereas res_x, res_y and res_z relates to resolution of voxel in the X, Y and Z direction. Moreover, x, y and z are the coordinate points of the selected voxel.

3.1.3. Average Hounsfield Units

CT imaging gives the information of tissue attenuation with Hounsfield Unit (HU) which can represent the intensity value of each voxel [14]. Average HU of each object is calculated in (3) as follow:

$$HU_{avg} = \sum_{i=1}^{n} \mu_i \Big/ n \quad (3)$$

Here, HU_{avg} is average HU for each object, n is the number of voxels in an object. μ is the HU value of each voxel in an object.

3.1.4. Volume Ratio (VR)

When most of urinary calculi are non-smooth and irregular objective, volume of stone is different with volume of sphere with the same area [15]. Based on this property, volume ratio (VR) is modified in this study, as formulated in (4).

$$VR\ (Volume\ Ratio) = V_{sph} \Big/ V_{obj} \quad (4)$$

Here, V_{obj} is the volume of the test object (by equation (1)) and V_{sph} is the volume of sphere with the same area of the test object. The formula of V_{sph} is mathematically formulated in (5) referring to [16].

$$Volume\ of\ sphere: V = \sqrt{(SA)^3 \Big/ 36\pi} \quad (5)$$

3.1.5. Volume Difference

Volume difference is another geometric feature as defined in (6).

$$Volume\ Difference = V_{obj} - V_{sph} \quad (6)$$

Here, V_{obj} is volume of a test object (the selected stone) and V_{sph} is volume of a sphere with the same surface area as test object.

3.1.6. Proposed New Features

The internal structure of the stone is consisting of the alternate concentric layers [17]. Mostly, the concentration of core region is higher than that of peripheral regions of the stone [18]. The HU value of the stone outer layer can different with that of the stone inner layer. Therefore, the following two modified features are evaluated to compare the composition of the outer and inner layers of the stone.

3.1.7. Average HU in core region (HU_{core})

Firstly, the estimated core region of an object is created by using Morphological erosion with structuring element size changed adaptively based on diameter object size [19]. Using Euclidean distance transform [20], the longest diameter of an object is developed as the following algorithm 1. After estimating the longest distance of an object, the morphological kernel size is calculated by taking 80% of longest distance. And then, the border region of an object eliminated by morphological erosion. According to this procedure, the core region is extracted from an object.

Finally, the average HU value of the core region (HU_{core}) is calculated by using (3).

Algorithm 1: Estimation of size of longest distance

Step 1. Set all pixel coordinates (x, y, z) to $(r_x, r_y, r_z) = x * res_x, y * res_y, z * res_z$
Step 2. Initiate $L_{max} = 0$
Step 3. For i in range 2 to N, and N is the number of points
 For j in range 2 to N
  For k in range 2 to N

$$d_i = \sqrt{(x_i - x_{i-1})^2 + (y_j - y_{j-1})^2 + (z_k - z_{k-1})^2} \tag{7}$$

   If $d_i > L_{max}$, then $L_{max} = d_i$
   End
 End
Step 4. Solution=L_{max}

3.1.8. Core-periphery variation in Houns -field Units (HU_{var})

Another proposed feature extraction is core-periphery variation (HU_{var}) which is formulated as follows:

$$HU_{var} = HU_{whole} - HU_{core} \tag{8}$$

where HU_{var}, HU_{core} and HU_{whole} are core-periphery variation in HU value, average HU in core region and average HU in whole object.

3.2. Shape eature

Nowadays, shape features become more attention in solving medical imaging problems because of their support, the main visual cues for diagnosis and treatment process [21]. In this study, four common shape features in [22] and one modified feature include as follows:

3.2.1. Eccentricity

It is the ratio of the maximum length of object to the minimum length of object that is perpendicular to the maximum length.

$$Eccentricity = \frac{Major\ axis\ of\ the\ 3D\ object}{Minor\ axis\ of\ the\ 3D\ object} \tag{9}$$

3.2.2. Size of ROI

The size of object is the longest distance of an object which can be measured by using the algorithm 1.

3.2.3. Solidity

The solidity is the pixels in the convex hull (H) divided by the area of the shape region (A_s).

$$Solidity = {}^{A_s}/_{H} \tag{10}$$

3.2.4. Sphericity 1

It is a measure of the roundness of the object that is relative to a sphere. Using volume of object (in equation (1)) and surface area of object (in equation (2)), it can compute as follows.

$$Sphericity = \sqrt[3]{36 \times \pi \times V^2} / A \tag{11}$$

3.2.5. Sphericity 2

In this study, a modified shape feature is calculated by comparing the surface area of test particle and that of standard sphere. It is the ratio of the surface area of a sphere $A_s$with the same volume such as test particle, and the surface area of a test particle A_p (in equation (2)).

$$Solidity = {A_s}/{A_p} \tag{12}$$

3.3. First Order Statistical Feature

The proposed study uses the common statistical features: variance, skewness and kurtosis described in [11]. In the statistical feature extraction, texture of image is statistically calculated from an individual pixel without considering the relationship with neighbor pixel.

3.4. 3D Gray Level Co-occurrence Matrix (3D GLCM)

Volumetric textures obtained from 3D GLCM are useful to investigate the distribution characteristics of each organ in the input CT image. To analyze texture feature values and to facilitate urinary calculi classification, the proposed study uses the eight common 3D GLCM features: Energy, Entropy, Correlation, Contrast, Sum Mean, Homogeneity, Dissimilarity and Autocorrelation [23] [24].

3.5. 3D Gray-Level Run-Length Matrix (3D GLRLM)

3D GLRLM gives the size of homogeneous texture that runs for each gray level. The proposed study also uses the eleven common 3D GLRLM features presented in [25] [26]. They are Short Emphasis (SRE), Long Run Emphasis (LRE), Gray-Level Non-uniformity (GLN), Run-Length Non-uniformity (RLN), Run Percentage (RP), Low Gray-Level Run Emphasis (LGRE), High Gray-Level Run Emphasis (HGRE), Short Run Low Gray-Level Emphasis (SRLGE), Short Run High Gray-Level Emphasis (SRHGE), Long Run Low Gray-Level Emphasis (LRLGE), Long Run High Gray-Level Emphasis (LRHGE), namely.

3.5. 3D GLSZM (Gray-Level Size Zone Matrix)

3D GLSZM measures and judges gray level zones from an image. The number of neighbors (connected voxels) that share in the same gray level intensity is defined as a gray level zone.

This study employs the thirteen 3D GLSZM features presented in [11]. These 13 features are Small Zone Emphasis (SZE), Large Zone Emphasis (LZE), Gray-Level Non-uniformity (GLN), Zone-Size Non-uniformity (ZSN), Zone Percentage (ZP), Low Gray-Level Zone Emphasis (LGZE), High Gray-Level Zone Emphasis (HGZE), Small Zone Low Gray-Level Emphasis (SZLGE), Small Zone High Gray-Level Emphasis (SZHGE), Large Zone Low Gray-Level Emphasis (LZLGE), Large Zone High Gray-Level Emphasis (LZHGE), Gray-Level Variance (GLV), and Zone-Size Variance (ZSV).

4. Performance Evaluation

4.1. Data Acquisition

All the experiments are conducted on the collection of CT images for urinary calculi disease from No_2, Defense Services General Hospital, Yangon, Myanmar. Using this dataset, the pre-processing scheme (segmentation) proposed in [27] can segment the selected objects (stone and non-stone). All segmented objects (stone and non-stone) from 75 patient dataset are used for the performance analysis. In this study, six kinds of feature extraction methods are proposed to extract the stone among the selected objects.

4.2. Performance Comparison across Five Classifiers

To evaluate and analyze the result, the performance of five different classifiers have been adopted to achieve the highest possible performance with suitable execution time. The results are conducted in term of accuracy, sensitivity and specificity [28]. The performance of each classifier is evaluated by using total 47 feature parameters for each object (stone or non-stone). The validation of the performance among the five classifiers is summarized in Table 1.

According to this comparative result, RF can support the best performance with classification accuracy of 94.84 %, sensitivity of 97.67 %, specificity of 80.97 % and execution time of 1.06 s. Therefore, RF is selected as the best predictor for urinary calculi classification.

4.3. Experimental Results of Six Feature Extraction Techniques

With the number of features, the performance (accuracy, sensitivity and specificity) of six feature extraction techniques is compared to evaluate the optimal feature extraction techniques. The performance of each feature extraction technique is evaluated through RF classifier for urinary calculi classification as shown in Table 2.

Table 1. Performance Evaluations of RF, SVM, NB, DT and K-NN Classifiers

Classifier	Accuracy (%)	Sensitivity (%)	Specificity (%)	Execution time (second)
RF (Random Forest)	94.84	97.67	80.97	1.06
SVM (Support Vector Machine)	94.65	97.84	78.18	1.5
NB (Naïve Bayes)	85.53	83.49	91.89	0.03
DT (Decision Tree)	92.95	95.26	82.82	0.23
K-NN (K-Nearest Neighbors)	92.3	94.95	78.42	1.03

Table 2. Performance Comparison of Six Types of Feature Extraction Techniques

Feature Extraction Method	Number of Features	Accuracy (%)	Sensitivity (%)	Specificity (%)
Geometric Feature	7	94.38	97.2	85.84
Shape Feature	5	91.95	96.75	43.35
First Order Statistical Feature	3	90.8	96.95	65.60
3D GLCM	8	92.7	96.23	81.04
3D GLRLM	11	91.09	95.38	76.29
3D GLSZM	13	92.3	95.7	78.66
Total Features	47	94.84	97.67	80.97

Result of this comparative analysis, geometric feature extraction can achieve the highest performance among all proposed methods. It can support the accuracy of 94.38 % and the sensitivity of 97.2 % which is almost the same with the performance of feature extraction model using total 47 features. Moreover, the specificity of geometric feature (85.84%) is higher than not only five proposed methods but also the feature extraction using whole feature set.

4.4. Time Comparison Analysis

This subsection presents a comparison of the computational costs of the six feature extraction techniques. Typical simulation costs have been generated based on the proposed data set consisting of 75 patients. Average execution time of each feature extraction techniques is presented in figure 2.

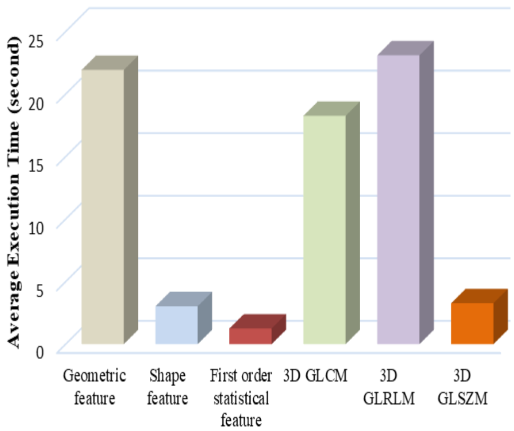

Figure 2. Time Comparison of Six Types of Feature Extraction Techniques

In the experiments, feature extraction using all 47 features is taken over 70 second in average. While comparing execution time of each feature extraction group, shape feature (3.03s), first order statistical feature (1.25 s) and 3D GLSZM (3.27 s) are executed significantly faster than geometric feature (21.92 s), 3D GLCM (18.25 s) and 3D GLRLM (23.09 s). Generally, the execution time is depended on the number of features that used for feature extraction. Although 3D GLRLM execution applied only 11 features, its average execution time is longer than 3D GLSZM that used 13 features. According this analysis, the execution time depends on not only number of features but also its computation complexity. Therefore, it is important to find out the most relevant features from all available features.

4.5. Performance Evaluation of Proposed New Modified Features

In this section, a performance comparison is evaluated by comparing the classification results between with and without the proposed novel and modified features. For this analysis, the proposed feature selection is performed on two dataset using geometric features with and without two modified features as shown in Table 3.

Table 3. Performance Comparison Results of Geometric Feature Extraction Methods without and with Two Modified Features

Feature Extraction Method	Accuracy (%)	Sensitivity (%)	Specificity (%)
Geometric Feature without two modified features	90.17	91.41	88.83
Geometric Feature with two modified features	94.38	97.2	85.84

The resulting experiments clearly indicate that two proposed features can improve the accuracy and sensitivity of conventional geometric features up to 4% and 6%, respectively. It can valid that the proposed two modified features are effective and efficient in urinary calculi classification by providing high prediction performance.

4.6. Statistical Analysis of Feature Weighting

In this section, all available features are ranked based on the weighted value in order to identify the most relevant features. The weighted value of each feature is calculated using four methods: weight by gain ratio, weight by information gain, weight by Gini index and weight by accuracy. In table 4, top 15 most ranked features (among all proposed 47 features) are summarized in descending order.

The features with higher weight are considered more relevant features for the perdition. According to the results of the experiment, all features in geometric feature extraction are the most relevant feature among all proposed features. Because four feature weighting methods result the geometric feature with high weighted levels such as Average HU (Rank 1 in all methods), Volume Difference (Rank 2 in three methods & 10 in other), Average HU in core region (Rank 3 in all methods), Core-periphery HU variation (Rank 4 in three methods & 5 in other), Volume Division (Rank 8 in two methods, 9 & 12 in others) and Volume (Rank 4 in three methods & 7 in other). Therefore, it can identify that the geometric features are the most optimal features from all available features for urinary calculi classification.

Table 4. The Rank of Feature Parameter in Geometric Features

Weight By Gain Ratio	**Weight By Information Gain**	**Weight By Gini Index**	**Weight By Accuracy**	**Rank**
Average HU	Average HU	Average HU	Average HU	1
Volume Difference	Volume Difference	Volume Difference	Homogeneity	2
Average HU in core region	Average HU in core region	Average HU in core region	Average HU in core region	3
Volume	Core-periphery HU variation	Core-periphery HU variation	Core-periphery HU variation	4
Core-periphery HU variation	Homogeneity	Homogeneity	Contrast	5
Homogeneity	LZLGE	LZLGE	Kurtosis	6
solidity	Volume	Volume	Volume	7
SZE	Volume Division	Volume Division	LRLGE	8
Volume Division	SZE	SZE	LRHGE	9
LZLGE	solidity	LGZE	Volume Difference	10
Contrast	LGZE	solidity	SZE	11
LRLGE	Surface Area	LRLGE	Volume Division	12
Kurtosis	Contrast	Surface Area	Correlation	13
LGZE	LRLGE	Contrast	LZLGE	14
Surface Area	Entropy	Dissimilarity	solidity	15

5. CONCLUSION

In this paper, a comparative analysis of urinary calculi classification models was presented by six different feature extraction techniques. Classification performance of each technique was evaluated using RF classifier. The experiments were also conducted in term of three kinds of classification accuracy rate: accuracy, sensitivity and specificity.

The results showed that geometric feature could provide higher classification accuracy comparing to other five methods. Although the accuracy and sensitivity of geometric feature were slightly less than the model using the whole features, it could distinctly reduce the number of features from 47 features up to 7 features. Together with less number of features, it could save about 70% of execution time compare with the model using all 47 features.

Most of the textural features based on voxel-by-voxel variation were impossible to support the stones and non-stone distinguishing because they had similar behavior (vary in size, shape, location and intensity values. Therefore, the proposed two features were developed based on region-by-region variation. According to the alternate concentric layers of urinary calculi, the proposed new methods were more robust and effective than the other selected textural features. When the weighted value of each feature was identified by using the feature weighting methods, the two proposed features (average HU in core region feature and Core-periphery HU variation feature) were ranked at the top 5 positions of the correlated features. And, other geometric features could also achieve the feature with the highest weighted values. The experimental results confirmed that geometric features extractions including two proposed features are very precise and efficient method for urinary calculi classification.

ACKNOWLEDGEMENTS

The author sincerely thanks to the doctors from No_2, Defense Services General Hospital in Yangon, Myanmar, for their effort, time and explanations about the calculi, and for providing the CT images including information to develop the proposed system.

The author would also like to express her heartfelt thanks to her parents for their encouragement throughout this time.

REFERENCES

[1] G. Foster, C. Stocks, and M. S. Borofsky, "Emergency Department Visits and Hospital Admissions for Kidney Stone Disease, 2009: Statistical Brief #139," *Healthc. Cost Util. Proj. Stat. Briefs*, vol. 56, no. 3, pp. 1–10, 2006.

[2] M. S. C. Morgan and M. S. Pearle, "Medical Management of Renal Stones," *Bmj*, vol. 2005, p. i52, 2016.

[3] H. J. Lee *et al.*, "Differentiation of Urinary Stone and Vascular Calcifications on Non-Contrast CT Images," *J. Digit. Imaging*, vol. 23, no. 3, pp. 268–276, 2010.

[4] R. Ray, R. Mahapatra, P. Mondal, and D. Pal, "Long-term Complications of JJ Stent and Its Management: A 5 Years Review," *Urol. Ann.*, vol. 7, no. 1, p. 41, 2015.

[5] "Extraction and Dimensionality Reduction of Features for Renal Calculi Detection and Artifact Differentiation from Segmented Ultrasound Kidney Images," in *International conference on computing for sustainable global development (INDIACom)*, 2016, pp. 3087–3092.

[6] J. Liu, S. Wang, E. B. Turkbey, M. G. Linguraru, J. Yao, and R. M. Summers, "Computer-aided Detection of Renal Calculi from Noncontrast CT Images using TV-flow and MSER Features.," *Med. Phys.*, vol. 42, no. 1, pp. 144–153, 2015.

[7] H. S. Lee, H. Hong, and J. Kim, "Detection and Segmentation of Small Renal Masses in Contrast-Enhanced Ct Images Using Texture and Context Feature Classification," in *2017 IEEE 14 th International Symposium on Biomedical Imaging*, 2017, pp. 583–586.

[8] A. Skalski, "Kidney Tumor Segmentation and Detection on Computed Tomography Data," *2016 IEEE Int. Conf. Imaging Syst. Tech.*, pp. 238–242, 2016.

[9] G. Sumana and P. G. A. Babu, "Prediction of Nephrolithiasis Based on Extracted Features of CT-Scan Images using Artificial Neural Networks," *Int. J. Adv. Res. Comput. Sci.*, vol. 8, no. 5, pp. 1700–1708, 2017.

[10] N. Khan, A. Adnan, and S. Basar, "Geometric Feature Extraction from Urdu Ligatures," in *International Conference on Recent Advances in Telecommunications, Informatics and Educational Technologies,* pp. 229–236.

[11] J. J. M. van Griethuysen *et al.*, "Computational Radiomics System to Decode the Radiographic Phenotype," *Cancer Res.*, vol. 77, no. 21, pp. e104–e107, 2017.

[12] X. Duan *et al.*, "Kidney Stone Volume Estimation from Computerized Tomography Images Using a Model Based Method of Correcting for the Point Spread Function," *J. Urol.*, vol. 188, no. 3, pp. 989–995, 2012.

[13] D. Legland, K. Kiêu, and M.-F. Devaux, "Computation of Minkowski Measures on 2D and 3D Binary Images," *Image Anal. Stereol.*, vol. 26, no. 2, p. 83, 2011.

[14] C. Celenk and P. Celenk, "Bone Density Measurement Using Computed Tomography," *INTECH*, 2012.

[15] A. H. Afaj and M. a. Sultan, "Mineralogical Composition of the Urinary Stones from Different Provinces in Iraq," *Sci. World J.*, vol. 5, pp. 24–38, 2005.

[16] N. Thein, "Automated False Positive Reduction and Feature Extraction of Kidney Stone Object in 3D CT Images," *Int. J. Intell. Eng. Syst.*, vol. 12, no. 2, pp. 62–73, 2019.

[17] J. Cloutier, L. Villa, O. Traxer, and M. Daudon, "Kidney stone analysis: 'Give me your stone, I will tell you who you are!,'" *World J. Urol.*, vol. 33, no. 2, pp. 157–169, 2014.

[18] V. K. Singh and P. K. Rai, "Kidney Stone Analysis Techniques and The Role of Major and Trace Elements on Their Pathogenesis: A Review," *Biophys. Rev.*, vol. 6, no. 3–4, pp. 291–310, 2014.

[19] R. Nurfauzi, H. A. Nugroho, I. Ardiyanto, and E. L. Frannita, "Autocorrection of Lung Boundary on 3D CT Lung Cancer Images," *J. King Saud Univ. - Comput. Inf. Sci.*, 2019.

[20] R. Nurfauzi, H. A. Nugroho, and I. Ardiyanto, "Lung Detection using Adaptive Border Correction," in *2017 3rd International Conference on Science and Technology - Computer (ICST)*, 2017, pp. 57–60.

[21] A. Jalalian, S. Mashohor, R. Mahmud, B. Karasfi, M. I. B. Saripan, and A. R. B. Ramli, "Foundation and Methodologies in Computer-aided

Diagnosis Systems for Breast Cancer Detection," *EXCLI J.*, vol. 16, pp. 113–137, 2017.

[22] M. N. Muhammad, D. S. Raicu, J. D. Furst, and E. Varutbangkul, "Texture Versus Shape Analysis for Lung Nodule Similarity in Computed Tomography Studies," *Int. Soc. Opt. Eng.*, vol. 6919, no. March, 2008.

[23] O. Boonsiri, K. Washiya, K. Aoki, and H. Nagahashi, "3D Gray Level Co-Occurrence Matrix Based Classification of Favor Benign and Borderline Types in Follicular Neoplasm Images," no. March, pp. 51–56, 2016.

[24] T.-Y. Kim, N.-H. Cho, G.-B. Jeong, E. Bengtsson, and H.-K. Choi, "3D Texture Analysis in Renal Cell Carcinoma Tissue Image Grading," *Comput. Math. Methods Med.*, vol. 2014, p. 536217 (12 pp.), 2014.

[25] D. Xu, A. S. Kurani, J. D. Furst, and D. S. Raicu, "Run-length Encoding for Volumetric Texture," in *The 4th IASTED International Conference on Visualization, Imaging, and Image Processing*.

[26] L. Lu, W. Lv, J. Jiang, Q. Feng, A. Rahmim, and W. Chen, "Robustness of Radiomic Features in Choline and FDG PET/CT Imaging of Nasopharyngeal Carcinoma: Impact of Segmentation and Discretization.," *Mol. Imaging Biol.*, vol. 18, no. 6, pp. 935–945, 2016.

[27] N. Thein, H. A. Nugroho, T. B. Adji, and K. Hamamoto, "An Image Preprocessing Method for Kidney Stone Segmentation in CT Scan Images," in *CENIM 2018*, 2018.

[28] Y. F. Riti, H. A. Nugroho, S. Wibirama, B. Windarta, and L. Choridah, "Feature Extraction for Lesion Margin Characteristic Classification from CT Scan Lungs Image," in *1st International Conference on Information Technology, Information Systems and Electrical Engineering (ICITISEE),* 2016, pp. 54–58.

Author

Biography

The author graduated with a Bachelor of Engineering degree from TU (Toungoo) in 2008. She completed her Master of Engineering in Information Technology (11th Batch) at Mandalay Technological University (MTU) from 1.6.2012 to 3.10.2014. She got her Ph.D. (13th Batch) at Yangon Technological University (YTU) on 26.5.2023. The author began her academic career as a Demonstrator at TU (Toungoo) on 8.6.2009 and later served as a Demonstrator at PTU from 12.6.2009 to 30.9.2015. She was promoted to Assistant Lecturer at PTU from 1.10.2015 to 31.3.2016 and continued in the same role at TU (Toungoo) from 4.4.2016 to 3.12.2018. She joined West Yangon Technological University (WYTU) as a Lecturer on 4.12.2018 and was promoted to Associate Professor on 20.9.2021, a position she held until 11.10.2024. Since 14.10.2024, she has been serving as an Associate Professor at TU (Toungoo). Her research has been published in prestigious journals, including "Mandalay Technological University Journal of Science, Engineering and Technology, 2021", "Yangon Technological University Journal of Engineering, 2022", and "Journal of Engineering Technology and Applied Physics, 2023". She has also presented her work at "The 24th International Computer Science and Engineering Conference, 2020". Her research focuses on 3D CT imaging, with contributions such as the removal of unwanted objects, automated size measurements, density estimation, and analysis of kidney stone heterogeneity. Her current research interests include advanced image processing techniques for medical applications.

AMAZON PRODUCT REVIEWS SENTIMENT ANALYSIS USING LEXICON

Khin Kyawt Kyawt
University of Computer Studies, Magway, Myanmar
khinkyawtkyawt155@gmail.com

ABSTRACT

During the past decades, online market places have been popular. The online sellers and merchants request their customers to express their opinions about the products. Nowadays, individual and grouping depend heavily on website for consumers' reviews in their agreement on buying the product. Product manufacturer also needs to take time for analyzing the huge number of opinions. This paper expresses about the sentiment analysis, the process of mining the texts, in order to distinguish the extract written by the user. So, this paper proposes the classification of product reviews whether they are positive or negative or neutral by using lexicon and Naïve Bayes classifier. The objectives of this study are threefold: (1) accurately classify the sentiment polarity of reviews, (2) effectively identify customer attitudes, and (3) efficiently analyze large volumes of product reviews. This paper proposes a framework for reviews data using Vander lexicon-based approach. Positive reviews are found the more and negative reviews are found the least in this paper.

KEYWORDS

Sentiment analysis, Vander lexicon, text classification, Opinion mining

1. INTRODUCTION

Nowadays, Twitter, Facebook, Blog and Amazon have become a vital role of human living in recent day. People can share their opinion (sentiment analysis) on each and every happening of the life. Thus sentiment analysis is useful to extract and understand their attitudes on certain topics.

Lexicon-based approach is a straightforward and factual approach to Sentiment Analysis. Lexicon-based signify the numbers of positive and negative words in the text and the most frequently used will be counted.

For classification with Machine learning approach, positive, negative and neutral words will need to be pre-labeled before it can be applied to actual classification task. Machine learning uses classifiers such as Naïve Bayes, SVM, etc. Lexicon-based methods can be used to automatically label data, which can then be used to train machine learning models. This is particularly useful when labeled data is scarce. Lexicon-based approach is used in this paper. It gives off recommendations for eliminating the negative aspects of individuals.

The more the size of training data, the higher accuracy. This paper expresses the following facts. In section 2, we express background theory and in section 3, we express related work. In section 4, we explain the proposed technique. In section 5, steps of proposed approach are discussed.

2. BACKGROUND THEORY

Sentiment analysis is opinion mining. It is also a natural language processing problem and used to extract subjective information from texts and to analyze people's opinion, sentiments, evaluation towards entities such as materials, servicing, organization. The aims of sentiment classification to classify positive, negative and neutral words in the reviews. It applies a machine learning approach, a lexicon-based approach and hybrid approach in this paper.

There are three levels in sentiment analysis: Document level, Sentence level and Aspect level. Document level is used to classify a whole document which expresses a positive or negative sentiment. Sentence Level is used to classify each sentence that expresses a positive, negative or neutral opinion. Aspect Level is used to classify based on the facts.

3. Related Works

The purpose of this paper is to classify amazon reviews as positive, negative and neutral. It uses two approaches such as lexicon-based approach and machine learning approach. Lexicon-based approach performs sentiment analysis at document level by calculation the sentiment score of the product reviews that are already defined in lexicon to obtain training set.

Thakare Ketan Lalji and Sachi N. Deshmukh (2016) discuss the literature survery related to this paper to this paper, and the methodologies for twitter sentiment detection, in the work "Twitter Sentiment Analysis using Hybrid Approach." They show the results of experiment they done on different twitter datasets.[1]

In the research "Twitter Sentiment Analysis for Product Review Using Lexicon Method" by Amlan Chakrabarti and Paramita Ray (2017), they propose a framework for sentiment analysis using R software which can analysis sentiment of users on Twitter data using Twitter API.They have done both document level and aspect level analysis based on the proposed methodology, which helped in decision making.[2]

The study "Sentiment Analytics: Lexicons Construction and Analysis" by Bo Yan (2017) discusses about the specialized lexicon for the petroleum domain. It is hypothesized that coupling a specialized lexicon to a general lexicon, such as SentiWordNet, will produce better results. The results suggest that this hypothesis is supported.[3] The results from the study "Sentiment Classification on Amazon reviews using machine learning approaches" by Sepideh Paknejad (2018) showed that in terms of accuracy the SVM approach achieves better results than Naïve Bayes approach when the whole data set was used as training and testing data set. However, both algorithms reached promising accuracies of at least 80% [4].

The work "Sentiment Analysis on IMDb Movie Reviews Using Hybrid Feature Extraction Method" by H.M. Keerthi Kumar, B.S. harish, H.K. Darshan (2018) clearly differentiate between a positive review and negative review. Thus, results obtained are highly promising both in terms of space complexity and classification accuracy.[5] Machine learning approach includes SVM, NB, Maximum Entropy and KNN. This paper use lexicon-based approach. Removing the punctuations, emoji and transformation of upper case to lower case can be conducted After noise removal, we use Vader sentiment analysis tool.

4.THE PROPOSED FRAMEWORK

To improve the performance of sentiment analysis we use the following Figure 1.

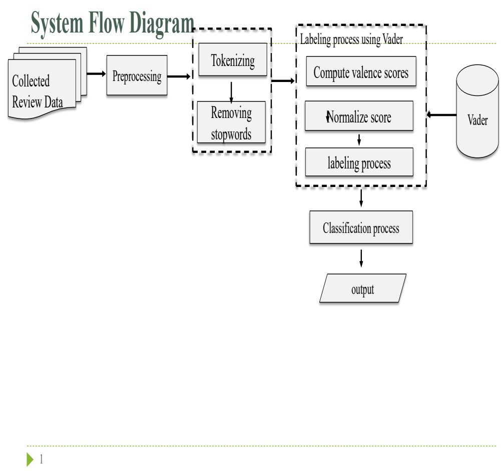

Figure 1. Workflow for sentiment Analysis

STEPS OF PROPOSED APPROACH

The Sentiment Analysis of reviews includes following steps.

4.1 Data Collection

The data is obtained by scraping with google chrome web scraper and manually to store required data into review data collection.

4.2 Pre-processing

Unnecessary data will need to be cleaned from the reviews data. This stage comprises of removing the punctuations, emoji and transformation of upper case to lower case. Then, we use the method word tokenize () to split a sentence into words. A stop word is a commonly used word (such as "the", "a", "an", "in"). After noise removal, we obtain the training set by using Vader sentiment analysis tool. The process of stemming reduces the inflection words in the language.

4.3 Feature Extraction

Feature extraction has two stages namely– lexicon-based feature extraction and Machine learning based features extraction.

Lexicon-based methods extract features based on a predefined dictionary of sentiment words. Machine learning methods extract features from training data, allowing them to learn more complex and context-aware representations of sentiment. The choice between these approaches depends on the specific application, the availability of training data and the desired level of accuracy and interpretability.

Rule-based sentiment analysis tool used for text sentiment analysis is VADER (Valence Aware Dictionary and Sentiment Reasoner) and is also a lexicon. The approach maps words to sentiment by building not only a lexicon but also a dictionary of sentiment. The system uses this dictionary to analyse the sentiment of product review text.

4.4 Compute Positive, Negative, Neutral

Table 1: Product Review Content

Review ID	Content
Review 1	The phone is super cool.
Review 2	It wastes your money buy this defective phone.
Review 3	I received defective piece
Review 4	This is a really nice phone; the quality of the camera is amazing.
Review 5	Expensive, but is a great cellphone with advance technology.
Review 6	It is a product.
Review 7	It is normal device.

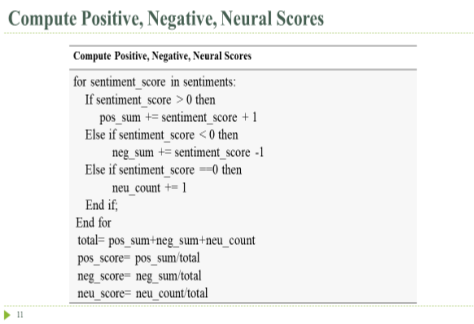


```
for sentiment_score in sentiments:
   If sentiment_score > 0 then
       pos_sum += sentiment_score + 1
   Else if sentiment_score < 0 then
          neg_sum += sentiment_score -1
   Else if sentiment_score ==0 then
          neu_count += 1
   End if;
End for
total= pos_sum+neg_sum+neu_count
pos_score= pos_sum/total
neg_score= neg_sum/total
neu_score= neu_count/total
```

Figure 2: Positive, Negative, Neutral Score

5. Total Score

The total score (sentiment score) is calculated by summing the sentiment (valence) scores of each word in the lexicon. Calculate total score of all positive valence scores and all negative valence scores: total score, x

$$x = \sum_{i=1}^{n} pos\_valence\_score + neg\_valence\_score$$

The total score is modified according to the rules, and then normalized to be between -1 and +1.

5.1 Normalize Score: Compound score for Analyzing Sentiment

Normalize the score to get **compound score**:

$$norm\_score = \frac{x}{\sqrt{x^2+\alpha}} \qquad (1)$$

where x = sum of valence scores and α = Normalization constant value is 15.

5.2 Compound Score

Typical threshold values are:

(compound score >=0.05) positive sentiment:

(compound score>-0.05)and (compound score<0.05) neutral sentiment:

(compound score<=-0.05) negative sentiment:

The pos, neu, and neg sentiment scores are texts that fall in each category.

6. CLASSIFICATION

Classification is the process of assigning labels to the reviews. Data collection, pre-processing, feature extraction using lexicon-based approach are described in this paper And then the texts are classified as positive, neutral and negative. Typically, threshold values are: compound score values greater than 0.05 is positive, compound score values between -0.05 and 0.05 is neutral and compound score values under -0.05 is negative. Explanation of proposed Approach.

Step 1: Data Collection

The data is obtained by scraping with google chrome web scraper and manually to store required data into review data collection.

Table 2: Sentiment Valence Score

Sentiment Word	Valence Score
cool	1.3
nice	1.8
Super	2.9
good	1.9
bad	-2.5
terrible	-2.1
defective	-1.9
great	3.1
amazing	2.8
poor	-2.1

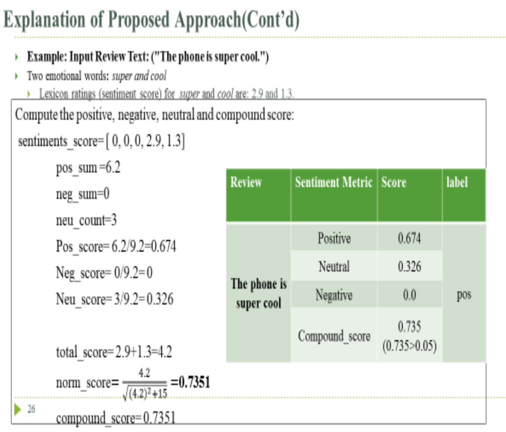

Figure 2: Positive Sentiment review

6.1 Explanation of Double Negatives Sentences

A double negative is using two negative words or phrases in a sentence. A double negative is produced when we use two negative words in a clause so that it would create a positive effect. This is not a simple sentiment problem, it's total natural language understanding (negation, context, etc.). Some examples of double negatives:

She is not incorrect.

Time is not unlimited.

The phone is not poor.

Negation Handling is important part while sentiment analysis. Many sentences contain the negation word that shifts the polarity of the sentence. This approach solves the problem when the system find any negation term in sentence. And the system multiplies the negation scalar value to valence scores of sentiment word. (Neg_scalar= -0.74)

Example: Input Review Text. ("The phone is not poor.")

Lexicon ratings (sentiment score) for poor is -2.1.

Explanation of Negatives Sentences (Cont'd)

Example: Input Review Text: ("The phone is not poor.")

Lexicon ratings (sentiment score) for poor is -2.1.

Compute the positive, negative, neutral and compound score

Neg_scalar= -0.74

sentiments_score= [0, 0, 0, 0, -2.1] => = [0, 0, 0, 0, 1.554]

pos_sum =2.554

neg_sum= 0

neu_count= 4

Pos_score= 0.39

Neg_score= 0

Neu_score=0.61

total_score= 1.554

norm_score= $\frac{1.554}{\sqrt{(1.554)^2+15}}$ = **0.372**

compound_score= 0.372

Review	Sentiment Metric	Score	label
The phone is not cool	Positive	0.39	pos
	Neutral	0.61	
	Negative	0	
	Compound_score	0.372(0.372> 0.05)	

29

Figure 3: Double Negative Sentence review

6.2 Labeling process using Vader

Labeling process using Vader

Review Text	Pos_score	Neg_score	Neu_score	Norm_score	Compound_score	label
Review 1	0.674	0	0.326	0.7351	0.7351	pos
Review 2	0	0.325	0.675	-0.5228	-0.5228	neg
Review 3	0	0.592	0.408	-0.4404	-0.4404	neg
Review 4	0.408	0	0.592	0.7841	0.7841	pos
Review 5	0.447	0	0.553	0.7684	0.7684	pos
Review 6	0	0	1	0	0	neu
Review 7	0	0	1	0	0	neu

30

Figure 4: Labeling process for training reviews

Input Review Text:

Review8: It is normal one.

Review9: Defective product

Review10: Nice phone perfect one

Labeling process using Vader

Review Text	Pos_score	Neg_score	Neu_score	Norm_score	Compound_score	label
Review 8	0	0	1	0	0	neu
Review 9	0	0.744	0.256	-0.4404	-0.4404	neg
Review 10	0.765	0	0.235	0.7579	0.7579	pos

31

Figure 5: Labeling process for testing reviews

The input review8 results is neutral.

The input review9 results is negative.

The input review10 results is positive.

6.3 Performance Evaluation

The shoes of comments reviews data 1000 obtained from Amazon. We collected reviews from 1000, 700 reviews use for training data and 300 reviews use for testing data. We used F-measure, Precision, Recall, and Accuracy to analyze the performance of reviews. F-measure is a value between Precision and Recall. Accuracy focuses on the aggregates of exact prophecies. Precision and Recall are effective ways to evaluate the correction of classes.

PR represents precision,

RE is Recall,

FM is F-measure,

True Positive is TP,

False Positive is FP,

True Negative is TN,

False Negative is FN,

Accuracy is ACC Respectively,

$$PR=\frac{TP}{TP+FP}$$

$$RE=\frac{TP}{FN+FP}$$

$$FM=2\frac{PR.RE}{TP+FP}$$

$$ACC=\frac{TP+TN}{TP+FP+TN+FN}$$

Table 3. Four matrix calculation results

	Positive	Negative	Neutral
Accuracy	96%	96%	96%
Precision	95%	95%	90%
Recall	95%	95%	90%
F-Measure	95%	95%	90%

These evaluation results show 96% accuracy in sentiment calculation.

7. CONCLUSION

This paper has explored the sentiment analysis of the product reviews from Amazon by using Lexicon-Based Approach. We can realize the importance of the Sentiment Analysis. Thus, this paper aims to conduct Sentiment Analysis of product reviews by classifying reviews into positive, negative and neutral sentiment. Based on the results of this paper, positive sentiment is mostly found and the least one is negative sentiment. Moreover, Sentiment Analysis enables the company to find out the customer's opinion about its product. Sentiment Analysis helps to obtain the solutions and satisfactions from customer.

ACKNOWLEDGMENT

First and foremost, I would like to express my gratitude for the permission to submit this paper. I would also like to offer my deep and sincere gratitude to my supervisor her effort, time in reading and patience to help me in accomplishing this paper. It was a great privilege and honor to work and study under her guidance. Furthermore, I am extremely grateful to my companions who have given me their precious ideas and invaluable knowledge throughout the paper. Finally, I am extending my heartfelt thanks to my family for their encouragements and support to accomplish this paper.

REFERENCES

[1] SEPIDE PAKNEJAD, Sentiment classification on Amazon reviews using machine learning approaches. DEGREE PROJECT IN TECHNOLOGY, FIRST CYCLE, 15 CREDITS STOKCKHOLM, SWEDEN 2018.

[2] Kalpana Algotar and Ajay Bansal, Detecting Truthful and Useful consumer Reviews for Products using Opinion Mining. Arizona State University, Mesa AZ 85212 USA [Kalgotar, ajay.banssal] @ asu.edu

[3] H. M. Keerthi Kumar1, B. S. Harish2, H. K. Darshan3, Sentiment Analysis on IMDb Movie Reviews Using Hybrid Feature Extraction Method.JSSRF, JSS TI Campus, Mysuru, Karnataka (India)2 Department of Information Science and Engineering, JSS Science and Technology University, Mysuru, Karnataka (India)3 Department of Information Science and Engineering, Sri Jayachamarajendra College of Engineering, Mysuru, Karnataka (India)

[4] Thakare Ketan Lalji1, Sachin N. Deshmukh, Twitter Sentiment Analysis Using Hybrid Approach.1, 2Department of Computer Science and T,Dr. Babasaheb Ambedkar MarathwadaUniversity, Aurangabad.

[5] Bo Yuan, Sentiment analytics: Lexicons construction and analysis (2017). Masters Theses. 7668.

[6] Paramita Ray1and Amlan Chakrabarti2, Twitter Sentiment Analysis for Product Review Using Lexicon Method.2017 International Conference on

Data Management, Analytics and Innovation (ICDMAI) Zeal Education Society, Pune, India, Feb 24-26, 2017

[7] Taboada, M., Brooke, J., Tofiloski, M., Voll, K., & Stede, M. 2011. Lexicon- based methods for sentiment analysis.Comput Linguist. 37, (2): 267--307.

[8] A. Ortigosa, J. M. Martín, and R. M. Carro. “Sentiment analysis in Facebook and its application to e- learning.” Computers in Human Behavior Vol. 31, pp.527-541. 2014.

[9] Alan R. Hevner, Salvatore T. March, Jinsoo Park, Sudha Ram. (2004). Design

[10] Science in Information Systems Research. DIS Quarterly, 75-105.

[11] S. ChandraKala1 and C. Sindhu2, “OPINION MINING AND SENTIMENT CLASSIFICATION: A SURVEY,”.Vol .3(1), Oct 2012,420-427

[12] Richard A Berk. Statistical learning from a regression perspective. Springer, 2016.

[13] Multi Perspective Question Answering (MPQA). OnlineLexicon“http://www.cs.pitt.edu/mpqa/subj_lexicon.html”.

[14] Ding, X., Liu, B., & Yu, P.S. 2008. A holistic lexicon-based approach to opinion mining. In: Proceedings of the International Conference on Web Search and Web Data Mining (WSDM '08). ACM, New York, NY, USA. pp. 231-240

[15] Maharani, W. (2013). Microblogging sentiment analysis with lexical based and machine learning approaches. Information and Communication Technology (ICoICT), 2013 International Conference (pp. 439-443). Bandung: IEEE.

[16] Kyomin Jung, Byoung-Tak Zhang, Prasenjit Mitra. (2015). Deep Learning for the Web. the 24th International Conference on World Wide Web (pp. 1525-1526). International World Wide Web Conferences Steering Committee

Authors

Biography

I am Daw Khin Kyawt Kyawt. I began my employment at the Government Computer College, Magway on the 9th of March, 2005. I got B.Sc (Maths) in 2002, D.C.Sc (Q) in 2004. I am a Master Degree Holder specializing at information science in 2022. I am an assistant lecturer at University of Computer Studies (Bamaw) at FCST Department. Now, I am on duty as an attachment at University of Computer Studies, Magway because of current situation. I got one paper in Volume 03, Issue 02 National Journal of Parallel and Soft Computing Organized by University of Computer Studies, Yangon in December, 2022.

SYNTHESIS AND SURFACE FEATURES OF MOLARITY BASED ZNS-ZNO NANOCOMPOSITE FILMS

Yaemar Soe[1], Thaung Hlaing Win [2], and Zin Min Myat [3]

[1,2] Department of Physics, Pakokku University
[3] Department of Physics, West Yangon University

yaemarsoe219@gmail.com, thaung.naing001@gmail.com

ABSTRACT

Zinc Sulfide-Zinc Oxide (ZnS-ZnO) nanocomposite powders have been firstly prepared by varying the molar ratios at different temperatures for 2 h by co-precipitation method. The films of ZnS-ZnO nanocomposite have been fabricated on silicon substrate by spin coating technique. X-rays Diffraction (XRD) has been used to examine the phase formation and crystal structure of ZnS-ZnO samples. The morphology and microstructure properties of ZnS-ZnO samples have been characterized by Scanning Electron Microscopy (SEM). The molarities dependence of ZnS-ZnO nanocomposite films have been promised for future optoelectronic, solar cell applications and ferroelectric materials.

KEYWORDS

Synthesis, surface feature, ZNS-ZNO powder, films, XRD, SEM.

1. INTRODUCTION

As important II-VI semiconductor, ZnO and ZnS contain only earth- abundant elements and have been intensively studied in a wide range of UV sensors, lasers, field emitters, nanogenerators, solar cells, photocatalysis, etc. Unfortunately, both ZnO and ZnS had a large band gap (Eg =3.37eV and 3.67 eV for ZnO and ZnS, respectively), and thus there is almost no adsorption in the visible light region, which largely limits their application in visible-light- driven water splitting. Recently, the heterostructures of ZnO and ZnS have attracted theoretical and experimental interest because the combination of these two wide band gap semiconductors can yield a novel material with the photoexcitation threshold energy lower than the individual components, leading to improved physical and chemical properties. According to our knowledge, apart from ZnS/ZnO hybric nanowires, few literatures were reported on ZnS/ZnO nanocomposites used as effective catalysts for visible light photocatalytic hydrogen production [1].

The preparation of reported ZnS/ZnO hybrid nanowires was conducted by a high-temperature hydrothermal method involving the use of expensive and toxic, which makes it difficult to be scaled up and does serious harm to environmental protection and people's health. Therefore, new preparation strategy of ZnS/ZnO heterostructure is greatly desirable to make the best use of ZnO and ZnS for solar energy application [2].

Thin film plays an important role in the nanotechnology and nanoscience development. Solar cell is an important application of thin film technology from the point in view of global energy crunch, which converts the energy of the solar radiation into useful and constructive electrical energy. Window material is the main condition for thin film solar cells, which allows passing through; the visible region of solar spectrum but reflects the IR Radiation [3].

A large number of different deposition techniques are used for the construction of thin films for structural, morphological and optical applications. Thin film silicon photovoltaics are one of the emerging technologies to produce electricity from sunlight. Materials with different optical band gaps are synthesized by changing the silicon phase and by forming compounds with other elements like carbon or germanium. Materials with different optical band gaps can be easily combined to form multiple stacks that exploit a larger part of the solar spectrum increasing the efficiency of the photovoltaic device [4].

2. EXPERIMENT

2.1. Synthesis ZnS-ZnO Nanocomposite Powder

Zinc oxide (ZnO), zinc sulphide (ZnS), and sodium hydroxide (NaOH) were used as starting materials in this study. All chemical reagents used in this experiment were obtained from commercial sources as guaranteed grades.

These chemical have been used as received without further purification. ZnS-ZnO nanocomposites were prepared by co-precipitation method. Firstly, the starting materials were weighed with digital balance. Distilled water is used as solvent.

Suspension solutions of homogeneous ZnS-ZnO nanocomposite were synthesized by mixing of aqueous solution of ZnO and aqueous solution of ZnS. They were stirred vigorously with magnetic stirrer for 7 h [5]. Then, sodium hydroxide (NaOH) aqueous solution with different molarities (0.2 M-0.4 M) was gently added to the above precursor solution under vigorous stirring until pH reached to 11.

The reaction mixture was refluxed for 2 h at 80 °C. The as-prepared precipitates were filtered with filter papers and washed several times with deionized water to remove the impurity. The prepared precipitates were dried at 120 °C for 1h.

After that, the dried composite powders were annealed in a muffle furnace at 500 °C and 600 °C for 2h. The powders were grinded to obtain smaller size of powders with agate motor for 10 h. These composite nanopowders were characterized by XRD and SEM for phase formation, morphological and structural properties. The block diagram of sample preparation of ZnS-ZnO nanocomposite powder was shown in Figure 1.

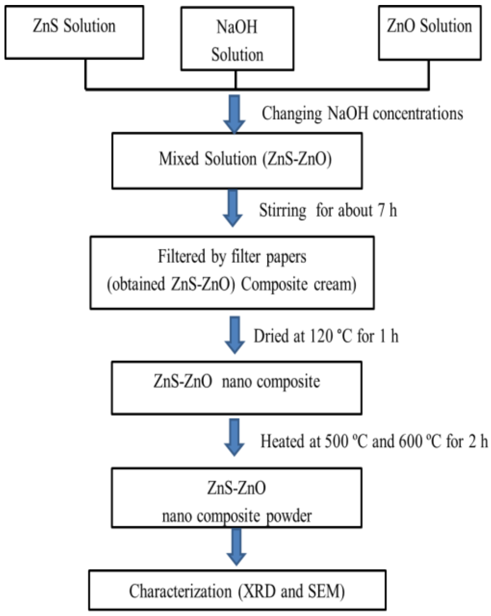

Figure 1. Flow charts of ZnS-ZnO Nanocomposite powder

2. 2. Substrate Preparation for ZnS-ZnO Nanocomposite Thin Films

To prepare the ZnS-ZnO thin films, the substrate preparation was firstly used. Some of the substrate required cleaning before the film deposition because selecting a substrate for deposition of thin films is the most important factor which dictates not only the quality of deposited film, but also the feasibility of growth of the film. When selecting a substrate for thin film deposition the substrate should provide mechanical support only rather than interact with the thin except from sufficient adhesion.

Hence it was important to clean these substrates properly before they were deposited into the film. The p-Si (100) (1 cm × 1 cm) wafer was used as a substrate. Ultrasonic cleaning process was made for clean substrate preparation. The Si wafer was washed in boiling acid acetone (60 °C), then in boiled propanol (50 °C) for 5 min to remove greasy film.

It was immersed in nitric acid HNO_3 for 3 min in order to remove ionic contamination. It was etched in buffered hydrofluoric acid for 2 min to remove oxide films. It was cleaned in distilled water and dried on flat-oven at 100 °C for a few minutes and finally, clean Si-wafer was formed.

2.3. Sample Preparation of ZnS-ZnO Nanocomposite Films

The substrate used in this study was p-Si (100). The p-Si (100) wafer of dimension (1 cm × 1 cm) and thickness of 280-300 µm were used as substrate. Before film fabrication p-Si (100) substrate was cleaned by using ultrasonic cleaning method. The resulting ZnS-ZnO nanocomposites powder was dissolved by using 2-Methoxyethanol. The mixed solution was stirred with magnetic stirrer for 3 h. After that, the precursor solutions which were then coated on silicon substrate by using spin coating technique as shown in Figure 2. The operation parameters were shown in Table 3.1. The well dissolved precursor solutions were poured onto the cleaned p-Si (100) substrate which was placed on substrate holder of spinner. The spin speed was 2000 rpm, the substrate temperature was 120 °C and the spinning time was 30 s. After fabrication, ZnS-ZnO thin films were annealed at the temperature 500 °C and 600 °C respectively for 2 h. Finally, ZnS-ZnO nanoscale thin films were successfully obtained. Surface morphology and grain size of the thin films were investigated with Scanning Electron Microscope (SEM). The block diagram of ZnS-ZnO thin films were as shown in Figure 2. Figure 3 shows the experimental procedure of ZnS-ZnO nanocomposite Films.

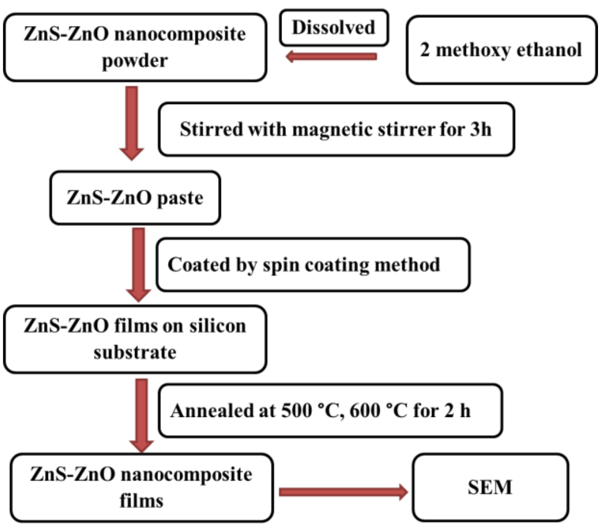

Figure 2. The flow charts of ZnS-ZnO thin films

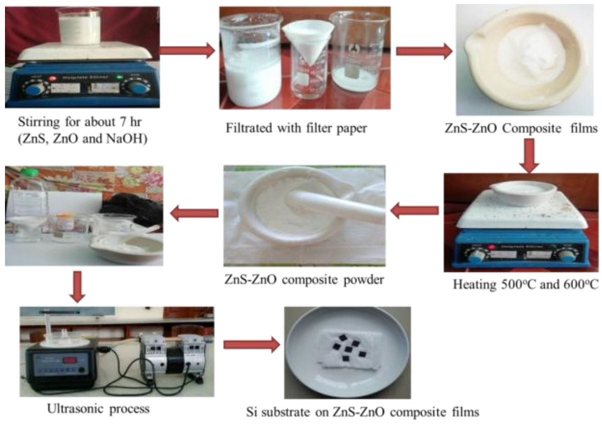

Figure 3. The experimental procedure of ZnS-ZnO composite films

3. CHARACTERIZATION

3.1. X-ray Diffraction (XRD) Measurement

The crystalline structure of ZnS-ZnO powder was examined using X-ray diffraction (XRD) technique. The peak heights are roughly proportional to the ray intensity. The grain size, texture of grains, crystal defect densities phase structure developments, lattice parameters and "d" values of the calcined ZnS -ZnO nanocomposite samples are investigated by X-ray diffractometer using Cu-K_α = 1.54056 Å radiation. The photograph of the RIGAKU-RINT 2000 X-ray Diffractometer was shown in Figure 4.

Figure 4 The photograph of the RIGAKU-RINT 2000 X-ray Diffractometer

3.2. Scanning Electron Microscopy (SEM)

A scanning electron microscope (SEM) is a type of electron microscope that produces images of a sample by scanning it with a focused beam of electrons. Specimens can be observed in high vacuum, low vacuum and in environmental SEM specimen can be observed in wet condition. The photograph of SEM machine was shown in Figure 5.

Figure 5. Photograph of JEOL-6000 Scanning Electron Microscope

4. RESULTS AND DISCUSSION

4.1. XRD Analysis of ZnS-ZnO Nanocomposite Powders

Structural properties of ZnS-ZnO powder were examined by XRD technique. It was performed using monochromatic CuKα radiation (λ = 1.54056 Å) operated at 40 kV (tube voltage) and 30 mA (tube current). Simple was scanned from 10º C to 70º C in diffraction angle 2θ with a step-size of 0.01º. The XRD profiles of ZnS-ZnO powder with different molar ratios were shown in Figure 6 (a-c) and 7 (a-c) for reaction temperature 500º C and 600º C. According to Figures, the upper side of XRD profiles were represented the observed profile while the lower side indicated the standard/reference JCPDS (Joint Committee on Powder Diffraction Standard) library file. There were nine diffraction XRD profile. All diffracted peak of observed spectrum well match with those of standard peaks. According to XRD pattern from figures the peaks were clearly observed. They were compared the data with the library or standard file. The most dominant peak was also occur at (101) for all powders. The crystallographic phases of samples were in good agreement with the typical hexagonal structure. The crystallite size was determined by the Debye-Scherrer formula.

$$G = \beta\lambda / (FWHM \times \cos \theta_B)$$

The XRD profile of ZnS-ZnO nanocomposite powder were also clearly observed for different molarities of NaOH aqueous solution compared the data with the standard or library file the most dominant peak was also occur at (101) for all samples On the XRD pattern lattice constant, lattice distortion diffraction angles, FWHM and crystallite size calculated and listed in Table 1.

Table 1. Lattice parameters and lattice distortion (c/a ratio) of ZnS-ZnO nanocomposite powder

ZnS-ZnO	Dominant peak	Crystalline size (nm)	FWHM (deg)	Lattice Parameters (A°)	
				a-axis	c-axis
0.2M (500 °C)	(101)	52.17	0.160	3.2680	5.2300
0.3M (500 °C)	(101)	45.13	0.185	3.2480	5.2000
0.4M (500 °C)	(101)	43.94	0.190	3.2473	5.2027
0.2M (600 °C)	(101)	44.89	0.186	3.2450	5.1991
0.3M (600 °C)	(101)	50.60	0.165	3.2455	5.2029
0.4M (600 °C)	(101)	46.38	0.180	3.2449	5.2017

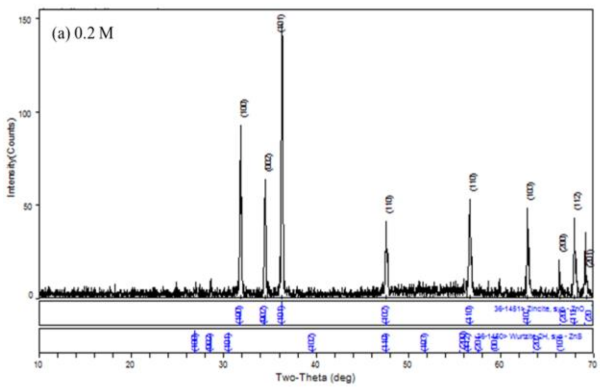

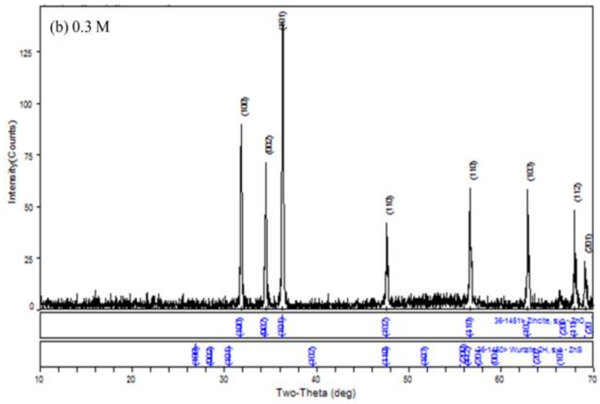

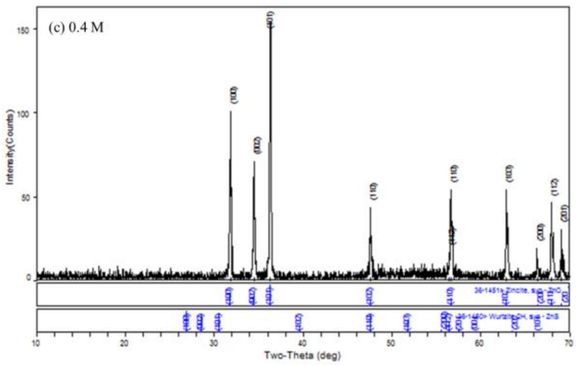

Figure 6 (a-c). XRD spectrum of ZnS-ZnO (0.2M, 0.3 M, 0.4 M) composite powder at 500ºC

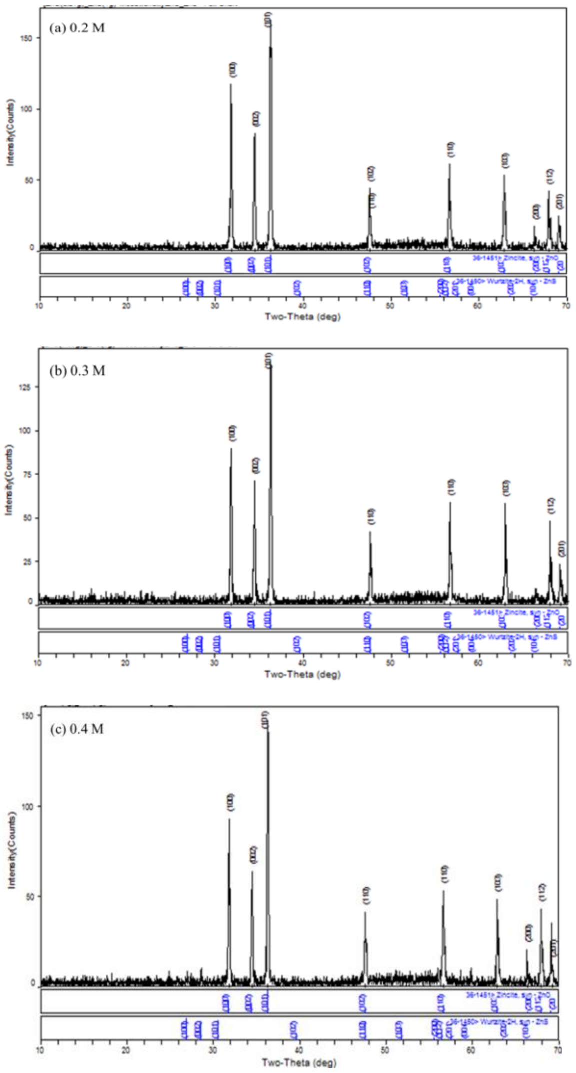

Figure 7 (a-c). XRD spectrum of ZnS-ZnO (0.2 M, 0.3 M, 0.4M) composite powder at 600 ºC

4.2. SEM Analysis of ZnS-ZnO Nanocomposite Powders

SEM images of ZnS-ZnO powders at different molar ratios at 500 ºC and 600 ºC were shown in Figure 8 (a-c) and Figure 9 (a-c). As the detail analysis of SEM image, it was found that flat and crack free and uniform particle size. This image consisted of circular features known as rosette structure in microstructure. The grain sizes of ZnS-ZnO (0.2M), ZnS-ZnO (0.3 M) and ZnS-ZnO (0.4M) at 500 ºC were found to be 0.537 µm, 0.594 µm and 0.606 µm respectively.

At 600 ºC, ZnS-ZnO (0.2M), ZnS-ZnO (0.3M) and ZnS-ZnO (0.4M) were found to be 0.438 µm, 0.463 µm, 0.594 µm respectively. Both microstructures were oriented toward right side and uniform grain distribution was clearly observed. The formations of grains were changed by the concentration of different molar ratios.

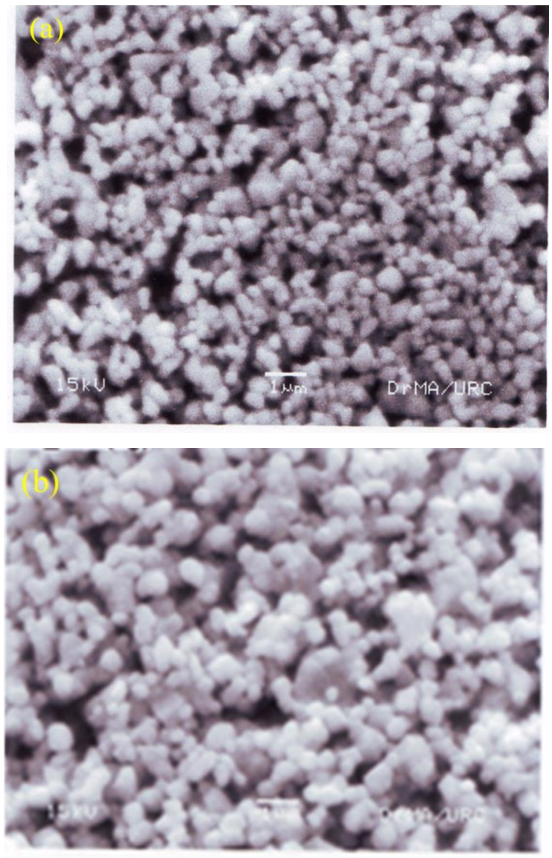

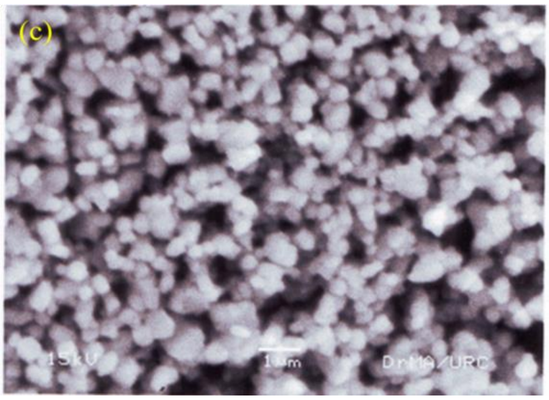

Figure 8 (a-c). SEM image of ZnS-ZnO composite powder (0.2M, 0.3M, 0.4M) at 500 ºC

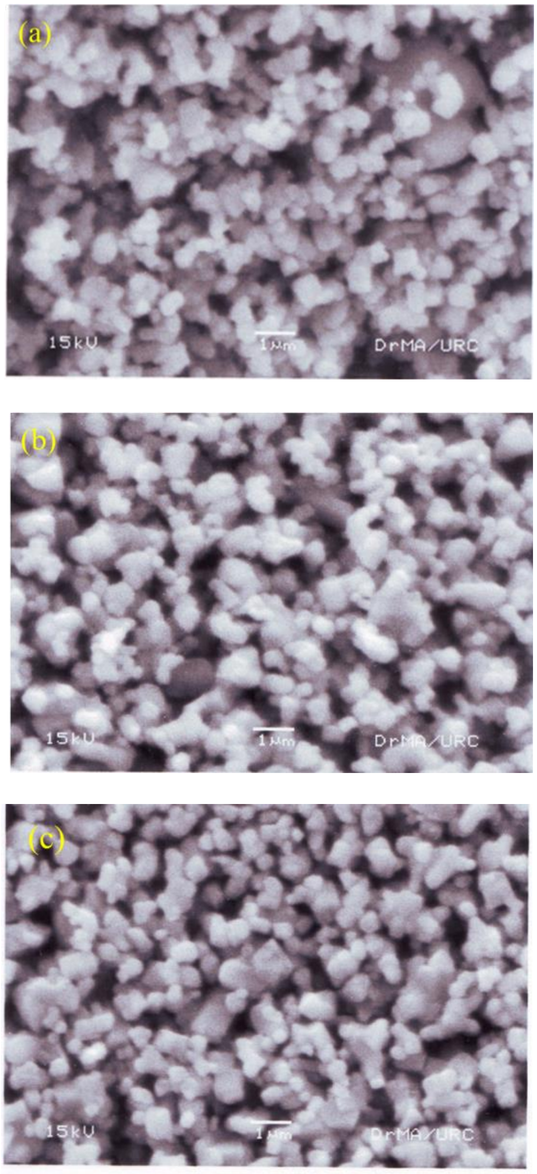

Figure 9 (a-c). SEM image of ZnS-ZnO composite powder (0.2M, 0.3M, 0.4M) at 600 ºC

4.3. SEM Analysis of ZnS-ZnO Nanocomposite Films

Surface morphology of ZnS-ZnO nanocomposite films on p-Si (100) substrates were carried out by SEM analysis. SEM images of ZnS-ZnO nanocomposite films at different molar ratios at 500 ºC and 600 ºC were shown in Figure 10 (a-c) and 11 (a-c). As the detail analysis of SEM image, it was found that flat and crack free and uniform particle size. This image consisted of circular features known as rosette structure in microstructure. The grain sizes of ZnS-ZnO (0.2M), ZnS-ZnO (0.3M) and ZnS-ZnO (0.4M) at 500 ºC were found to be 0.68 µm, 0.73 µm and 0.81 µm respectively. At 600 ºC, ZnS-ZnO (0.2M), ZnS-ZnO (0.3M) and ZnS-ZnO (0.4M) were found to be 0.72 µm, 0.78 µm and 0.85 µm respectively. From SEM analysis, the surface of the films became rough and greater grain size after annealing different temperatures. On the other side, the achieving relatively films cracking was increased with the increase in greater molarity of NaOH at each temperature. Therefore the formations of grains were changed by the concentration of different molar ratios.

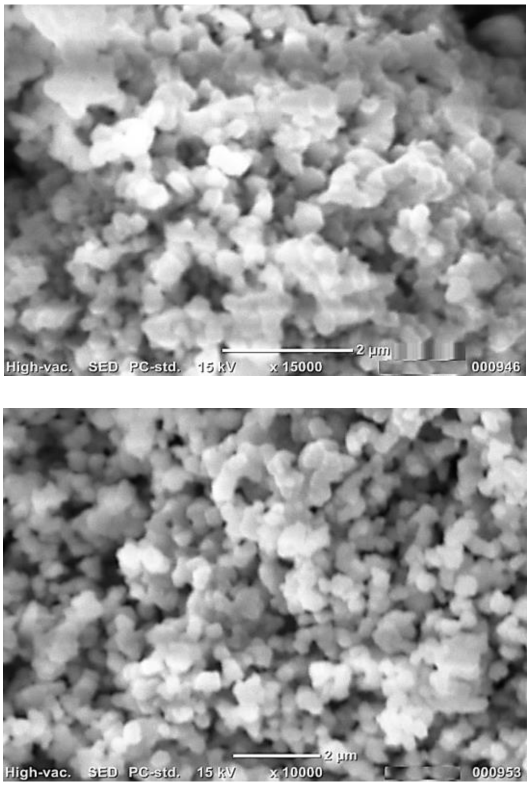

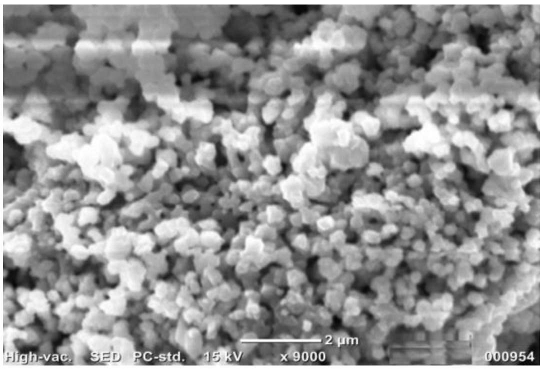

Figure 10 (a-c). SEM image of ZnS-ZnO composite film (0.2 M, 0.3, 0.4M) at 500 ºC

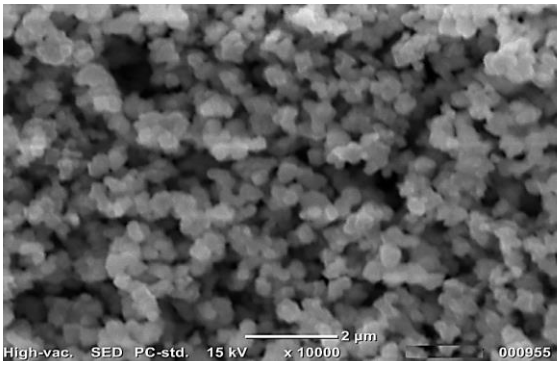

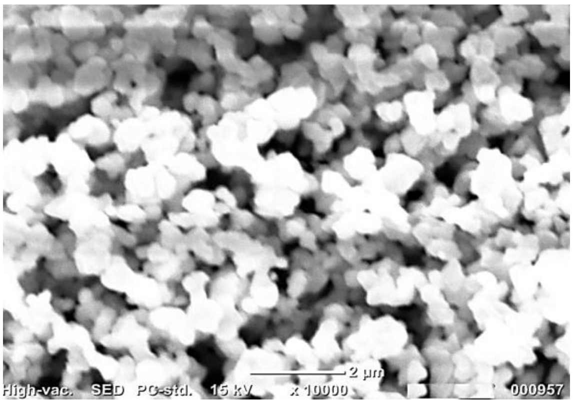

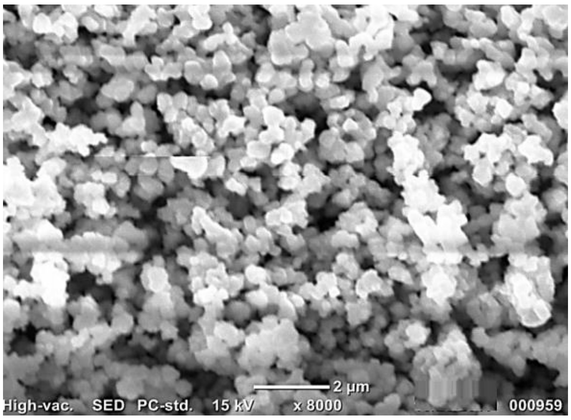

Figure 11 (a-c). SEM image of ZnS-ZnO composite film (0.2, 0.3 M, 0.4 M) at 600 ºC

5. Conclusion

Zinc Sulfide-Zinc Oxide (ZnS-ZnO) nanocomposite powders have been firstly prepared by varying the molar ratios at different temperatures for 2 h by co-precipitation method. The films of ZnS-ZnO nanocomposite were successfully fabricated on silicon substrate by spin coating technique. According to XRD analysis, information lattice parameters, FWHM and crystallite size have been regarded with the as-prepared powders. The crystal structure of ZnS-ZnO powders was observed to be hexagonal for all fabricated powders. According to the SEM images of ZnS-ZnO nanocomposite thin films, they were significantly observed that nanocomposite thin films were successfully formed onto P-type silicon (P-Si) substrates by spin coating method. SEM images were observed that all powders and films were crack-free and showed uniform grain distribution. It was well known that ZnS-ZnO thin film provided a good deposition on Si substrate. From the experimental results, the structural and surface morphology of ZnS-ZnO nanocomposite films on Si substrate were successfully investigated and the properties of ZnS-ZnO thin films were depended on process temperatures and different molarities. The experimental data resulted from this research work are credible and applicable in use for low-cost-Si-based thin film solar cell.

Acknowledgements

We would like to thank Dr Tin Tun Aung, Acting Rector, Pakokku University. We are also thankful to Dr Khin Khin Htoot, (Pro-rector), Pakokku University. We would like to express my gratitude to Dr Win Mar (Professor and Head) and Dr Win Myint Kyu (Professor), Department of Physics, Pakokku University, for their kind permission to give us the opportunity to do research. We would like to express my appreciation to the department of physics, University of Mandalay for their use of research facilities.

References

[1] J. Liu *et al*., Colloids Surf. A, **302** (2007) 276.

[2] H.S. Shin *et al*., J. Colloid Interf. **274** (2004)

[3] J.I. Hussain *et al*., Adv. Mat. Lett. **2** (2011) 188.

[4] S.L. Hsu *et al*., Int. C. Nan. Biosens, **2** (2011)

[5] S. Kpaoor, Langmuir, **14** (1998) 102.

Authors

Biography

First A. Author: Daw Yaemar Soe

Demonstrator

Department of Physics

Pakokku University

First B. Author –Dr Thaung Hlaing Win

Lecturer

Department of Physics

Pakokku University

Second C. Author – Dr Zin Min Myat

Associate Professor

Department of Physics

West Yangon University